DEVELOPMENT OF SCALABLE AND EXPEDITIOUS ADDITIVE MANUFACTURING PROCESS: A SOLUTION TO HIGH PRODUCTION ADDITIVE MANUFACTURING

By

Hoa Xuan Nguyen

A DISSERTATION

Submitted to
Michigan State University
in partial fulfillment of the requirements
for the degree of

Mechanical Engineering – Doctor of Philosophy

2022

ABSTRACT

DEVELOPMENT OF SCALABLE AND EXPEDITIOUS
ADDITIVE MANUFACTURING PROCESS:
A SOLUTION TO HIGH PRODUCTION ADDITIVE MANUFACTURING

By

Hoa Xuan Nguyen

For the past 40 years, metal additive manufacturing (AM) technologies with the capability of fabricating highly complex metal components with virtually no geometrical limitations, have enabled new opportunities in product designs and performance, while reducing total cost and shortening lead time, improving material efficiency and creating more sustainable products. A significant attention and interest of manufacturing industry lies on where metal AM can replace or improve production capability of traditional manufacturing (TM). Currently, the inherent difference between metal AM and TM leads to two separate manufacturing regions: metal AM is best suited for producing complex parts in small quantities while TM dominates high volume production. While metal AM processes are capable of providing individually designed products with a high level of details, TM processes with their fast, precise, and efficient production in combination with the long-established, quality assured, and widely implemented manufacturing techniques makes the competition incredibly difficult for AM when it comes to high volume production.

As metal AM field evolves with an increasing demand in highly complex and customizable products, there is a critical need to fill in the gap in terms of production speed between metal AM and TM processes. This dissertation presents the development of the scalable and expeditious additive manufacturing (SEAM) process, which capitalizes on the advantages of binder jet printing and stereolithography principles to produce a new metal AM processing route. The SEAM process is not only suitable for high production environment but also capable of fabricating components with excellent accuracy and resolution. Once fully developed, the process is well suited to bridge the productivity gap between metal AM and TM processes, making it an attractive candidate for further development and future commercialization as a solution to high production AM.

After several proof-of-concepts, two fully functional prototypes were designed specifically for the processing of metal suspension, and subsequently constructed at Michigan State University. The relationships between cure depth and metal particle size for several metal suspensions were characterized, whose results were used to determine the appropriate processing conditions for each suspension. An innovative 2-step curing strategy was devised and applied to the printing process, which not only prevents sedimentation of metal powder particles in the print bed but also enables the fabrication of overhang geometry without supporting structures. Using the developed printing technique and processing parameters, 3D green objects were successfully fabricated for all the metallic alloys of interests. A series of experiments were subsequently carried out to characterize the thermal decomposition of the photopolymer, whose results were used to develop a debinding cycle that completely removes the binder while maintaining part structural integrity. The activated liquid phase sintering process of SS420 parts were optimized by utilizing analysis of variance, which arrived at an optimal sintering conditions that produce parts with above 99.7 % relative density without any geometrical distortion. For Haynes 214, the supersolidus sintering behavior was characterized with respect to sintering temperature and holding time. The transient deformation behavior of the sintered parts with respect to holding time and temperature was also captured, whose results were capitalized to develop a 2-step sintering technique to produce fully dense parts with complete shape retention. The development of a numerical sintering model, the Olevsky-Skorohod model, was studied and implemented in a finite element analysis software, which can be used to aid the prediction of part density evolution and deformation during the sintering process.

ACKNOWLEDGEMENTS

To Dr. Haseung Chung, for your unwavering support and belief in me, your invaluable patience and constant feedback,

To Dr. Patrick Kwon, for your generous knowledge and expertise,

To my committee, for your guidance and encouragement,

To my partner, Semiha, for being who you are,

To my family, my friends, my colleagues,

To my pets,

And to everyone else that I met along the way,

Thank you,

Hoa

TABLE OF CONTENTS

LIST OF TABLES

LIST OF FIGURES

KEY TO ABBREVIATIONS

AM Additive Manufacturing

BJP Binder Jet Printing

DED Directed Energy Deposition

DLP Digital Light Processing

DMD Digital Micromirror Device

EBM Electron Beam Melting

EDM Electro-discharge Machining

EDS Energy Dispersive X-Ray Spectroscopy

IR Infrared Radiation

ISO International Organization for Standardization

LCD Liquid Crystal Display

LED Light-Emitting Diode

MIM Metal Injection Molding

SEAM Scalable And Expeditious Additive Manufacturing

SEM Scanning Electron Microscope

SLA Stereolithography

SLM Selective Laser Melting

TM Traditional Manufacturing

TGA Thermo-Gravimetric Analysis

ODS Oxide Dispersion Strengthened

PBF Powder Bed Fusion

PM Powder Metallurgy

UMAT User-defined Material Model

UV Ultraviolet

CHAPTER 1

INTRODUCTION

1.1 Introduction

For the past 40 years, metal additive manufacturing (AM) technology with the capability of fabricating highly complex metal components with virtually no geometrical limitations, have enabled new opportunities in product designs and performance, while reducing total cost and shortening lead time, improving material efficiency and creating more sustainable products [1]. A significant attention and interest of the manufacturing industry lies on where metal AM can replace or improve production capability of traditional manufacturing (TM) [2]. Currently, the inherent difference in process principles between metal AM and TM leads to two separate manufacturing regions: (1) metal AM is best suited for producing complex parts in small quantities and (2) TM dominates high volume production [3]. While metal AM processes are capable of providing individually designed product with a high level of details, TM processes with their fast and efficient production with great precision, in combination with the long-established, quality assured, and widely implemented manufacturing techniques makes the competition incredibly difficult for AM when it comes to high volume production [4].

As metal AM field evolves with an increasing demand in highly complex and customizable products [5], there is a critical need to fill in the gap in terms of production speed between metal AM and TM processes. This dissertation presents the development of the scalable and expeditious additive manufacturing (SEAM) process, which capitalizes on the advantages of binder jet printing and stereolithography principles to produce a new metal AM processing route. The SEAM process is not only suitable for high production environment but also capable of fabricating components with excellent dimensional accuracy and resolution. Once fully developed, the process is well suited to bridge the productivity gap between metal AM and TM processes, making it an attractive candidate for future development and commercialization as a solution to high production AM.

1.2 SEAM process working principles: Hybridization of binder jet printing and stereolithography principles

1.2.1 Binder jet printing

Binder jet printing (BJP) is a beamless metal AM technique that forms two-dimensional (2D) geometry by selectively dispensing liquid binding agents on a thin layer of metal powder. The layers are subsequently stacked on a powder bed system to form three-dimensional (3D) green parts (Fig. 1.1). Thermal treatments, including debinding and high temperature sintering, are then carried out on the green parts to achieve the final metal objects [6].

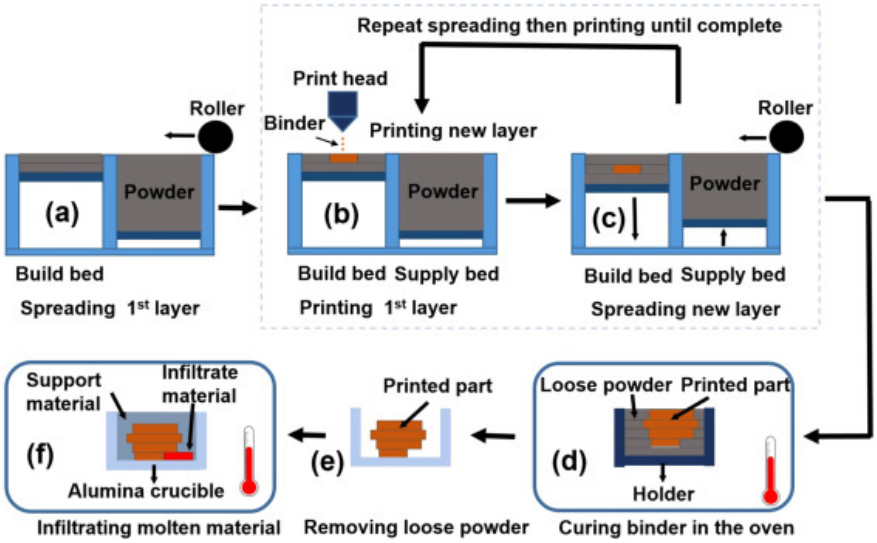

Figure 1.1 Binder jet printing schematic diagram [6].

In comparison to other metal AM technologies, one of the most important advantages of BJP is the ability the fabricate components with isotropic microstructures. BJP is also robust in fabricating green parts with virtually no limitation on the powder material [7]. Moreover, BJP can leverage the mature knowledge based on debinding and sintering of powder metallurgy (PM) and metal injection molding (MIM) technologies, which in many cases is directly applicable to BJP [8].

1.2.2 Stereolithography

Stereolithography (SLA) is an AM technology that involves the irradiation of ultraviolet (UV) light, typically by a laser or digital light projection (DLP) module, on a surface of a photosensitive liquid resin in a 2D pattern. Similar to most free-forming techniques, the patterns are extracted from a computer-aided design (CAD) model, or scanned data from physical parts using imaging technologies such as magnetic resonance imaging (MRI) or computer tomography (CT). Upon UV irradiation, photoinitiator molecules in the resin are excited, forming free radicals and other reactive species, which initiates the cross-linking or photopolymerization of the resin [9]. As a result, the resin solidifies to a defined depth, causing it to adhere to the build substrate or the previous printed layer. The printing substrate then moves vertically a layer thickness increment, and the process repeats until the final solid 3D object is formed (Fig. 1.2).

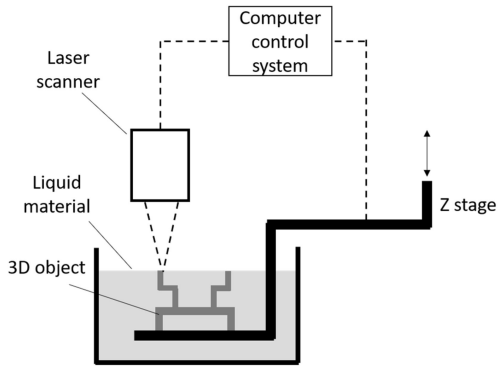

Figure 1.2 Stereolithography process schematic diagram [9].

SLA has been known as the fastest rapid prototyping technology available, due to the unique ability to generate 2D layer geometry in a single exposure using DLP projection [10]. Regarding accuracy and resolution, SLA is superior to all other AM techniques. Commercially available SLA machines are capable of generating extremely fine features with an accuracy of 20 μm, while the smallest details that other AM technologies can achieve typically fall between 50–200 μm in size [11]. Furthermore, the use of two-photon polymerization has recently enabled the ability to fabricate nano-sized features using SLA [12].

1.2.3 SEAM process overview

1.2.3.1 SEAM process working principles

SEAM process combines the working principles of BJP and SLA processes. Figure 1.3 shows the essential steps and workflow of the SEAM process.

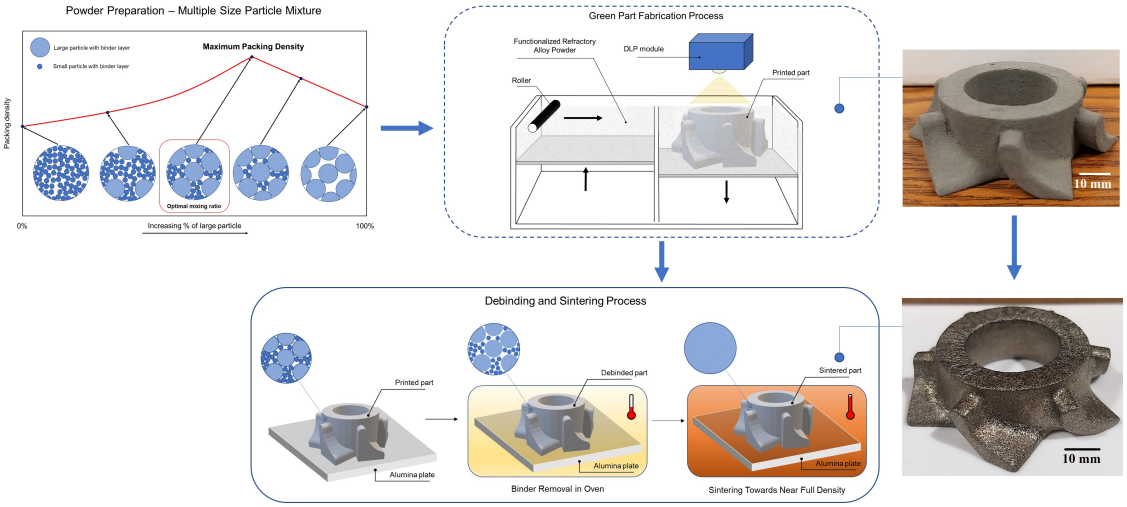

Figure 1.3 SEAM process schematic diagram with basic steps and workflow.

Step 1: A photosentitive suspension, which consists of metal powder and photopolymer resin is formulated. The suspension properties must satisfy several criteria: High powder volume loading, suitable viscosity, and processable in a layer-by-layer fashion using SLA techniques.

Step 2: The suspension is shaped into three-dimensional (3D) green parts using SLA technique. In a layer-by-layer fashion, patterned UV light is irradiated onto the suspension surface, which induces photopolymerization of the resin. The cured resin acts as a binder, holding the metal particles together, forming the desired 2D layer geometry. The irradiation patterns are extracted from the 3D CAD models, similar to other AM techniques.

Step 3: The formed 3D geometry or green part is then subjected to appropriate thermal treatments for binder removal and high temperature sintering in the same manners as BJP process to achieve the final solid metal object.

1.2.3.2 Potential of SEAM process as a high production AM technology

One of the biggest advantages of the SEAM process over any other AM processes is its ability to generate large geometries efficiently. This can be achieved by layer projection using a DLP module to generate a whole layer geometry by a single UV light exposure, which can be capitalized to significantly increase the fabrication speed, surpassing any point-by-point layer creation methods. Fabrication time in BJP and other beam-based powder bed fusion (PBF) processes is directly related to layer geometry, i.e. a large and complex geometry will take more time to be produced [13]. In contrast, DLP projection enables the layer creation time to be a constant value for every layer, regardless of layer geometry. For a large-scaled fabrication system with complex layer geometry or multiple geometries, the use of DLP projection is even more advantageous. PBF systems are also difficult to be employed on a large build area due to beam quality deterioration in the outer area of the print bed [14]. Addition of a second laser or electron beam to increase build size results in an overly complex and expensive system [15].

The second advantage of SEAM process in fabricating metal parts lies in the nature of the process which allows decoupling of the printing process and powder consolidation process. In the same manners as BJP process, SEAM printed parts are consolidated isothermally, which results in residual stress-free parts with uniform final microstructure and mechanical properties. In contrast, the quality of the final parts made from the beam-based PBF processes is difficult to predict due to the complex microstructural evolution and variation throughout the fabrication process [16].

And last but not least, once fully developed into a practical AM technology, the SEAM process offers a significant reduction in cost-per-part of additively manufactured components, which is unattainable with any other currently available AM technologies. The total manufacturing cost of SEAM process and other beam-based PBF processes in general can be categorized into three main areas: initial capital cost (printing system, sintering and/or heat treatment furnaces), fabrication cost (labor, energy consumption), and post processing cost (stress relief, surface finishing to practical standard).

- In terms of the initial capital cost, both PBF and SEAM processes require high temperature furnaces to attain stress relief for PBF processes [17] or to enable sintering for SEAM. However, the PBF printing systems are well-known to be extremely costly due to their complexity in design as well as the use of expensive laser melting system which also requires accurate position control [15]. On the other hand, with its design simplicity and the utilization of an affordable DLP projection curing module, SEAM printing system can be constructed for a fractional cost of PBF systems.

- For fabrication cost, PBF processes follow a linear cost model with respect to fabrication time as part number or volume increases, e.g., the higher number of parts produced or the larger the parts geometry, the longer the time required to fabrication and therefore, the higher the energy consumption and cost. The SEAM process offers a significant reduction in fabrication time, as its layer generation time is independent of number of parts and layer geometry complexity. Moreover, the SEAM process offers cost advantage in fabricating multiple parts simultaneously, due to the ability of debinding and sintering multiple parts in the same heating cycle, which can significantly reduce the energy consumption cost. Additionally, in the situations that the target components require joining of multiple sub-components, SEAM process also offers the unique ability to co-debind and co-sinter multiple green parts together in a single heating cycle to achieve the final joined and assembled components. Producing the same assembled components using PBF processes requires not only the fabrication of sub-components, followed by necessary post processing steps, but also a final mechanical joining and sealing, which further increases both the total time and cost of the manufacturing process.

- For post processing operations, as-built SLM parts require heat treatment for residual stress relief and several following surface finishing steps to attain the desirable quality [17]. On the other hand, due to the isothermal consolidation environment, as-built parts fabricated by SEAM process are residual stress-free, and thus, additional heat treatment to relieve

residual stress or microstructure homogenization is not required. While a few studies have recommended a subsequent step of isostatic hot pressing after the sintering process to further eliminate the residual porosity, this dissertation will demonstrate the feasibility to achieve fully dense parts with a single sintering cycle using multiple different techniques. With regard to surface finish, parts produced by furnace sintering and especially sintering in presence of liquid phase are superior to laser printed parts [18]. As the initial surface roughness plays a critical role in determining the required number of subsequent surface finishing steps [19], SEAM process offers time and cost reduction in attaining the desired final surface quality.

If the SEAM process can be fully realized as a practical metal AM technique, it has the potential to provide a substantial reduction in production time and cost, while being capable of high volume production. Moreover, the advantages on part surface quality, along with uniform microstructure and free of residual stress, can put SEAM process significantly ahead of other competing metal AM technologies.

1.3 Dissertation outline

While the fundamentals of the SEAM process are built upon pre-existing AM techniques, new scientific challenges arise at every development stage, including printing system design and construction, green part fabrication, binder removal, and sintering process. This dissertation is structured with each chapter from 3-6 focusing on each individual aforementioned development stage, identifying their limitations and scientific challenges, and providing the author's efforts and solutions to overcome those challenges. The results of this dissertation will demonstrate the feasibility of the newly developed SEAM process as a practical, economical, and high production metal AM technology.

Chapter 2 presents the current status review of metal AM processes. The advantages and shortcomings of currently available metal AM technologies in comparison with traditional manufacturing processes are discussed. An in depth state-of-the-art literature review on all metal AM processes is also included, which identified the limitations of each processes in terms of fabrication capability, production speed, and manufacturing cost. Finally, the scientific challenges and research

objectives of the development of the SEAM process as a solution for high production AM technique are presented.

Chapter 3 focuses on the system development of the SEAM process. Several proof-of-concept experiments were carried out using different UV patterning techniques, which resulted in the design and construction of a new 3D printing system specifically suitable for the processing of metal suspensions. Detailed information on the system's specifications, chosen components, as well as working mechanism are presented. The design and on-going progress of the development of the second prototype with improvement in fabrication capability as well as functionalities are also included.

Chapter 4 discusses the green part fabrication steps of the SEAM process. The relationships between cure depth and particle size for several metal suspensions were characterized, whose results were used to determine the appropriate processing conditions (UV energy dosage, curing time, layer thickness) for each suspension. An innovative 2-step curing strategy was devised and applied to the printing process, which not only prevents sedimentation of metal powder particles in the print bed but also enables the fabrication of overhang geometry without support structures. Using the developed printing technique and processing parameters, 3D green objects were successfully fabricated, which were ready for thermal post-processing steps to achieve the final metal parts.

Chapter 5 presents the debinding procedure for the green objects fabricated by SEAM process. A series of studies and characterizations were carried out on the thermal decomposition of the chosen photopolymer under different environments and holding temperatures. Consequently, the optimal thermal debinding cycle was determined, which not only completely removes all the binder from the green parts but also maintains the debinded parts structural integrity. Characterizations on post-debinded parts have shown a maximum binder residual of 0.04 wt%, which is negligible in most cases.

Chapter 6 presents the sintering routes for Stainless steel 420 (SS420) and Haynes 214 alloys with SEAM process. For SS420, an analysis of variance was carried out on pre-existing sintering data from BJP parts to determine the effect of sintering additives and sintering temperature on the

final part relative density. Consequently, a sintering optimization matrix with varied sintering aids addition wt.% and sintering temperature was designed for the SEAM process. Test coupons were fabricated accordingly to the designed matrix and their relative density values were measured to determine the optimal sintering conditions for SS420. Sintered coupons with relative density of above 99.7% was achieved. For Haynes 214, the supersolidus sintering behavior of the material was characterized with respect to sintering temperature and holding time. The transient deformation behavior of Haynes 214 cylindrical coupons with respect to holding time was also studied and captured, which enabled the development of a 2-step sintering technique, resulted in an enhancement in the final relative density and complete shape retention of the final sintered part. Additionally, sintering experiments with boron nitride as sintering aids was carried out to determine the feasibility of using activated liquid phase sintering to process Haynes 214. Fabricated samples exhibited partial melting with carbide precipitates at the melt zones, which hindered full part densification. The last section of this chapter presents the development of the Olevsky-Skorohod sintering model in Abaqus to predict part density evolution, shrinkage, and distortion throughout the sintering process. The model was implemented using a user-defined material model (UMAT) subroutine, solved with Abaqus Standard, and the results were verified using literature data.

Chapter 7 presents the processing and mechanical properties of oxide dispersion strengthened (ODS) Haynes 214 alloy using selective laser melting (SLM) technology. While the work in this chapter does not directly related to the rest of the work in this dissertation, the author deemed it worthy to be included due to the significant scientific findings as well as the time and effort spent by the author on this topic of study. A systematic approach in identifying the optimal processing conditions for all formulations of Haynes 214 and Haynes 214 ODS alloys using SLM was devised and carried out, which resulted in the successful fabrication of high temperature testing coupons and a functional heat exchanger assembly. The effect of feedstock preparation techniques on the dispersion of ODS particles in the fabricated parts is discussed along with the efforts on crack-healing by laser remelting on high-ODS-inclusion feedstock. The benefits of ODS particles inclusion on the mechanical properties of Haynes 214 at high temperature are also presented.

CHAPTER 2

METAL ADDITIVE MANUFACTURING: THE CURRENT STATUS

2.1 Introduction

The International Organization for Standardization (ISO) defines additive manufacturing (AM) as "technologies that, based on a geometrical representation, create physical objects by successive addition of material" [20]. AM technologies in general and metal AM technologies in particular, which were once only trusted as prototyping techniques, have now emerged as a viable solution to produce functional end-use components for several industries including automotive, aerospace, defense, and biomedical [21]. The capability of fabricating highly complex components with virtually no geometrical limitations of metal AM has driven advancement in product designs and performance, improved material efficiency, and reduced lead time and total cost. A significant attention and interest have been directed towards the adoption of metal AM in the manufacturing sector to replace and improve production capability of traditional manufacturing processes [22]. However, the inherent difference in process principles between metal AM and TM leads to two separate manufacturing regions: (1) metal AM is best suited for producing complex parts in small quantities and (2) TM dominates high volume production.

This chapter first provides a comparison between metal AM and TM processes, which identifies the current advantages and shortcomings of metal AM technologies. A state-of-the art literature review on all metal AM processes is then presented, and limitations of each process on production capability, manufacturing cost, as well as concerns on part microstructure and performance are discussed. Finally, the scientific challenges and research objectives on the development of the SEAM process as a high production metal AM manufacturing technology is outlined.

2.2 Metal additive and traditional manufacturing - A comparison

Since the production of the first commercialized AM system by EOS more than 25 years ago, the comparison between metal AM and TM has always been a highly debated and developing conversation. However, it can be narrowed down to three main attributes: production volume, complexity/customization capability, and cost of manufacturing [23].

High volume production has always been the leading focus of TM technologies, as part unit manufacturing cost decreases with number of unit produced. Fast and efficient production with great precision and high repeatability are undeniable advantages of TM processes such as milling, turning, laser cutting, etc. over AM. Moreover, the long-established manufacturing techniques, quality assured, and widely implemented industrial of TM processes make the competition incredibly difficult for AM when it comes to high volume production [3–5] . AM processes take a small edge in offering the possibility of eliminating forging and joining by printing a complete part in one build. A niche example is the metal acetabular cup used in hip surgery, which traditionally had to be manufactured using a combination of multiple TM processes (forging, machining, coating, etc.), now can be fabricated in one print on a metal powder bed fusion machine (Fig. 2.1) [24]. Nevertheless, when it comes to high production manufacturing, the capital investment required to create an assembly and production lines for AM processes is simply not a financially feasible investment for manufacturers [25].

AM processes' capability to provide individually designed product with a high level of details is the primary attribute that sets them ahead of TM in specialized industries such as aerospace and medical, which value complexity and customization potential over mass production volume [26]. While TM processes also offer minor product variations, their manufacturing cost drastically increases with level of customization. AM processes can deliver extremely customizable products at a lower cost-per-part (Fig. 2.2). The most famous example is 17.2 million Invisalign braces fabricated in 2012 alone by Align Technologies using AM stereolithography printers [27]. Furthermore, the absence of lead time and quick design adaptation in AM processes are the key characteristics that attract companies, in order to stay ahead of the market and competitors with new innovations [2].

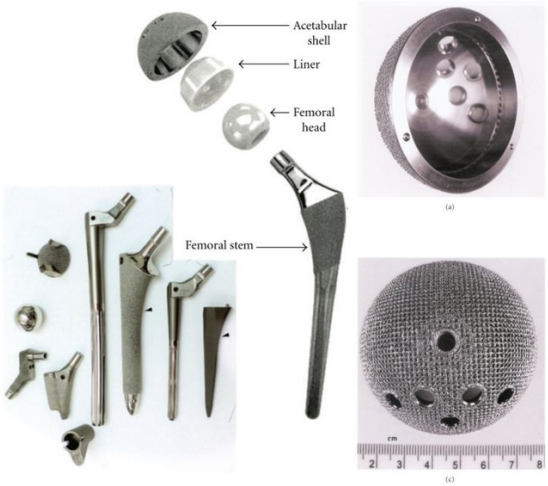

Figure 2.1 Acetabular cup produced by electron beam melting process in a single build [24].

Manufacturing cost depends on a number of factors: manufacturing method, production volume, and part complexity. Studies have been conducted to provide cost models to determine the breakeven point in terms of manufacturing costs for AM and TM [23, 25]. Findings have shown that in the particular case of fabricating a small plastic lever, AM powder bed fusion had a lower unit cost in comparison with injection molding when the total production volume is below 10,000 [1]. AM also offers manufacturers to trade volume production for parts customizability and complexity, which can only be quantified on a case-by-case basis [23].

As metal AM field evolves as a whole with rapid development in new technologies, materials, and applications, there is an increasing demand in the production of highly complex and customizable products. 3DHubs forecasted a doubling in total market cap of AM over the next 5 years, with 65% engineering businesses sourced or produced more 3D printed parts in 2020 from the previous year [29]. Additionally, 54% of engineering businesses increased and 30% maintained their usage of 3D printing for functional end-use parts, demonstrating that AM should no longer be seen only as a rapid prototyping technique. However, it was also noted that the critical barriers that has been holding back full adoption of AM processes in general and metal AM in particular have been identified as high total manufacturing cost and low production capabilities of the currently available technologies [26].

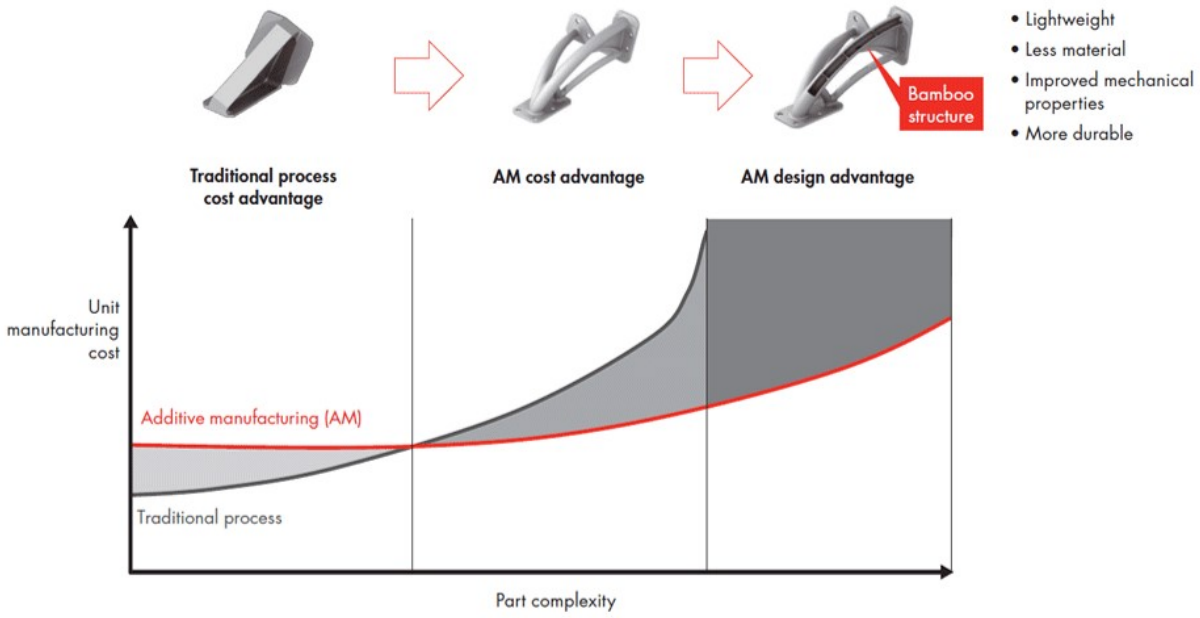

Figure 2.2 AM processes provide cost and design advantages over TM when it comes to producing part with high level of complexity [28].

2.3 Metal additive manufacturing - state of the art

2.3.1 Beam-base metal AM technologies

The American Society for Testing and Materials (ASTM) highlighted powder bed fusion (PBF) and directed energy deposition (DED) methods as the key beam-based approaches for fabricating metals and alloys [30,31]. Due to their ability to fabricate parts with excellent resolution (sub 30 μm) and high relative density of above 99% with superior mechanical properties, SLM and EDM are the currently dominant processes for printing highly demanding functional parts [32–34]. DED process, while having the advantage of high deposition rate and build volume, lacks the capability to fabricate parts with high resolution, and is often used as a net-shape fabrication process [24, 25]. In all of the aforementioned beam-based technologies, the sophisticated melting and rapid solidification of the powder result in columnar and highly orientated grains with anisotropic and generally unpredictable mechanical properties [35–37]. Delamination and part distortion are also a critical concern due to the high thermal stress and rapid solidification during the fabrication process [38–40]. Moreover,

commercialized beam-based metal AM systems are extremely expensive and energy inefficient due to the use of high energy beams [41–43]. Other drawbacks of beam-based metal AM technologies includes difficulty in scaling up system size, limited printing speed, subpar surface quality, and inability to process non-weldable metals [30, 41–44].

2.3.2 Beamless metal AM technologies

Beamless metal AM techniques have recently gaining significant traction as a solution to effectively overcome the above limitations of the beam-based technologies [31, 45]. Beamless metal AM technologies can massively reduce cost of productions, as their systems and operating cost are extremely inexpensive in comparison to beam based metal AM systems [46]. Higher printed part resolution and surface finish can also be obtained with optimized processing conditions [46]. Moreover, uniform microstructure with almost no residual thermal stress in final printed parts is their biggest advantage over beam-based metal AM processes [41, 43, 47]. The three key processes of beamless metal AM are material jetting, material extrusion, and binder jet printing (BJP) [47]. Material jetting processes such as liquid metal printing and aerosol jetting deposit droplets of build materials which then solidify via cooling or polymerization to form green objects [48, 49]. High temperature sintering is then carried out to achieve near fully dense parts. Material extrusion operates in a similar manner, but the feedstock is a composite of metal powder and binder, in a filament or pellet form that can be extruded [50–52]. Binder jet printing, which forms green parts by dropping binder droplets on thin layers of metal powder, is arguably the most prominent beamless metal AM technology that has been developed and widely adopted to produce complex 3D parts from a variety of materials, including metals, ceramics, polymers, and other alloys [53–56]. Other notable beamless metal AM processes include additive friction stir deposition (AFSD) [57], ultrasonic AM (UAM) [58, 59], wire and arc AM (WAAM) [60], cold spray AM (CASM) [61], electrochemical AM (EFAB) [62], and 3D screen printing [63]. While these processes have had some success in producing 3D metal parts, they are either near net-shape processes (CSAM, AFSD, WAAM) or suffer from low printing speed (UAM, EFAB), high material wastage (UAM), limited

choice of materials (EFAB) and build volume (UAM, EFAB) [31, 57–60].

Beamless metal AM processes have successfully produced metal parts with a wide range of materials (copper, titanium, aluminum alloys, stainless steel, tungsten, cobalt-chrome, magnetic materials, etc.), high accuracy (50 μm to 100 μm resolution), smooth surface finish (R_a of 6 μm), and isotropic microstructure and comparable mechanical properties to parts fabricated by metal injection molding [30, 31, 41–43]. The main limitation of beamless metal AM processes is difficulty to attain fully dense metal parts, which has been the focus of many studies [41–43, 53–55]. While extensive efforts have been made, typical relative density of beamless AM processes is 95-97%, which requires post processing heat treatment such as HIP and material infiltration to fully densify the final parts [64, 65]. Thus, overall time and production cost significantly increases. Formation of oxides and carbides in parts' microstructure also require critical effort and attention to resolve [57]. Commercialized beamless metal AM systems are also relatively small in scale, and typically designed for prototyping and only suitable for low production [42].

2.4 Scientific challenges and research objectives

2.4.1 Scientific challenges

2.4.1.1 Printing system development

While SEAM process working principles can be defined as a combination of BJP and SLA principles, the printing systems developed for both technologies are not suitable for the processing of a highly filled metal suspension. The most important aspects that require significant attention in the design and construction of a printing system for SEAM process are:

- The sedimentation behavior of metal suspension: Due to the inherent density difference between metal powder and photopolymer resin, the sedimentation behavior of the metal particles in the suspension is inevitable. As it is critical to maintain the suspension homogeneity throughout the printing process, appropriate strategies must be devised to not only maintain the suspension's composition in the supply zone but also in the printing area. Inhomogenous

feedstocks can result in undesirable compositional variation in the printed part, which is detrimental to the subsequent debinding and sintering steps.

- Curing system selection: A suitable curing system must provide sufficient energy in a reasonable amount of time to generate a cured layer geometry. In highly-filled suspension systems, light scattering from the particle surfaces can lead to difficulty in achieving adequate cure depth, which requires a combination of high UV exposure intensity as well as long exposure time to overcome [66–68]. Moreover, as the development of SEAM process is aimed towards a system with high volume and high production capability, the speed, scalability, and cost of the curing system must also be taken into consideration.

2.4.1.2 Metal suspension cure depth characterization

A suitable candidate of metal suspension for SEAM process must satisfy several requirements:

- A sufficiently high particle loading must be achieved in the suspension to ensure part quality [69–71]. It is crucial to minimize the resin content in the suspension to prevent defects during debinding and sintering and to obtain a dense and homogeneous final part. The initial packing density of the metal particles have also proven to be critical in aiding the sintering process for a fully dense final object [55, 56].

- Suspension stability must be maintained during the fabrication process, including in the material delivery system and on the printing substrate. Due to the difference in density between powder and resin in the suspension, undesired segregation between powder and resin is inevitable and must be negated [72].

- An appropriate cure depth must be achieved with short exposure time to ensure good interlayer adhesion and minimize fabrication time. A long patterning time for each layer results in an excessively long printing process, which is working against the motivation of this system development [66, 67]. Moreover, light bleeding and the resultant resolution loss are concerns with long UV exposure time in SLA based processes [69, 70].

- The suspension must attain an appropriately low viscosity level in order to ensure good layer recoating [72].

Various materials have been successfully shaped into ceramic-based composite structures using SLA principles by mixing ceramic powders such as silica, silicon nitride, alumina, and hydroxyapatite with acrylate or epoxy resins [69–73]. On the contrary, limited works on the fabrication of metal parts using SLA principles were reported due to multiple technical challenges:

- Sedimentation of metal particles in the suspension is difficult to prevent due to the significant density difference between metal powder and resin. In ceramic suspensions, the use of dispersing agent is sufficient to negate this effect [66].

- An effective cure depth of metal suspension has not been produced due to the predominance of light scattering and absorption [67]. In order to develop a practical curing process using metal suspension, it is crucial to improve the cure depth of such suspensions to 100 - 200 μm as the particle sizes of metal powder typically fall into this range [72].

Therefore, the key to enable the green part fabrication step of the SEAM process is to characterize the relationship between the curing depth and other controlling parameters (metal loading, particles sizes, layer curing time). Thereafter, the curing depth of metal suspensions can be improved to a practical level and the appropriate printing parameters can be determined.

2.4.1.3 Developing appropriate debinding and sintering process to attain full density

SEAM process fall into the a beamless metal AM technology category, as its post-printing heat treatments procedures are identical to BJP and metal injection molding (MIM) processes. Therefore, SEAM process inherits the versatile ability to process different metal powders as well as isotropic part performance and properties from beamless processes. Needless to say, SEAM process also adopts all other issues that beamless metal AM encounters: difficulty in attaining fully dense part, requirement of post processing heat treatment, and oxides and carbides formation [53–56]. However, similar to material extrusion and BJP processes, SEAM process has the advantage of

leveraging the mature knowledge base of powder metallurgy (PM) and sintering technology to tackle those issues [31].

Achieving a complete debinding and clean of carbon has also been a major focus of research in PM and MIM [74]. Generally, this is achieved by heating the parts slowly up to the holding temperatures where the binder evaporates. Thermogravimetric analysis of the feedstock has become a standard practice to determine the ramping rate and holding temperature of the debinding cycle. Providing gas flow to the debinding chamber to expunge the generated gas from the binder also improves the debinding behaviors as the flow constantly purify the environment [75]. Gas flow rate has been determined to depend on the binder system as well as the distribution and size of the powder particle size [75]. As an alternative method to air debinding, debinding in nitrogen gas has also been experimented on with success on specific type of binders [76, 77]. Well-developed debinding techniques for MIM has successfully prevents cracking and soot deposition inside of the parts, which have proven to be detrimental to the final chemical composition as well as causing slumping and distortion during sintering, brittleness, low ductility, and poor corrosion resistance in final mechanical properties [76].

Thermal debinding of green parts are typically accomplished in open air environment to ensure the complete removal of the binder. Therefore, oxidation of metal powder during this thermal cycle is inevitable [78]. High purity hydrogen gas has been employed to reduce the surface oxide layers formed on metal powders. Good success has been found in Mo powder as the reduction ratio of its oxide particles is up to 0.98 [79, 80]. Iron nano powder has also been produced by hydrogen reduction of Fe_2O_3 at several heating rates and holding temperatures [80]. Oxide layer reduction in hydrogen of copper, nickel, and steel powder has also been studied and documented [81, 82]. Moreover, vacuum sintering has also proven as an effective method to significantly remove oxides and impurity from the powder particle during sintering [83, 84].

The use of multi-modal powders has been demonstrated to be an effective approach to improve the packing density of powders, and thus surface finish and final sintered density [85–87]. Sintering aids (activated sintering) have also been explored in PM practice and successfully applied in 3D

printing applications [88–91]. Vacuum sintering offers unique advantages of evaporating the oxide layers and removing impurities on metal powder particles at elevated temperature, which enhances the sintering behaviors [83, 84].

2.4.1.4 Shrinkage and distortion prediction by numerical modelling

For beamless metal AM technologies being developed to become a suitable industrial production process, there is a significant demand for quality control for the sintering process i.e. shrinkage and distortion prediction. The introduction of numerical methods can be a solution in the investigation of part densification and microstructural evolution. Finite element simulations of sintering in combination with experimental data allow quantitative predictions of sintering distortion and part final properties. Therefore, computer simulation could be a more effective technique in the optimization of the process in comparison to the traditional method of trial and error [92, 93].

The earliest solid state sintering models of green compacts were two-sphere model for the early sintering stage [94], cylindrical pore channel model for the intermediate state [95, 96], and spherical pore model for the late sintering state [97]. Since then, many other models with more sophisticated mechanism were developed [98, 99]. Liquid phase theory has also gained some attention with many ongoing theoretical works [100]. More recent theoretical work on both solid and liquid state sintering takes into accounts of additional effects such as gravity, anisotropic shrinkage, particle orientation, and external loads [101]. Numerical simulation results have also been applied to new sintering methods like microwave sintering or sinter forming [102]. In many instances, the results have shown a good agreement between numerical prediction and experimental findings [92, 93].

2.4.2 Research objectives

The research objectives of this dissertation are:

1. Develop a printing system for SEAM process which is suitable for the processing of metal suspension. The system should also be scalable with high production capability.

2. Characterize the relationship between cure depth and other controlling parameters of metal suspensions. Consequently, develop appropriate processing conditions for different metal suspensions for the green part fabrication step. The metal materials of interest include SS420, SS316, Haynes 214, and Amdry 386.

3. Investigate the thermal decomposition behavior of the chosen photopolymer and devise a clean and complete debinding cycle for the fabricated green parts.

4. Develop sintering strategies for SEAM printed parts to achieve full density without geometrical distortion. The metals of interest for this study are SS420 and Haynes 214. Additionally, a numerical model needs to be developed to predict sintering shrinkage and distortion that can be combined with experimental data for final part quality control.

CHAPTER 3

SEAM PROCESS: SYSTEM DEVELOPMENT

3.1 Introduction

At the fundamental level, SEAM process' working principles can be defined as the combination of BJP and SLA principles. However, the currently existing hardwares of either BJP or SLA are not suitable for the processing of SEAM process' target material, a highly filled metal-photopolymer suspension. BJP is carried out on a powder bed system, which is specifically designed to process metal powder feedstock. SLA technology has evolved through many hardware design iterations, but each one of them is optimized for the printing of liquid photopolymer. Therefore, the development of SEAM process calls for the design and fabrication of a new printing system that is specifically suitable to process metal suspensions.

This chapter first reviews the hardware apparatus and working mechanism of relevant commercially available AM printing systems, including the powder bed system and several design iterations of SLA process. Fundamental flaws in using the aforementioned systems to process metal suspensions are identified. Consequently, design considerations in the development of the printing system for SEAM process are discussed. Multiple proof-of-concept (POC) experiments were carried out with the purpose of demonstrating the feasibility to generate 2-D layer geometry using metal suspension and different UV patterning techniques. Thereafter, a first fully functional prototype of the SEAM process was designed and constructed. Detailed information on the prototype's specifications, chosen components, as well as working mechanism are presented. The design and on-going progress of the development of the second-generation prototype with improvements in fabrication capability as well as functionalities are also included in this chapter.

3.2 Relevant AM processes and systems

3.2.1 The powder bed system

A powder bed system consists of a powder feed or supply tank, which contains the powder feedstock, and a build tank, which contains the printing platform where the part is fabricated. For each layer, a recoater blade or roller spreads a thin layer of metal powder from the supply tank to the printing platform. The 2D layer pattern generation is carried out by a selective melt of the powder by a laser or electron beam (for SLM and EBM processes) [13] or by delivering small droplets of binding agent in a pattern (for BJP process) [6]. After each layer is finished, the printing platform moves downwards by a layer thickness increment. At the same time, the supply piston moves upwards, and the blade recoats the printing platform with a fresh layer of powder. 2D layer pattern is then again generated on the fresh powder layer and the whole process then repeats until the 3D part is completed. Loose powder can subsequently be removed to retrieve the printed parts, which are ready for further post processing operations to obtain final parts. Figure 3.1 demonstrated the working principles of the powder bed system for the SLM process.

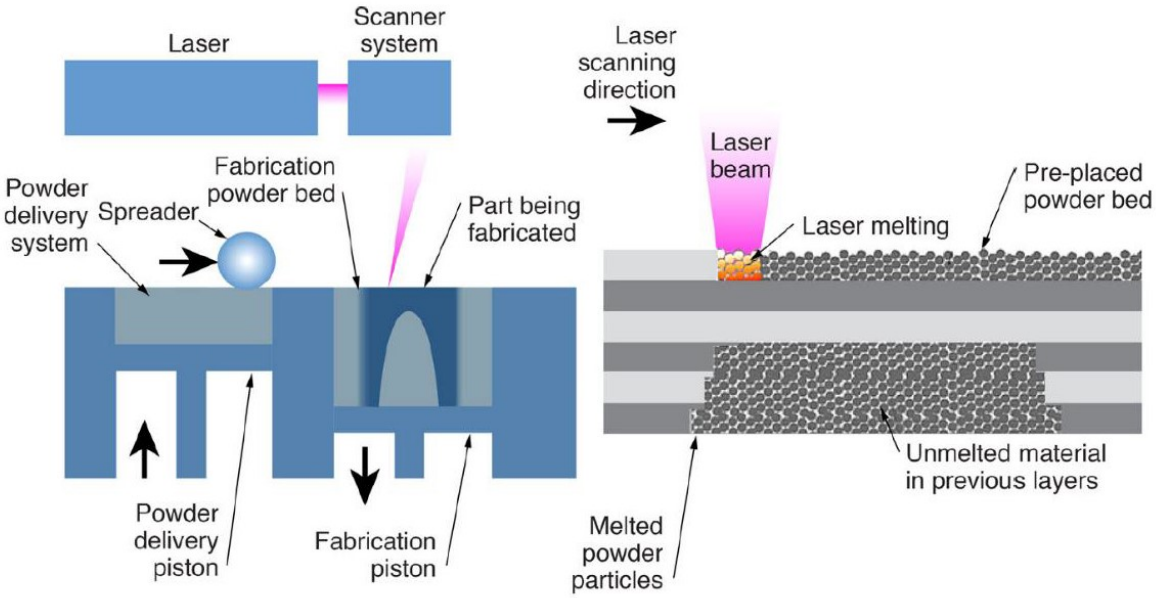

Figure 3.1 Powder bed system working principles for the SLM process. Reprinted from [103].

3.2.2 Stereolithography (SLA)

3.2.2.1 Laser-based stereolithography (SLA)

The earliest SLA system consists of a photopolymer resin vat, a galvanometric laser beam, and a motorized Z stage (Fig. 3.2a). The print platform is attached to the Z-stage which can move incrementally up and down to control the layer thickness. 2D layer patterning is carried out by selectively photopolymerizing the resin using X-Y movement of the laser beam across the resin surface. In this system design, optical precision issue arises due to the defocus of the laser beam at the outer area of the print platform, leading to undesirable non-uniformity as well as resolution loss [10] .

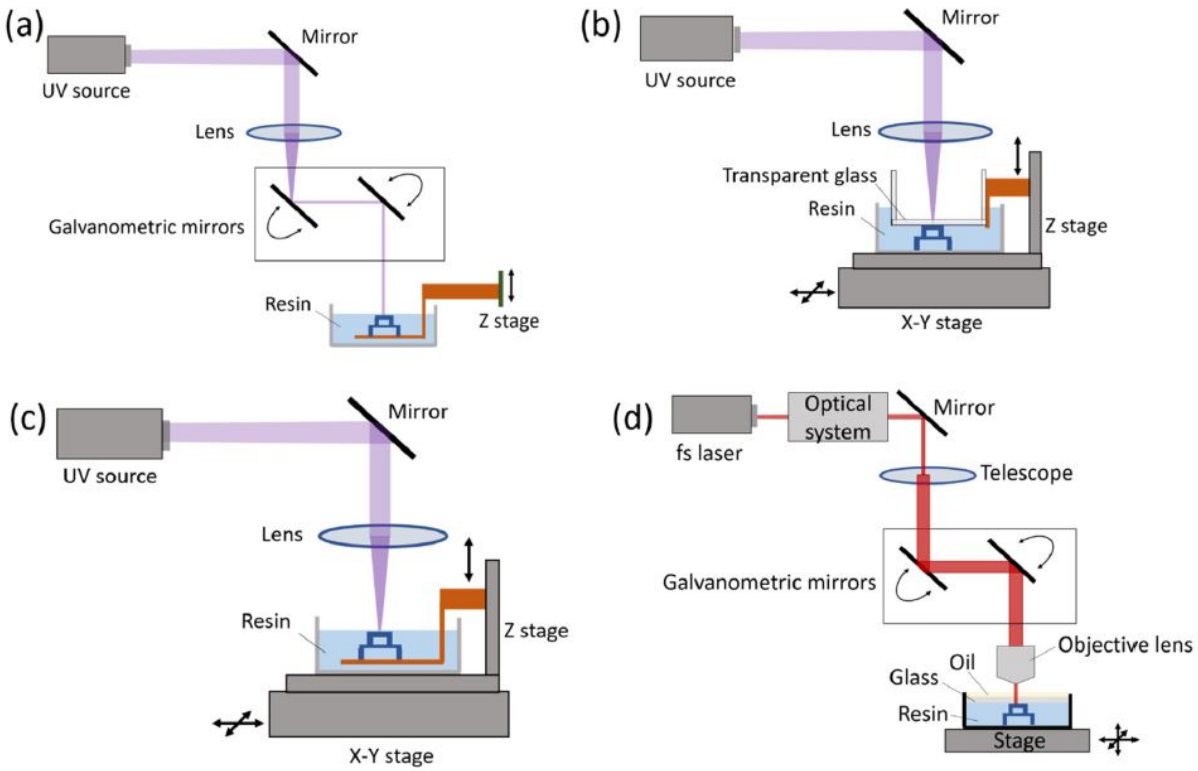

Figure 3.2 (a) Stereolithography system with galvanometric system. (b) The constrained surface system. (c) The free surface system. (d) Two photon polymerization system. Reprinted from [10].

The second iteration of SLA system, also known as constrained surface system, replaces the

galvanometric mirrors with an X-Y stage, which allows movement of the whole resin vat (Fig. 3.2b). The layer thickness is controlled by a transparent glass, which is connected to a motorized Z stage. Polymerization is initiated by the laser beam irradiating through the glass, onto the thin resin surface, forming the 2-D geometry below the glass. The constrained surface system allows for a steady and uniform laser intensity across the resin surface, which prevents defocusing as well as optical errors [11]. However, polymerizing through a glass window leads to a critical draw-back as the cured resin also adheres to the glass window [104].

The free surface system is introduced as a solution to this problem, by removing the glass window and connecting the printing platform to the motorized Z stage (Fig. 3.2c). Similar to the constrained surface system, the X-Y stage allows movement of the resin vat. The 2-D pattern is formed by synchronized movements of the printing platform and the X-Y stage, while the laser beam remains stationary. The free surface stereolithography system is the first system to be commercialized, as it has shown excellent capability in fabricating structures in micron scale with great precision and accuracy [105].

A more recent and noteworthy SLA system is the two-photon polymerization system (Fig. 3.2d). By focusing femtosecond laser pulses onto a narrow spot on the resin surface, photopolymerization of the resin is initiated by the absorption of two photons simultaneously. Two photon SLA significantly reduces the photopolymer excitation volume, which allows for the fabrication of parts with spatial resolution of under 100 nm [12].

3.2.2.2 Projection-based SLA

Figure 3.3 shows a typical schematic for a top-down projection-based SLA system. The laser scanning system has been replaced with a dynamic mask, either a liquid crystal display (LCD) or a digital micromirror device system (DMD). The inclusion of dynamic mask system allows for the fabrication of each layer by a single patterned UV exposure [105]. For the LCD mask, each pixel of an LCD screen is a small unit cell containing a molecule with adjustable orientation. Each orientation of the molecule corresponds to either a transparent or opaque state, which allows

for image patterning. The subsequently developed DMD dynamic mask contains of up to several millions of micromirrors, each can be independently controlled to reflect the incoming light ray onto or away from the resin surface. The bottom-up system (Fig. 3.4) was also developed as an alternative design [10].

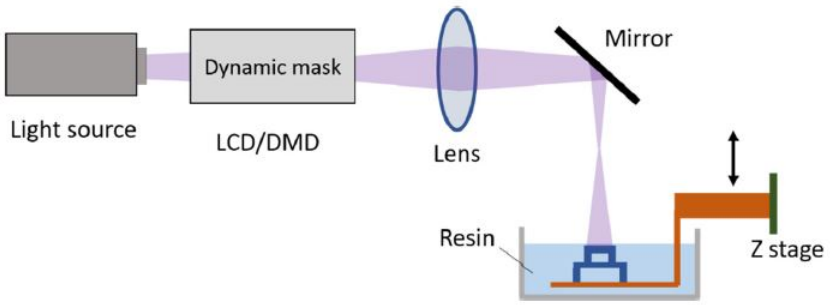

Figure 3.3 The top-down projection stereolithography system with LCD/DMD masking. Reprinted from [10].

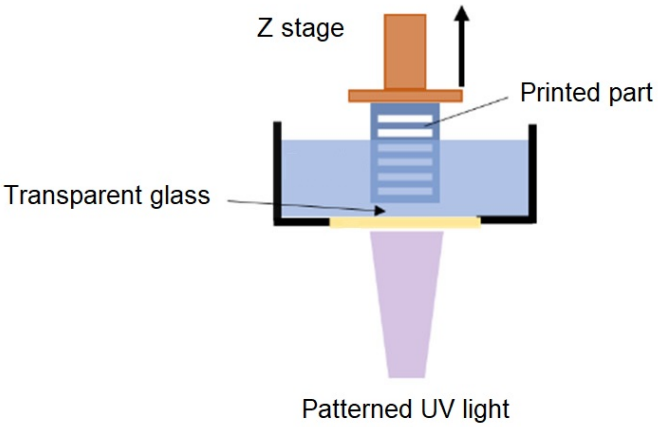

Figure 3.4 The bottom up projection stereolithography system with LCD/DMD masking. Reprinted from [10].

Although the LCD mask system is relatively less expensive and easier to set up, its shortcomings include low transmission of light in UV region, large pixel size, and relatively poor contrast, which significantly limit the further development of the system [12]. On the contrary, with UV light transmission compatibility, small pixel size, high contrast, and superior pixel switching speed, the DMD mask system has become the method of choice in the design of projection-based SLA [10].

3.3 SEAM system design challenges and considerations

One of the most critical challenges in the development of SEAM process hardware as well as the processing of highly filled metal suspensions is difficulty in maintaining the suspension's stability during the printing process. The sedimentation velocity of a spherical metal particle in a liquid photopolymer can be derived from Stoke's law [106] as:

$$v = \frac{2}{9}\frac{(\rho_p - \rho_f)}{\mu} g R^2 \tag{3.1}$$

where v is the sedimentation velocity, ρ_p is the density of the particle, ρ_f is the density of the fluid, g is the gravitational field strength, R is the radius of the spherical particle, and μ is the fluid viscosity.

Since the density of a typical metal powder material is multiple times higher than that of a photopolymer resin, the sedimentation behavior of the metal particles in the suspensions is inevitable. This undesirable behavior can compromise the composition of the metal suspension over time and is detrimental to the printing process, which requires consistent and homogeneous material for every layer. Both the powder bed system and all the design iterations of SLA processes cannot accommodate for this behavior, as they require the feedstock to be pre-filled either in the supply piston or material vat, and stay idle throughout the printing process. Figure 3.5 demonstrates the sedimentation behavior over time of a typical metal suspension consisting of 90 wt.% Haynes 214 powder (Oerlikon Metco - Plymouth, Michigan, USA) and 10 wt.% CPS 3010 photopolymer (Colorado Photopolymer Solution - Boulder, Colorado, USA), which corresponds to a 55.6% volume percentage of powder. The densities of the metal powder and photopolymer resin are 8.05 g/cm^3 and 1.12 g/cm^3, respectively.

The second challenge in the processing of metal suspension lies in the inherently weaker inter-layer bonding strength of suspensions in comparison to pure resin used in traditional SLA processes [70]. The bottom-up SLA system design is especially susceptible to this behavior. As the part is gradually printed while being pulled upwards out of the material tank, gravitational force exerted on every layer also gradually increases, which can eventually result in inter-layer cracking and

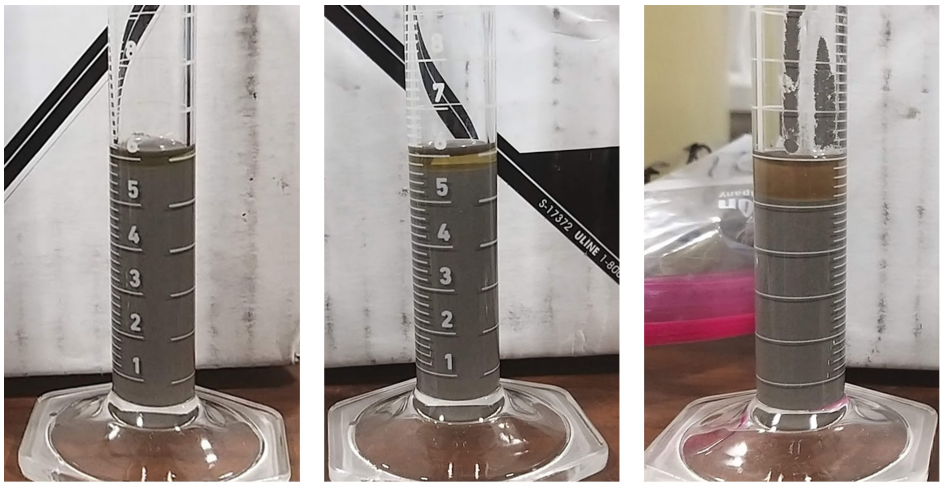

Figure 3.5 Sedimentation behavior of Haynes 214 suspension over time. In the graduated cylinder: grey region - Haynes 214 powder; transparent green region - photopolymer resin. Reading unit is ml.

part delamination [69]. The high density of metal powder further intensifies this effect, which can significantly limit the part fabrication capacity. Therefore, a top down system design is more desirable, as gravitational force does not oppose the inter-layer bonding.

The third challenge in the development of SEAM process hardware arises in the selection of a suitable curing system for metal suspensions. Since the mixture is highly filled with metal particles, light scattering results in the difficulty of achieving an adequate layer cure depth and inter-layer bonding, which requires a combination of high UV exposure intensity as well as extended exposure time to overcome [66]. A laser system ensures a sufficient curing power density, while maintaining a high resolution. However, on a production scaled system with a large build platform, the use of a laser is inferior to an image projection module in term of processing speed. Moreover, the nature of the point-by-point layer creation of laser scanning and the constant segregation of powder and resin in the print bed will result in layer non-uniformity. This effect will further intensify on a large print bed due to the extended time needed to scan the geometry, as well as the inherent deterioration of beam quality in the outer area on the print bed [15]. The use of multiple lasers is a possible solution, but at the cost of a highly complex and expensive system design. As the development of the SEAM process is aimed towards a scalable system with high production speed and capacity, a

dynamic mask curing system with its low cost and the ability to generate a complete 2D geometry quickly with a single exposure is more suitable.

In summary, the key design considerations for the development a SEAM printing system for the processing of metal suspensions are:

- The suspension must be kept homogeneous during the printing process. A mixing system should be utilized, which should also capable of dispensing the suspension onto the printing platform layer by layer.
- A top-down system design is preferred due to the weaker inter-layer bonding strength of suspension layer comparing to pure photopolymer resin.
- A dynamic mask curing system is desirable to ensure high printing speed as well as layer uniformity. However, the curing system must be carefully chosen to ensure adequate UV light intensity for photopolymerization initiation of the suspension.

3.4 Proof-of-concept experiments

3.4.1 Materials and methods

A series of experiments were carried out to determine the feasibility of processing metal suspensions using three distinct patterning techniques: physical mask, LCD digital mask, and DMD digital mask. All experiments were carried out using the top-down projection setup. Specifications on the UV curing systems used and experimental setup will be provided in the next sections.

Metal suspensions with a volume percentage of 56% metal powder loading was formulated and used for all experiments. The metal powder used was SS420, with particle size of -55/+22 μm. All metal powder used in this dissertation is provided by Oerlikon Metco (Plymouth, Michigan, USA). CPS1030 (Sigma-Aldrich - St. Louis, MO, USA) was chosen as the photopolymer resin, due to its relatively low viscosity, commercially availability, as well as curing wavelength compatibility with existing lab equipment. The recommended curing wavelength of the CPS1030 is 320 - 500 nm,

and all available laboratory UV light sources are of 405 nm wavelength. Detailed information on CPS1030 is provided in Table 3.1.

Table 3.1 CPS3010 photopolymer resin properties.

Photopolymer resin	CPS1030
Form	Liquid
Viscosity	55 cP
Density at ambient temperature	1.16 g/ml
Modulus (after curing)	750 MPa
Recommended curing wavelength	320-500 nm

For each experiment, the metal suspension was first spread into a thin layer on a flat printing platform, which was subsequently exposed to UV irradiation using the aforementioned patterning techniques for different irradiation time duration of 30, 60, and 90 seconds. Uncured materials were then removed and photopolymerization behavior of the suspensions were inspected for each experiment. In the cases that photopolymerization of the suspensions occurred and layer patterns were formed, additional thin layers of metal suspension were spread on top of the cured layer and again irradiated by UV light. This process was repeated up to a total of 10 layers.

3.4.2 Physical mask experiment

This experiment evaluates the processability of metal suspensions by **directly exposing a high intensity UV light source**.

3.4.2.1 Experimental setup

The physical mask used in this experiment was an aluminum sheet with dug-out holes of 5 cm in diameter, which allows light to pass through and form circular exposure patterns on the printing platform placed 1 cm underneath. Thin layers of the formulated SS420 suspension was spread onto the printing platform manually using a doctor blade. A 25 W UV LED light (Shenzhen Chanzon Technology - Guangdong, China) was employed as the UV curing component, which

directly irradiates 405 nm UV light through the physical mask, onto the printing platform. Figure 3.6 shows the experimental setup.

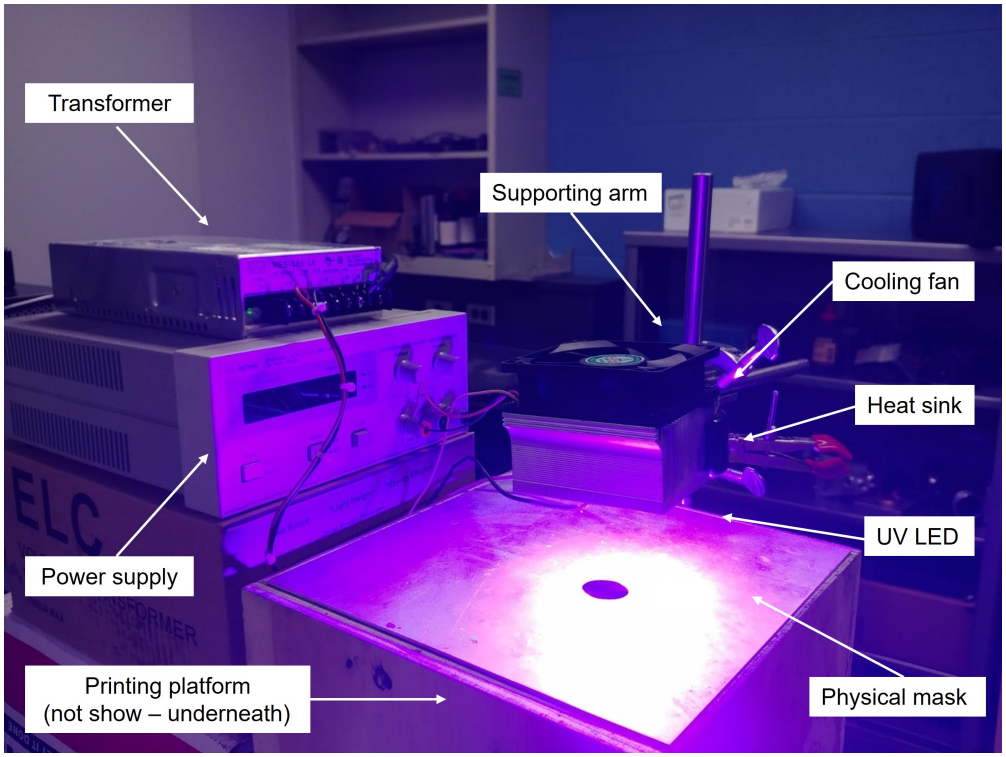

Figure 3.6 Physical mask experimental setup, showing the UV irradiation from the LED light source through the dug out hole on the mask.

3.4.2.2 Results and discussion

For all the experiments carried out with different layer irradiation time, photopolymerization was observed and circular patterns of 5.8 cm in diameter were formed. The difference in diameter between the dug-out hole on the physical mask and the pattern formed was due to the 1 cm gap distance between the mask and the printing platform. Additional layers were fabricated for each experiments up to a total of 10 layers. Figure 3.7 shows the sample fabricated with the layer irradiation time of 30 seconds.

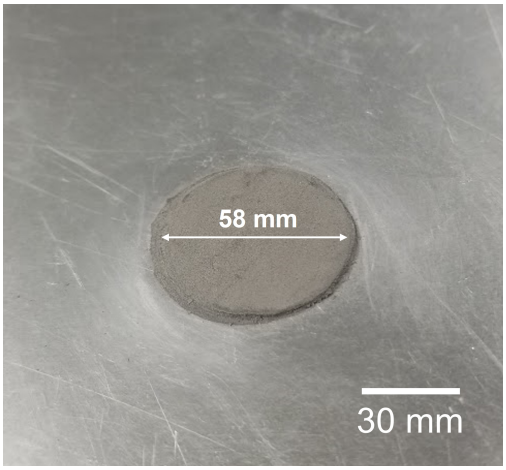

Figure 3.7 5.8 cm diameter disk fabricated using physical mask setup. 10 layers were fabricated with the irradiation time of 30 seconds for each layer.

3.4.3 Modified SLA system experiment

This experiment evaluates the processability of metal suspension using a **modified SLA system with LCD digital mask**.

3.4.3.1 Experimental setup

The Anycubic Photon S (Fig. 3.8 (left)), a commercialized SLA LCD-based bottom-up 3D printer (Anycubic - Shenzen, China), was disassembled and reconstructed into a top-down projection setup (Fig. 3.8 (right)). The original UV LED (5 W power, 405 nm wavelength) of the printer was replaced with new 405 nm UV LED units with higher power of 25 W and 50 W (Shenzhen Chanzon Technology - Guangdong, China) for this experiment. The protective funnel was manufactured and used in the setup to prevent unwanted natural light exposure to the LCD screen and the underneath printing platform.

3.4.3.2 Results and discussion

For the experiments using the 25 W UV LED unit, no photopolymerization was observed for all irradiation times. A follow-up experiment was carried out with an extended irradiation time of 5 minutes and a very weak photopolymerized layer was observed. The 25 W LED unit was subse-

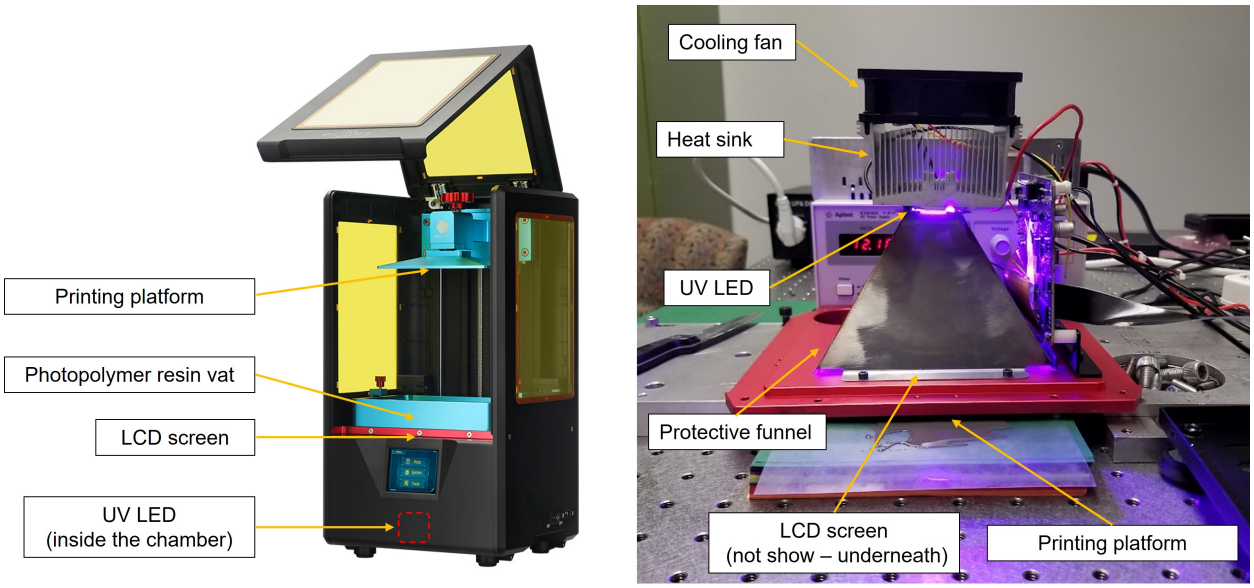

Figure 3.8 Left: Original LCD-based bottom-up Anycubic SLA 3D printer; Right: Modified SLA system setup, showing the top-down projection through an LCD mask; the original LED chip has been replaced with a higher power unit.

quently replaced with a 50 W unit. After 30 seconds of irradiation time, no photopolymerization was observed. Additionally, a dead zone on the LCD was observed, indicating that the 50 W LED has damaged the liquid crystal cells in the LCD screen.

In order to explain the results of the experiments, it is necessary to understand the working principles as well as the components of an LCD screen panel. Fig. 3.9 shows an exploded view of a typical LCD screen. Unpolarized light from a back light unit travels through the first polarizing filter, which only allows vertically oriented light to pass through. Without the liquid crystal layer, all the emitted light will be blocked by the second (crossed) polarizing filter. However, the arrangement of the molecules in the liquid crystal layer can be controlled electrically. In natural state, the molecules positioned themselves in a helical, or twisted structure, which rotates the incident light by 90°. The rotated light wave is now aligned with the second polarizing filter, and can travel to the color filter to form a colored pixel. On the other hand, if a sufficient voltage is applied between the negative and positive electrodes, the liquid crystal molecules untwist, and the incident light's orientation remains unchanged, and the emitted light is blocked by the second polarizing filter, which results in a dark pixel [107]. LCD screens used in SLA process in general and the Anycubic 3D printer in

particular are monochromatic, i.e. they only generate black and white pixel as the color filter has been removed.

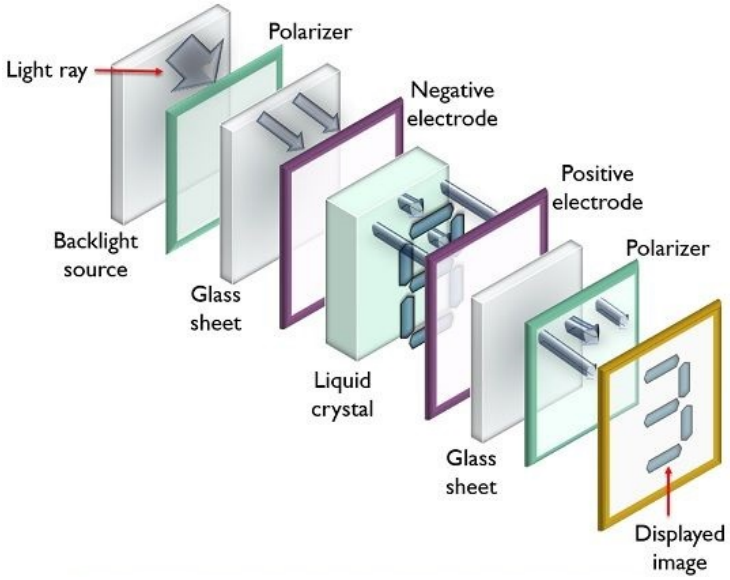

Figure 3.9 Components and working principles of an LCD panel [108].

Liquid crystal molecules have been found to be extremely susceptible to damage from UV (<400 nm) and IR (>750 nm) light. Therefore, the polarizing films are usually selected so that their transmission wavelength range falls into the visible light region [109]. Typical film polarizers for visible light have an average transmission of 38%, with under 20% transmission in near UV region [110] . Monochromatic LCD screens used the SLA processes typically transmits only 6 - 10% of light at the 405 nm wavelength [111]. This extremely low transmissivity, in combination with light scattering phenomena of metal suspensions makes it extremely difficult to provide sufficient energy through an LCD screen to initiate photopolymerization. The 25 W LED unit could not overcome these issues, resulting in photopolymerization of the metal suspension only after an extended time of irradiation. The 50 W LED unit provided a higher light intensity, and therefore, a higher energy dosage. However, even a short time usage resulted in damage of the LCD screen. High intensity light exposure has been found to be detrimental to life and functionalities of the liquid crystal molecules [112].

In conclusion, LCD digital masking is not a suitable technique to process metal suspensions due

to its limited near-UV light transmission. A different masking technique must be explored for the development of SEAM process.

3.4.4 Modified DLP projector experiment

This experiment evaluates the processability of metal suspension using a **modified DLP projector with DMD digital mask**.

3.4.4.1 Experimental setup

A commercialized DLP projector (S343, Optoma - New Taipei City, Taiwan) was positioned facing downwards towards the printing platform (Fig. 3.10). The unit is equipped with a 203 W metal-halide lamp as the light source. More detailed information on the projector can be found in Table 3.2. A holder frame was manufactured to place the projector at its minimum working distance of 25 cm. Two sets of experiments were carried out. First, the as-received DLP projector was used. Subsequently, the projector's color wheel was replaced with a FSQ-KG5 heat absorbing bandpass filter (Newport - Irvine, CA, USA), which prevented deep UV light transmission to the DMD chip. UV light with wavelength under 325 nm has been found to be detrimental to DMD mirrors' life and functionalities, as it is highly absorbable by the DMD mirrors [113]. The transmissible wavelength range of the filter is shown in Fig. 3.11.

Table 3.2 Optoma S343 DLP projector specification.

Projector name	Optoma S343 DLP Projector
Light source	203 W metal-halide lamp
DMD Chip	Texas Instrument SVGA DMD
Uniformity	80%
Projection screen size	27.7" - 304.4"

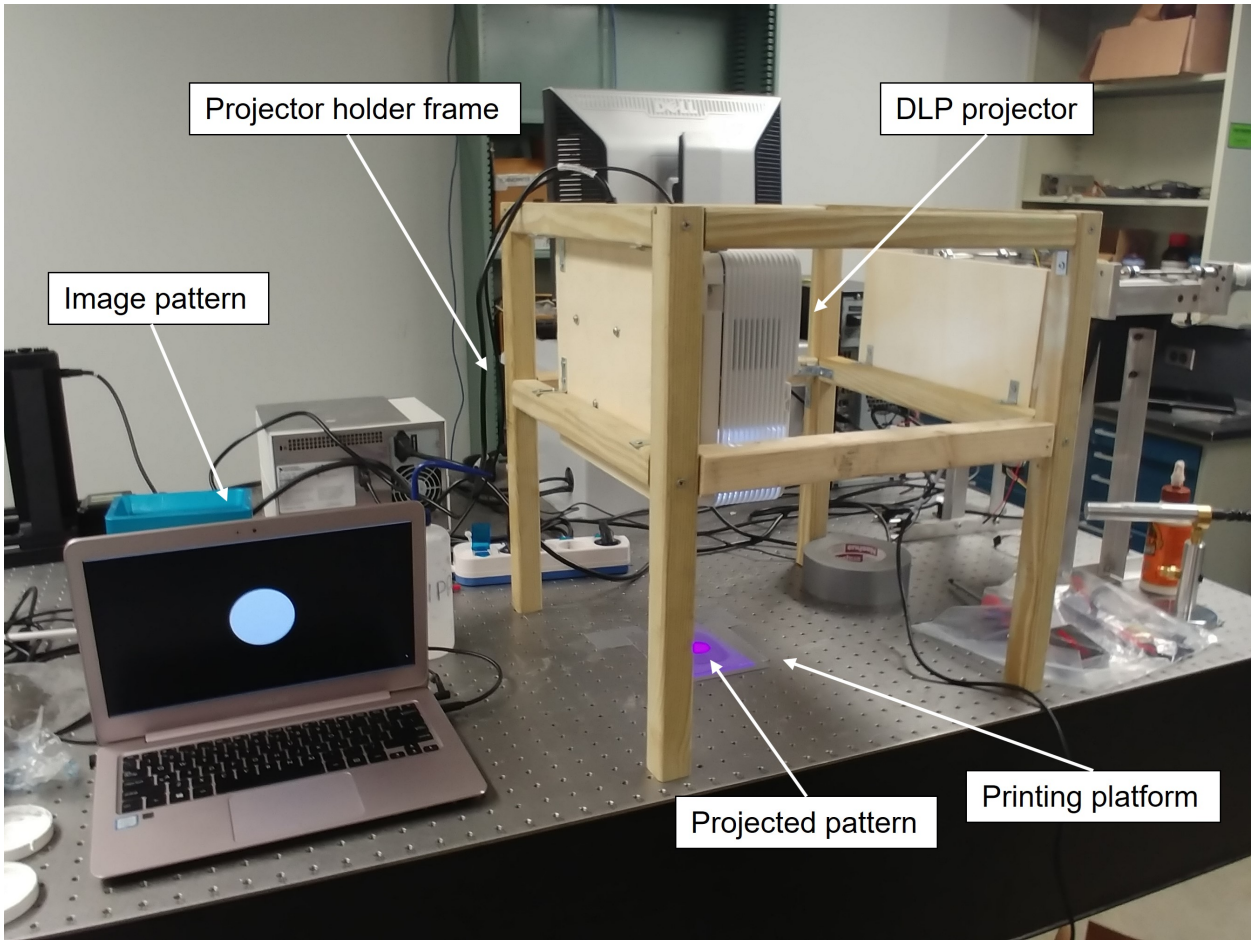

Figure 3.10 Modified DLP projector experimental setup showing a circular projected pattern onto the printing platform. The color wheel has been replaced with the bandpass filter in this image.

3.4.4.2 Results and discussion

In the experiments carried using the unmodified projector, with all irradiation times, no photopolymerization was observed. After the color wheel was removed and replaced with the bandpass filter, photopolymerization of the metal suspension was observed after 90 seconds of irradiation time. Circular disk and tensile bar shaped samples were successfully fabricated with a total of 10 layers (Fig. 3.12). A follow-up experiment was carried out using the modified projector, to fabricate a 4 x 3 matrix of blocks with 1 x 1 cm cross section (Fig. 3.13). A total of 20 layers were manually spread and cured with 90 second irradiation time per layer, resulted in parts with 1 mm in height. However, the two bottom right parts could not be fabricated, as can be seen in Figure 3.13.

DLP projectors utilize DMD chip to project and display patterns and images. A DMD chip consists

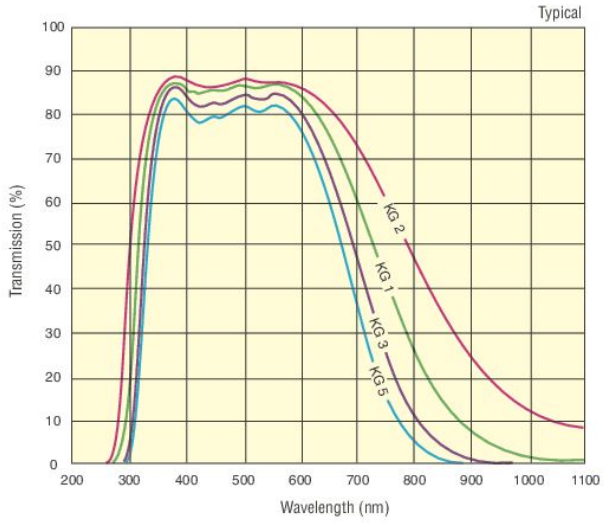

Figure 3.11 Transmissible wavelength range of the FSQ-KG5 heat absorbing bandpass filter (light blue line). Data from [114].

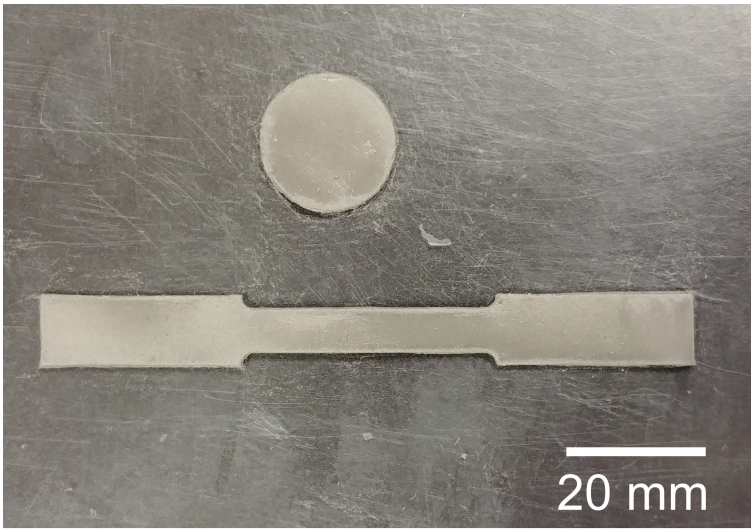

Figure 3.12 Fabricated disk and tensile bar by the modified DLP projector. The color wheel in the projector has been replaced by a bandpass filter.

of millions of highly reflective, individually controlled micromirrors. The mirrors can be tilted at an angle of ±12°and as often as 16000 cycles per second to direct incident light towards (ON mode) or away (OFF mode) from the projector lens, which creates a grey scale projection image [115]. The shade or brightness of each pixel on the image depends on the frequency of the mirror in ON mode. The DMD chip is synchronized with a spinning color wheel, which splits the original light source into red (R), green (G), and blue (B), creating individual RGB colored images. As the human eyes

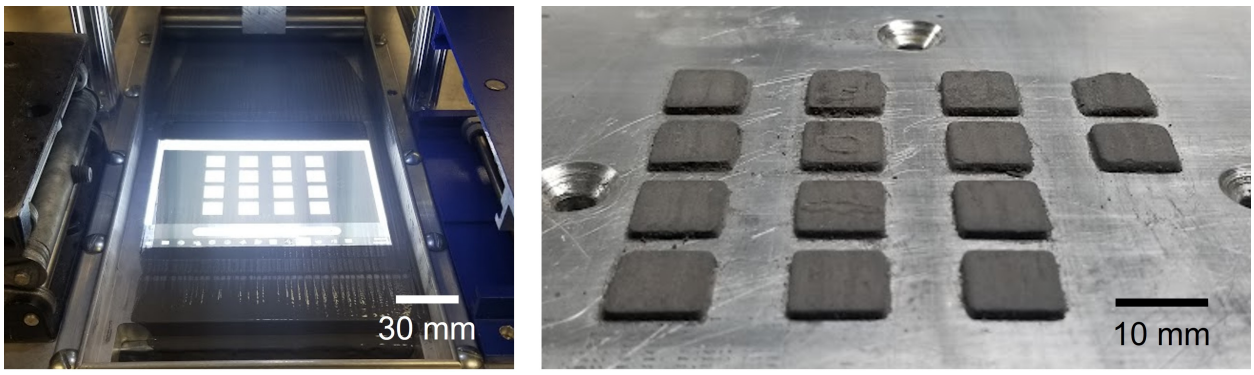

Figure 3.13 Left: Projected pattern by the modified DLP projector. Right: Corresponding fabricated parts from the projected patterns. The bottom 2 parts failed to fabricate due to the low light uniformity of the projector.

continuously average the incident light on the retina every 1/50th of a second, full spectrum color images can be achieved by controlling the display rate of individual RBG images [116]. Schematic of the working principles and components of a typical DLP projector is shown in Figure 3.14.

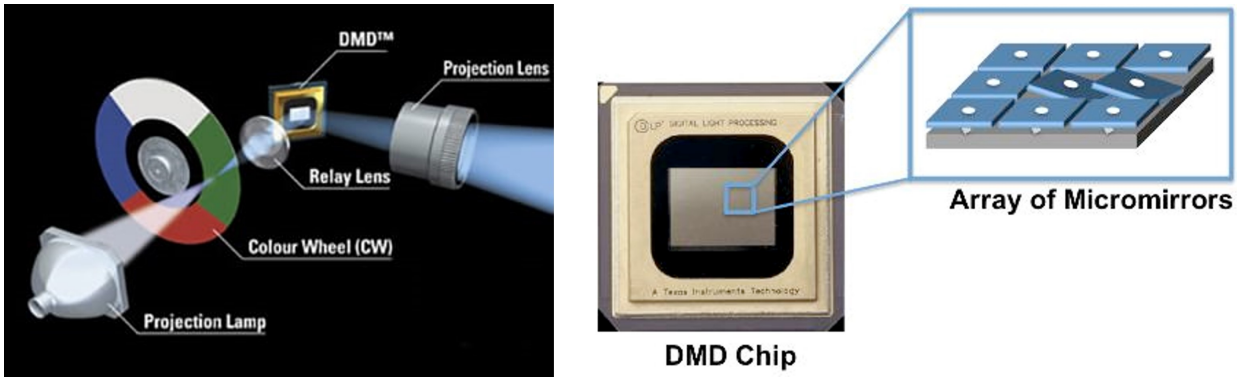

Figure 3.14 Schematic of the working principles and components of a typical DLP projector [117].

In essence, the color wheel is a set of dichroic mirrors, which allows visible light to pass through and either absorbs or reflects away UV and IR light [118], resulting in a reduction in energy output from the original light source. Moreover, a portion of the output irradiation falls outside of the absorbing wavelength of the photopolymer resin (320 - 500 nm). Therefore, photopolymerization could not be obtained in the experiments with the unmodified projector. Figure 3.15 shows the spectral distribution of RGB part of the original light source after being filtered by the color wheel of a DLP projector [119], showing a majority of the transmitted light falls outside of the absorbing region of the photopolymer resin.

Removal of the color wheel allows the full spectrum of the original light source to pass through, which has been a known technique since the early development of SLA technologies [120]. Typical metal halide lamps used in DLP projectors outputs a wide range of radiation wavelength, from deep UV to far IR region (Fig. 3.16) [121]. The addition of the heat absorbing bandpass filter in this experiment was aimed at reducing possible heating and optical damage to the DMD mirrors, while still allowing the projector to produce an effective radiation output in the 300 - 700 nm wavelength range, which encompasses the curing region of the photopolymer resin. After replacing the color wheel with the band pass filter, sufficient energy was provided for photopolymerization of the suspension, resulted in successful fabrication of the samples. The failed fabrication of the bottom two samples was due to the low uniformity of the projector at 80%, i.e. the outer area of the projection plane receives 80% of the irradiation intensity in comparison to the center area.

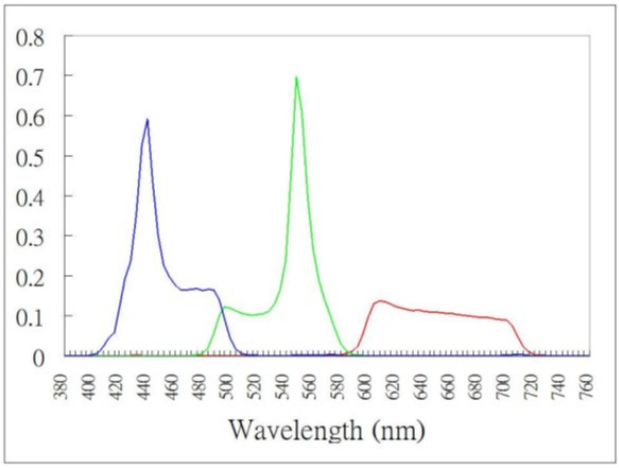

Figure 3.15 Spectral distribution of RGB part of the original light source after filterd by the color wheel of a DLP projector [119].

3.4.5 Conclusion

The proof-of-concept experiments carried out using different lighting techniques have demonstrated the feasibility in processing metal suspension using DMD digital mask technology. Multiple samples have been successfully fabricated in a layer by layer fashion using a DLP projectors with modified optics. The selection of the curing system has proven to be critical in the metal suspension

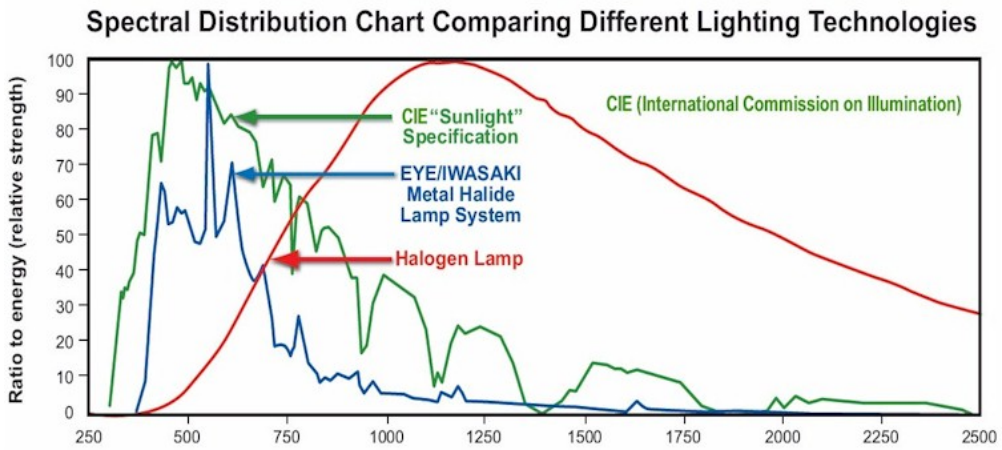

Figure 3.16 Irradiation spectrum of different lighting technologies typically used in DLP projectors [121]. Metal halide lamp spectrum is represented by the blue curve, showing a majority of irradiation falls above 500 nm wavelength, with a minor portion falls below 300 nm.

processing. Sufficient radiation power for photopolymerization, compatible wavelength with the photopolymer resin, and high projection uniformity are the important criteria that should be taken into consideration for a suitable curing system in the development of the SEAM process.

3.5 First-generation prototype

3.5.1 Prototype design and specifications

The previous experiments have demonstrated the feasibility in processing metal suspensions using DMD digital masking and top-down projection setup. Additionally, a mixing module must also be employed to maintain the metal suspension's homogeneity throughout the printing process. Based on these finding, the printing system of SEAM process was designed with the schematic working principles shown in Figure 3.17.

The system adopts the powder bed design with the print bed, which is lowered by one-layer thickness until the part is completely printed. The conventional supply bed is replaced by a top down deposition system, which also serves as a mixing module. The system functions as follows: (a) mixing module deposits a sufficient amount of the suspension for one layer while constantly mixing the suspension homogeneously, (b) a roller pushes the suspension from the deposition area

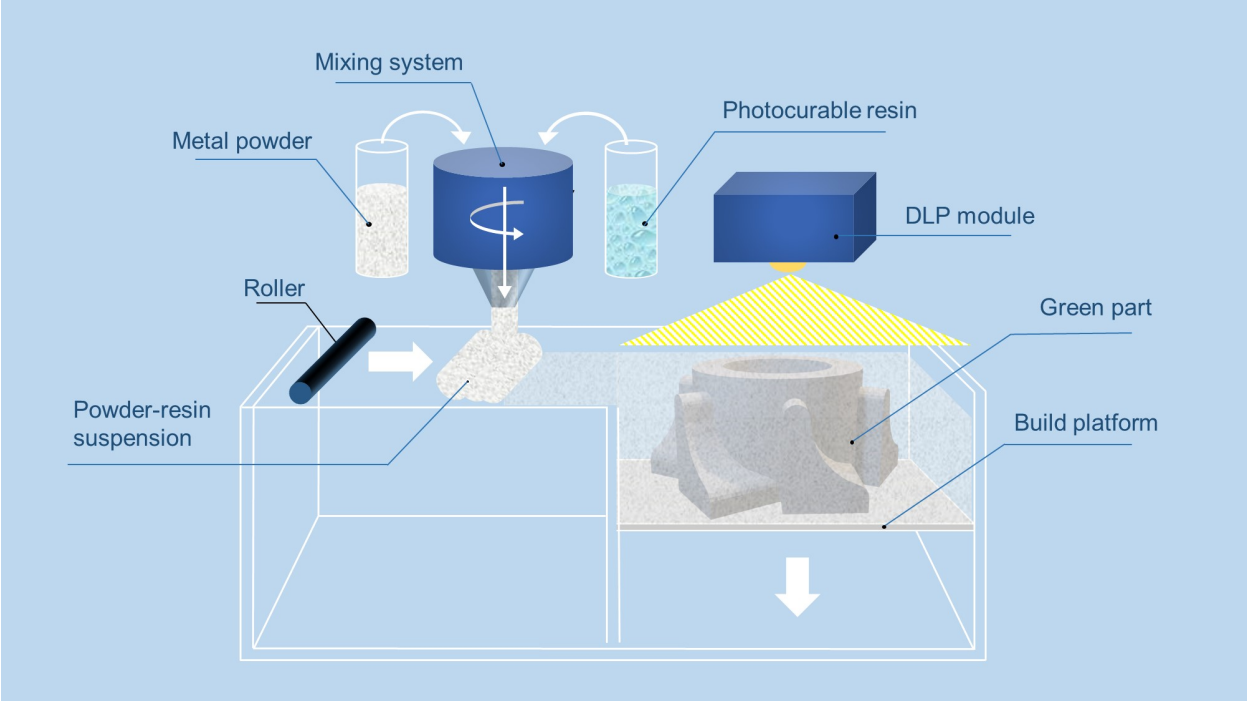

Figure 3.17 Schematic diagram of the working principles of SEAM process.

to the print bed, (c) DLP module projects the desired pattern on each layer of the print bed, (d) print bed moves down by a layer thickness, and (e) the process repeats until the 3D part is completed. A first-generation fully-functional SEAM system was designed constructed (Fig. 3.18).

A printing platform with dimensions of 125 x 125 mm is connected to an ETH032 high-force screw drive electric cylinder (Parker Hannifin - Cleveland, OH, USA), which allows for a minimum moving distance of 50 μm. The mixing and dispensing module for the system is the 5-RPD-D1B Pressure Slurry Dispenser (Crist Instrument - Hagerstown, MD, USA), which includes a stirrer to provide a constant mixing of the media and deliver the consistent amount of suspension in a controlled pressure. The 3DLP9000 (Digital Light Innovations - Austin, TX, USA) is selected for the UV curing module. The 3DLP9000 is specifically designed for 3D printing purposes, providing high uniformity and low distortion to help maximize the power delivered to the resin. The unit utilizes an LED as the light source with the wavelength of 405 nm, which is appropriate for the resins used in this dissertation, and many other commercially available resins on the market. The resolution of the unit is 100 μm pixel size with a maximum projection size of 192mm x 320mm.

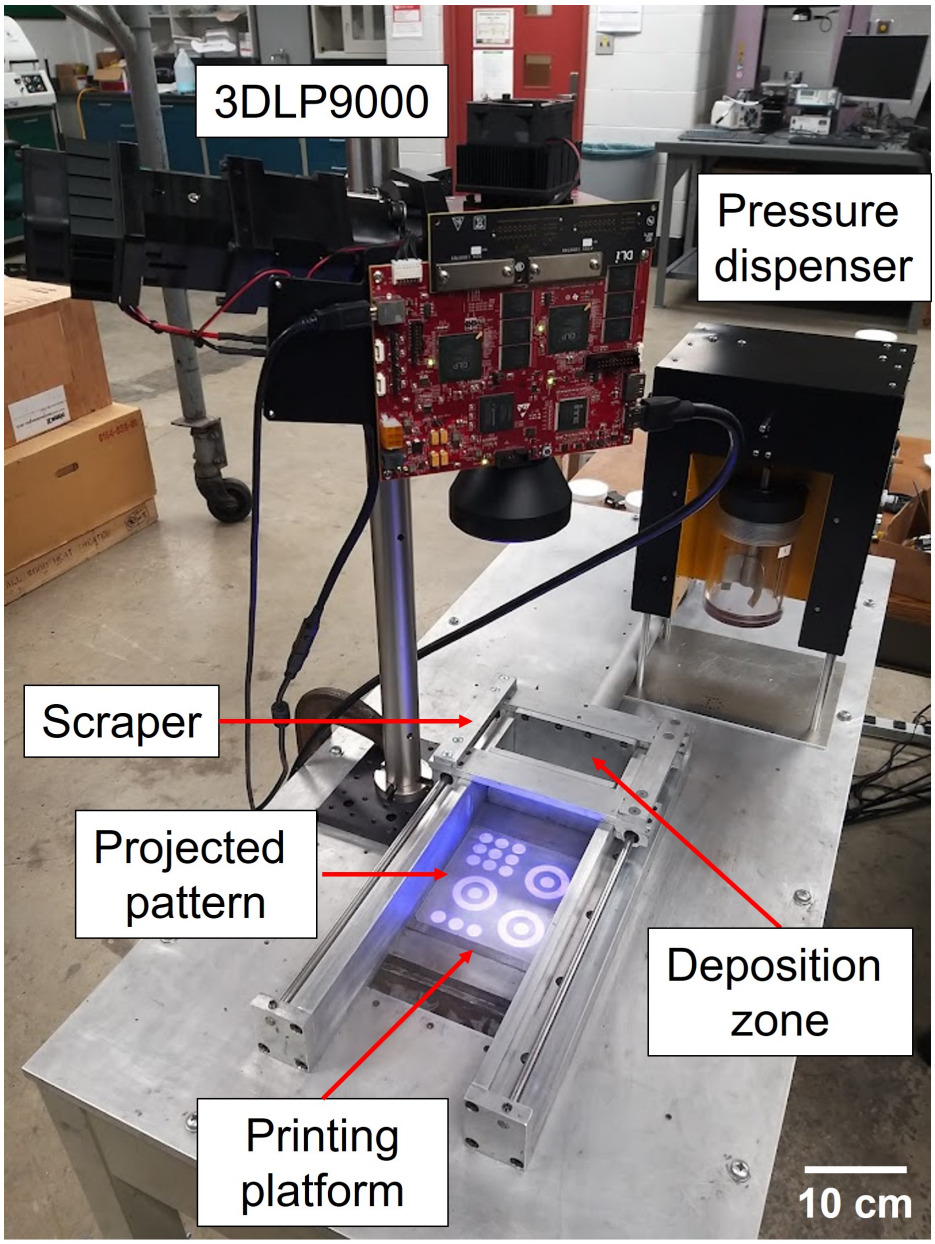

Figure 3.18 First-generation SEAM system protoype showing its main components.

The scraper is connected to the HDA12-2 linear actuator (Servocity - Winfield, Kansas, USA) with a maximum moving speed of 2 in/s. The double-bladed scraper design was employed to ensure layer flatness of both forward and backwards movements. NanoDLP, an open-source SLA slicer and controller software, was used to control and display the layer image pattern. Detailed information on all the components of the SEAM printing system prototype are provided in the Appendix.

3.5.2 Green parts fabrication demonstration of SEAM first-generation prototype

Several metal powder materials (SS420, stainless steel 316 (SS316), Haynes 214, and Amdry386) have been successfully shaped into 3D green objects using the first-generation prototype of SEAM process (Fig. 3.19). The chemical compositions of all the metal powders in this dissertation can be found in the Appendix. Detailed information on the printing process of all the aforementioned materials is presented in chapter 4 of this dissertation.

Figure 3.19 Demonstration parts fabricated using SEAM Process first-generation prototype. Top-left: Haynes 214 snowflake; Top-right: SS420 Mini heat exchanger; Bottom-left: Haynes 214 mini heat exchangers; Bottom-right: SS316L turbine.

3.6 Second-generation prototype

The second-generation prototype of SEAM process with a larger build volume and an improved resolution in z-direction is designed and constructed (Fig. 3.20 - 3.21). The build envelope's dimension is 200 x 200 x 200 mm, with 50 μm minimum travel distance of the print platform. The pressure mixer and dispenser have been replaced with an overhead mixer (Laboratory mixer LM5-A- Silverson, MA, USA) with an accessible material container for an easy addition of material as well as monitoring of the mixture quality during the printing process. A pneumatically controlled pinch valve with an inner rubber sleeve compatible with abrasive material was utilized as the suspension dispensing mechanism. The material guides connected to a pair of scrappers/doctor blades were designed to ensure the delivery of the suspension onto the platform as well as a smooth layer deposition on the printing platform. A linear stage (MS Linear Stage, Thomson Industries Inc, IL, USA) was connected to a servo motor (NTE-212-CONS - Nidec, Kyoto, Japan) to control the movement of the guides and scrapers. A ball screw (FSI-195-9702 - Thomson Industries Inc, IL, USA) with 350 mm travel distance was connected to a servo motor (NTE-320-CONS - Nidec, Kyoto, Japan) to provide sufficient support for the printing platform, while ensuring a smooth and high precision movement of the z axis. Detail information on all components of the second-generation prototype can be found in the Appendix.

3.7 Conclusion

In this chapter, multiple proof-of-concepts experiments were carried out to evaluate the feasibility of processing metal suspension using different UV patterning techniques. DLP projector systems with the use of digital micromirror devices have proven to be capable of providing sufficient light energy to initiate photopolymerization of the suspension to create 2D layer geometries. A first fully functional prototype of the SEAM process with a DLP curing module was then designed and constructed. Demonstration of 3D green parts fabricated by the prototype using different metal suspensions were presented. A second-generation prototype of the SEAM process with improvements in fabrication capability as well as functionalities is also being developed.

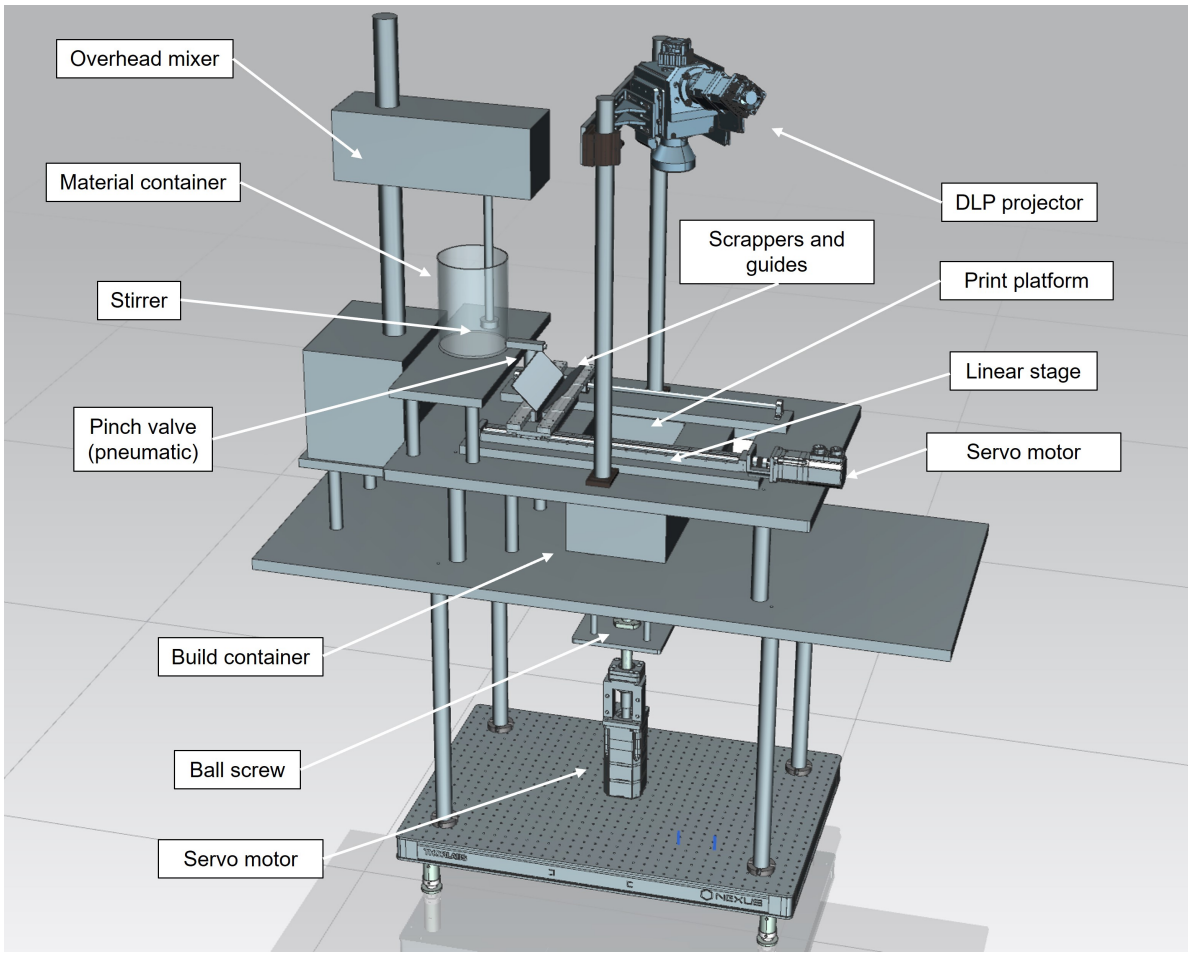

Figure 3.20 CAD model of the second-generation prototype showing the main components.

Author's note: *A portion of this chapter has been published in: H. X. Nguyen, H. Suen, B. Poudel, P. Kwon, and H. Chung, "Development of an innovative, high speed, large-scaled, and affordable metal additive manufacturing process," CIRP Annals, vol. 69, no. 1, pp. 177–180, Jan. 2020, doi: 10.1016/j.cirp.2020.04.069.*

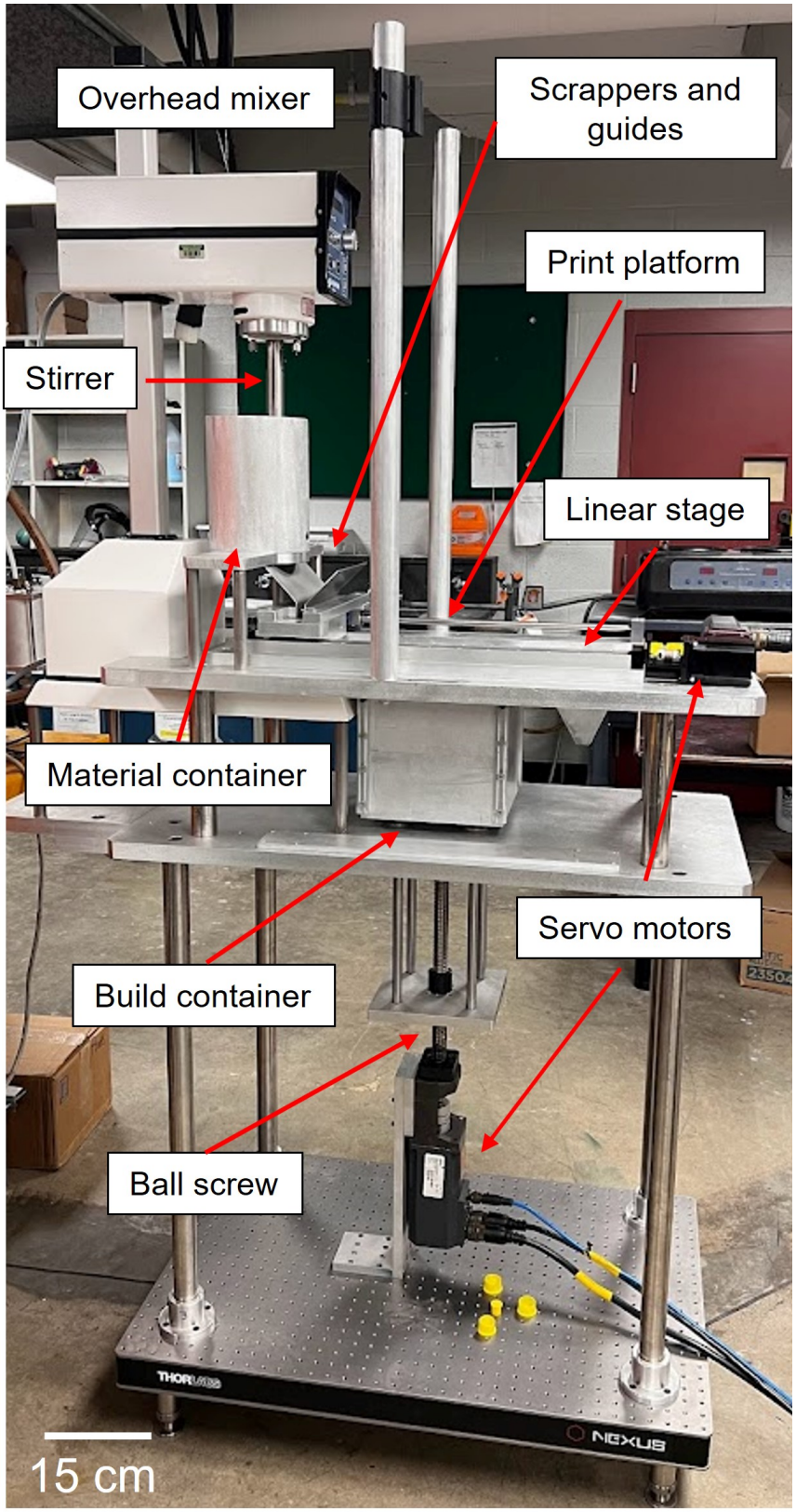

Figure 3.21 The constructed second-generation prototype showing the main components. The DLP projector is not included.

CHAPTER 4

SEAM PROCESS: GREEN PART FABRICATION

4.1 Introduction

The green part fabrication process of the SEAM process consists of the photopolymerization of a photosensitive metallic powder suspension where the photopolymer is selectively cured from liquid to solid state, which holds the metal particles together and forms the desired geometry. This chapter first provides the literature reviews on photopolymerization fundamentals as well as previous attempts on processing metal suspensions using SLA techniques. Challenges and limitations on shaping metal suspension into 3D objects are identified. Formulation requirements of a metal suspension suitable for SLA processing in general and the SEAM process in particular are discussed.

Experiments were carried out to characterize the relationship between cure depth and metal particle sizes. Consequently, appropriate processing conditions including UV energy dosage, cure time, and layer thickness were determined for SS420, SS316, Haynes 214, and Amdry 386 metal suspensions. An innovative 2-step curing strategy was devised and applied to the printing process, which not only prevents sedimentation of metal powder particles in the print bed but also enables the fabrication of overhang geometry without support structures. All the aforementioned alloys were successfully shaped into three dimensional green objects, which were ready for subsequent thermal post-processing steps to achieve fully dense metal parts. A procedure to obtain a multi-size powder mixture and subsequently, a metal suspension with improved powder packing density was also presented in this chapter.

4.2 Stereolithography of metal-photopolymer suspensions - current status

4.2.1 Photopolymerization fundamentals

Photopolymerization is defined as a technique that uses visible (vis) or UV light to initiate and propagate a polymerization reaction, forming a linear or crosslinked polymer structure [122] in photocurable resin. Photocurable resins, initially in liquid state, are converted into solid state upon irradiation of light. They typically consist of three main ingredients: photoinitiators, monomers, and oligomers.

- **Photoinitiator** generates either free radicals (in free radical polymerization) or H^+ (in cationic polymerization) upon UV/vis light irradiation, initiating the reaction. They subsequently attack functional groups in the monomers or oligomers, turning them into reactive species, which propagates the formation of the longer polymer chains.

- **Monomers** are low molecular weight molecules, and typically are added with the purpose of reducing the viscosity of the resin in traditional SLA process. In ceramic stereolithography, monomers are the main components since low viscosity of the resins is required. Common free radical-based monomers are methacrylates and acrylates. Epoxides are the most widely used cationic-based monomers.

- **Oligomers** are molecules with relatively high molecular weight and longer chain structures, which commonly are consisted of multiple monomer units. They play a major role in determining the final chemical and physical properties of the cured resin. However, they usually come in the form of viscous liquids, which can be hard to process using SLA techniques [123].

Figure 4.1 demonstrates the initiation, propagation and termination of a typical free radical photo-polymerization process. Monomers and oligomers used in photo-curable resins are typically multi-functional, i.e. they have two or more functional groups. Therefore, on top of the formation of linear chains, cross-linkings are also formed between the linear chains forming a network structure.

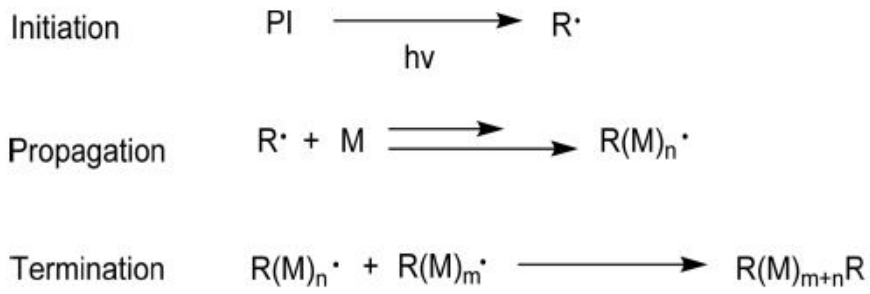

Figure 4.1 Initiation, propagation, and termination processes of radical photopolymerization [124].

After the reaction is initiated, the active chains propagate and grow, until their activity is lost by termination process [124]. In both radical and cationic polymerizations, termination typically occurs by radical-radical coupling mechanism. Presence of oxygen can also capture the radicals, causing the reaction to be terminated. Cationic polymerization is not sensitive to oxygen, and the polymer chains can propagate even after light exposure [122]. However, as SLA processes require a high degree of dimensional control, cationic photocurable resins are not desirable. Most of commercially available photocurable resins are free radical-based polymers [123].

4.2.2 Stereolithography of metal suspensions

Very limited research has been carried out on the processing of metal-filled photopolymer suspensions using SLA techniques.

Corbel et al. [68] first attempted to fabricate micro-components using aluminum powder and HDDA monomer-based resin. Multi-layer structures were fabricated with layer thickness of 15 μm (Fig. 4.2). However, post-debinded and sintered parts demonstrated poor density as well as electrical conductivity due to heavy oxidation of aluminum powder during the thermal cycles.

Lee et al. [66] demonstrated the feasibility of fabricating micro-electrical devices using copper-photopolymer suspensions using a stereolithography system with galvanometric laser scanning design. A recoater blade was added on top of the vat to ensure the level and flatness of the suspension surface. A new photopolymer was developed, which consists of 1,6-hexanediol-diacrylate (HDDA) and trimethylol propane triacrylate (TMPTA) as monomers, N-vinyl-2-pyrrolidone (NVP) for

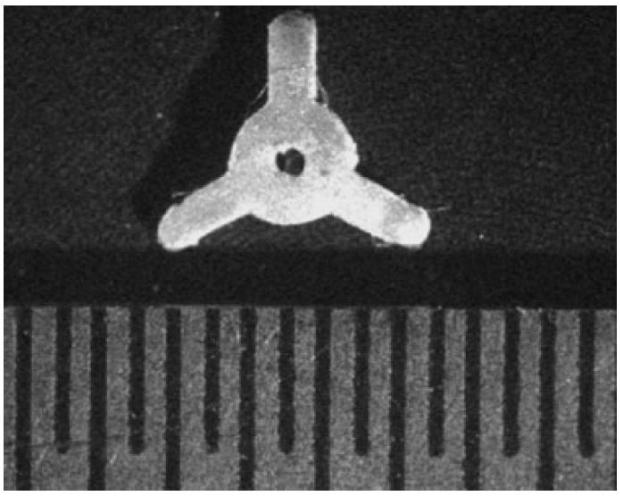

Figure 4.2 Green aluminum micro gear at 80 wt.% powder loading [68].

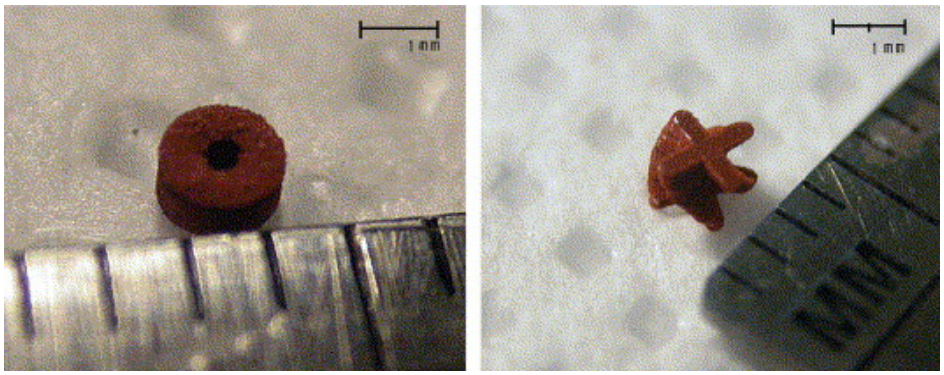

Figure 4.3 Copper micro-components by Lee et al. [66].

dilution, and dimethoxy phenyl acetophenone (DMPA) for photopolymerization initiation. Triton X-100 dispersant was also added to enhance UV laser light penetration. Small components with sizes under 3 cm were fabricated and subsequently sintered to produce copper parts with good electrical conductivity (Fig. 4.3). The study also poses several difficulties: high viscosity of the suspensions, low light penetration, and high porosity level in final structures.

Bartolo et al. [67] studied the curing kinetics of tungsten and cobalt filled suspensions produced with unsaturated resin (Crystic 272) and epoxy (EC 130 LV). The photo-initiators selected were the radicalar initiator 2,2-dimethoxy-1,2-diphenylethan-1-one (Irgacure 651) and the cationic initiator 4-methylphenyl [4-(2-methylpropyl)phenyl]-hexafluorophosphate (Irgacure 250). In order to decrease the viscosity of the formulated suspensions, styrene was used for dilution, which has been

found to have minimal effect on curing behaviors. The results have shown that an increase in UV light intensity and photo-initiator concentration lead to a higher reaction rate. A hybrid resin system with both unsaturated and epoxy resin can be used in combination with metallic powder was formulated for SLA processing. However, at high metallic particle packing, the light scattering effect leads to a decrease in UV light penetration as well as resin conversion fraction.
While previous studies have indicated the potential in processing metal suspension using SLA, two major challenges remain unsolved:

- An effective cure depth of metal suspension has not been produced due to the predominance of light scattering and absorption. Limited cure depth resulted in a limited layer thickness, which made the processing time excessively long, even for the fabrication of small objects. In order to develop a practical curing process using metal suspension, it is crucial to improve the cure depth of the suspensions to 100 - 200 μm [73, 125].

- Sedimentation of metal particles in the suspension is difficult to prevent due to the significant density difference between metal powder and resin. In ceramic suspensions, the use of dispersing agent is sufficient to negate this effect [71, 72]. Such phenomenon has not been replicated for metal suspensions. A strategy to control metal suspensions for practical fabrication will be presented in later sections .

4.3 Experimental procedure

4.3.1 Metal suspension cure depth characterization

The governing equation for cure depth was derived from the standard expression for the turbidity of suspensions [70, 126]:

$$C_d = \frac{d}{Q\emptyset} ln \frac{E}{E_c} \tag{4.1}$$

where C_d is the cure depth, d is average particle size, $\emptyset$ is volume fraction of powders, E is the energy dosage per area of the light source, and E_c is the critical energy below which photopolymerization

does not occur. The value Q should be calculated numerically for different situations [126] but for ceramics, it is generally agreed to be:

$$Q = \left(\frac{\Delta n}{n_0}\right)^2 \left(\frac{d}{\lambda}\right)^2 \tag{4.2}$$

where Δn is the refractive index difference between the ceramic (n_p) and the resin (n_o), and λ is the light source wavelength.

This model has been validated by empirical results and it was concluded that the cure depth is controlled by refractive index difference and particle size in ceramic suspensions [72]. However, such relationship has not been established for metal suspensions. To improve cure depth of metal suspensions, it is crucial to determine the governing factors, e.g. refractive index difference and particle size, and understand how to manipulate such factors to achieve a desirable cure depth. Since refractive index is a material dependent factor, experiments must be carried out to characterize the relationship between particle size and cure depth in metal suspension. For each of the materials presented in this chapter, different powder sizes were used to create suspensions with the same powder volume fraction of 0.56, which is a typical particle loading fraction for highly-filled suspensions for SLA [11]. The UV curable resin used in this chapter and for the rest of the work in this dissertation was CPS 3010 (Colorado Polymer Solutions, Denver, Colorado) with a room temperature viscosity of 12 cP and an optimal curing wavelength of 405 nm. The CPS3010 was recommended by the manufacturer as an improved version of the CPS1030 used in the previous section, due to its higher reactivity when irradiated to UV light as well as increased stability under natural light. The composition of the resin shown in Table 4.1 is mostly proprietary information of the manufacturer.

The suspensions were then spread to a single layer with controlled layer thickness on a powder bed system. The layer was sequentially exposed to a desired geometry with controlled UV energy dosage at the wavelength of 405 nm. After the unexposed suspension was removed, the desired geometry can be retrieved. Figure 4.4 shows an example of the experimental setup with the left

Table 4.1 Chemical composition of CPS3010, data provided by Colorado Photopolymer Solution.

Chemical Name	**CAS-No**	**Wt/Wt**
2-Propenoic acid, 1,6-hexanediyl ester	13048-33-4 < 67.5	>= 60 - < 80 %
Polythiol	Proprietary*	>= 10 - < 20 %
Methacrylate ester	Proprietary*	>= 5 - < 10 %
Photoinitiator	Proprietary*	>= 1 - < 5 %

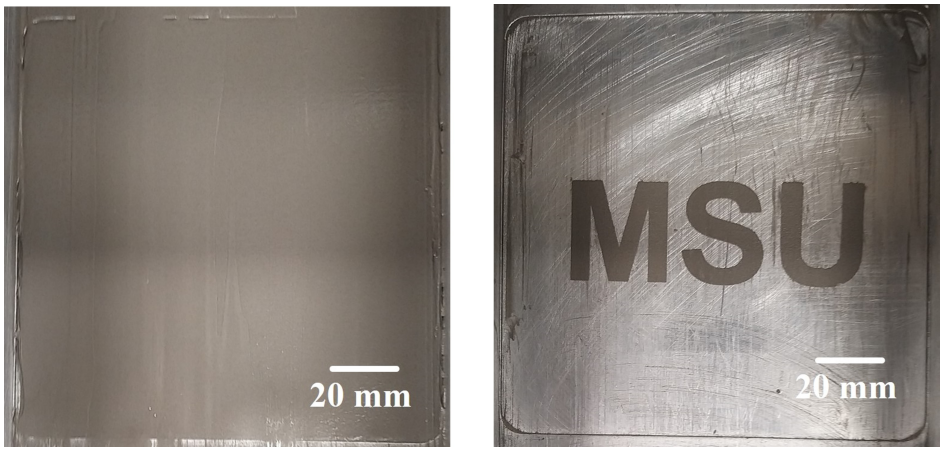

Figure 4.4 Metal suspension cure depth experimental setup. Left: Initial layer spread on the printing bed; Right: Layer geometry after UV patterning and removal of loose material.

picture shows the initial layer and the right picture shows the layer geometry after patterning and removal of loose material. Two important phenomena were observed for each experiment:

- Photopolymerization: photopolymerization occurred when the given energy dosage exceeded the suspension critical energy E_c.
- Plate adhesion: plate adhesion occurred when the cure depth C_d exceeded the layer thickness.

From the experimental results, the relationship between powder size, energy dosage, critical energy, and cure depth of the suspension can be characterized for all available powder sizes of each metal material. While the exact cure depth and critical energy dosage for each suspensions could not be determined using this experimental method, the information provided was sufficient to derive appropriate processing parameters for the suspensions, i.e., UV exposure time and layer thickness. for the successful green part fabrication process.

4.3.2 Optimal powder mixing ratio determination

A well-established method to improve green density and consequently the density of sintered part is increasing the packing density of the initial powder feedstock by using bimodal or multi-modal powder mixing [56]. In a well-packed powder mixture, the smaller powder particles fill in the interstitial voids between the larger particles and hence increase the overall packing density. Benefits of better green density are not only limited to improvement in sintered density but also better surface quality and less shrinkage. Studies have shown that it is not only possible to increase the green density of the printed part by mixing two or more powder sizes, but also to predict the optimal mixing ratios of multiple powder mixture, using a linear packing model [127]. The predicted green packing density, γ, of i powder constituents is calculated by:

$$\gamma_i = \frac{\beta_i}{1 - \sum_{j=1}^{i-1} \left[1 - \beta_i + b_{i,j}\beta_i \left(1 - \frac{1}{\beta_j}\right)\right] y_j - \sum_{j=i+1}^{n} \left[1 - a_{i,j}\frac{\beta_i}{\beta_j}\right] y_j} \tag{4.3}$$

where a_i, j and b_i, j are the loosening and wall effect parameters, respectively and can be calculated by:

$$a_{i,j} = \sqrt{1 - \left(1 - \frac{d_j}{d_i}\right)^{1.02}} \tag{4.4}$$

$$b_{i,j} = 1 - \left(1 - \frac{d_i}{d_j}\right)^{1.50} \tag{4.5}$$

An in-house Python code was developed to utilize Equation 4.3 which takes the tapped powder density of two or more powder sizes as input to calculate the optimal mixing ratio. The Python code is included in the Appendix section.

Given two or more powder sizes, a procedure to determine the optimal packing density can be carried out as follows:

1. 100 grams of each powder size is tapped for 20 minutes at 150 rpm up to 5 times in a graduated cylinder using a powder tapping device. The tapped packing density of the powder is taken as the average of all measurements.

2. The calculated tapped density of each powder size is used as input to the code to determine the optimal packing ratio.

3. The different powder sizes are combined according to the obtained packing ratio, and can be mixed using a high-speed mixer or a bench top ball mill.

The powder tapped density for the available powder sizes of each metal material will be experimentally determined, and the optimal size composition of their powder mixture was calculated. Consequently, an optimal powder mixture was produced, using a bench top high-speed mixer (DAC 150.1 FVZ, FlackTek SpeedMixer – SC, USA) operating at 1500 rpm for 90 seconds. The powder mixture was subsequently combined with the photopolymer resin, CPS3010, to create the optimal suspension for each metal material.

4.3.3 Fabrication strategy

4.3.3.1 2-step curing strategy

As discussed in the previous chapter, due to the higher density of metal powder in comparison to the photopolymer, the metal suspension is constantly separating, with the metal powder settling out of the suspension (Fig. 4.5a). While this issue can be solved initially by the constant mixing of the suspension in the dispenser, its effect is detrimental on the print bed. At the uncured area, where the suspension is not solidified, a thin layer of pure photopolymer initially forms on top as the metal powder settles down. As the fabrication process proceeds, more layers of suspension are delivered, and more powder particles are settled to the bottom, a thicker layer of pure photopolymer is gradually developed. The thick liquid layer of photopolymer formed on top of the print bed cannot provide sufficient support for the next layer of suspension to be recoated (Fig. 4.5b).
In order to overcome the segregation of the suspension on the print bed, a 2-step curing strategy was devised and employed for the SEAM process (Fig. 4.5c). Before the layer geometry is projected by the DLP projector for a complete photopolymerization, the whole print area is exposed to UV light for a very short amount of time. The given low dosage of UV light partially photopolymerizes, or "soft-cures", the suspension, converting it to a quasi-liquid state, which not only prevents the metal powder from settling out but also provides sufficient strength for the layer to support

subsequently recoated layers, allowing the fabrication process to proceed. Finally, UV light is irradiated selectively corresponding to the desired geometry to fully photopolymerize or "geometry cure". After all the layers are fabricated, the soft-cured regions can be easily removed to retrieve the printed parts.

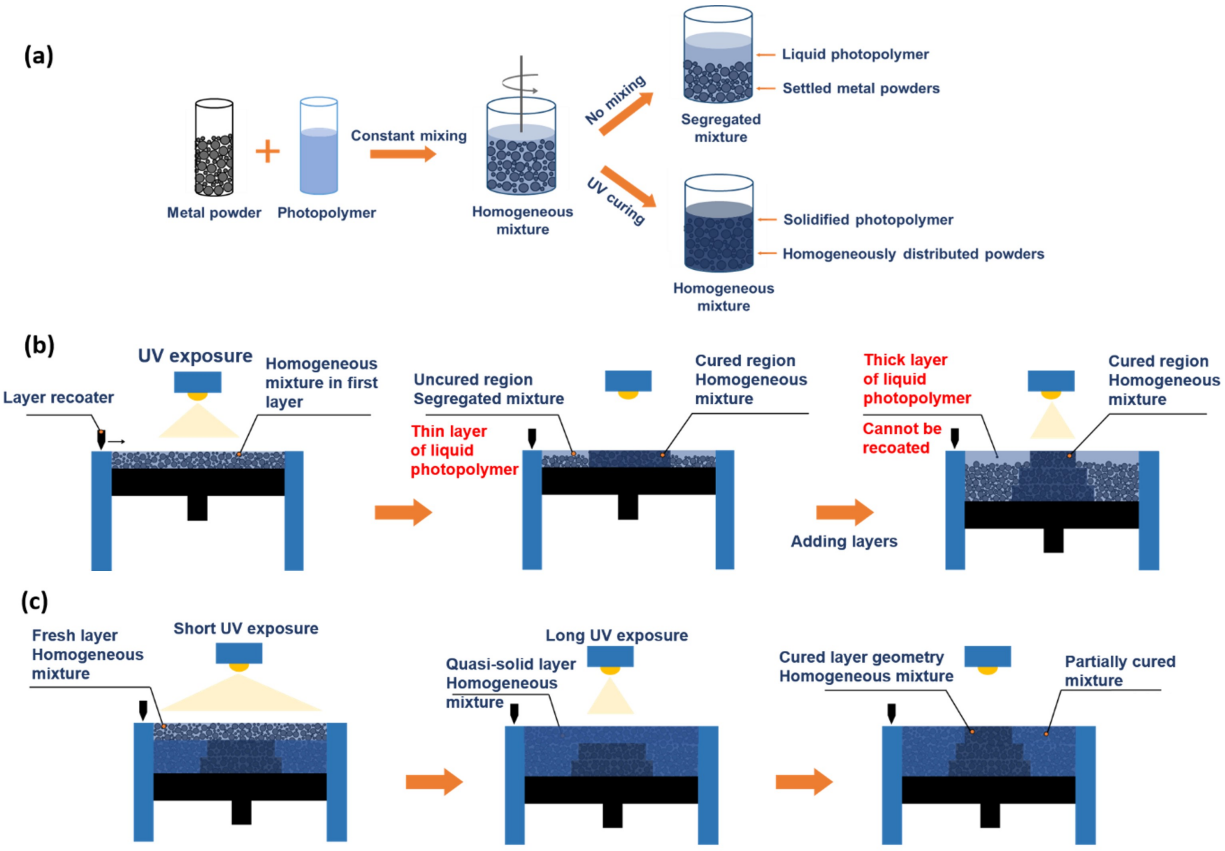

Figure 4.5 Schematic diagram of (a) Sedimentation of metal powder in the suspension, (b) printing challenges due to the gradual separation of metal and photopolymer resin in the print bed, and (c) the proposed 2-step curing strategy.

4.3.3.2 Soft-curing time determination

Single layers of metal suspension were spread on the printing platform at a controlled layer thickness. For each layer, the 2-step curing strategy was carried out, with different soft curing time of 1, 2, and 3 seconds, while holding the geometry cure time constant. The post-curing layer geometry was retrieved and inspected to determine the optimal curing time for metal suspensions of each metal.

4.4 Experimental results

4.4.1 Stainless steel 420

4.4.1.1 Cure depth, critical energy, and energy dosage

Single layer of SS420 suspensions was spread on the printing platform with controlled layer thickness of 50, 100, and 200 μm, and was irradiated with patterned UV light with controlled energy dosage level of 62.5, 125, and 187.5 mJ/cm^2. For the -106/+45 μm powder suspension, photopolymerization and plate adhesion were achieved at all layer thickness and energy dosage, indicating that the minimum E_c was below 62.5 mJ/cm^2 and the maximum C_d value was greater than 200 μm. In the case of -53/+22 μm powder suspension, photopolymerization only occurred with the energy dosage of 187.5 mJ/cm^2 and plate adhesion was observed with 50 μm and 100 μm layer thickness. In the experiments with -22/+5 μm powder suspension, no photopolymerization was achieved for all layer thicknesses and energy dosages, indicating an E_c exceeded the maximum given energy dosage of 187.5 mJ/cm^2. The experiments were repeated with higher energy dosage values and photopolymerization took place at 750 mJ/cm^2. Plate adhesion was found at only 50 μm layer thickness. The result is summarized in Table 4.2.

Table 4.2 Activation energy and cure depth for different SS420 powder sizes.

Particle size (μm)	**E_c (mJ/cm^2)**	**C_d (μm)**
-106/+45	E_c < 62.5	C_d > 200
-53/+22	125 < E_c < 187.5	100 < C_d < 200
-22/+5	≈ 750	50 < C_d <100

4.4.1.2 Optimal powder mixing ratio

The optimal powder mixing weight ratio of the two powder sizes, -106/+45 μm and -53/+22 μm was calculated to be 67.5:32.5 large:small powder size. The mixture packing ratio shows an approximately 4% improvement over that of the single sized starting powder. The tapped density and packing ratio of the optimal 2 size powder mixture were calculated using the model, and

subsequently verified experimentally. The results are summarized in Table 4.3.

Using the -53/+22 μm powder and the optimal two-size powder mixture, suspensions with 56% volume loading was produced. Boron nitride (BN) was also added into the starting powder to enhance the densification behavior during the sintering process. Detailed information on sintering optimization of SEAM printed SS420 parts with BN inclusion will be presented in chapter 6 of this dissertation.

Table 4.3 Tapped density of individual SS420 powder size and optimal 2 size powder mixture.

Particle size (μm)	**Tapped density (g/cm^3)**	**Packing ratio (%)**
-106/+45	4.63	59.86
-53/+22	4.59	59.35
Optimal 2 size powder mixture (theoretical)	4.90	63.4
Optimal 2 size powder mixture (experimental)	4.78	61.8

4.4.1.3 Fabrication parameters

The results in previous section on the relationship between SS420 particle size, cure depth, and critical energy density have indicated that an appropriate energy dosage to produce a cure depth of above 100 μm for the single size powder suspension is between 125 and 187.5 mJ/cm^2, which corresponds to a curing time between 40 and 60 seconds. Experimentally, it has been determined that the curing time of 40 seconds was sufficient to produce good interlayer bonding. Therefore, the processing parameters used for the single sized -53/+22 μm powder suspension were 40 seconds of geometry curing time and 100 μm layer thickness.

For the two-size powder mixture suspension, the presence of larger powder particles resulted in a lower energy dosage required to produce sufficient curing depth. The processing parameters were determined to be 30 seconds of geometry curing time and 150 μm layer thickness.

For the soft-curing experiment, it was observed the curing time of 3 seconds resulted in visible resolution loss of the layer geometry (Fig. 4.6). On the other hand, good quality layer geometry

was produced with 1 and 2 seconds of soft-curing time. The soft-curing time used to process both SS420 suspensions were 2 seconds.

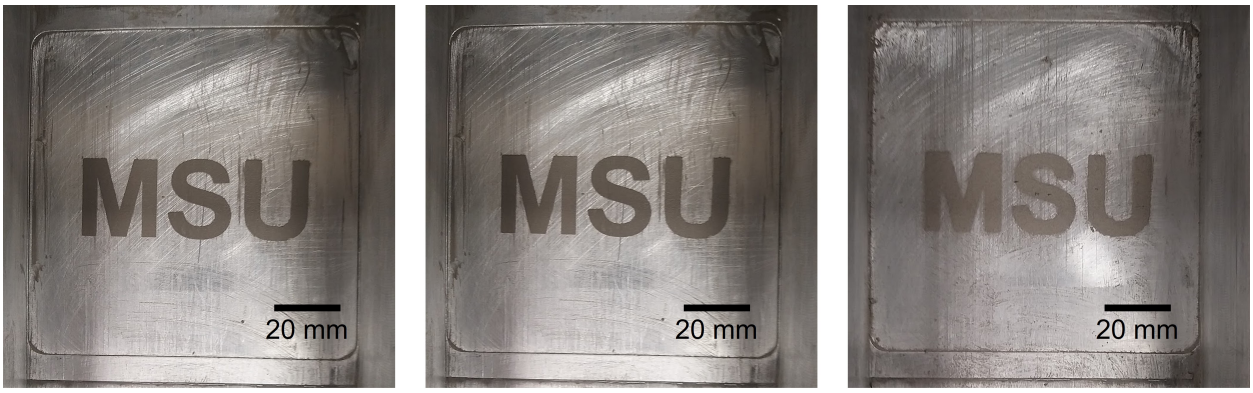

Figure 4.6 Single layer geometry after different soft-curing time of 1, 2, and 3 seconds. Visible resolution loss is observed with 3 seconds of soft-curing time.

4.4.1.4 Fabricated parts

Multiple sample sets which consist of cylindrical coupons, square blocks, and long bars were produced using both the single-size and two-size powder mixture suspension. Figure 4.7 shows the typical test coupons fabricated in a single build. A green turbine was also fabricated using the single size powder suspension to demonstrate the process capability in producing 3D structures. The turbine wings with overhang geometries were fabricated without any support structures, due to the soft-cured area providing sufficient strength to hold up the overhang structures. The 2-step curing strategy has not only solved the suspension segregation issue in the print bed but also enabled the capability to fabricate overhang geometries without the need of additional support structures.

4.4.2 Stainless steel 316

4.4.2.1 Cure depth, critical energy, and energy dosage

The critical energy dosage and cure depth for each SS316L powder were determined by the single layer curing experiments in the same manners as SS420. The experimental results are summarized

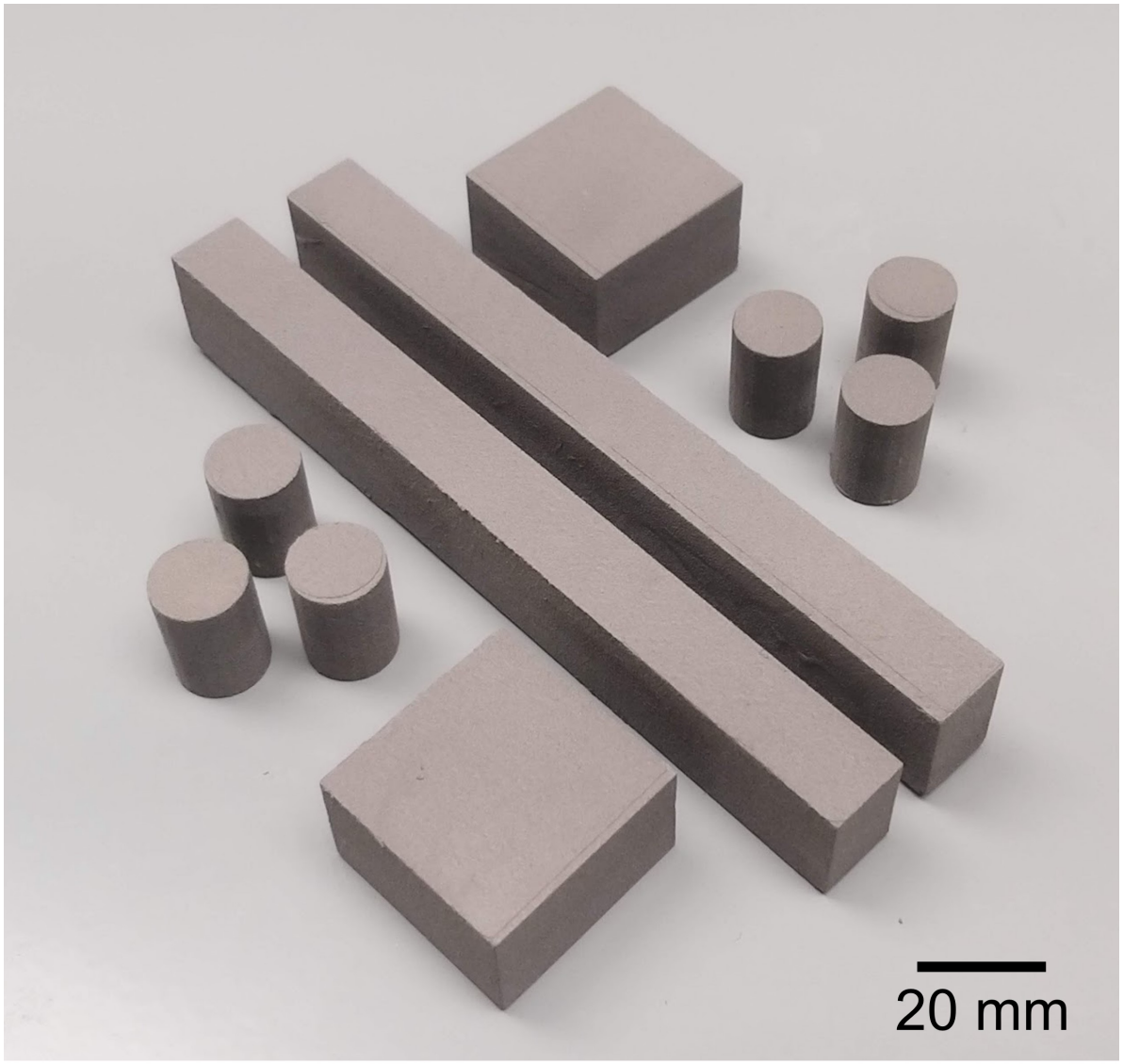

Figure 4.7 SS420 green sample set fabricated from a single build using 2 size powder mixture suspension by SEAM process.

in Table 4.4. As expected, the cure depth and activation energy of SS316L powder were similar to the values of SS420 powder, due to the similar particles size range between the two materials.

Table 4.4 Activation energy and cure depth for different SS316L powder sizes.

Particle size (μm)	**E_c (mJ/cm^2)**	**C_d (μm)**
-106/+45	E_c < 67.5	C_d > 200
-45/+15	125 < E_c < 187.5	100 < C_d < 200

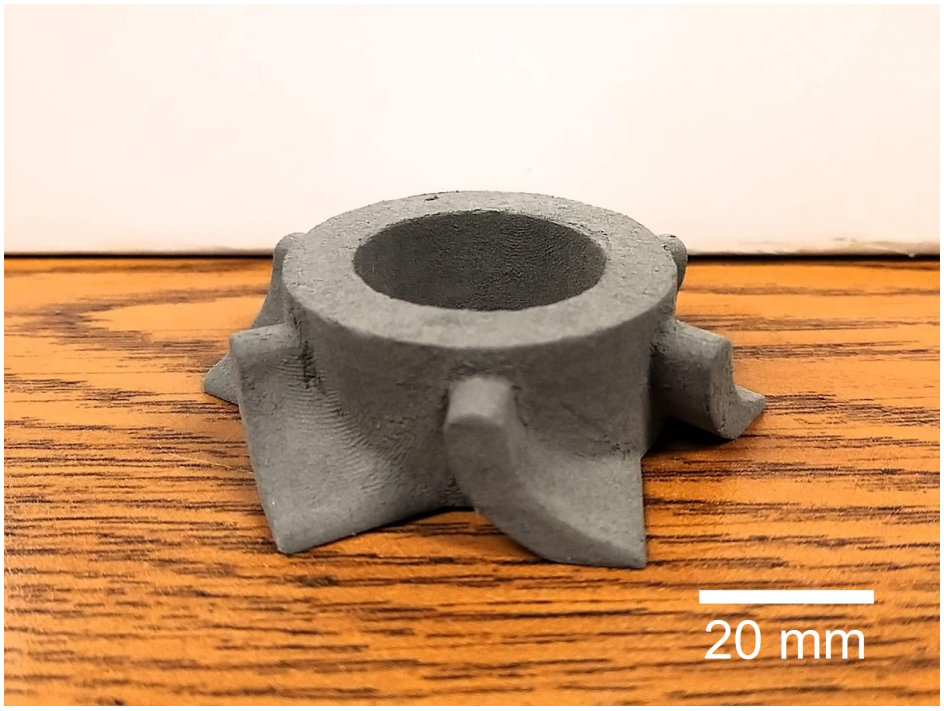

Figure 4.8 SS420 green turbine fabricated by SEAM process.

4.4.2.2 Optimal powder mixing ratio

Through the tapping tests and the powder mixing model, the optimal mixing weight ratio of SS316L large:small powder sizes was determined to be 65:35. The mixture packing ratio shows an approximately 6% improvement over that of the single sized starting powder. The tapped density and packing ratio of the optimal two-size powder mixture were calculated using the model, and subsequently verified experimentally. The results are summarized in Table 4.5.

Table 4.5 Tapped density of individual SS316L powder size and optimal 2 size powder mixture.

Particle size (μm)	**Tapped density (g/cm^3)**	**Packing ratio (%)**
-106/+45	4.79	59.98
-45/+15	4.89	61.28
Optimal two-size powder mixture (theoretical)	5.50	68.98
Optimal two-size powder mixture (experimental)	5.30	66.45

4.4.2.3 Fabrication parameters

Experimental results in section 4.4.2.1 have indicated that for the smaller powder size suspension, in order to produce a cure depth of between 100 and 200 μm, an energy dosage level of between 125 and 187.5 mJ/cm^2 was required, which was equivalent of 40 to 60 seconds of curing time. For the two-size powder mixture suspensions, a cure time of 40 seconds have been experimentally determined to produce a good layer bonding at 100 μm layer thickness. An appropriate soft-cure time was also determined to be 2 seconds for each layer.

4.4.2.4 Fabricated parts

Figure 4.9 shows a sample set produced by SEAM process using the SS316L powder mixture suspension made of two powder sizes. Multiple green turbines as well as cylindrical and small block coupons were fabricated. A smaller turbine with overhang wings were also produced, which has been previously shown in Figure 3.19 (bottom right).

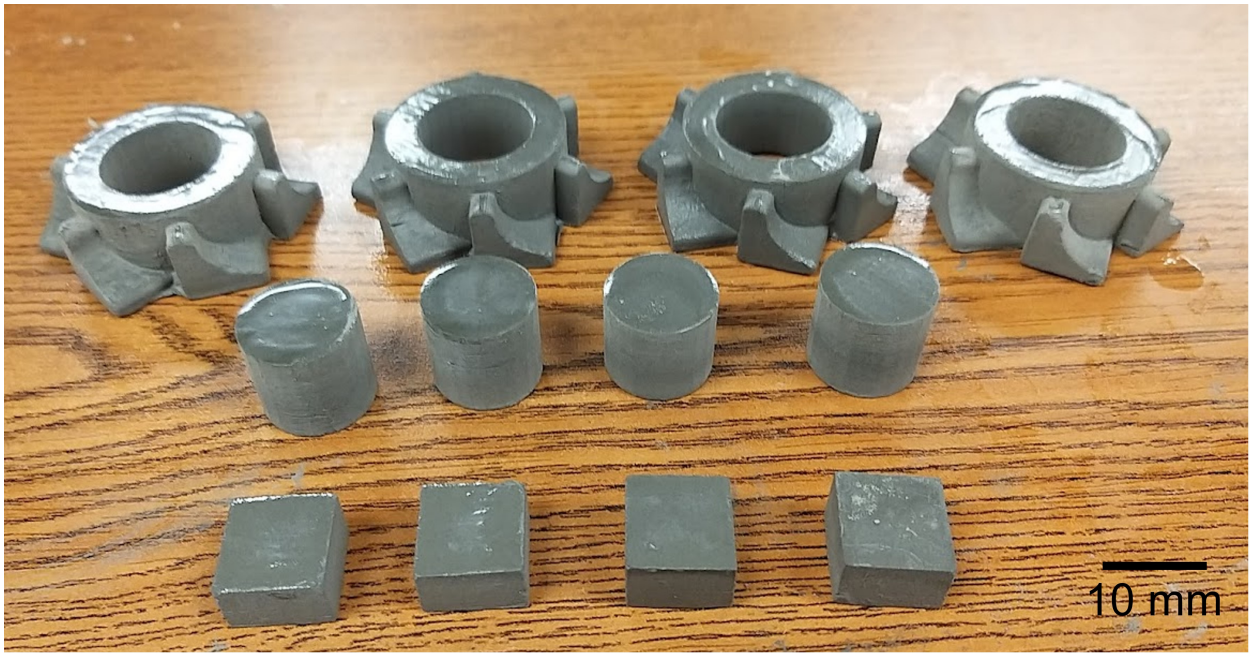

Figure 4.9 SS316L green sample set fabricated from a single build by SEAM process.

4.4.3 Haynes 214

4.4.3.1 Cure depth, critical energy, and energy dosage

Single layer of Haynes 214 suspensions was spread on the printing platform with controlled layer thickness of 150, 200, and 250 μm, and was irradiated with patterned UV light with controlled energy dosage level of 62.5, 125, and 187.5 mJ/cm^2. Two particle sizes tested were -15/+45 and -45/+150. As the eventual goal is to create a powder mixture of both powder sizes, the minimum layer thickness for fabrication must be higher or equal to the largest particle size, i.e. 150 μm. Therefore, a minimum layer thickness of 150 μm was selected for this experiment. For the larger powder size, a cure depth of 250 μm was achieved for all the given energy dosages. For the smaller powder size, a cure depth of 150 μm was produced in only the experiment with 187.5 mJ/cm^2. The results are summarized in Table 4.6.

Table 4.6 Activation energy and cure depth for different Haynes 214 powder sizes.

Particle size (μm)	**E_c (mJ/cm^2)**	**C_d (μm)**
-45/+150	E_c < 67.5	C_d >250
-15/+45	125 < E_c < 187.5	150 < C_d < 200

4.4.3.2 Optimal powder mixing ratio

Through the tapping tests and the model, the optimal mixing weight ratio of Haynes 214 large:small powder sizes was determined to be 66:34. The mixture packing ratio shows an approximately 8% improvement over that of the single sized starting powder. The tapped density and packing ratio of the optimal two-size powder mixture were calculated using the model, and subsequently verified experimentally. The results are summarized in Table 4.7.

Haynes 214 suspensions with the metal powder volume loading of 56% were produced using the optimal two-size powder mixture and CPS 3010. 0.5 wt% BN was also added into the powder mixture as sintering aid. The sintering behavior of Haynes 214 with and without sintering aids was investigated and the results are presented in chapter 6 of this dissertation.

Table 4.7 Tapped density of individual Haynes 214 powder size and optimal 2 size powder mixture.

Particle size (μm)	Tapped density (g/cm^3)	Packing ratio (%)
-15/+45	4.60	57.33
-45/+150	4.74	59.05
Optimal 2 size powder mixture (theoretical)	5.55	69.06
Optimal 2 size powder mixture (experimental)	5.234	65.18

4.4.3.3 Fabrication parameters

Experimental results in section 4.4.3.1 have indicated that for the smaller powder size suspension, in order to produce a cure depth of between 150 and 200 μm, an energy dosage level of between 125 and 187.5 mJ/cm^2 was required, which was equivalent of 40 to 60 seconds of curing time. For the two-size powder mixture suspensions, a cure time of 45 seconds have been experimentally determined to produce a good layer bonding with a layer thickness of 150 μm . An appropriate soft-cure time was also determined to be 1 seconds for each layer.

4.4.3.4 Fabricated parts

Figure 4.10 shows a sample set produced by SEAM process using Haynes 214 2 size powder mixture suspension. Cylindrical coupons were fabricated for sintering optimization experiments. The 14 cm long bars can be machined into thin tensile bars after sintering step for high temperature mechanical testing. A pair of heat exchanger plates with 4 cm in size and 4 mm thickness with 3D twisted fin geometry were also fabricated. Figure 3.19 also shows a Haynes 214 snowflake which demonstrates the level of small feature that the SEAM process is capable of producing.

4.4.4 Amdry 386

4.4.4.1 Cure depth, critical energy, and energy dosage

Single layers of Amdry 386 suspensions were spread on the printing platform with controlled layer thickness of 150, 200, and 250 μm, and were irradiated with patterned UV light with controlled

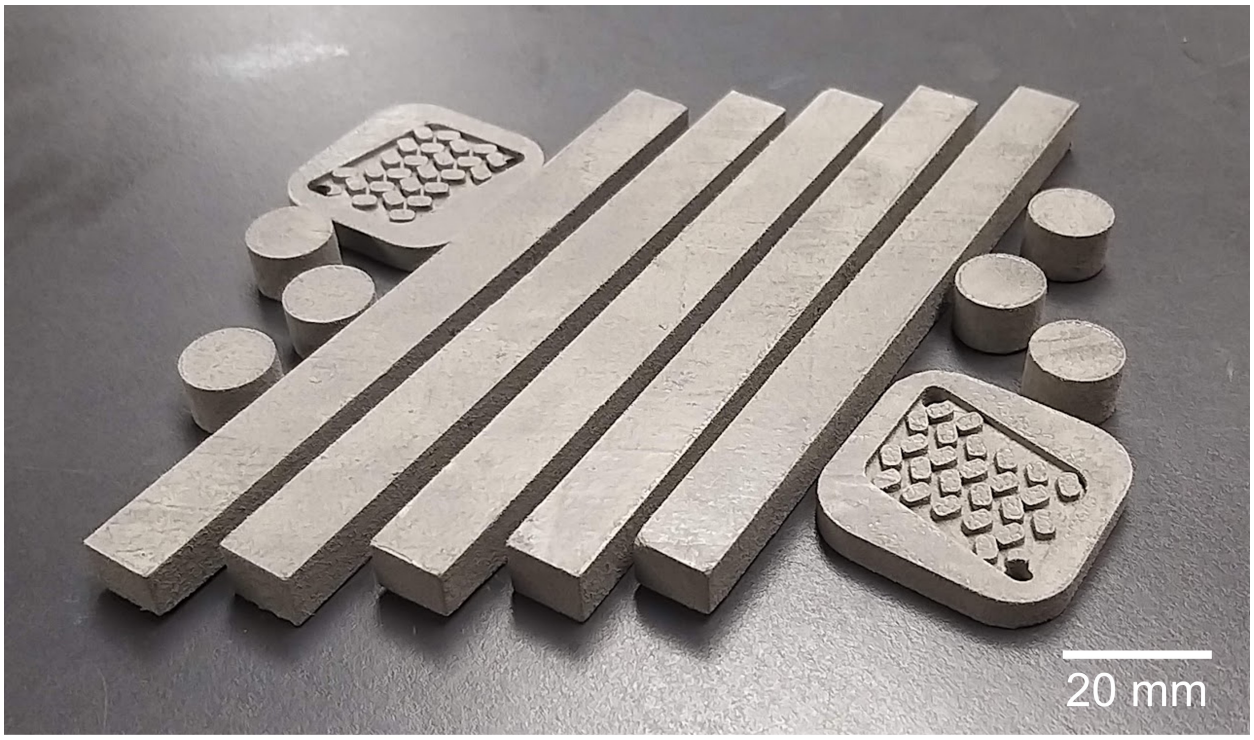

Figure 4.10 Haynes 214 green sample set fabricated from a single build by SEAM process.

energy dosage level of 62.5, 125, and 187.5 mJ/cm^2. The two particle sizes tested were -8/+65 and -45/+125. Since the the maximum particle size of the larger size powder is 125 μm and the resolution of the z motor is 50 μm, a layer thickness of 125 μm cannot be attainable. Thus, the minimum layer thickness tested in this experiments was selected to be 150 μm. For the larger powder size, a cure depth of 250 μm was achieved at all the given energy dosages. For the smaller powder size, a cure depth of 150 μm was produced in only the experiment with 187.5 mJ/cm^2. The results are summarized in table 4.8.

Table 4.8 Activation energy and cure depth for different Amdry 386 powder sizes.

Particle size (μm)	**E_c (mJ/cm^2)**	**C_d (μm)**
-45/+125	E_c < 67.5	C_d > 250
-8/+65	125 < E_c < 187.5	150 < C_d < 200

4.4.4.2 Optimal powder mixing ratio

The optimal mixing weight ratio of Haynes 214 large:small powder sizes was determined through the tapping tests and the model to be 67:33. An approximately 7% improvement was attained in the two-size powder mixture over that of the single sized starting powder. The packing ratio as well as tapped density of the optimal two-size powder mixture were calculated using the numerical model, and subsequently verified experimentally. The results are summarized in Table 4.9. Amdry 386 suspensions with metal powder volume loading of 56 % were produced using the optimal two-size powder mixture and CPS 3010 for subsequent printing process.

Table 4.9 Tapped density of individual Amdry 386 powder size and optimal 2 size powder mixture.

Particle size (μm)	**Tapped density (g/cm^3)**	**Packing ratio (%)**
-8/+65	4.62	65.61
-45/+125	4.44	63.13
Optimal 2 size powder mixture (theoretical)	5.05	71.76
Optimal 2 size powder mixture (experimental 0.6726 , 0.3274)	4.87	69.24

4.4.4.3 Fabrication parameters

Experimental results in section 4.4.4 have indicated that for the smaller powder size suspension, in order to produce a cure depth of between 150 and 200 μm, an energy dosage level of between 125 and 187.5 mJ/c^2 was required, which corresponds to the curing time of between 40 to 60 seconds. For the two-size powder mixture suspensions, the cure time of 50 seconds have been experimentally determined to produce a good layer bonding with a layer thickness of 150 μm. The cure time required was slightly longer, which can be attributed to the inclusion of smaller particles of less than 10 μm in diameter. An appropriate soft-cure time was also determined to be 1 seconds for Amdry 386 suspension.

4.4.4.4 Fabricated parts

Besides the typically sample set, a full-size heat exchanger plate of 50 x 100 x 5 mm dimensions with 3D twisted fin was successfully fabricated (Fig. 4.11). The fin width was approximately 1 mm at the largest cross section, and the minimum gap between two nearby fin structures was 0.5 mm.

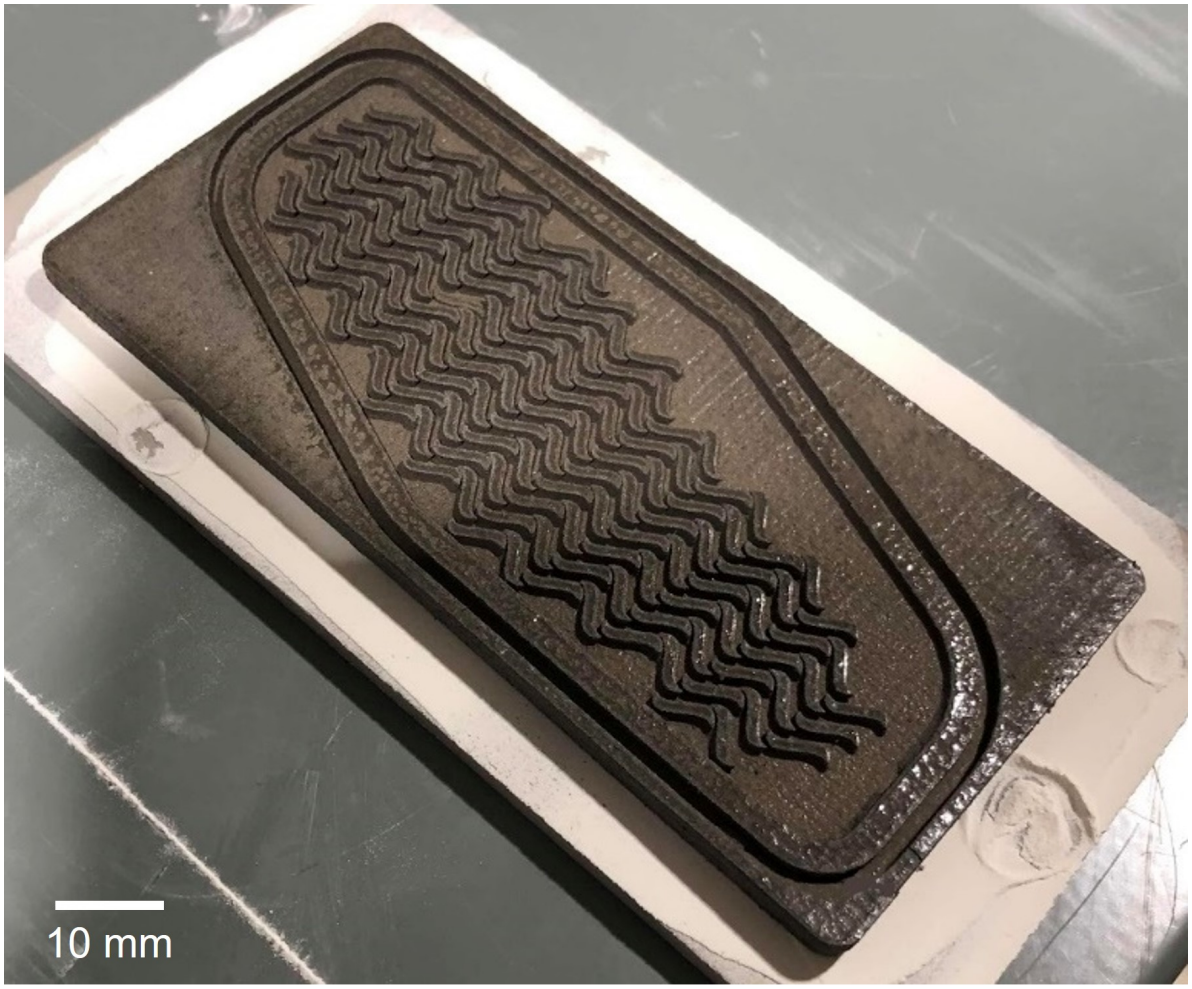

Figure 4.11 Amdry 386 full size heat exchanger fabricated by SEAM process.

4.5 Cure depth testing device

The single layer curing experiments have shown to provide important insights into the relationship between cure depth, critical energy level, and particle size of each metal suspensions. For each suspension, the number of total experiments required is the product of the number of different particle sizes, number of energy dosage levels, and number of layer thicknesses. For example, in order to test three different powder sizes at three different energy dosage level and two different layer thicknesses, a total of 3 x 3 x 2 = 18 experiments must be carried out separately. In order to reduce the number of experiments, as well as time and material waste, a cure depth testing device was constructed (Fig. 4.12 (left)).

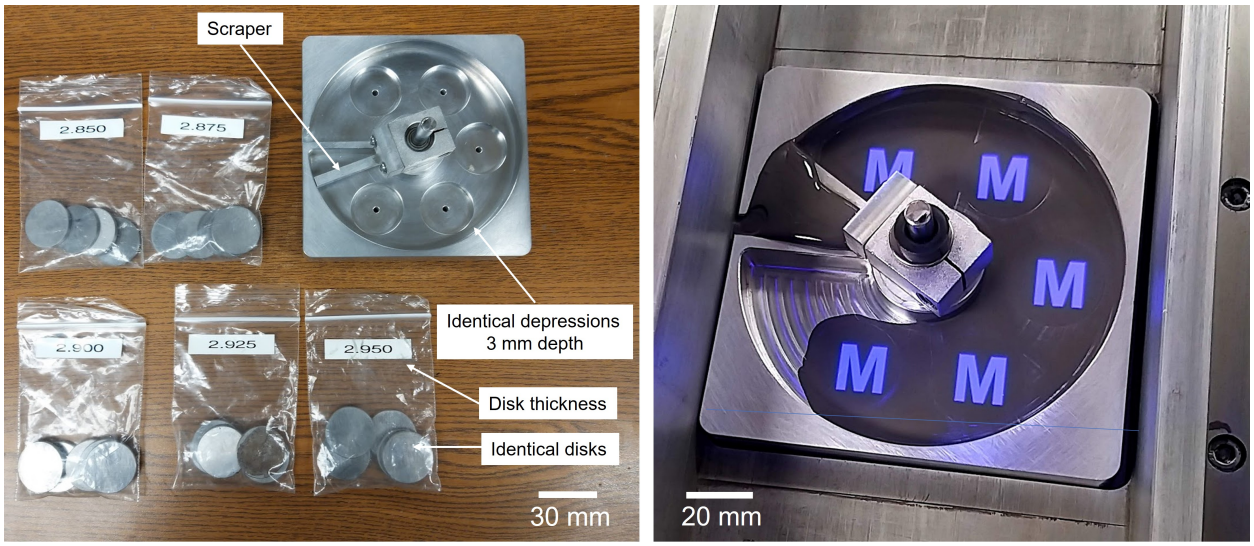

Figure 4.12 Left: Cure depth testing device with 30 mm circular depressions and circular disks with different thicknesses. Right: Testing of a Haynes 214 suspensions at 5 different layer thicknesses at the same time.

The device consists of a platform with 5 identical 30 mm circular depressions, and a scraper which can rotate around the platform to deliver the suspension. The 30 mm diameter disks of different thicknesses (2.850, 2.875, 2.900, 2.925, 2.950 mm) can be inserted into the depression, which results in different gap distances of 150, 125, 100, 75, and 50 μm. Using this device, five different layer thicknesses can be tested in a single experiment, which significantly reduces the total number of required experiments. Additionally, 5 different energy dosage levels can also be tested in a single

experiment, by inserting disks with the same thickness into the depressions to produce the same gap distance, while controlling the UV exposure time at each disk location using the projection software. Figure 4.12 (right) shows the testing of a Haynes 214 suspensions at 5 different layer thicknesses at the same time.

4.6 Conclusion

In this chapter, the relationships between cure depth and metal particle size of SS420, SS316, Haynes 214, and Amdry 386 metal suspensions were characterized, whose results were used to develop their appropriate processing conditions (UV dosage, cure time, layer thickness) for the SEAM process. Three-dimensional green objects of all metal suspensions were successfully fabricated using the first-generation prototype of the SEAM process using the determined processing conditions. A 2-step curing strategy was devised and applied to the printing process, which not only prevents sedimentation of metal powder particles in the print bed but also enable the fabrication of overhang geometry without support structures. A procedure to obtain multi-size powder mixtures and metal suspensions with improved powder packing density was also presented in this chapter.

Author's note: *A portion of this chapter has been published in: H. X. Nguyen, H. Suen, B. Poudel, P. Kwon, and H. Chung, "Development of an innovative, high speed, large-scaled, and affordable metal additive manufacturing process," CIRP Annals, vol. 69, no. 1, pp. 177–180, Jan. 2020, doi: 10.1016/j.cirp.2020.04.069.*

CHAPTER 5

SEAM PROCESS: DEBINDING PROCESS

5.1 Introduction

In essence, SEAM printed green parts are composites which consist of metal powder particles and cured photopolymer. The photopolymer acts as a binder that temporarily holds the metal powder in their intended shape. From a compositional perspective, SEAM green parts, injection molded parts, and binder jet printed parts are in many ways similar, but not completely identical. Regardless, for those all processes, the binder must be completely removed from the parts before they undergo high temperature sintering to obtain final metal objects.

This chapter first reviews the current status and techniques of the binder removal or debinding process carried out in metal injection molding (MIM) and BJP, both of which have been well studied and developed. Similarities and differences in the development of the debinding process for SEAM process in comparison with the aforementioned processes will be identified. Key considerations as well as possible adaptation of the debinding techniques used for MIM and BJP will be discussed. A series of studies and characterizations of the binder system for SEAM process will be presented, which ultimately results in the development of a debinding procedure that not only completely removes the binder from the green parts but also maintains the structural integrity of the debinded parts. Analysis on post-debinded parts have shown a maximum binder residual of 0.4 wt.%, which is negligible in most cases.

5.2 Current debinding techniques

5.2.1 Debinding of metal injection moulded parts

5.2.1.1 Binder system composition

The basic composition of an injection molded feedstock consists of metal powders and polymeric binder that make the mixture moldable in an MIM machine. The polymeric binder system itself is composed of two components: primary binder and secondary or backbone binder [128].

Primary binder, which typically makes up of the larger portion of the binder system, is easily removable, either thermally or chemically. The removal of primary binder opens up a network of pores throughout the green part, which enables the safe removal of the secondary binder at the later steps [129].

The secondary binder's main purpose is to hold the metal powder particles in place, while the primary binder is being removed. Higher temperature and reducing environment are required to eliminate the secondary binder, which also allows for the formation of diffusion bonds between the metal powder particles. At the end of secondary binder removal step, the debinded parts are a network of metal powder particles with diffusion bonds connecting them, which are often called the part metal skeleton [130].

5.2.1.2 Primary debinding

Primary debinding can be carried out using several techniques, each depends on the chemical composition and decomposition behavior of the binder.

- **Thermal debinding** is usually carried out on the traditional MIM wax-based system. Molded parts are heated very slowly in an electrically heated oven, at a typical ramp rate of 0.5 °C/min up to a temperature of 200 °C. The holding time is strictly a function of part size [128]. Therefore, thermal debinding of primary binder can take an excessively long time to be completed. Moreover, extended heating time can also degrade the secondary binder, which

makes the part fragile and difficult to handle. Thermal debinding for primary binder is now obsolete and rarely used in practice.

- **Solvent debinding of wax-based system** is the most contemporary and widely used technique for primary binder removal. Molded parts are immersed in a solvent bath that is chemically compatible to dissolve the binder used. A heated bath with circulatory flow of the solvent can also be used to speed up the process. The solvent is drained from the part afterwards, which now can be air dried and ready for secondary debinding step [131]. The complete removal of the binder can be evaluated based on the theoretical densities of the metal powder and binders, as well as their weight composition in the green part. It is also important to note that the holding time for a complete binder dissolution depends on part size, composition, and powder size [132].

- **Debinding of water-soluble system** is a noteworthy recent technique. Similar to solvent debinding, the molded parts are submerged in a water tank, often heated to dissolve the binder, and therefore the use of chemicals is eliminated [128].

5.2.1.3 Secondary debinding

After the primary binder was removed, the molded part shape is held together by the secondary or backbone binder. The interconnected network of pores revealed by the removal of primary binder allows for a safe removal of the secondary binder without causing defects in the parts.

Typically, the secondary binder is a thermoset. Therefore, high temperature as well as reducing environment are required for this step. The process usually involves heating the part up to the holding temperature at a slow ramp rate, depending on the decomposition behavior of the binder, and then hold for a duration of time until the binder is fully removed. Any residual of the primary binder in the part should also be eliminated during this step [130].

In order to achieve a safe debinding cycle and defect-free debinded part, thermo-gravimetric analysis (TGA) of either the initial powder-binder feedstock or the binder alone is required. TGA

data provide information necessary to determine the optimal holding temperature as well as ramping rate of the debinding cycle. The ramping rate during TGA usually mimics the ramping rate of the real debinding cycle in the furnace. The temperatures at which significant weight loss occurs during TGA are the typical point of interests as they dictate the holding temperatures as well as ramping rate of the debinding cycle [132, 133]. When the secondary debinding step is completed, diffusion bonds are formed among the metal powder particles, which hold the part in its intended geometry. The debinded metal skeleton can now be transported to a high temperature furnace for final sintering.

5.2.2 Debinding of binder jet printed parts

5.2.2.1 Binder composition

The exact chemical composition of the binder used in BJP is the proprietary information of ExOne [55, 56]. However, previous research was able to identify the binder's main ingredients: ethylene glycol monobutyl ether (EGBE), isopropanol (IPA), and ethylene glycol (EG). It is important to note that the evaporation temperatures of EGBE and IPA is 17.1 °C and 80.1 °C, respectively. During the printing process, EGBE evaporates due to the heated chamber and therefore the binder jetting printed green parts consist of metal powder, IPA, and EG.

5.2.2.2 Thermal debinding process

The binder removal process of binder jet printed parts is carried out thermally in two steps:

1. The green part is heated up in an electrically heated air oven to 150 - 200 °C, which is above the evaporation temperature of IPA. At this temperature, IPA is removed while EG is cured and harden to hold the metal powder particles together to keep the intended shape.

2. The green part is heated up to a higher temperature in a reducing environment, either air, pure H_2 gas, or a mixture of Ar and H_2 gases, for the removal of EG.

Studies have shown that, in most cases, a complete binder removal can only be achieved by debinding in air environment, and debinding in other reducing environment results in the residual which is 0.13 - 0.4 wt% of the total binder used [56]. However, debinding in air inevitably leads to oxidation of metals and in some cases, has significantly detrimental effect in the sintering and performance of the final parts [55].

5.3 Debinding process for SEAM binder system

A successful debinding process completely eliminates the polymeric binder from the green part, while retaining the structural and chemical integrity of the metal skeleton structure. From a green part compositional perspective, MIM and SEAM green parts are similar, as the interstitial space between the powder particles are filled with polymeric binder. However, the binder system for MIM generally consists of primary and secondary (backbone) binders, while binder for SEAM is solely photopolymer. Primary binder can be removed chemically or thermally at a low temperature, which exposes a network of pores while the metal skeleton is secured by the backbone binder, allowing for the safe removal of the backbone binder at higher temperature [128, 129, 132, 133]. On the other hand, photopolymerization leads to thermosetting products with crosslinked macromolecular network that are intrinsically difficult to degrade biologically or chemically [122–124]. Therefore, the cured photopolymer binder in SEAM green parts can only be removed thermally. Issues arise as the lack of clear exit path for binder evaporation makes SEAM green parts especially prone to cracking during the debinding process. Additionally, incomplete binder removal can also lead to distortion, poor mechanical properties and undesirable change in the material chemistry of the final part [134]. Therefore, to achieve complete binder removal of SEAM green parts while maintaining part structural and chemical integrity, the decomposition behavior of the binder must be carefully characterized. To determine the optimal thermal debinding cycle, three critical attributes must be studied: debinding environment, temperature, and ramp rates.

5.3.1 CPS3010 thermal decomposition characterization

5.3.1.1 Thermal decomposition environment

Figure 5.1 shows the weight percentage of cured polymer samples of CPS3010 over time in air, argon, and nitrogen gas during the TGA experiments. The samples were heated up from room temperature at a heating rate of 10 °C/min to a high holding temperature of 800 °C, which ensures the maximum decomposition of the polymer. The results indicated that air debinding was the most effective as the final sample weight reduced most significantly among the three environments. While the final weight percentage recorded is not zero (1.62 wt.% as shown in Fig. 5.1) due to an increase in chamber gas pressure at elevated temperature, visual observation of the TGA sample holder at the end of the experiment in the air environment showed no residual left in the sample, indicating a complete decomposition and evaporation of the polymeric binder. On the other hand, powder residues were found at the end of the experiments with argon and nitrogen. The optimal debinding environment for CPS3010 is determined to be air.

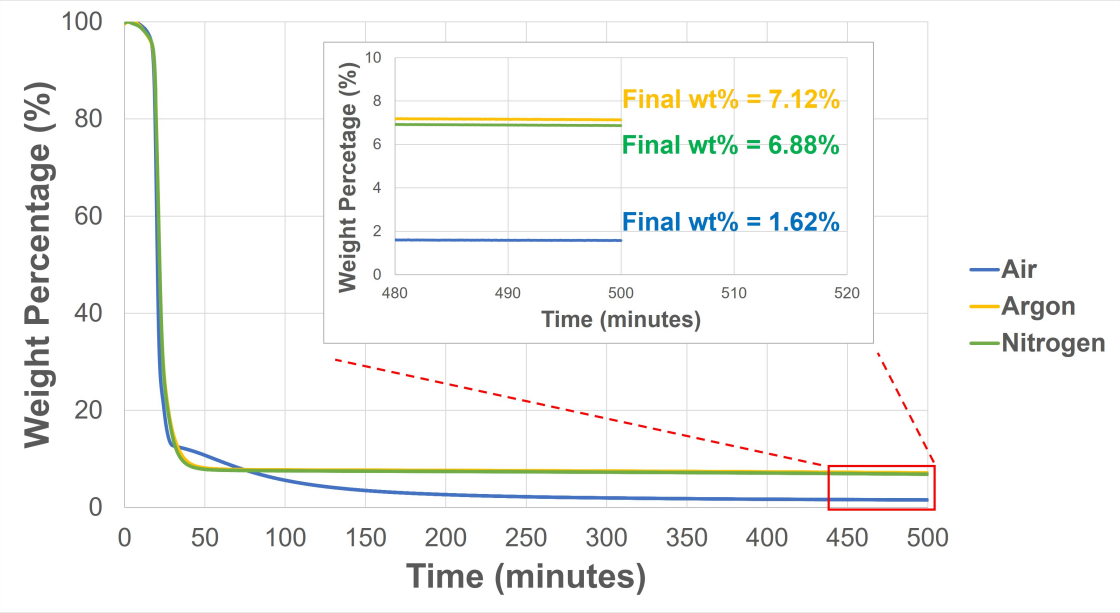

Figure 5.1 TGA results of CPS3010 holding at 800 °C in different environments.

5.3.1.2 Thermal decomposition temperature

Figure 5.2 shows the weight percentage of cured polymer samples over time in the air environment under different holding temperatures. The data indicate that the holding temperatures of 430°C and 450 °C are the most effective, which resulted in identical final weight percentages. Visual inspection also confirmed complete decomposition with both holding temperatures and no residue after the experiments. The optimal holding temperature was decided to be 430 °C to minimize oxidation of the metal powder during the debinding process.

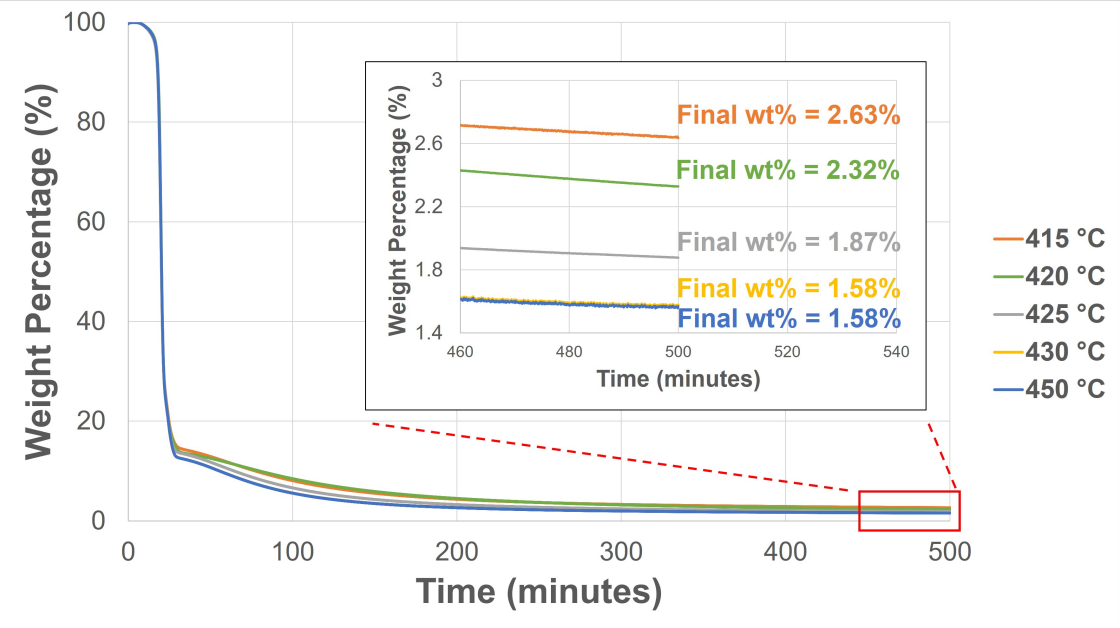

Figure 5.2 TGA results of CPS3010 at different holding temperatures in air.

5.3.1.3 Thermal decomposition rate

Figure 5.3 shows the change in the weight percentage of the cured polymer while heating up to 500 °C in the air environment. The ramping rate was kept low at 1 °C/min. The results have shown that the polymer has the decomposition onset temperature and the rapid decomposition temperature at 150 °C and 325°C, respectively.

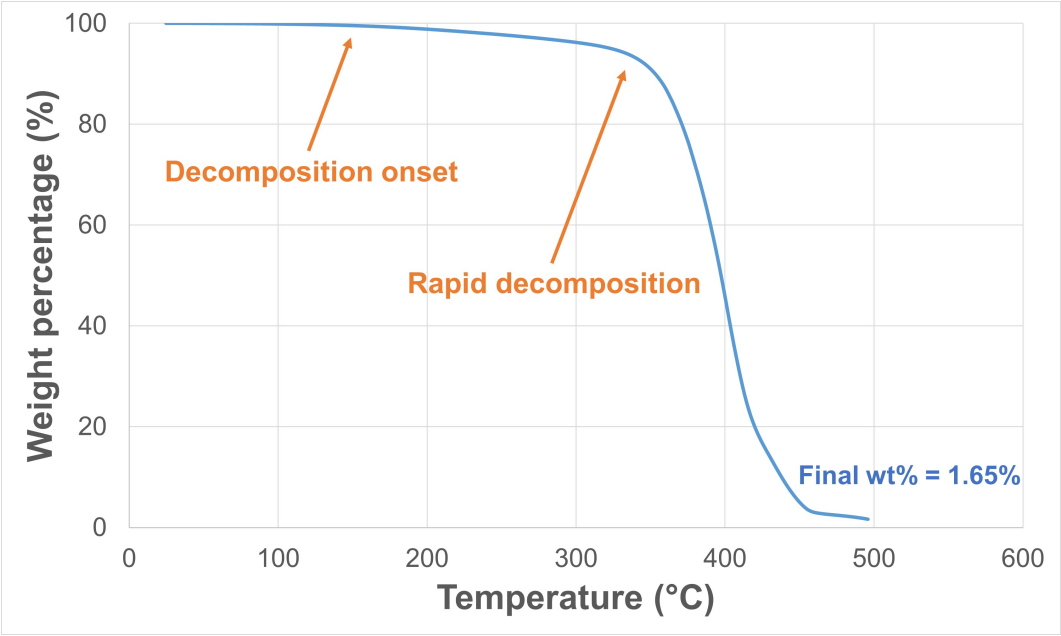

Figure 5.3 TGA results of CPS3010 holding at 800 °C in different environments.

Results from the previous sections have indicated an optimal holding temperature to be 430 °C in the air environment for the debinding process of SEAM green samples. As the decomposition of the binder begins at 150°C, the appropriate heating rate must be determined experimentally for the temperature range between 150 °C and 430 °C. Thermal cycles with different heating rates of 5, 3, and 1 °C/min in the temperature range between 150 °C and 430 °C were carried out on the green cylindrical coupons. For all the cycles, the initial ramp rate was 10 °C/min up to 150 °C, and the dwell time at 430 °C was 6 hours. Debinded samples were subsequently inspected visually for physical defects.

Debinded samples under the higher heating rates of 5 and 3 °C/min experienced cracking along the printing direction (Fig 5.4 (left)). On the other hand, the debinded sample with the heating rate of 1°C/min resulted in no visible defects (Fig. 5.4 (right). With the higher heating rates of 5 and 3 °C/min, the quick rise in temperature induced a rapid decomposition of the binder. The generated high escape gas pressure in combination with insufficient exit paths can result in parts cracking along the printing direction, which is a typical defect of thermal debinding processes [132–134]. By lowering the heating rate to 1 °C/min, a slow and stable decomposition of the binder was achieved,

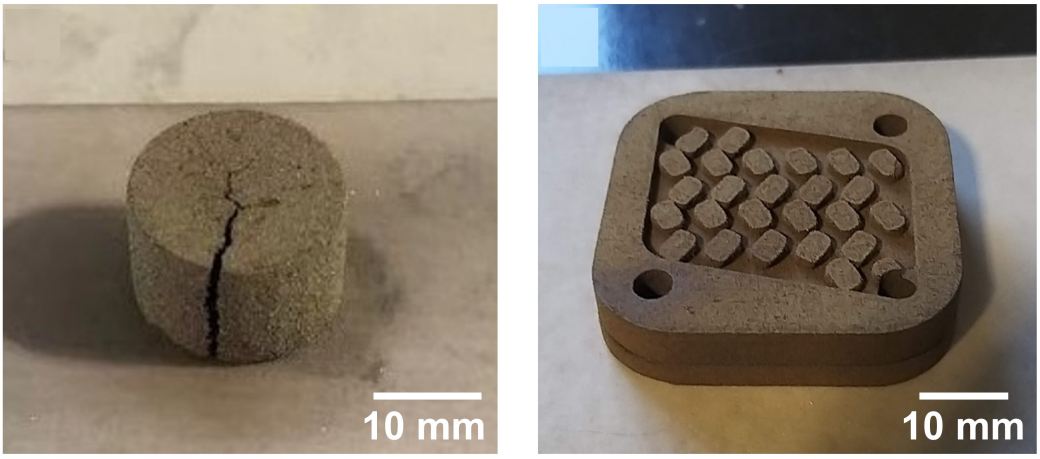

Figure 5.4 Left: Debinded cylindrical coupon under heating rates of 5 °C/min, showing vertical cracks. Right: Debinded heat exchanger assembly under 1 °C/min, resulted in a defect-free part.

resulting in defect-free debinded samples.

5.4 Binder removal effectiveness evaluation

5.4.1 Evaluation by weight change

During the debinding cycle, evaporation of the photopolymer and oxidation of the metal powder particles occur simultaneously. Therefore, at the end of the debinding cycle, the sample final weight change reflects the weight loss of photopolymer evaporation and oxidation weight gain. In order to measure the weight of carbon residue, the total weight change of the green sample as well as the oxidation weight gain must be determined.

5.4.1.1 Experimental setup

During the debindng process, two phenomena happen simultaneously: (1) the removal of the binder from the green parts and (2) the oxidation of the metal powder. Therefore, the total weight change of the green part after the debinding process is the sum of the binder weight change and the oxidation weight change. If the total weight change of the green parts and the oxidation weight change during the debinding step can be measured, the binder weight change as well as the binder removal effectiveness can be calculated.

TGA experiment was carried out on virgin Haynes 214 powder in air environment at 430 °C to determine the oxidation weight gain during the debinding process. The temperature profile mimics the optimal debinding cycle: Sample is heated 10 °C/min to 430 °C, dwell for 6 hours, and cool down to room temperature. The cooling down step is necessary to obtain an accurate reading of the final weight value. TGA experiment with the same conditions is also carried out on a thin single-layer green sample to determine the total weight change of the green part during the debinding process. Since the green sample is a thin flat layer, it can be assumed that the exposed surface area is similar to the experiment with virgin powder for an accurate calculation.

5.4.1.2 Results and discussion

Figure 5.5 shows the TGA results for both experiments, which indicated a 9.8278% weight loss of the green sample and an oxidation weight gain of 0.1483% of the pure Haynes 214 powder at the end of the heating cycle.

For an analysis of the data, consider the simple case of a 100 g green sample. The known volume percentage of metal powder in the green sample is 55.6%, which corresponds to 90 wt% the total weight of the suspension. Therefore, the weight of the metal powder and photopolymer in the green sample were 90 and 10 g, respectively. From the TGA results for the green part (Fig. 5.5 (top)), the experimental total weight loss of the 100 g green sample after debinding can be calculated by:

$$\Delta\textbf{Weight (total)} = \text{Total weight} * \frac{\text{Weight loss percentage}}{100} = -9.8278g$$

From the TGA results for the pure Haynes 214 powder, the total oxidation weight gain of 90 g of metal powder in the green sample can be calculated by:

$$\Delta\textbf{Weight (oxidation)} = \text{Metal powder weight} * \frac{\text{Oxidation weight gain percentage}}{100} = 0.13347g$$

The relationship between total weight loss, photopolymer weight loss, and oxidation weight gain is given by:

$$\Delta\textbf{Weight (total)} = \Delta\textbf{Weight (photopolymer)} + \Delta\textbf{Weight (oxidation)}$$

which gives **ΔWeight (photopolymer) = -9.96127 g**. Results from section 5.3.1.2 indicated the complete burnout of the photopolymer at 430 °C. Therefore, the **ΔWeight (photopolymer)(theoretical) = -10 g**. The binder removal effectiveness can be calculated by:

$$\textbf{Binder removal effectiveness} = \frac{\Delta\textbf{Weight (photopolymer)(experimental)}}{\Delta\textbf{Weight (photopolymer)(theoretical)}} * 100\% = 99.6127\%$$

which indicates a 0.4% residue from the binder. The small difference between experimental and theoretical values may be attributed to possible chemical reaction between metal powder and the binder, diffusion of carbon into the metal matrix, and experimental errors during TGA and green part fabrication process.

5.4.2 Evaluation by microstructural analysis

During high temperature sintering and solidification, carbon residue can react with the metal to form carbide phases within the part microstructure, typically at the grain boundaries [135]. The three main carbides present in Ni superalloys are MC, M_6C and $M_{23}C_6$ with M representing Ti, Cr, Nb, Mo, Hf and Ta [136]. Therefore, as the starting powder of Haynes 214 contains minimal amount of carbon, micro-structural analysis to identify carbide phases presence can be used as an indicator of the binder removal effectiveness of the debinding cycle.

5.4.2.1 Experimental setup

Cylindrical samples were debinded in optimal and sub-optimal conditions and were subsequently sintered at 1390 °C for 6 hours in a vacuum environment. A chemical composition analysis and comparison were then carried out using an EDS detector (Oxford Instruments X-Max - Abingdon, UK) on the sintered samples. The sub-optimal debinding conditions include debinding in argon and nitrogen gas at 800 °C, and in air environment at the lower holding temperature of 425 °C.

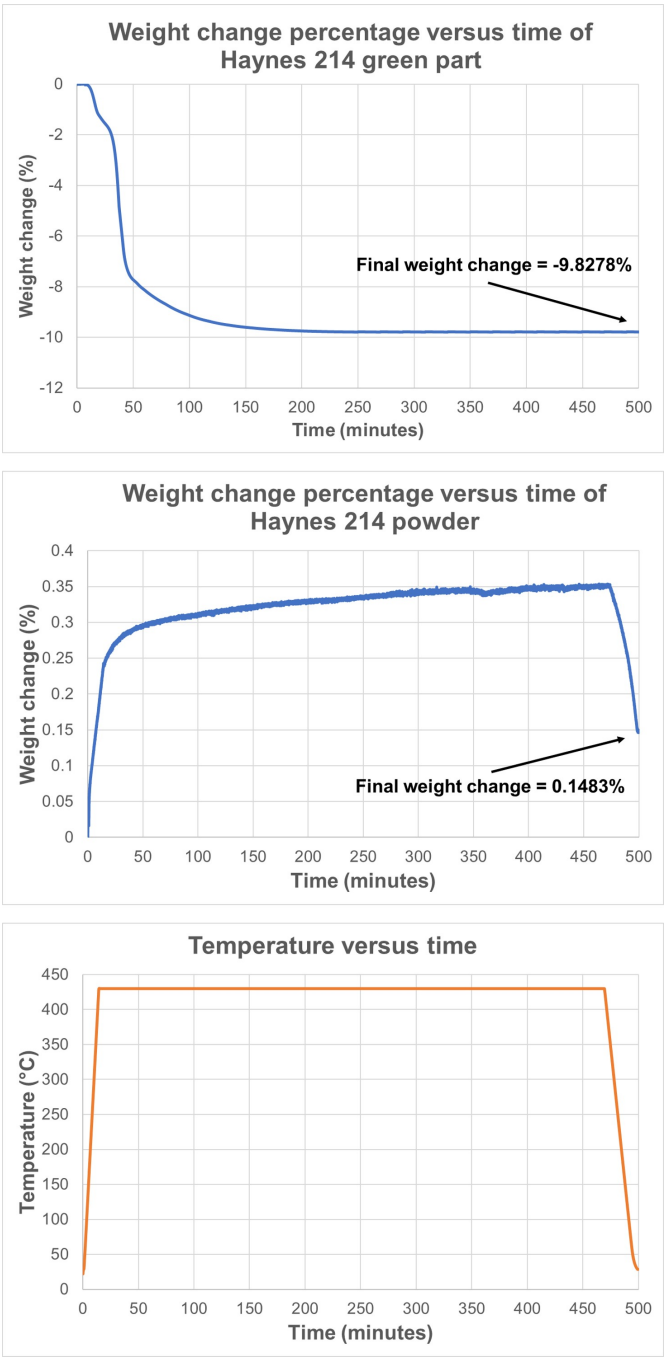

Figure 5.5 Top: TGA data for Haynes 214 green part in air environment; Middle: TGA results for Haynes 214 powder in air environment; Bottom: Temperature profile for both TGA experiments.

5.4.2.2 Results and discussion

In the microstructure of each sample debinded under sub-optimal conditions, EDS analysis revealed the formation of aluminum oxide and chromium carbide precipitates (Fig. 5.6). The chemical

compositions of the regions of interests are shown in Table 5.1. Since the carbon content in the initial powder is negligible, the excess carbide in the sintered part must have been originated from the residue after the binder burnout process. On the contrary, the sample debinded with the optimal thermal cycle contains no carbide precipitates, despite the presence of aluminum oxide inclusions. This indicates that the binder phase has been fully eliminated. Aluminum oxide forms rapidly at temperatures above 400 °C [137], and thus its presence is expected under the current processing conditions.

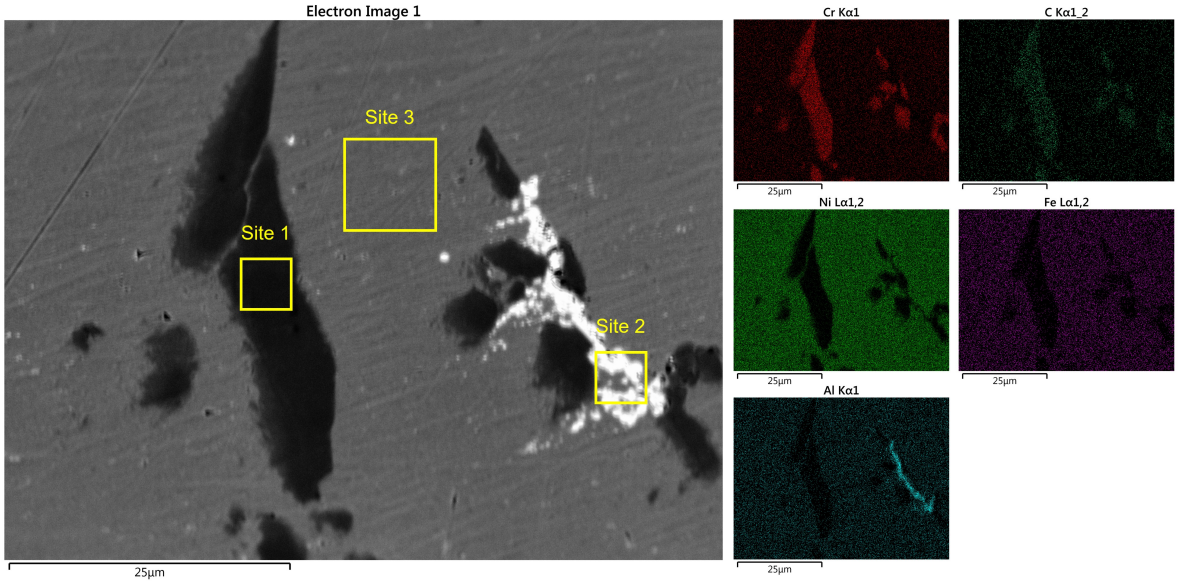

Figure 5.6 EDS mapping of Haynes 214 sample debinded at 425 °C and subsequently sintered at 1390 °C for 6 hours. Chromium carbide and aluminum oxide zones are present.

Table 5.1 Elemental analysis results of the Haynes 214 sample debinded at 425 °C and subsequently sintered at 1390 °C for 6 hours.

Composition in weight percentage						
Element	**Ni**	**Cr**	**Al**	**Fe**	**C**	**O**
Site 1	-	88.7	-	-	11.3	-
Site 2	71.7	11.5	4.0	4.0	2.6	6.2
Site 3	74.9	13.0	5.3	4.3	3.2	-

5.4.3 Evaluation by green part imaging

5.4.3.1 Experimental setup

Cylindrical samples were debinded under air environment at 400 °C and 430 °C for 6 hours and chemical composition analysis and comparison were then carried out using an EDS detector on powder samples from the post-debinded parts. EDS was also carried out on the virgin Haynes 214 powder for a baseline comparison.

5.4.3.2 Results and discussion

Figures 5.7 - 5.9 show the EDS mappings of the virgin powder, and post-debinded powder samples at 400 °C and 430 °C for 6 hours. Tables 5.2 - 5.4 show the composition of selected sites on each of the powder samples. The measured composition of the virgin Haynes 214 powder is as aligned with the its nominal composition provided by manufacturer, with an artificial carbon content count between 2.6 - 5.4 wt.%. For the powder sample debinded at 400 °C for 6 hours, visible polymer residue network can be observed wrapping around the powder particles (Fig. 5.8). Chemical analysis revealed an elevated concentration of both carbon and oxygen, further confirming presence of polymer residue in the sample. On the contrary, the powder sample debinded at 430 °C for 6 hours did not display visible polymer residue (Fig. 5.9). The carbon wt.% reading is between 4.0 - 4.8 %, which falls within the same carbon range as the virgin Haynes 214 powder. However, oxygen was detected on the particle surface, with a 1.5 - 3.5 wt.% reading from the compositional analysis. Haynes 214 powder is expected to oxidize in air environment at this temperature range as all of Haynes 214 elements, including Ni, Cr, Fe, and Al have been known to oxidize at temperature above 400 °C [137–139]. Some initial neckings among the particles can also be observed on this powder sample. While the chemical composition analysis by EDS does not provide an exact quantitative finding on effectiveness of the debinding process, the results from this study in combination with previous sections have indicated a minimal carbon residue in the debinded part.

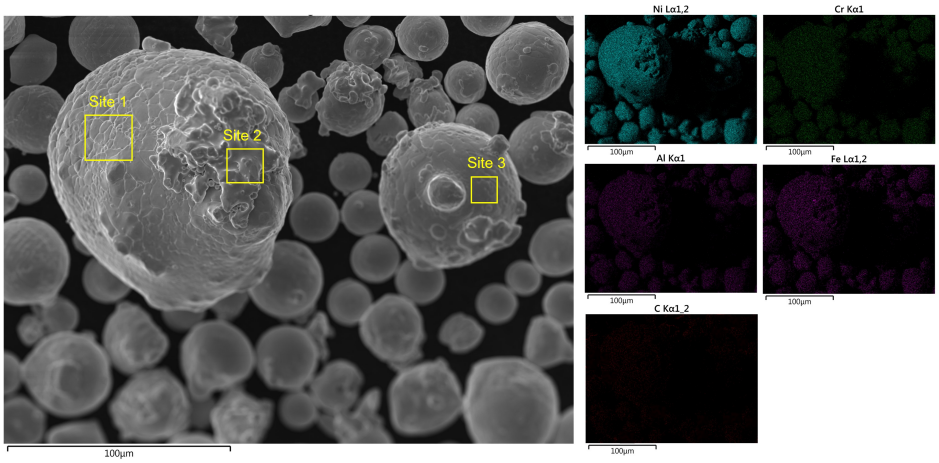

Figure 5.7 EDS mapping images of the virgin Haynes 214 powder.

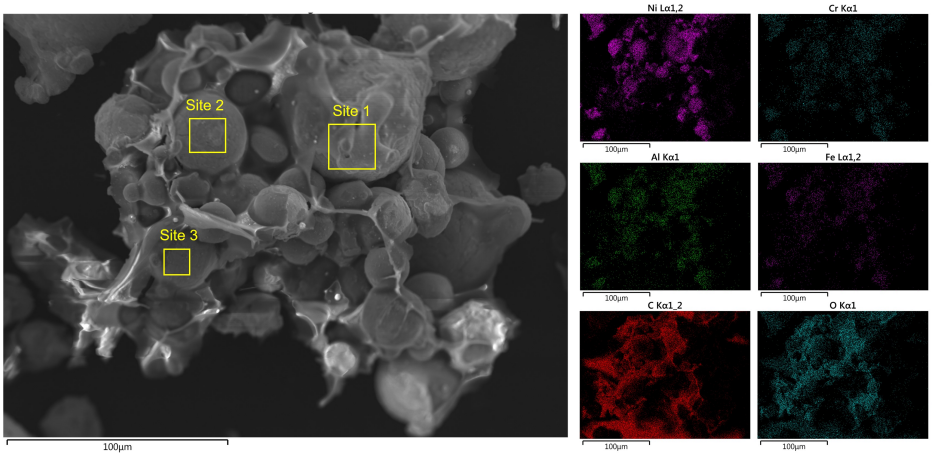

Figure 5.8 EDS mapping images of the Haynes 214 powder sample after debinded in air environment at 400 °C for 6 hours.

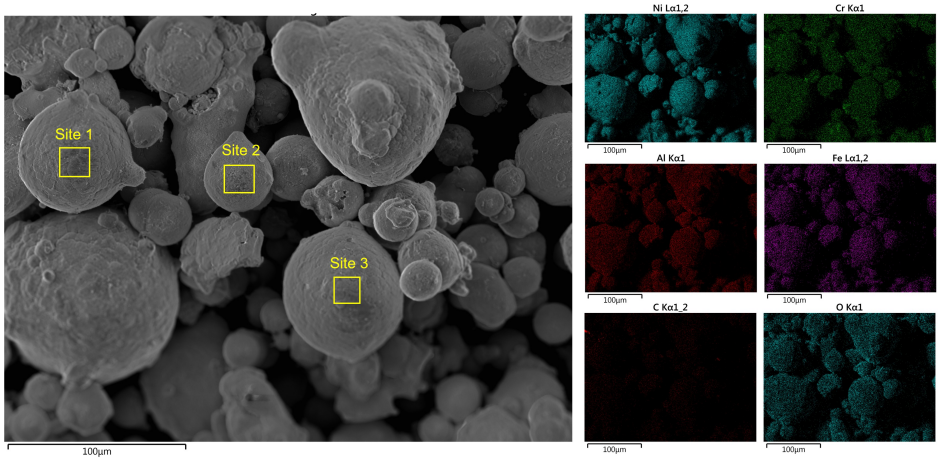

Figure 5.9 EDS mapping image of the Haynes 214 powder sample after debinded in air environment at 430 °C for 6 hours.

Table 5.2 Elemental analysis results of the virgin Haynes 214 powder.

Composition in weight percentage						
Element	**Ni**	**Cr**	**Al**	**Fe**	**C**	**O**
Site 1	74.3	13.9	5.0	4.2	3.3	-
Site 2	74.8	13.2	4.9	4.5	2.6	-
Site 3	71.9	13.5	4.8	4.4	5.4	-

Table 5.3 Elemental analysis results of the virgin Haynes 214 powder debinded at 425 °C for 6 hours.

Composition in weight percentage						
Element	**Ni**	**Cr**	**Al**	**Fe**	**C**	**O**
Site 1	22.7	6.7	1.2	1.9	52.7	14.8
Site 2	20.2	5.6	1.5	2.3	50.9	19.5
Site 3	21.5	7.2	2.0	3.9	49.1	16.3

Table 5.4 Elemental analysis results of the virgin Haynes 214 powder debinded at 430 °C for 6 hours.

Composition in weight percentage						
Element	**Ni**	**Cr**	**Al**	**Fe**	**C**	**O**
Site 1	70.4	14.1	4.5	3.5	4.0	3.5
Site 2	72.5	13.5	4.2	3.8	4.5	1.5
Site 3	71.8	14.2	4.0	4.0	4.8	1.2

5.5 Conclusion

In this chapter, a series of studies and characterizations of the binder system for SEAM process is presented, which ultimately results in the development of a debinding procedure that not only completely removes the binder from the green parts but also maintains the debinded parts' structural integrity needed for subsequent processes. Analysis on post-debinded parts have indicated a maximum binder residual of 0.4 wt%, which is negligible in most cases. Imaging on the debinded powder as well as cross-sectional analysis on the sintered parts are in good agreements with the finding, as no carbon residue was found by the chemical composition analysis. SEAM debinded parts without any physical defects were attained using the developed optimal debinding cycle in this chapter.

Author's note: *A portion of this chapter has been published in: H. X. Nguyen, H. Suen, B. Poudel, P. Kwon, and H. Chung, "Development of an innovative, high speed, large-scaled, and affordable metal additive manufacturing process," CIRP Annals, vol. 69, no. 1, pp. 177–180, Jan. 2020, doi: 10.1016/j.cirp.2020.04.069.*

CHAPTER 6

SEAM PROCESS: SINTERING PROCESS

6.1 Introduction

After the binder is removed, the part consists of a network of metal powder particles connected to each other by weak diffusion bonds. This metal network, or skeleton structure, then undergoes thermal treatment at high temperature to obtain a final dense metal object, i.e., the sintering process. Fundamentally, sintering is not a simple process. It is a one way event consisting of many atomic diffusion mechanisms, driven by the external thermal energy and the inherently high surface energy of powder particles. In the author's opinion, the most difficult aspect of sintering is while the process is transient, with many characteristics of the sintering body constantly change over time during the heating cycle, it is only possible to capture and study the post-sintered part. Therefore, the information gathered for each sintering cycle only provides a glimpse into the series of events that occurred and thus, improvement can only be made incrementally, and the development and optimization of sintering techniques have always been largely by trial-and-error. However and more importantly, while it is not possible to observe the exact events occuring during the sintering process, learning and understanding the fundamentals behind the sintering process, including mass transport mechanisms, sintering stages, sintering forces, part percolation structure behaviors, etc. are the key for developing successful sintering techniques for full densification and shape retention of the part.

This chapter first presents a literature summary on the fundamentals of sintering process, covering the thermodynamical and mass transport events during the heating cycle, followed by a review on liquid phase sintering. Liquid phase sintering is a special topic of interest of this dissertation. The sintering efforts carried out on the material of interests, SS420 and Haynes 420, both centered around liquid phase sintering techniques. Activated liquid phase sintering by sintering aids addition was carried out on SEAM printed SS420 samples, and the processing conditions were optimized

to achieve parts with high density and no geometrical deformation. For Haynes 214, part relative density was characterized with respect to holding time and temperature during supersolidus sintering. The transient deformation behavior of the sintered parts with respect to holding time and temperature was also captured, whose results were used to develop a 2-step sintering technique to produce fully dense parts with complete shape retention. While the sintering efforts presented in this dissertation was carried out only on SEAM printed parts, the techniques can be applied to all other debind-and-sinter based technologies such as MIM and BJP. At the end of the chapter, the development of a numerical sintering model, based on the Olevsky-Skorohod model, was studied and implemented in a finite element analysis software, which can be used to aid the prediction of part density evolution and deformation during the sintering process.

6.2 Fundamentals of sintering

By definition, the sintering process is a "thermal treatment for bonding particles into a coherent, predominantly solid structure via mass transport even that often occur on the atomic scale. The bonding leads to improved strength and lower system energy" [18]. From a thermodynamics perspective, sintering process is driven by surface energy reduction - spherical particles with large surface area give up surface energy to build bonds among them, lower the system total energy to form a stronger solid structure [140]. The initial stage of sintering induces neck formation among the particles. A classic example that demonstrates the particle necking phenomena when heated is the SEM image of bronze particles with formed solid necks after sintering at 800 °C (Fig. 6.1) [141]. The immediate stage begins with the onset of grain growth while the pores remain interconnected. The final stage of sintering consists of pores collapsing and rounding, which also decrease the rate of grain growth. Several transport mechanisms are involved in each stage of sintering (Fig. 6.2) [18, 140, 141].

At ambient environment, the atoms in metal material are not mobile, thus the metal particles do not sinter in an observable time range. However, the atoms become much more mobile at higher temperature, especially the temperatures close to the material's melting point. An increase in atomic

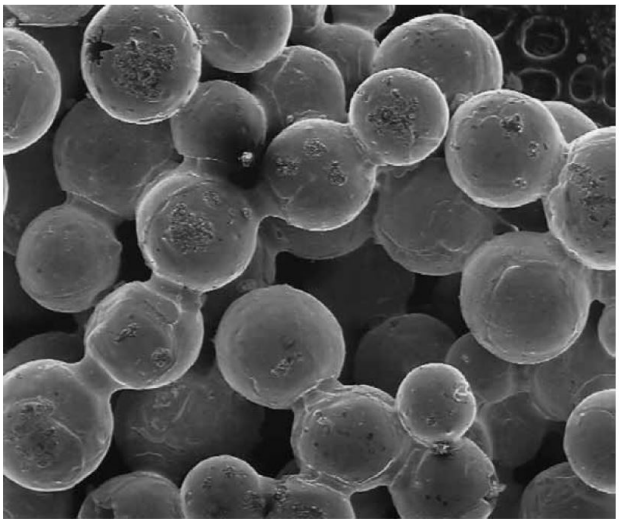

Figure 6.1 SEM image of the 28 μm bronze particles after sintering at 800 °C showing necks forming between the particles [18].

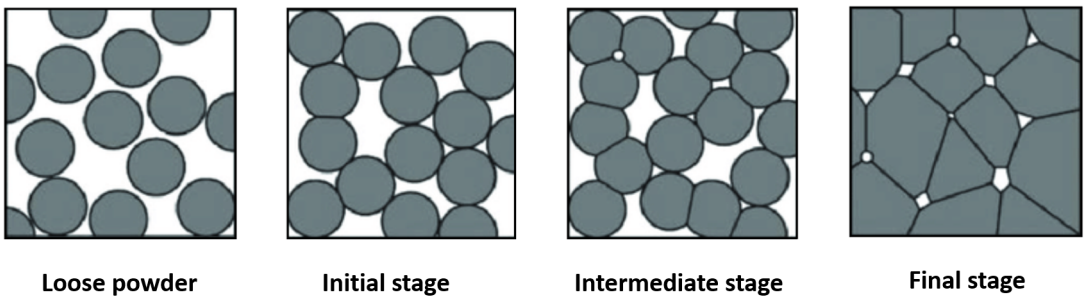

Figure 6.2 Three stages of sintering process [140].

activity at elevated temperature leads to newly formed bonds among the atoms, and eventually results in visible necks formed between the particles in the macro scale. The formation of necks and eventual bonding of the particles and densification of the body are driven by thermodynamics of the particle network while the system's temperature controls the rate of sintering [142].

6.2.1 Sintering thermodynamics

The thermodynamical cause of the sintering process is the high surface energy inherent to powder particles. On an atomistic scale, the surface of metal powder consists of atoms with broken bonds, which is directly related to surface energy. Therefore, surface energy is depended on material and crystal orientation, and is higher for higher melting temperature materials, which have relatively

higher atomic bonding [18].

In essence, sintering is a process of repeatedly creating vacancies and diffusing atoms into the vacancies. The activation mechanism for sintering is heat, which is provided to the sintering body at elevated temperature. The input heat is converted to kinetic energy of the atoms to dislodge from their original position to diffuse into new vacant sites [143]. An equation was developed to determine the activation energy, Q, that is required to initiate movement of an atom:

$$D_v = D_0 exp\left(-\frac{Q}{RT}\right) \tag{6.1}$$

where D_v is the diffusion coefficient, D_0 is the atomic vibrational frequency, T is the absolute temperature, R is the universal gas constant, and Q is the activation energy [140].

Temperature is the dominant factor that influences sintering rate, as higher temperature induces higher atom activities. Particle size, heating rate, applied pressure, sintering atmosphere, and liquid phase presence are other important factor that characterize sintering behavior of the body [143]. Sintering in presence of liquid phase is a special topic of interest, and will be covered in a later section.

6.2.2 Mass flow mechanisms

Mass flow mechanisms during sintering can be separated into two categories: surface transport and bulk transport.

6.2.2.1 Surface transport

Surface transport originated from the imperfections of crystalline solids. Vacancies, kinks, adatoms, and other defects on the surfaces are essentially sites with dense population of broken bonds and high surface energy. Atomic motions when thermally activated seek to lower this population as well as surface energy [140].

Surface diffusion events are initiated by an atom at a defect site breaking away from its existing

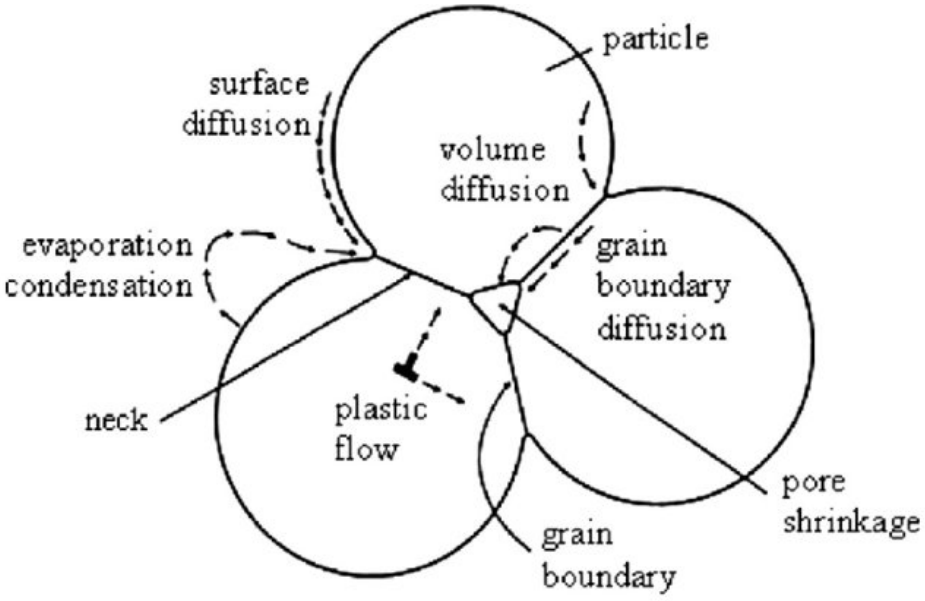

Figure 6.3 Mass transport mechanisms during the sintering process.

bond. The atom then moves quickly across the surface in a random direction, eventually reattaches itself to an available surface defect site [143]. The three surface transport mechanisms are:

- Evaporation-condensation or vapor transport occurs dominantly on a convex surface, where the vapor pressure is higher. Atoms on the surface break away, travel across pores and deposit on a nearby convex surface. Overtime, the convex surfaces flatten out and concave surfaces are filled with mass transported from the convex surface. Higher temperature accelerates vapor transport due to higher vapor pressure. Vacuum or partial vacuum sintering environment hinders vapor transport due to lower number of gas molecules [143].

- Surface diffusion occurs with an atom dislodging itself from a defect sites, and redeposit itself on a near by defect site. The rate at which surface transport occurs depends on the population of defect sites as well as the temperature of the body, which must provide sufficient energy to activate the motion of the atom [142].

- Surface lattice diffusion typically involves movement of an interstitial atom or vacancy near the surface, which then reemerges on another surface or neck region after traveling through the lattice structure [144].

The most important property and distinction of surface transport from bulk transport is that **surface transport does not produce shrinkage and densification**. As a matter of fact, surface transport works against densification [140]. Due to their lower energy activation, surface transport mechanism is initiated at lower temperature range, and dominates the mass flow process during heating up to the sintering temperature [144]. However, mass flow is originated and terminated at the particle surface to produce necking between the particles. The atoms are simply rearranged and vacancies are not terminated, and therefore, the spacing between the center of the particles are unaffected, which results in no densification and shrinkage of the body [145].

6.2.2.2 Bulk transport

Bulk transport is the main mechanism that produces shrinkage and densification during sintering. There must be a reduction in the particle spacing or distance between the particles' centers for densification to occur. Therefore, mass flow must begins from the particle interior, with a deposition at the neck or grain boundary. Vacancies are then eliminated by grain boundary movements [146]. The three bulk transports mechanisms are:

- Grain boundary diffusion occurs due to the inherent misalignment of crystals as a results of repeated misorientations. Due to the higher surface energy at the grain boundaries, atomic jump frequency is multiple magnitudes higher than jump frequency at a regular lattice. The activation energy required for grain boundary diffusion is typically immediate between volume and surface diffusion [146].

- Volume lattice diffusion induces a vacancy flow to the neck grain boundary, which produces densification. The vacancies are then terminated at the grain boundaries by grain boundary diffusion [147].

- Plastic flow is achieved by dislocation movements or micro creep due to high surface tension of the powder, as well as the higher atomic mobility under high temperature. The role of plastic flow is more significant during the early stage of sintering, when the surface tensions

are high. As the body densifies, surface energy is consumed, and the effect of plastic flow is diminished [148].

6.2.3 Liquid phase sintering

Liquid phase of sintering is a special topic of interest in this dissertation. The sintering techniques carried out on the alloys of interest in this dissertation all involve the generation of liquid phase to accelerate densification. Therefore, in order to develop suitable and optimal sintering strategies and cycles, it is of utmost importance to have an understanding of the mechanisms and controlling parameters of liquid phase sintering, as well as the events that take place at different thermal stages [18].

Figure 6.4 depicts the liquid phase sintering stages of a mixed powder system. During heating, the sintering additives undergo phase transformation into liquid phase. Consequently, the formed liquid spread over surface of the metal particles, dissolving the pre-existing bond, which allows for grain rearrangements. Capillary action pulls the metal particles together at an accelerated rate, and liquid phase at the boundary enhances mass transport rate due to solubility of solid phase in liquid phase, resulting in the densification of the body [149]. Liquid phase sintering is also applicable in the alloy powder systems, where lower melting point constituents exist, which leads to a partial melting of the particles. Tool steels are examples of alloy powders that densify by liquid phase sintering [150].

In an ideal liquid phase sintering system, solid phase has high solubility in liquid phase for mass transport enhancement, and liquid phase stays on the grain boundary throughout whole sintering process. This sintering mode is termed **persistent liquid phase sintering**. In a less ideal situation, liquid phase has high solubility in liquid phase, which dissolves into the solid over time after its formation. This sintering mode is termed **transient liquid phase sintering** [18]. In systems that both solid and liquid are insoluble in each other, the rate of sintering is strictly dependent on the rate of solid state sintering, and liquid phase is simply a pore filling agent [142].

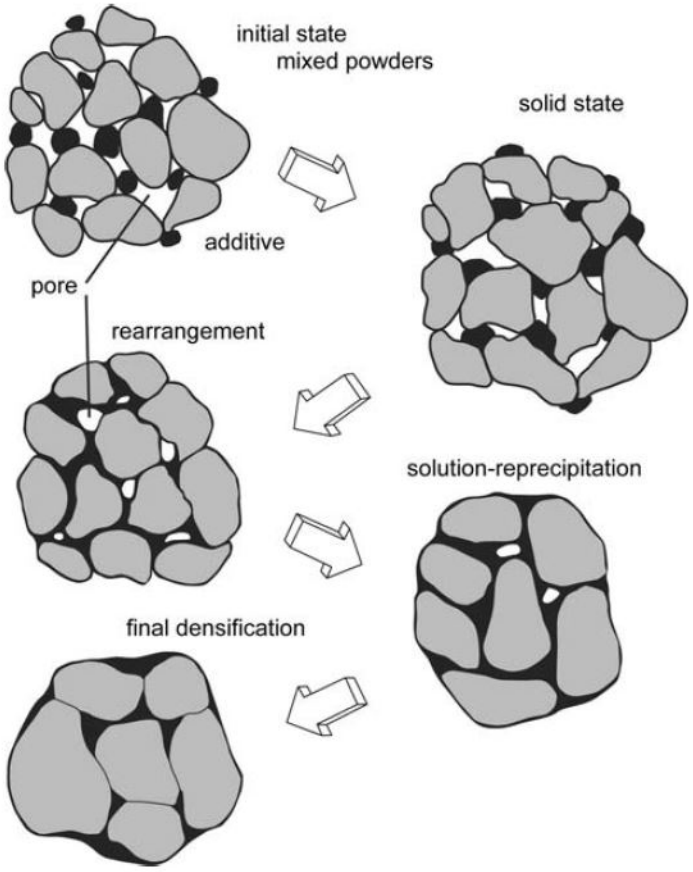

Figure 6.4 Schematic of liquid phase sintering of a mixed powder system. Grey particles represent metal powders, Black particles represent sintering additives [18].

6.2.3.1 Liquid phase sintering events

Pre-liquid stage sintering is identical to solid-state sintering of mixed powders. Surface transport mechanisms dominate during this stage to form necks between the particles without significant densification. Diffusion rate is influenced by particle size and green body density [144].

Liquid formation occurs when the temperature of the body reaches the melting point of the sintering additives or the low melting constituent in alloys. Capillary action aids the rearrangement of the particles into a favorable packing coordination to reduce the overall system's energy [150]. As discussed, an ideal situation is when solid phase has high solubility in liquid phase. When the opposite occurs, the formed liquid is chemically aggressive and penetrates the solid-solid interface, which can cause separation of grain as well as swelling [18].

Solution-reprecipitation is the main densification mechanism after particle rearrangement. The process involves first the partial dissolution of a particle solid surface (preferably high energy regions) into the liquid, followed by diffusion through the liquid phase, and finally re-precipitate onto another particle surface (preferably low energy regions). Bulk transports mechanisms such as grain boundary diffusion and volume diffusion take place to further densify the body [140].

Final stage of the sintering body, which consists of solid grains with liquid fully or partially occupy the space between them, is a slow process of grain growth and pore annihilation. In transient liquid phase sintering, the rate of sintering at the final stage is identical to solid state sintering. In persistent liquid phase sintering, the solution-precipitatation mechanism dictates the sintering speed. The sintering process completes when the body reaches its minimum energy configuration [141].

6.2.3.2 Porosity

Pores are interparticles voids, which could not be filled during sintering. Other types of pores are induced by gas phases caused by evaporation of polymer residue or volatile metals [18].

An important behavior of the evolution of pores during the sintering cycle happens at the later stage of sintering, where grain growth and pore coalescence happen simultaneously due to Ostwald ripening. In the case that gases trapped in the pore are soluble in the metal matrix, grain boundary diffusion aids the gas transport, resulting in further densification. However, if the pores are filled with insoluble gas, the required balance between liquid-vapor surface energy and the pore pressure acts against densification. Furthermore, at extended sintering time, insoluble gas-filled pores coarsen and enlarge, causing detrimental effect on part density and mechanical performance [151]. The pore pressure P_G, is calculated by the equation:

$$P_G = \frac{4\gamma_{LV}}{d_P} \tag{6.2}$$

where γ_{LV} is the liquid-vapor surface energy and d_P is the pore diameters.

6.2.3.3 Contiguity and part strength

The contiguity C_{SS} is defined as the fraction of solid-solid contact surface area as a fraction of the total microstructure interfacial area:

$$C_{SS} = \frac{S_{SS}}{S_{SS} + S_{SL}} \tag{6.3}$$

where the solid-liquid surface area per grain is S_{SL} and the solid-solid surface area per grain is S_{SS}. During the pre-liquid stage, as the body is heated up, part contiguity gradually increases over time as necks are formed between the particles, increasing the body rigidity. At liquid formation, part contiguity drops dramatically due to the dissolution of solid bonds in liquid phase. As solution-reprecipitaion occurs, particle solid bonding slowly increases until the body reaches its lowest energy configuration, which corresponds to a gradual increase of contiguity and an eventual stabilization [146].

During liquid phase sintering, part yield strength is directly related to the bonding strength of the metal skeleton and capillary force between the particles. Capillary forces between the particles are more significant to part strength in the early stage of sintering, especially at liquid formation and during rearrangement process. They diminish as the part is sintered to its full density, where solid-solid bonding between the particles provides the majority of part strength and rigidity [149]. The yield strength of a part at the sintering temperature, σ, is calculated by:

$$\sigma = \frac{3V_S}{2}\left(P_n + \sigma_0 C_{SS}\right) \tag{6.4}$$

where V_S is the solid volume fraction, P_n is the mean capillary pressure on a grain surface, and σ_0 is the inherent solid-solid bonding strength at the sintering temperature [148].

The importance of part contiguity and its relationship with part strength are represented in the above equation. It is also important to point out that part contiguity is a **measurable quantity**, and can be used as an indicator of part yield strength at any point during the sintering process. It is impossible to evaluate the exact value of part yield strength during the high temperature sintering. Moreover, German et al. [148] also noted that at the sintering temperature, if the contiguity value

of the body falls below a critical level of 0.38, then the solid-solid phase makes no contribution to compact strength, resulting in shape distortion of the body.

6.3 Sintering of various alloys with SEAM process

6.4 Stainless steel 420

6.4.1 Previous related work

The sintering of additively manufactured SS420 parts is a well-studied topic. Studies were first carried out to densify binder jet printed parts by bronze melt infiltration [152, 153]. Parts were pre-sintered at different holding temperatures, and subsequently placed in contact with molten bronze at 1120 °C for infiltration. Pre-sintering at 1400 °C resulted in the lowest open porosity level of 5%. Activated sintering by sintering aids addition has also proven to be an effective method to achieve higher part relative density. Elements such as silicon (Si), nitrogen (N), and boron (B) have been known to lower the eutectic point of iron, which can be added to the initial powder feedstock to generate a consistent liquid phase during high temperature sintering (Fig. 6.5) [55].

Presence of liquid phase at the particle surface greatly enhances the densification process by aiding particle rearrangement as well as enabling mass transport rate through liquid phase, which is typically multiple orders of magnitude faster than solid state diffusion [18, 140, 141]. SS420 printed parts by BJP which also include 12.5 wt.% addition of Si_3N_4 can be sintered at 1225 °C to achieve 95% dense part [154]. Do et al. carried out an extensive study on the effect of boron additives (B, BN, boron carbide (BC)) and sintering temperature on the densification of BJP printed parts [55]. Notably, samples with above 99.5% relative density with no geometrical distortion were successfully fabricated by using a multi-size powder mixture feedstock with 0.5 wt.% BN addition, followed by vacuum sintering. The work carried out in this section extends Do et al. work to develop appropriate sintering conditions for SEAM printed SS420 parts to achieve high density while maintaining part dimensional accuracy.

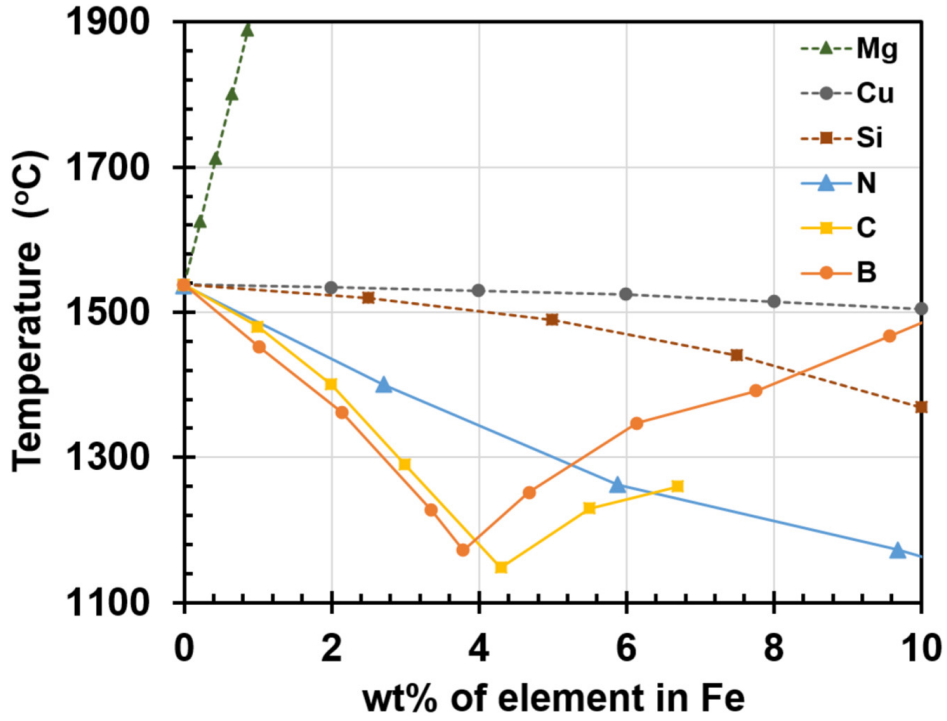

Figure 6.5 Liquidus line for various element at different concentration in iron [55].

6.4.2 Experimental setup

From a compositional perspective, SEAM and BJP printed parts are identical after the debinding step, assuming a complete removal of the binder. However, there are two main differences between the parts produced by the two processes:

- Initial powder packing density: the powder used in BJP is typically composed of multiple sizes with a high small:large particle radius ratio to achieve a higher packing density. By combining three different powder sizes with the average diameters of 82, 14, and 4 μm, a powder mixture with the packing density of 63.87% was produced for BJP. Several other studies also indicate the possibility of attaining powder packing density of above 70% for BJP parts by including small powder particle of 5 μm and below [55,56]. On the other hand, SEAM initial powder mixture cannot contain small powder particles, as their inclusion has been shown to significantly limit the curing depth of the later formulated metal suspension.

- Actual powder packing density in the feedstock: the powder feedstock used in BJP is the

Table 6.1 Relative density of binder jet printed samples fabricated with different weight addition of boron nitride and sintered at different holding temperatures. Data is extracted from [55].

		Additive addition (wt.%)			
		0.25	0.5	0.75	1
Sintering temperature (°C)	1200	90.13	99.53	91.47	92.22
	1250	92.13	93.66	94.10	95.66
	1300	92.78	94.62	94.41	95.16

as-produced multi-sized powder mixture. As the material is spread on the printing platform, the particles are loosely packed, and in contact with each other. In contrast, the feedstock used for SEAM process is a mixture of metal powder and liquid photopolymer, typically at a 50 - 60 vol% of metal particles. Therefore, interstitial spaces exist between the metal powder particles, which are filled with liquid photopolymer, resulting in an increase in inter-particle spacing. While the initial powder packing density is conserved as the green body densifies and shrinks during the sintering process, the initial inter-particle gap is inevitably higher in SEAM printed parts in comparison to BJP printed parts.

Therefore, there is a need for a re-optimization process of the sintering conditions for SEAM SS420 parts in order to attain final parts with high relative density while ensuring shape retention.

First, an analysis of variance was carried out on the published sintering data of SS420 [55] to gain further insight on the impact of sintering aids addition amount as well as sintering temperature on final part density. The initial published data was extracted and restructured into three different full fractorial design data sets for each type of sintering aids. An example of the data set is given in table 6.1 for the samples with addition of BN with 1 μm particle size (Sigma Aldrich, St. Louis, MO) as sintering aid. The studied factors are sintering aid weight percentage addition at 4 levels (0.25, 0.5, 0.75, and 1%), and sintering temperatures (1200 °C, 1250 °C, and 1300 °C). The response variable

was the relative density of the sintered part measured by Archimedes method. For each design of experiment, the null hypothesis and alternate hypotheses are as follows:

Null hypothesis: Sintering aid addition and sintering temperature does not affect the final part density.

Alternate hypothesis: Sintering aid addition and sintering temperature have statistical significance impact on the final part density at the alpha level.

Alpha level: 0.05.

Secondly, the previously determined optimal sintering conditions for binder jet printed SS420 part was applied to a SEAM printed coupon for a baseline relative density comparison. Subsequently, based on the measured density and previous analysis of variance results, an optimization matrix with varied sintering aid wt.% addition and sintering temperature was designed to identify the optimal sintering conditions for SEAM printed SS420 coupons. The matrix's parameters are shown in table 6.2. Each unit cell in the matrix corresponds to a different combination of boron nitride weight addition and sintering temperature.

Table 6.2 Optimization matrix for the sintering of SS420 samples printed with SEAM process. Each unit cell in the matrix corresponds to a different combination of Boron Nitride weight addition and sintering temperature.

		Additive addition (wt.%)			
		0.45	0.5	0.55	0.6
Sintering temperature (°C)	1240	A1	B1	C1	D1
	1250	A2	B2	C2	D2
	1260	A3	B3	C3	D3

6.4.3 Results and discussion

The analysis of variance on literature data of the sintering of binder jet printed SS420 parts has revealed that for all three cases with different sintering aids, both sintering temperature and additive addition has a significant impact on the final part relative density at the 0.05 alpha level. The main effect plots (Fig, 6.6) demonstrate that an increase in sintering temperature and weight addition of sintering aid both corresponds to an increase in final part relative density. As seen on the pareto charts, the effect of sintering aid weight addition is also more significant than holding temperature, especially in the case of BC and BN addition.

The optimal processing conditions for SS420 fabricated by BJP have been determined to be 1250 °C sintering temperature for parts with 0.5 wt.% of BN, resulted in a part final relative density of 99.63%. The same processing conditions were applied to SEAM printed sample, and the part density measured was 99.04%, which were averaged from three samples. The difference in final part density between SEAM and BJP printed parts can be attributed to the initial powder packing ratio. Due to the limitations on powder sizes, the experimental packing ratio of SEAM powder feedstock was 61.8%. However, as the powder mixture is combined with photopolymer resin at 55.6 vol% powder to formulate the suspension, presence of interstitial spaces between the powder particles where the presence of resin further reduced the actual green part packing density. On the contrary, as BJP feedstock is solely the metal powder mixture, a high green part relative density was achieved at 60%. An increase in the initial green packing density has been linked to improvements in final sintered density by many previous studies [55, 56, 143, 154].

As both sintering temperature and sintering aid addition have significant impact on the final part density, the optimization matrix for SEAM printed SS420 parts was designed with temperature varying from 1240 - 1260 °C and boron nitride weight addition varying from 0.45 - 0.6 wt.%, which expanded on the literature optimal condition values. Figure 6.7 shows the SEAM sintered cylindrical coupons corresponding to the designed matrix. The measured relative densities of all the coupons are presented in Table 6.3.

From the results, sample C2, B3, and C3 all achieved relative density of above 99.5%. Samples in

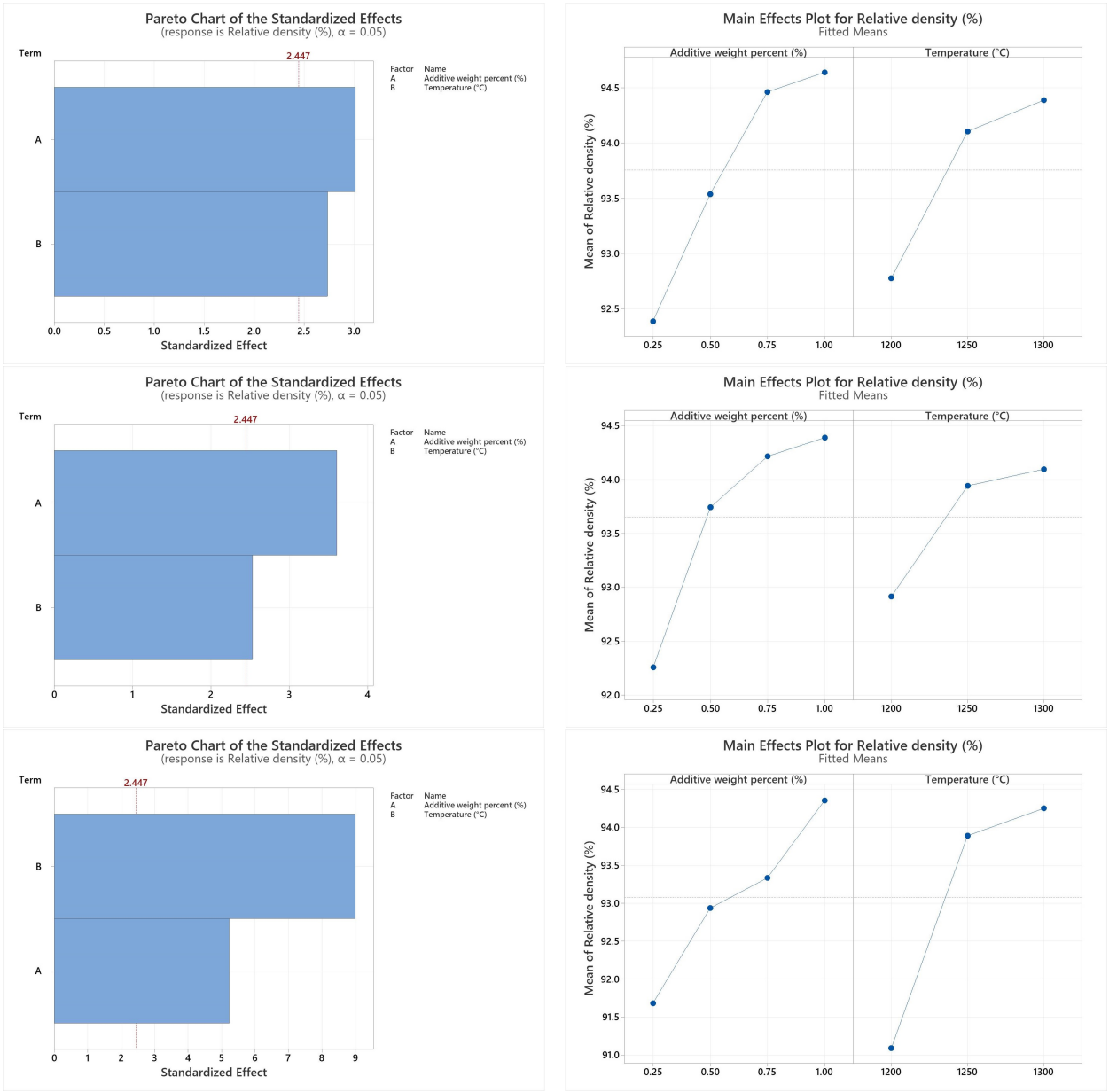

Figure 6.6 Pareto charts and main effect plots of sintering temperature and additive wt.% addition on final part relative density for different additives: Top - Boron, Middle - Boron carbide, Bottom - Boron nitride.

Table 6.3 SEAM fabricated SS420 coupons relative density results.

		Additive addition (wt.%)			
		0.45	0.5	0.55	0.6
Sintering temperature (°C)	1240	98.21	98.92	99.25	99.53
	1250	98.69	99.04	99.62	99.73
	1260	99.25	99.53	99.71	99.81

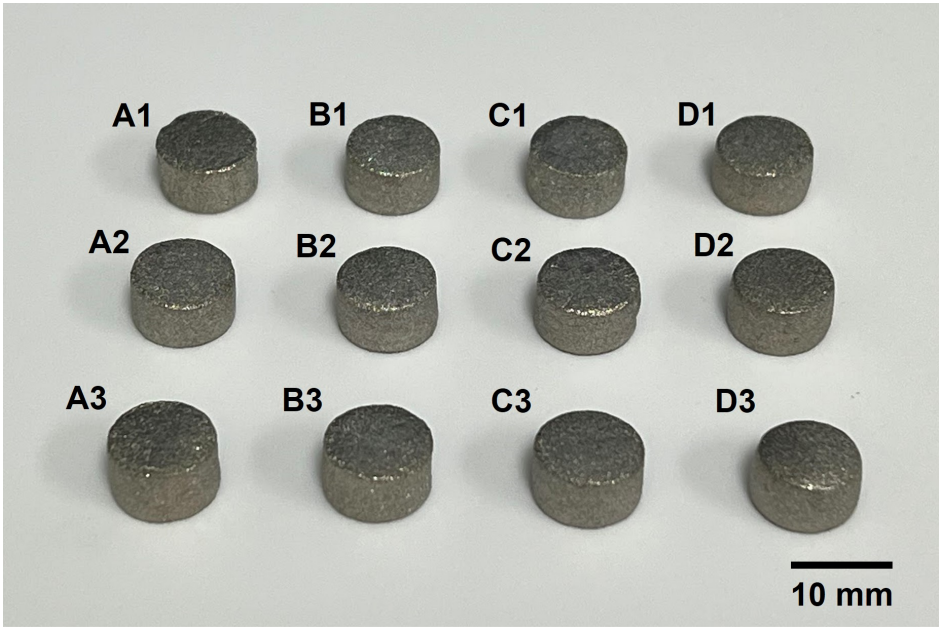

Figure 6.7 SEAM sintered SS420 coupouns corresponding to the designed optimization matrix. Samples in column D exhibited "barreling" deformation.

column D of the optimization matrix also exhibited good relative density. However, the intended geometry was not maintained with those samples, indicating a combination of excessive liquid phase presence and/or unnecessarily high sintering temperature [148]. The obtained data have also indicated that there exists other possible combination of sintering temperature and additive addition wt.% (higher additive addition with lower sintering temperature and vice versa) to achieve samples with good density and complete shape retention of the part. As these processing conditions

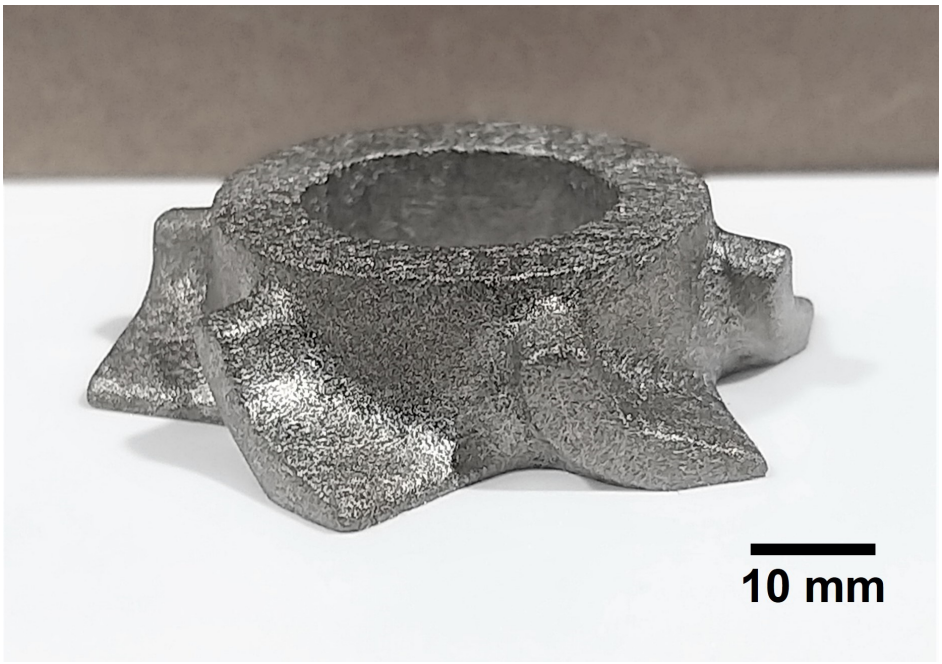

Figure 6.8 SS420 turbine fabricated by SEAM process.

directly affects the microstructure and mechanical properties of the fabricated components (grain size, hardness, chemical composition) [148, 155, 156], sintering conditions can be further tailored to suit the intended use and applications of the fabricated parts. A SS420 turbine was successfully sintered using the conditions developed in this section (Fig. 6.8).

6.5 Haynes 214

6.5.1 Supersolidus sintering of Haynes 214

6.5.1.1 Experimental setup

Haynes 214 green cylindrical coupons with 1 cm diameter and 2 cm height were fabricated using the SEAM process and subsequently underwent the binder removal step. The parameters for green part fabrication step as well as debinding cycle are presented in the previous chapters. The debinded cylindrical coupons were sintered in a tube furnace (Lindberg/Blue M, Thermo Fisher Scientific – MA, USA) under the vacuum condition at different holding temperatures of 1395, 1398, and 1400 °C. For each holding temperature, coupons were also dwelled at different holding durations of 2, 4,

6, 8, 10, 15, and 24 hours. The ramping rates were determined based on the furnace's manufacturer safety recommendations. Lower heating and cooling rates were used at higher temperature to prevent thermal shocking of the alumina tube, which can result in microcracking. The temperature profile for the sintering cycles is shown in Fig. 6.9. Relative densities of the sintered coupons were measured using Archimedes' method with 2-propanol alcohol used as the fluid medium. The coupons were then cut and polished, and micrographs of their cross section were studied under an optical microscope and a scanning electron microscope (SEM). EDS analysis was carried out for a chemical composition analysis on selected samples.

For the holding temperature of 1400 °C, additional samples were sintered at the holding time of 1, 3, and 5 hours and micrographs of all samples sintered at this temperature were taken to capture the time-dependent densification behavior of the material.

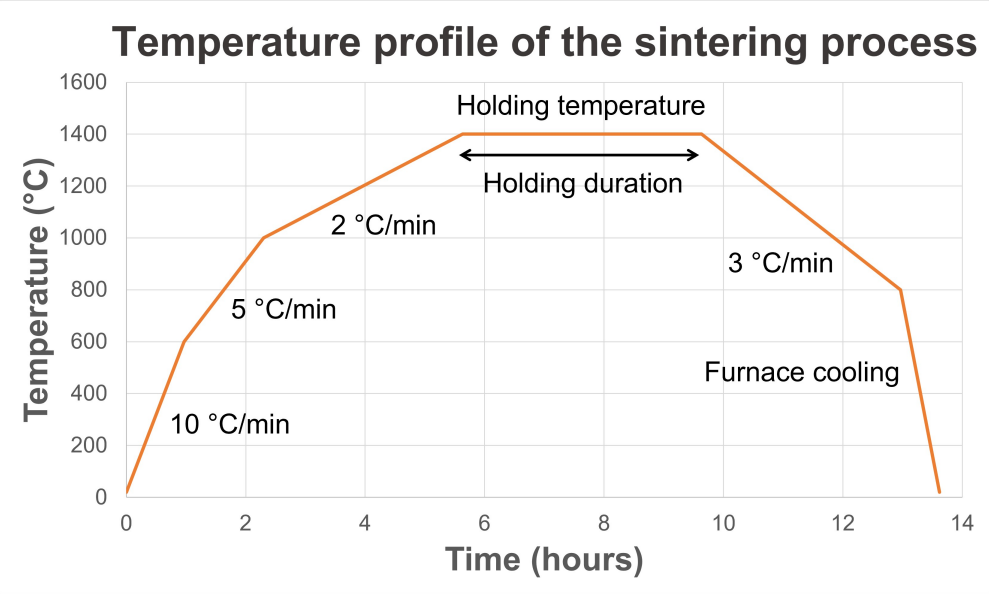

Figure 6.9 Temperature profile of the heating cycle for Haynes 214 sintering experiments.

6.5.1.2 Results

Figure 6.10 shows the recorded relative density values for all the sintered cylindrical coupons at different holding time and temperature. As the holding time increases, the relative density rapidly

increases to its maximum, followed by a gradual decline. In the early stage of holding time, the presence of liquid phase induces interparticle capillary actions, which accelerates the consolidation of the part [148, 149, 155]. EDS analysis of the sintered samples indicated presence of liquid phase as channels with elevated concentration of chromium were observed at the grain boundaries (Fig. 6.11). Micro-segregation of elements such as chromium into liquid phase at the grain boundaries in supersolidus sintering of nickel-based superalloys is well documented [157, 158].

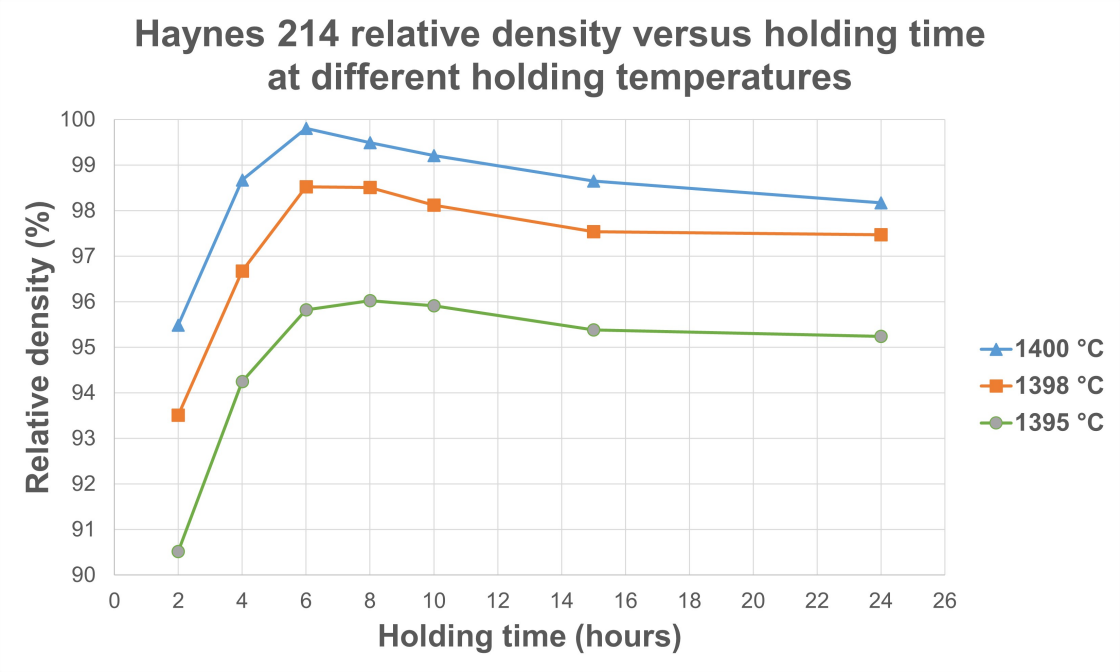

Figure 6.10 Recorded Archimedes' density values for Haynes 214 samples sintered at different temperature and holding durations.

Optical micrographs of samples sintered at 1400 °C at different holding time of 1-6 hours are shown in Fig. 6.12, which demonstrates the evolution of the densification process of Haynes 214. The long sintering process of Haynes 214 is in contrast with the sintering behavior of high liquid phase systems such as W-Cu, where a complete densification can be achieved within minutes of reaching liquid formation temperature (Fig. 6.13) [141]. As shown in figure 6.11, the liquid phase presence in Haynes 214 is minute, while the liquid phase fraction in the W-Ni system can be up to 30% [147].

The optical images of Haynes 214 sintered samples also revealed a second phase which appeared

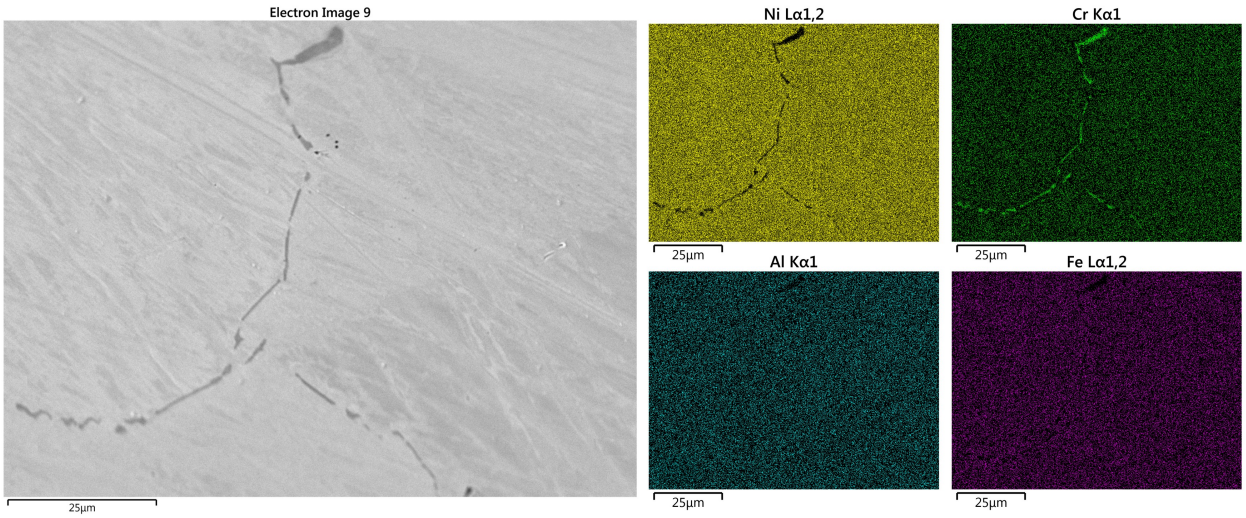

Figure 6.11 EDS mapping of Haynes 214 sample sintered at 1398 °C for 6 hours showing channels of elevated chromium concentration at the grain boundaries, indicating the presence of liquid phase during the sintering process.

to be dark spots scattering throughout the microstructure. SEM images of these areas showed clusters of bright spots embedded in possible cavities (Fig. 6.14). EDS analysis was carried out under backscatter mode, and results displayed an elevated concentration of oxygen and alunimum, and depletion of nickel, chromium, and iron at these regions (Fig. 6.15). As SEAM Haynes 214 samples was exposed to oxygen during the debinding process, oxidation of the metal powder before the sintering cycle is inevitable. Results from previous sections have also indicated presence of oxides in the debinded part. Formation of aluminum oxide is expected, as aluminum formed the most stable oxide out of Haynes 214's elements.

The decline in the part density with the longer holding times is a result of Oswalt's ripening, as insoluble and isolated pores coarsen and expand in the late-stage sintering, increasing the overall part porosity [159]. Figure 6.16 shows the optical micrographs of Haynes 214 sintered at 1400 °C at the holding duration of 6, 8, 12, and 24 hours, which correspond to a gradual decrease in relative density.

To understand the thermodynamic cause of pore coarsening and enlargement, consider two spherical pores of equal diameter. For each of the pore, the ideal gas law dictates:

$$PV = nRT \tag{6.5}$$

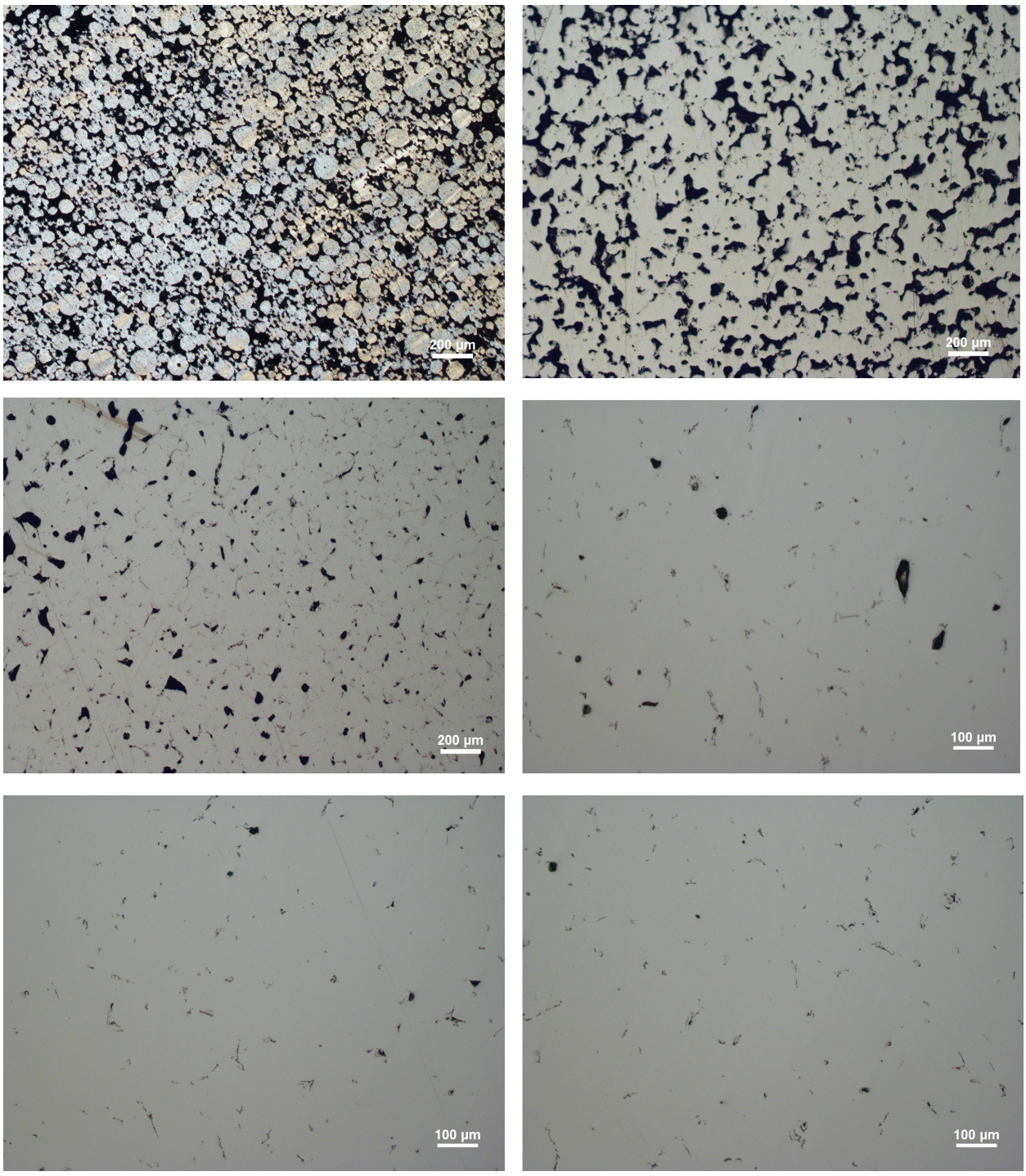

Figure 6.12 Optical micrographs of Haynes 214 samples sintered 1400 °C after a holding time of: From top-left to bottom-right: 1, 2, 3, 4, 5, and 6 hours.

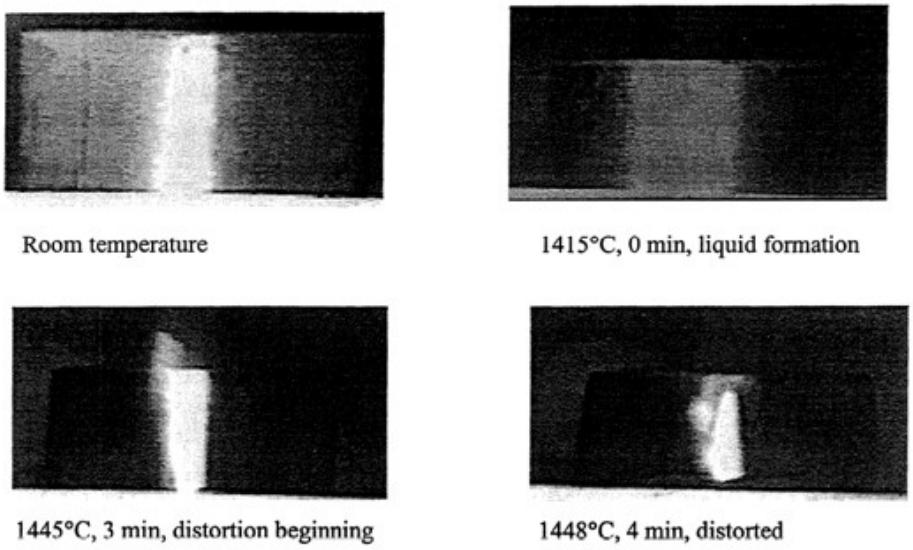

Figure 6.13 Real-time video images showing 80W-4Cu compact at different holding time and temperatures. Rapid deformation can be observed within minutes of liquid phase formation.

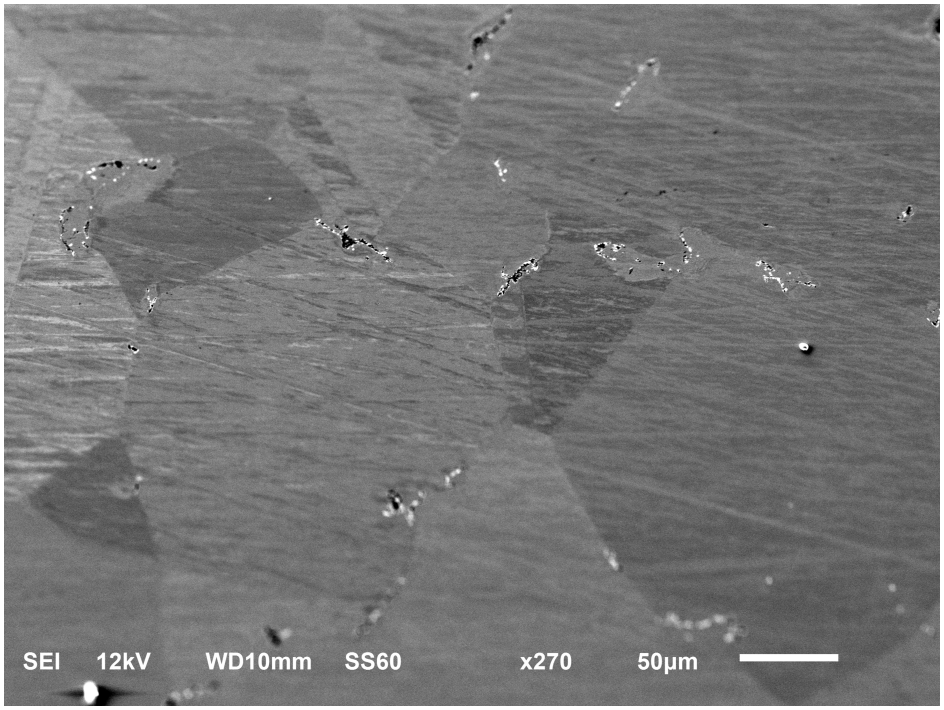

Figure 6.14 SEM image of Haynes 214 coupon, showing dark bright spots embedded in cavities.

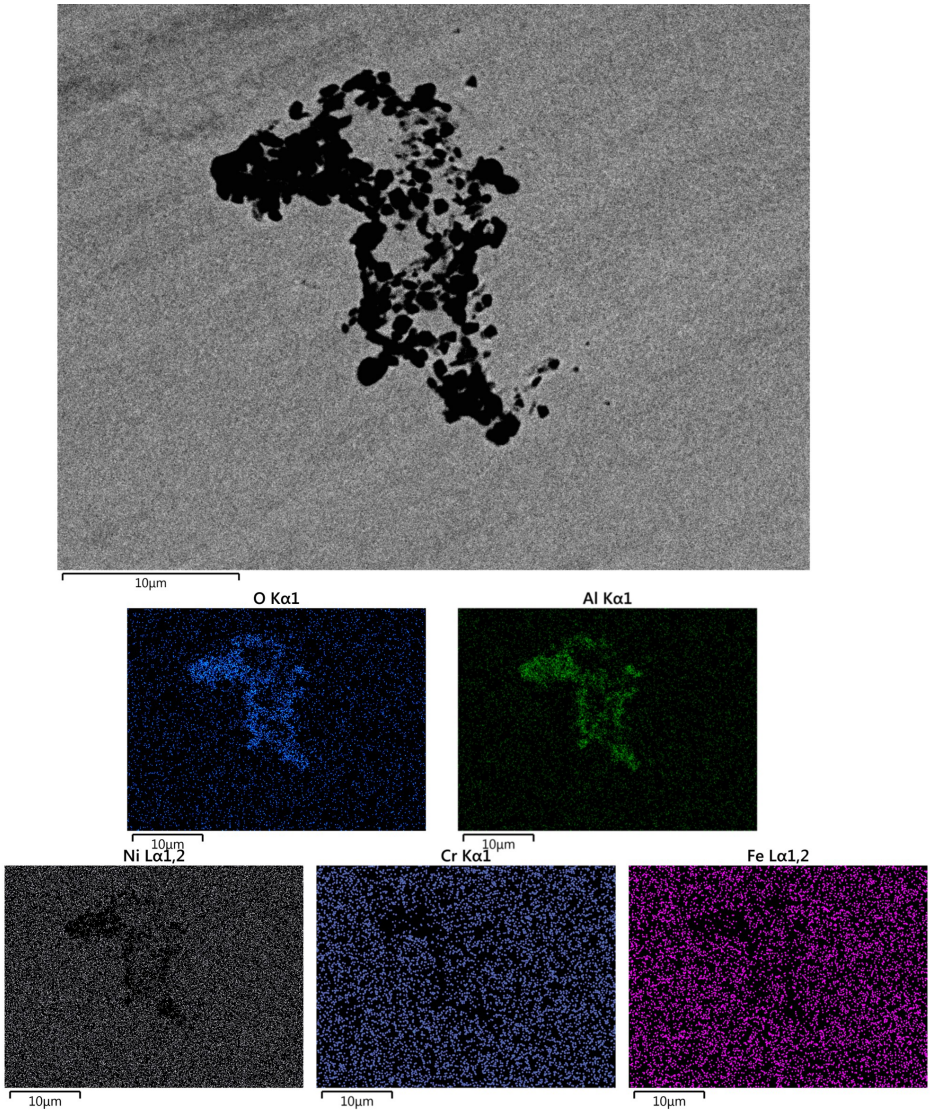

Figure 6.15 EDS mapping of the bright spots on Haynes 214 sintered coupons. An elevated signals of oxygen and aluminum was found.

with P and V are the pressure and volume, n is the number of molecules in the individual pores, T is the system temperature and R is the ideal gas constant. This equation can be used to solve for the initial individual pore diameter:

$$P_1 \pi \frac{d_1^3}{6} = n_1 RT, \; or \; P_1 = \frac{6nRT}{\pi d_1^3} \tag{6.6}$$

As the pores first coarsened and joined together into a single pore, the ideal gas law gives the relationship between volume and pressure in the new coalesced pore as:

$$P_2 V_2 = n_2 RT = 2n_1 RT \tag{6.7}$$

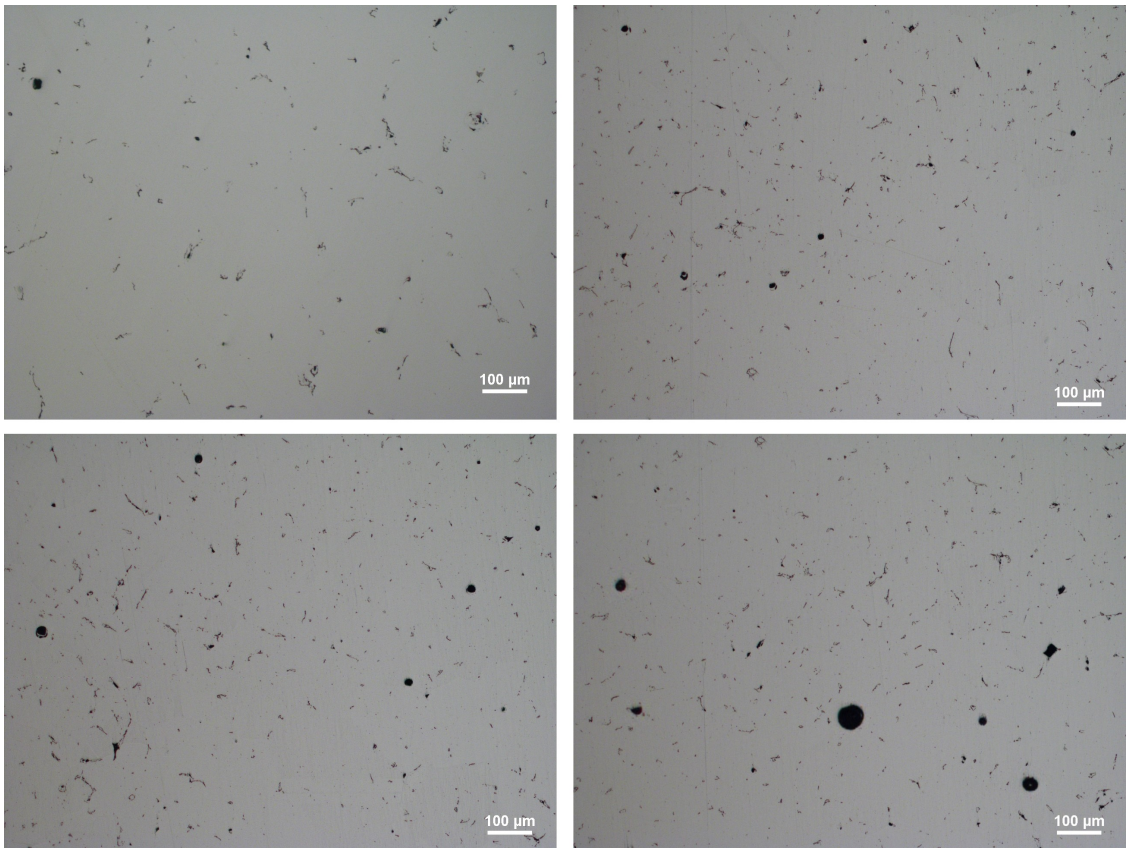

Figure 6.16 Optical micrographs of Haynes 214 samples sintered at 1400 °C after a holding time of a) 6 hours, b) 8 hours, c) 12 hours, and d) 24 hours. Pore coarsening and enlargement was observed at extended holding times.

As the pores first coarsened and joined together into a single pore, the ideal gas law gives the relationship between volume and pressure in the new coalesced pore as:

$$V_2 = 2V_1 \tag{6.8}$$

The new diameter of the coalesced pore can be calculated as:

$$\pi\frac{d_2^3}{6} = 2\pi\frac{d_1^3}{6} \; or \; d_2 = 1.23\, d_1 \tag{6.9}$$

The total surface area of the coalesced pore is then

$$\sum Surface\ area\ (coalesced) = \pi d_2^2 = \pi(1.23d_1)^2 = 1.51\pi d_1^2 \tag{6.10}$$

The total surface area of the initial individual pores is:

$$\sum Surface\ area\ (individuals) = 2\pi d_1^2 \tag{6.11}$$

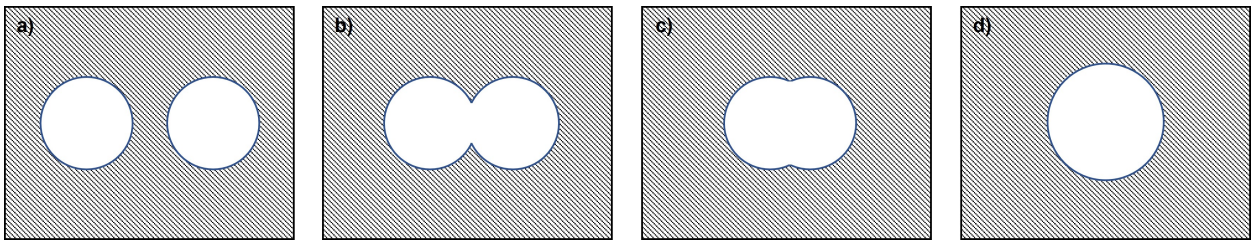

Figure 6.17 Schematic of pore coarsening process. a) Initial individual pores; b - d) From initial pore contact to final coalesced pore. Surface boundary was consumed to create a single new pore.

Therefore, after the two pores coalesce, there is a reduction in the total surface area. In essence, coalescence is a diffusion process, which is thermodynamically driven by the reduction of total surface energy [140]. Figure 6.17 depicts the consumption of the initial individual pores' surface area to create a coalesced pore. Rearrangement of the equilibrium equation in combination with equation gives the relationship between total surface energy and pore diameter:

$$\gamma_{LV} = \frac{Pd}{4} = \frac{6nRT}{4\pi d^3} d = \frac{3nRT}{2\pi d^2} \tag{6.12}$$

which indicates that a decrease in total surface energy, or a decrease in total surface area, requires an increase in the coalesced pore diameter for the system to regain energy equilibrium. As material diffuses and pores coalesce during late stage of sintering, often can also be viewed as a result of Ostwalt ripening, pore enlargement resulted in an increase in total porosity and an overall reduction in part final density [151].

An alternate explanation for pore coarsening and enlargement can be presented as: in accordance with a reduction in total surface area, internal pore pressure increases due to the conservation of the number of gas molecules in the pores, resulting in a pressure difference between the internal and external pressure resulted in an increase in pore volume, i.e. pore enlargement. Figure 6.18, reprinted from [160] demonstrates this analogy.

The highest relative densities achieved were 99.81% and 98.5% at the holding temperature of 1400 °C and 1398 °C, respectively, after 6 hours of sintering. However, the coupons sintered at 1400 °C exhibited the onset of the well-known "elephant foot" deformation in liquid phase sintering [18,140,141] (Fig. 6.19(a)), which indicates that the compact strength could not overcome the distortion driving force (i.e., gravitational force), and part contiguity fell below the critical level

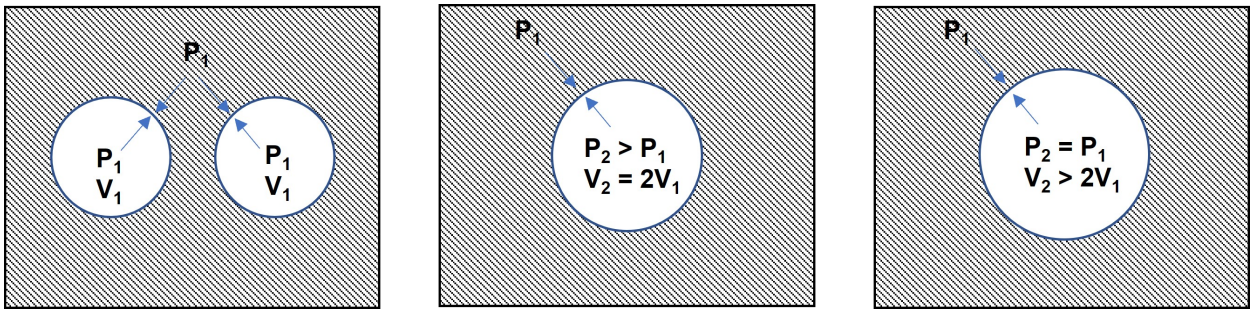

Figure 6.18 a) Initial individual pores in pressure equilibrium; b) Initial coalesce pore with higher internal pore pressure; c) Enlarged pore in pressure equilibrium.

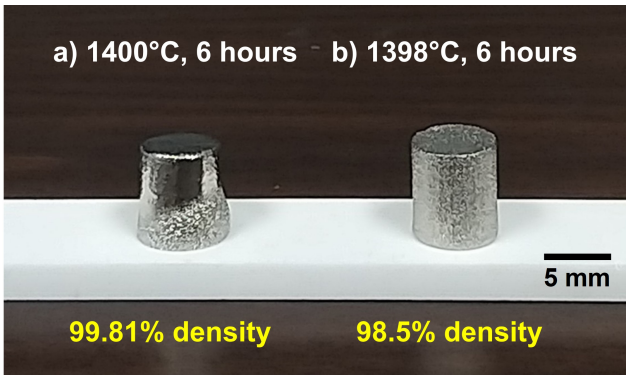

Figure 6.19 Haynes 214 cylindrical coupons with highest relative densities and their sintering conditions.

during the sintering process [18, 141, 142]. On the other hand, coupons sintered at 1395 °C and 1398 °C exhibited complete shape retention (Fig. 6.19 (b)).

In summary, the following key insights must be taken into consideration to further improve the sintering process for SEAM printed Haynes 214 parts:

- The maximum achievable relative density increases with an increase in holding temperature. To achieve a relative density above 99%, a holding temperature of 1400 °C or above must be used.
- However, the maximum holding temperature for a complete shape retention of the sintered part is found to be 1398 °C.
- Pore coalescent and growth are detrimental to part density after a prolonged holding time, which is after approximately 6 hours in this case.

6.5.2 2-step sintering to full density and deformation control

During liquid phase sintering, compact strength directly correlates to the capillary force acting on the particles and the strength of the percolation structure of the particle network. If compact strength falls below the gravity induces distortion driving force during the sintering cycle, distortion occurs. German et al. [148] proposed the following model to calculate compact yield strength:

$$\sigma = \frac{3V_S}{2}\left(P_n + \sigma_0 C_{SS}\right) \tag{6.13}$$

where V_S is the solid volume fraction, σ_0 is the inherent solid-solid bonding strength between the particles, C_{SS} is part contiguity, and P_n is the mean capillary pressure exerted on the surface due to liquid phase which can be calculated by

$$P_n = \frac{N_c F_n}{(\pi G)^2} \tag{6.14}$$

with N_c is total number of particle contacts at any given time, F_n is the mean capillary force per particle contact, and G is the mean particle diameter. Upon liquid phase formation during heating up to the sintering temperature, V_S decreases while P_n increases due to the presence of capillary action accompanied with liquid phase. The behavior of part contiguity C_{SS} is more complex. As previously defined, contiguity is the fraction of solid-solid contact surface area and the total microstructure interfacial area. When liquid phase is first formed, the solid bonds are partially dissolved, which leads to a decrease in dihedral angle and increase in liquid spreading on the particle boundaries, resulting in a decrease in part contiguity [18]. As the sintering process proceeds, solid diffusion through solution-precipitation occurs, which increases the solid-solid bonding and resulting in a gradual increase in part contiguity and a stronger percolation structure. As the body densifies and reaches its lowest energy configuration at the maximum achievable density, part contiguity value stabilizes [148]. Figure 6.20 demonstrates the dramatic drop and eventual stabilization in part contiguity of a W-8Ni compact upon liquid phase formation during heating up to 1550 °C [141]. The graphical representation of the relationship between compact strength, contiguity, part density, and distortion driving force is shown for both cases where there is a complete shape retention

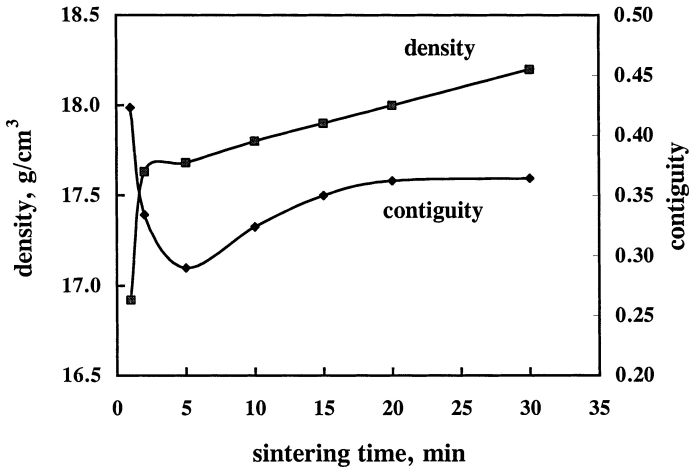

Figure 6.20 Density and contiguity versus time of a W-8Ni cylindrical coupon sintered at 1550 °C [141].

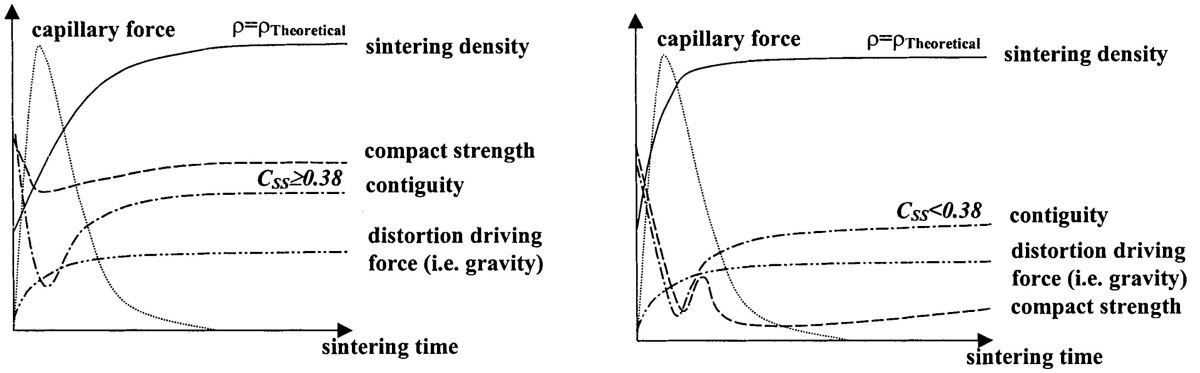

(a) Part retains intended shape (b) Part distorted and deformed

Figure 6.21 Relationship between compact strength, contiguity, part density, and distortion driving force for cases where (a) Part retained the intended shape and (b) part distorted and deformed. Reprinted from [148].

of the part (Fig. 6.21(a)) and where distortion occurs (Fig. 6.21(b)). The behavior of Haynes 214 cylindrical coupon sintered at 1398 °C for 6 hours corresponds to the left image, as the part maintained the intended shape at the end of the sintering cycle. The coupon sintered at 1400 °C for 6 hours corresponds to the right image, as part deformation occurred.

As part contiguity is a time and temperature dependent value, Equation 6.13 indicates that compact strength during the sintering process is also transient and temperature-controlled. The study presented in this section takes advantage of this behavior to first characterize and capture the transient deformation behavior of Haynes 214 green parts with varying holding time and temperature and

subsequently develop a 2-step sintering procedure to achieve fully dense parts while retaining their intended shape.

6.5.2.1 Experimental setup

First, the alumina tube furnace used in previous experiments was damaged and replaced with a new unit. Therefore, experiments were carried out to re-calibrate the previous processing conditions. The results are as follows:

- Sintering at 1388 °C for 5 hours yielded sample with 98.5 % relative density, which is equivalent to the previous holding at 1398 °C for 6 hours.
- Sintering at 1390 °C for 5 hours yielded sample with 99.78 % relative density, which is equivalent to the previous holding at 1400 °C for 6 hours.

The difference in temperature and holding time using the new alumina tube can be attributed to long term usage of the previous unit, and/or small difference in location of the thermocouples before and after the repairing process.

Using the new processing conditions, 2-step sintering cycles were designed to characterize the density evolution as well as shape deformation with respect to sintering time and temperature. 5 cylindrical coupons were sintered using the following heating cycles:

1. Coupons were first heated to the first holding temperature of 1388 °C using the same heating rates used in previous section. The dwell time for this step is 4 hours.
2. Coupons were then heated to the second holding temperature of 1390 °C at 1 °C/min, and subsequently dwelled for different time durations of 0, 15, 30, 45, and 60 minutes.
3. Coupons were cooled down to room temperature using the same heating rates used in previous section.

Archimedes density were measured for all samples, and their physical deformations are inspected visually.

6.5.2.2 Results

Figure 6.23 shows the measured relative density of all the samples, as well as their physical appearances and deformation degrees. The part strength profiles of the two baseline sintered samples at 1388 °C (baseline sample I) and 1390 °C (baseline sample II) for 6 hours were also sketched with the effect of distortion driving force (i.e. gravity). The estimated strength of the five sintered sample in this section were also estimated on the plot.

A gradual increase in relative density was observed in the five sintered samples as additional time was used in the second holding step at 1390 °C. The increase in holding time also corresponds to a transition in shape deformation: Samples 1 and 2 completely retained the intended shape, sample 3 displayed a very early onset of the "elephant foot" deformation, and significant slumping can be observed in samples 4 and 5, along with the baseline sample II. As the baseline sample I displayed no geometrical deformation, it was expected that sample 1 also exhibit the same behavior. For samples 2-5, the second holding step at 1390 °C increased the amount of liquid phase in the sintering body by partially dissolving the formed sintered bonds, leading to a decrease in solid-liquid interfacial energy and an enhancement in liquid penetration at the grain boundaries. The result is an improvement in pore filling as well as densification, along with a lower contiguity level and weaken yield strength of the body and an eventual shape deformation, all of which has been demonstrated by the gradual transition of the relative density and physical appearance of the 5 sintered samples.

The profiles of the baseline samples were sketched based on previous findings by German et al. [148]. Baseline sample II showed significant deformation, indicating that its yield strength dropped below the distortion driving force, represented by Figure 6.21 (b). On the contrary, baseline sample I exhibited good shape retention, and therefore its yield strength throughout the sintering cycle behaves in the same manner as Figure 6.21 (a), with the part strength never fell below the strength of the distortion driving force. While sample 2 also exhibited no deformation, the higher part density achieved along with the holding step at 1390 °C suggested an increase in liquid phase in the body, accompanied by a lower contiguity level, and therefore a lower yield strength

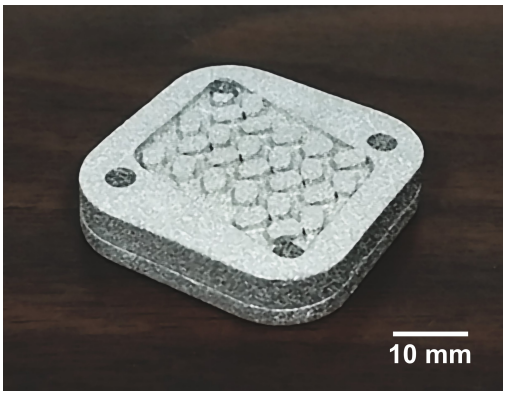

Figure 6.22 Haynes 214 heat exchanger assembly prototype fabricated by SEAM process using 2-step sintering technique.

according to Equation 6.4. Therefore, on Figure 6.23 the yield strength of sample 2 was placed between baseline sample I and but above the effect the distortion driving force. Similarly, sample 3 with the onset deformation was placed near the effect of distortion driving force line while sample 4 and 5 are placed below. The results from the measured relative density, physical appearances, and yield strength profiles have indicated a transient behavior of the sintered part in terms of part density and deformation degree with respect to the second sintering step holding time.

The traditional 1-step sintering at 1390 °C resulted in a below-critical-level part contiguity and yield strength, demonstrated by the fabricated sample's geometrical deformation. On the other hand, by using the 2-step sintering strategy, at the end of the first holding step at 1388 °C, sufficient time was provided for the sinter bonds to form, leading to a high yield strength and part contiguity. By taking advantage of the transient behavior of the part during the second holding step, an appropriate holding time can be designed to not only enhance densification but also retain a part yield strength and contiguity above the critical level, resulting in higher part final density with complete shape retention. Sample 2 sintered at 1388 °C for 4 hours, followed by a second sintering step at 1390 °C for 15 minutes achieved a relative density above 99.5 % with no geometrical distortion, which is unattainable with the traditional 1-step sintering technique. A heat Haynes 214 heat exchanger assembly prototype was fabricated using the developed 2-step sintering technique (Fig. 6.22).

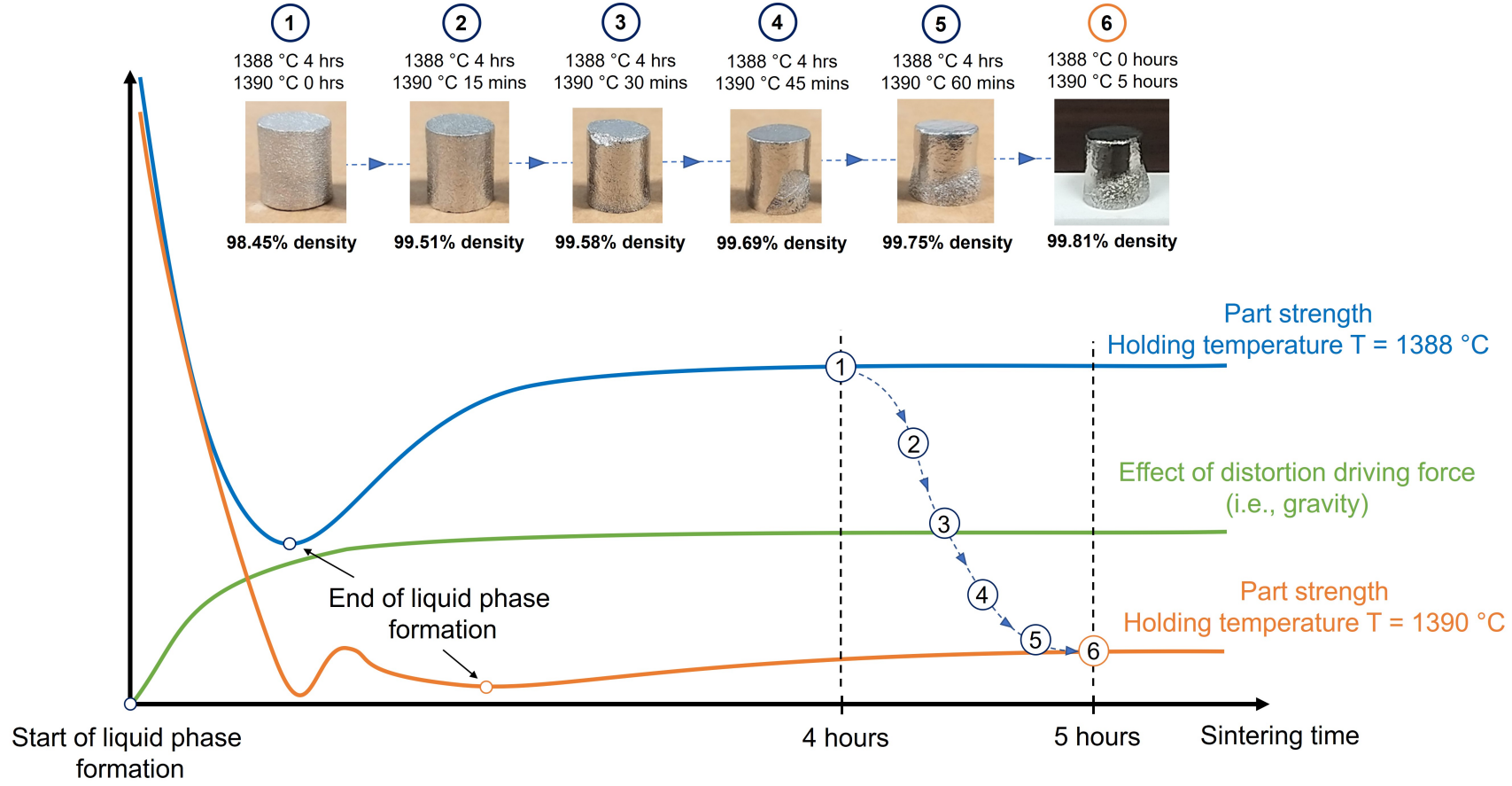

Figure 6.23 Relative density of all the sintered sample, as well as their physical appearances and deformation degrees. The part strength profiles of the baseline samples I and II are sketched with the effect of distortion driving force (i.e. gravity). The estimated strength of the 5 sintered sample in this section are also pinpointed on the plot.

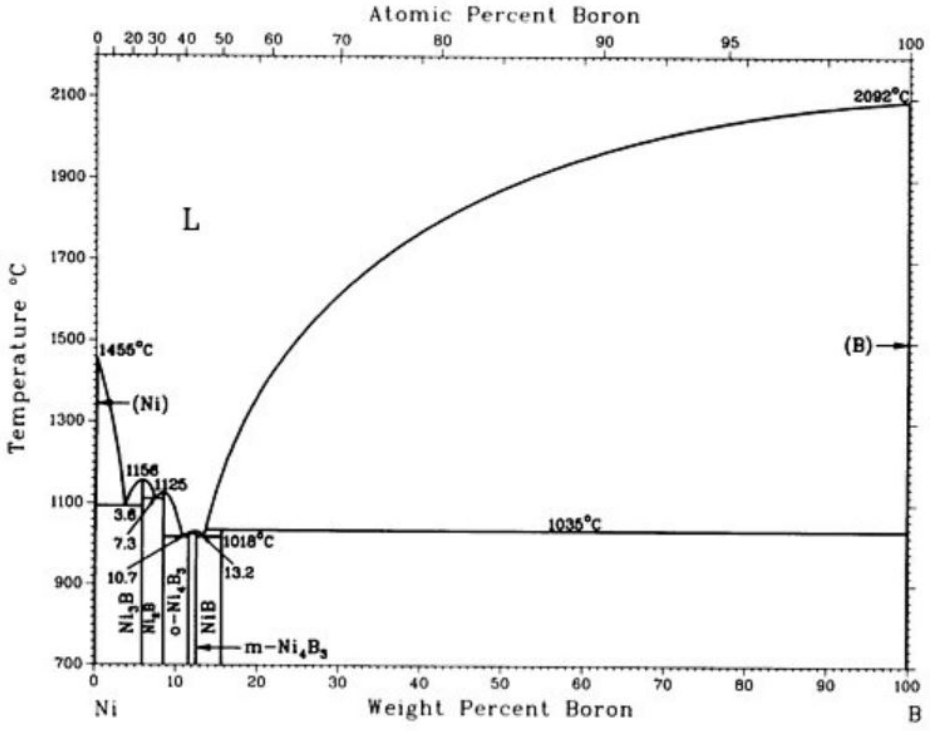

Figure 6.24 Nickel-Boron phase diagram [161]. Boron appreciably lowers the eutectic point temperature of nickel.

6.5.3 Activated sintering of Haynes 214

6.5.3.1 Experimental setup

As boron appreciably reduces the eutectic temperature of nickel (Fig. 6.24), boron nitride additive was explored as a sintering aid for Haynes 214. Suspension of Haynes 214 powder mixture and 0.25 wt.% addition of BN particles (Sigma Aldrich, St. Louis, MO) with size of 1 μm was formulated. Green cylindrical coupons of 1 cm in diameter and 1.5 cm in height were fabricated and debinded under the previously determined optimal heating cycle. Samples were sintered in vacuum at different holding temperature of 1210, 1220, 1230, 1240, and 1250 °C for 6 hours. Samples were sectioned and polished, and their microstructures were studied under an optical microscope, SEM, and EDS.

6.5.3.2 Results and discussion

All Haynes 214 + 0.25 wt.% BN coupon sintered at different temperature coupon exhibited partial melting behavior. Fully densified shells were observed on the exterior regions of the coupons. The shell thickness increases with an increase in holding temperature (Fig. 6.25). However, the inner cores of the samples are completely porous (Fig. 6.26). The partial melting regions were accompanied with lamellar precipitate zones (Fig. 6.27). EDS revealed an enrichment of chromium and boron in the lamellar precipitate zones (Fig. 6.28), where chromium contents as high at 40 % were recorded.

A previous study on the sintering of BN-doped KH20N80 alloy experienced identical partial melting behavior [162]. KH20N80 is a nickel-based alloy with 80 wt.% Ni, 20 % Cr, and can contain up to 1.5 % of impurities including silicon, manganese, titanium, iron, carbon, sulfur, and calcium. BN-doped KH20N80 samples sintered at 1600 °C in different environment (hydrogen, cracked amonia, and vacuum) all displayed partial melting behavior, where the melting process began on the surface and spread towards the center of the samples. Oriented lamellar precipitates were detected at the melt zones with elevated concentration of chromium. The study concluded that the most probable cause of partial melting is due to the reaction between boron nitride with chromium and nickel, and the increase in chromium concentration in the melt zones can be attributed to the preferential reaction between chromium and boron. It has also been suggested that the partial melting process began by the dissociation of boron and nitrogen, followed by a formation of liquid phase containing nickel and boron, and finally an enrichment of chromium and boride phase at the lamellar zones.

As partial melting was initiated from the surface of the coupons, which completely inhibited the densification of the inner region, it can be concluded that boron nitride is not a suitable sintering additive for Haynes 214. Future work might explore different sintering additives to enable activate sintering of Haynes 214 in particular and nickel based alloys in general.

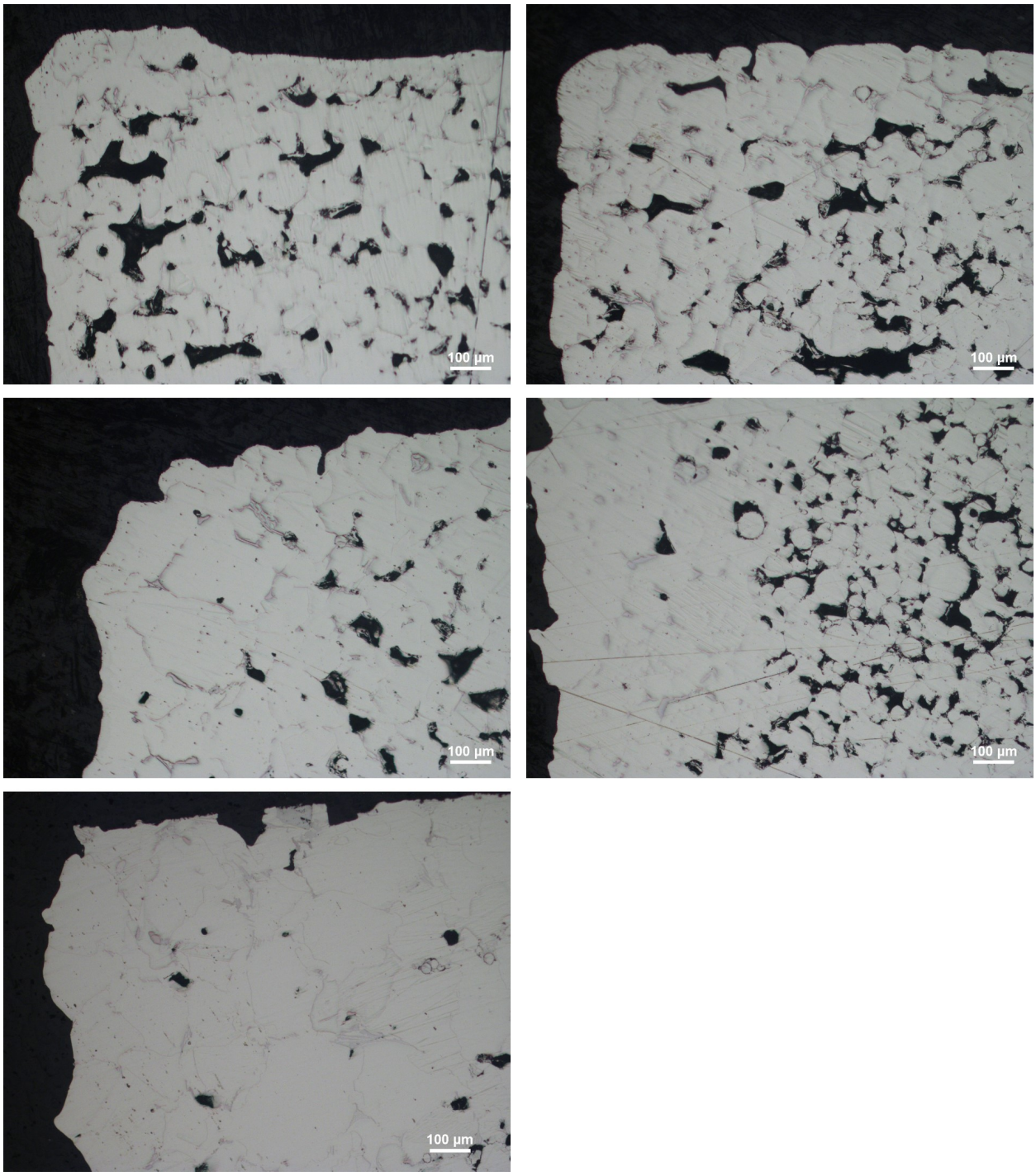

Figure 6.25 Optical images of the outer region of Haynes 214 + 0.25 wt. % BN SEAM coupons, showing a dense shell with thickness increased with increasing holding temperature. From top-left to bottom right: Holding temperature of 1210, 1220, 1230, 1240, and 1250 °C.

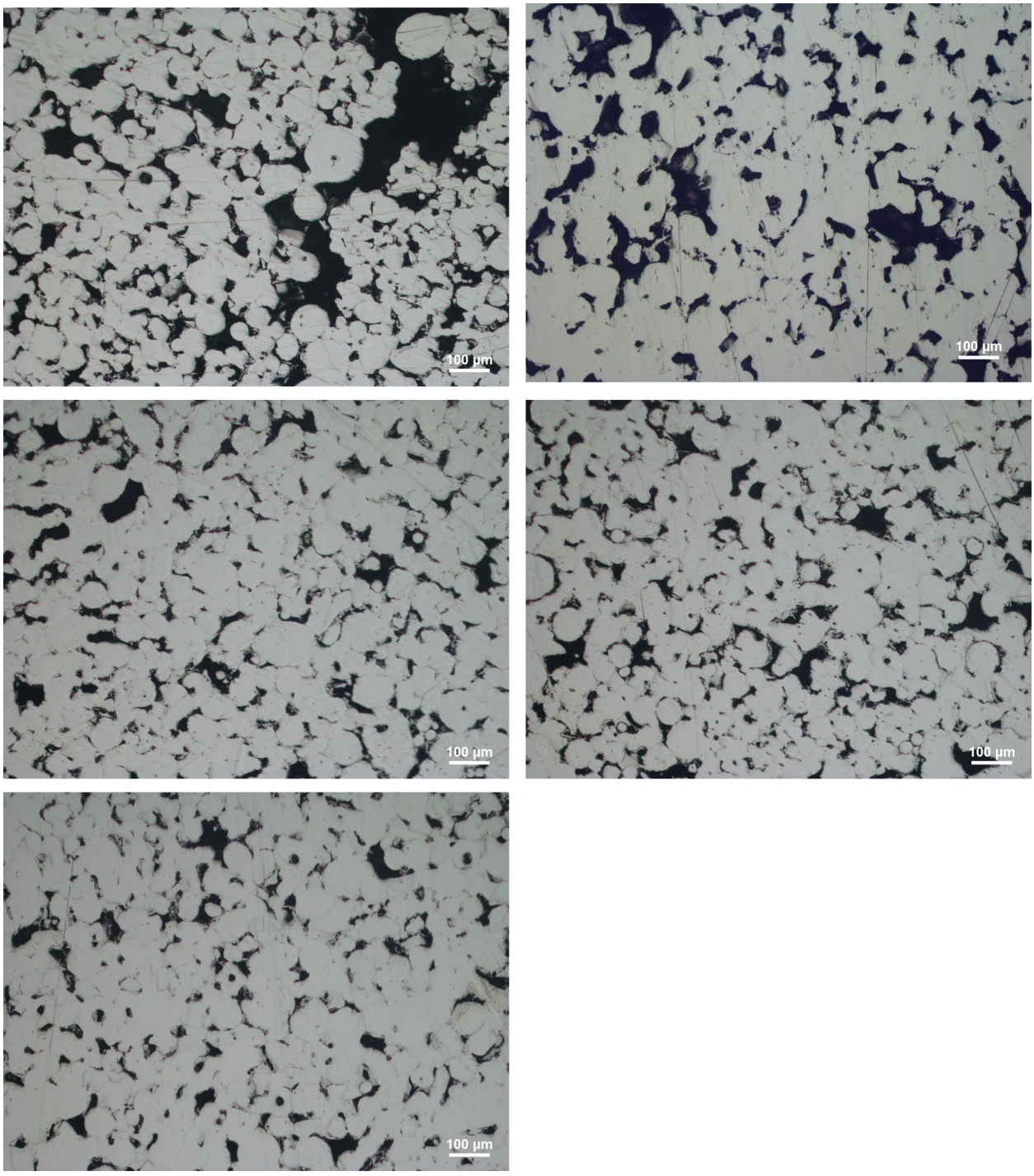

Figure 6.26 Optical images of the inner region of Haynes 214 + 0.25 wt. % BN SEAM coupons, showing a complete lack of densification in all cases. From top-left to bottom right: Holding temperature of 1210, 1220, 1230, 1240, and 1250 °C.

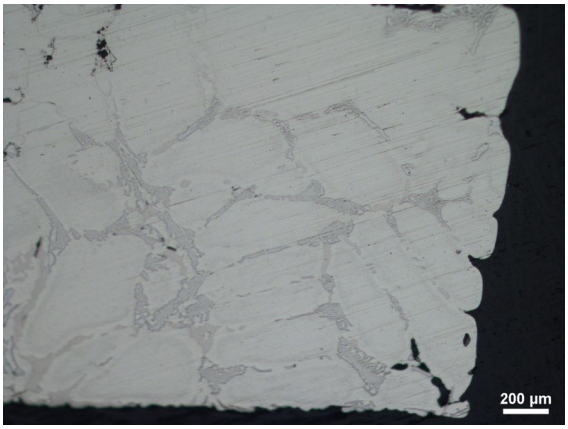

Figure 6.27 Optical images of the melt region of Haynes 214 + 0.25 wt. % BN SEAM coupon sintered at 1250 °C showing lamellar precipitate zones.

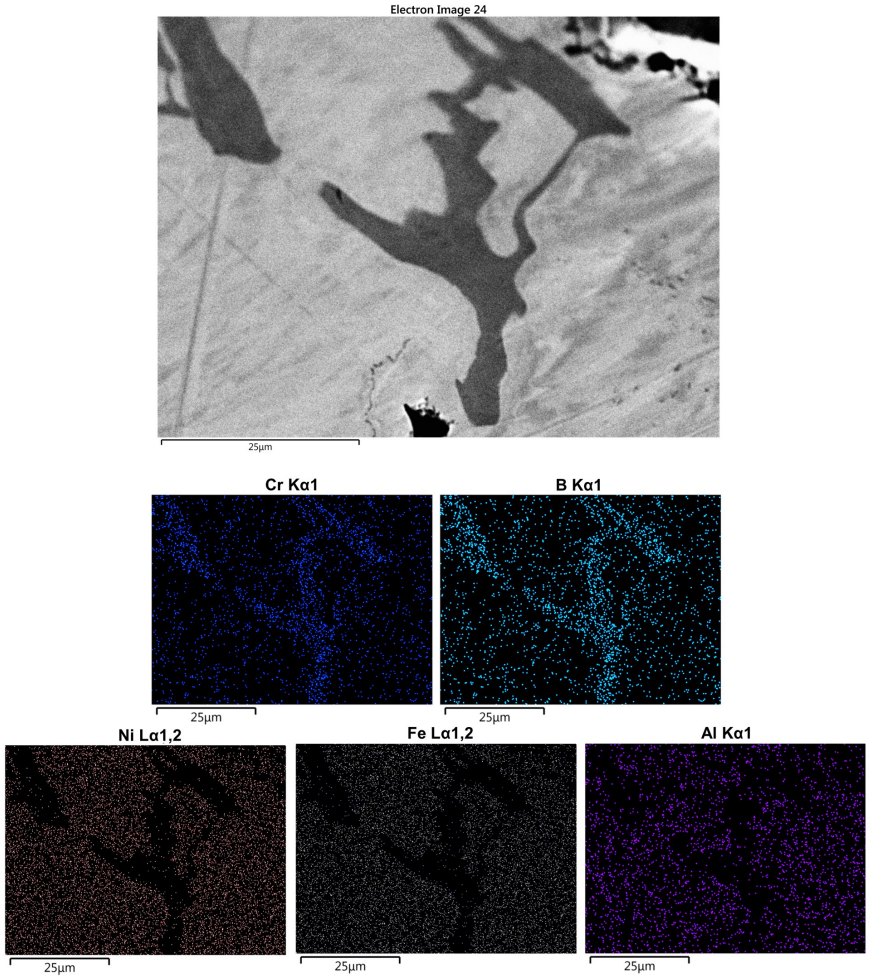

Figure 6.28 EDS mapping of the melt zone revealed an enrichment of chromium and boron at the lamellar zones.

6.6 The Olevsky-Skorod sintering model

As the SEAM process is being developed, there is a crucial need for sintered part quality control i.e. shrinkage and distortion prediction. While this task can be done simply by trial and error, the time and effort required would be enormous due to the nature of the process. The introduction of numerical study in combination with experimental data is a possible systematic solution to the quantitative prediction of sintering distortion and final part quality. The work presented here is built upon the viscoplastic constitutive model developed by Olevsky [163, 164] as an effort to quantify and predict the part properties outcome after the sintering process.

6.6.1 Olevsky analytical model for constitutive parameters

6.6.1.1 The constitutive equations and model parameterization

The original model was developed purely mathematically by Skorohod [163]. A phenomenological constitutive model was then developed by Olevsky for numerical simulations based on Newtonian viscosity and continuum mechanics [164]. The continuum formulation describes the sintering body as having two material phases including a core (skeleton) phase and a void (porous) phase. The core phase can be characterized as a linear or nonlinear viscous incompressible behavior. The void phase is assumed to be homogeneously distributed throughout the sintering body. An isotropic behavior is also assumed for the sintering body. The general form of the constitutive model is given by:

$$\sigma_{ij} = \frac{\sigma\left(W\right)}{W}\left(\varphi\dot{\varepsilon}_{ij}^{'} + \psi\dot{e}\delta_{ij}\right) + P_L\delta_{ij} \tag{6.15}$$

Each term in the equation is given in table 6.4.

Linear viscosity is the most widely used assumption for the sintering body, due to its simplicity as well as feasibility to be implemented numerically. Parameters from sintering experiments can also be applied in linear viscosity type model. The linear viscous form of the equivalent stress is represented by:

$$\sigma\left(W\right) = 2\eta_0 W \tag{6.16}$$

Table 6.4 Constitutive model parameters.

Parameters	**Symbol**
Cauchy stress tensor	σ_{ij}
Equivalent stress	$\sigma\ (W)$
Equivalent strain rate	W
Deviatoric strain rate tensor	$\dot{\varepsilon}_{ij}^{'}$
Trace of strain rate tensor	$\dot{e}$
Normalized shear viscosity	φ
Normalized bulk viscosity	ψ
Sintering stress	P_L
Kronecker delta	δ_{ij}

where η_0 is the initial shear viscosity of the solid body. The constitutive equation then can be expressed as:

$$\sigma_{ij} = 2\eta_0 \left(\varphi\dot{\varepsilon}_{ij}^{'} + \psi e\delta_{ij}\right) + P_L\delta_{ij} \tag{6.17}$$

The viscous sintering strain rate can be extracted by inverting this equation and is given as:

$$\dot{\varepsilon}_{ij} = \frac{\sigma_{ij}^{'}}{2G_{SOVS}} + \frac{\sigma_m - \sigma_{SOVS}}{3K_{SOVS}}\delta_{ij} \tag{6.18}$$

where σ_m is the hydrostatic stress tensor and $\sigma_{ij}^{'}$ is the deviatoric stress tensor. The effective viscosities can be calculated by:

$$G_{SOVS} = \eta_0\varphi \tag{6.19}$$

$$K_{SOVS} = \eta_0\psi \tag{6.20}$$

A simplified versions of the normalized viscosities and sintering stress can be obtained by:

$$G_{SOVS} = \eta_0\,(1-\theta)^2 \tag{6.21}$$

$$K_{SOVS} = \eta_0\frac{4\,(1-\theta)^3}{3\theta} \tag{6.22}$$

$$\sigma_{SOVS} = \frac{3y}{r_0}\,(1-\theta)^2 \tag{6.23}$$

where y is the surface tension between the particles, $\theta = 1-\rho$ is the ratio of pore volume, and r_0 is the initial powder particle radius. For the numerical implementation, the sintering stress can also be expressed by:

$$\sigma_{SOVS} = \frac{\sigma_{SOVS/ref}}{\rho_{ref}^2}\,(1-\theta)^2 \tag{6.24}$$

Table 6.5 Numerical Olevsky model input parameters for aluminum oxide.

Parameters	**Symbol**	**Value**
Shear viscosity	η_0	27 GPa
Reference density	ρ_{ref}	0.6
Sintering stress at reference density	$\sigma_{SOVS/ref}$	270 N/m^2

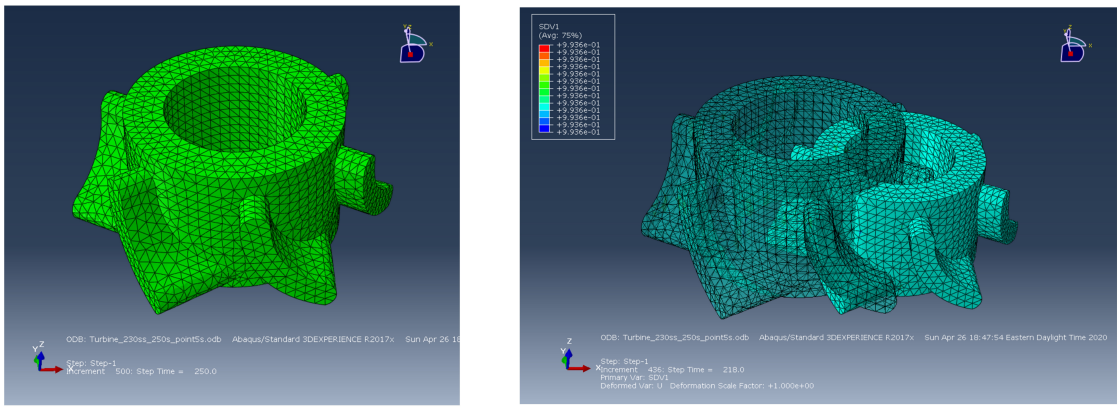

(a) Initial sintering body (b) Final sintering body

Figure 6.29 Olevsky analytical numerical simulation result for an aluminum oxide body.

The relative density of the sintering body can be related to the viscous sintering strain rate tensor by:

$$\frac{d\rho}{dt} = -\rho \frac{d\left(\varepsilon_{kk}\right)}{dt} \tag{6.25}$$

6.6.1.2 Results and discussion

Equation 6.21 - 6.25 were implemented in an user defined subroutine (UMAT) and was solved with Abaqus solver using the values given in Table 6.5 for the properties of aluminum oxide. Figure 6.29 shows the initial and final sintering body. The element type used was 4 node tetrahedron and the boundary condition used was U3 = 0 (fixed bottom surface). Figure 6.30 shows the relative density of the sintering body over time. The relative density value converged at 99.36% with total volume shrinkage of approximately 20%. The results from the implemented numerical Olevsky model have shown good agreement with not only experimental data but also literature sources [18, 165].

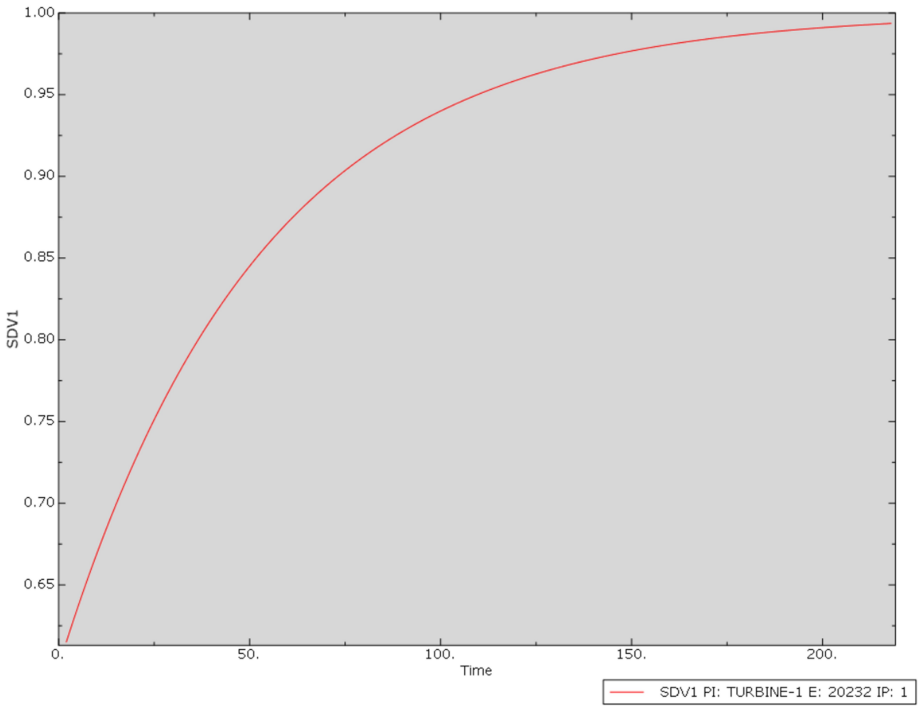

Figure 6.30 Olevsky analytical numerical simulation result - Relative density over time.

6.6.2 The modified SOVS model for aluminum oxide powder compaction

The biggest advantage of the phenomenological SOVS model is its feasibility for implementation in numerical simulations due to the relatively simple constitutive equations for predicting the solidification of the sintering body. The experimental data can also be adopted into mathematical expressions and curve fittings can yield the input parameters. However, Reiterer et al. [166] have found that the polynomial viscosity function did not accurately predict the solidification evolution in comparison with sintering experiments. Moreover, the original SOVS model did not take into account the influence of grain growth on the densification behavior. The model also lacks the relationship between sintering stress, grain growth, and relative density. Therefore, there is a need for further development of the phenomenological Olevsky model. Shinagawa et al. [167] proposed that the viscosity should be expressed as an Arrhenius type function of temperature and grain growth. The modified SOVS model was then developed by combining the original Olevsky model and Shinagawa's work.

6.6.2.1 The modified constitutive equations and model parameterization

The phenomenological constitutive equation described by Shinagawa et al. can be expressed as:

$$\dot{\varepsilon}_{ij} = \frac{1}{2\eta}\frac{1}{\rho^{2n-1}}\left[\sigma'_{ij} + \frac{2}{9{f_s}^2}\left(\sigma_m - \sigma_{SOVS}\right)\delta_{ij}\right] \tag{6.26}$$

The shear viscosity of the fully dense skeleton can be calculated by:

$$\eta_o = C_{s1}T\ exp\left(\frac{C_{s2}}{T}\right)d^3 \tag{6.27}$$

where C_{s1} and C_{s2} are constants that can be extracted from sintering experiments and curve fitting and d is the grain growth factor given by:

$$d^m = d_0^m + \beta T \tag{6.28}$$

The effective shear and bulk viscosity can be rewritten as:

$$G_{SOVS} = n_0\rho^{2n-1} \tag{6.29}$$

$$K_{SOVS} = 3f_S^2\eta_0\rho^{2n-1} \tag{6.30}$$

where $f_s\left(\rho\right) = \frac{1}{2.5\sqrt{1-\rho}}$. The sintering stress is expressed as:

$$\sigma_S = \frac{2\gamma}{\zeta R}\rho^{N_S}\left[\frac{\rho\left(1-\rho_0\right)}{\rho_0\left(1-\rho\right)}\right]^{1/3} \tag{6.31}$$

with ρ is the relative density, and ρ_0 is the initial green density. Equation 6.25 can be integrated to yield:

$$\rho\left(\varepsilon\right) = C\ exp(-\varepsilon_{kk}) \tag{6.32}$$

The relationship between density and strain then can be obtained by applying the initial conditions and is given by:

$$\rho\left(\varepsilon\right) = \rho_o\ exp(-\varepsilon_{kk}) \tag{6.33}$$

The equations were implemented in a UMAT subroutine and solved with ABAQUS. Parameters for aluminum oxide for the modified SOVS model are shown in table 6.6

Table 6.6 Modified Olevsky model input parameters for aluminum oxide.

Parameters	Symbol	Value
Viscosity Constants	C_{s1}	$7.82e^{15}$
	C_{s2}	$3.23e^{4}$
Exponential constant for bulk and shear viscosities	n	2.5
Sintering stress exponential constant	N_s	5.0
Sintering stress correction factor	ζ	0.5
Specific surface energy	γ	$0.9\ J/m^2$
Grain evolution exponent	m	1/0.37
Grain evolution coefficient	β	$4.84e^{-20}$
Grain radius	R	$1.5e^{17}\ \mu m$

6.6.2.2 Model verification

Verification of the implemented model relies on previous literature studies on the modified SOVS model. Nguyen [168] simulated the sintering of an aluminum oxide cylindrical sample of 8.9 mm in diameter positioned between 2 rigid punches to study the final density distribution and relative density over time. Cox et al. [169] repeated this simulation setup to study the density gradient evolution over the sintering time. The temperature profile is consisted of a 10 °C/min ramp rate to a holding temperature of 1450 °C for 60 minutes before a cooling down step. A force of 20 MPa was also applied in the axial direction after the attainment of sintering temperature. The numerical simulation setup for the sintering body as well as the temperature and pressure profile are shown in figure 6.31. The implemented modified SOVS model was applied to the same sintering body setup and sintering conditions (Fig. 6.32).

6.6.2.3 Results and discussion

Figure 6.33 shows the simulation results from Nguyen's work [168] and the implemented model showing similar dimensional change as well as final density distribution at the axial cross section of the cylinder. The relative density evolution over time graphs from both models are also in agreement such that the relative density rises rapidly as the temperature approaches the sintering temperature and converges towards 98%. Figure 6.34 shows the density distribution at the axial cross section of the cylinder from Cox's model and the implemented model. The results have shown

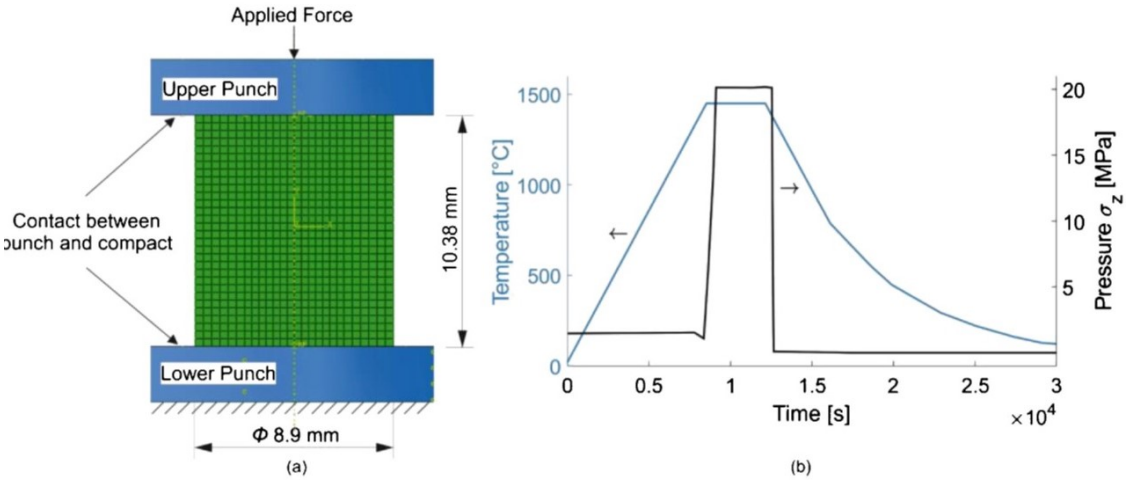

Figure 6.31 Numerical simulation setup for sintering body (left) and temperature and pressure profile (right).

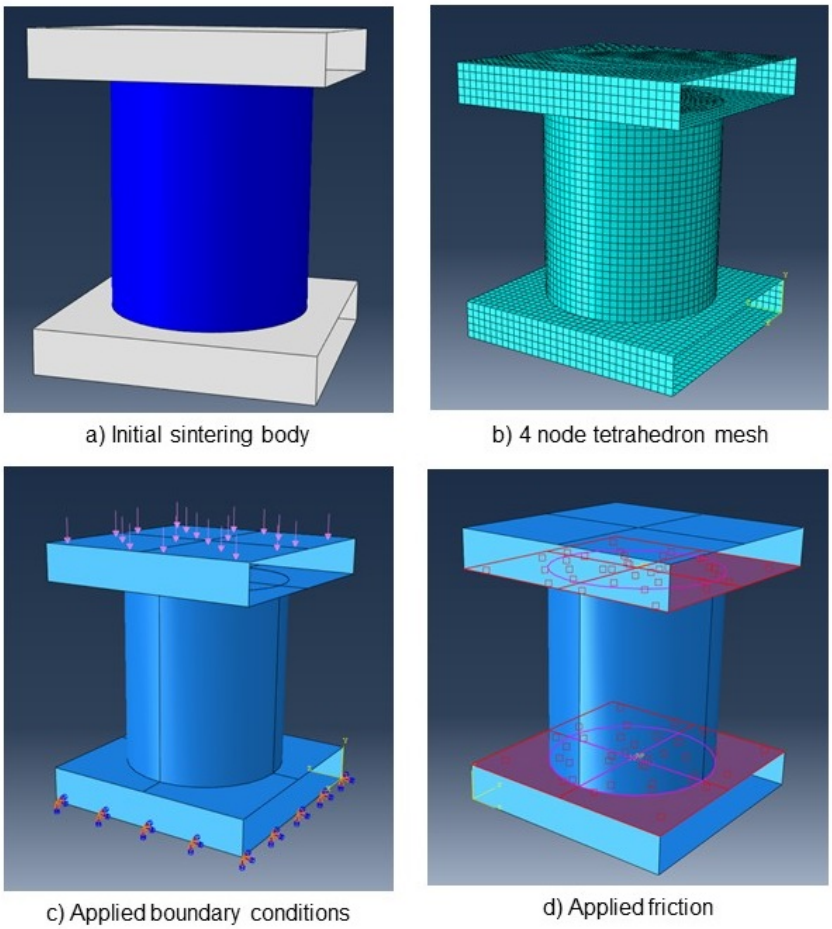

Figure 6.32 Numerical simulation setup for the implemented model.

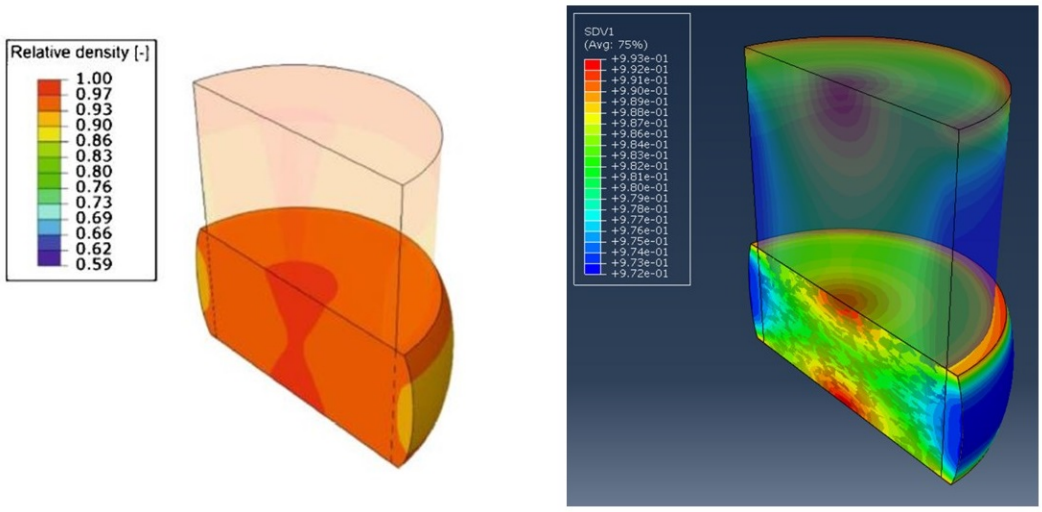

(a) Final density distribution at the axial cross section from Nguyen's model (left) and the implemented model (right).

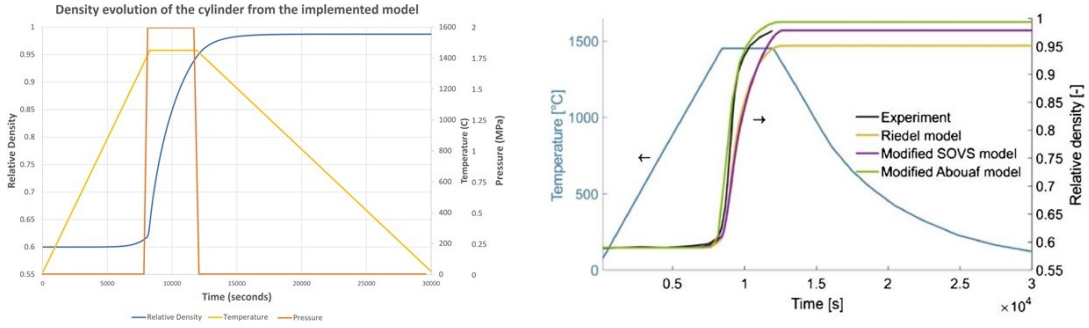

(b) Relative density evolution over time from Nguyen's model (left) and implemented model (right).

Figure 6.33 Result comparison with Nguyen's work [168] for the cylindrical sintering body.

good similarity between the two model, displaying a higher relative densities at the center of the cylinder and lower at the outer section. The deformation differences between the two model can be attributed to the difference in the pressure applied, as a Gaussian pressure field was used in Cox et al.'s model [169] while a uniform pressure field was used in the implemented model.

6.6.3 Conclusion

A modified SOVS model was developed and implemented in a UMAT subroutine in Abaqus with the purpose of predicting shrinkage and distortion of sintered parts produced by the SEAM process.

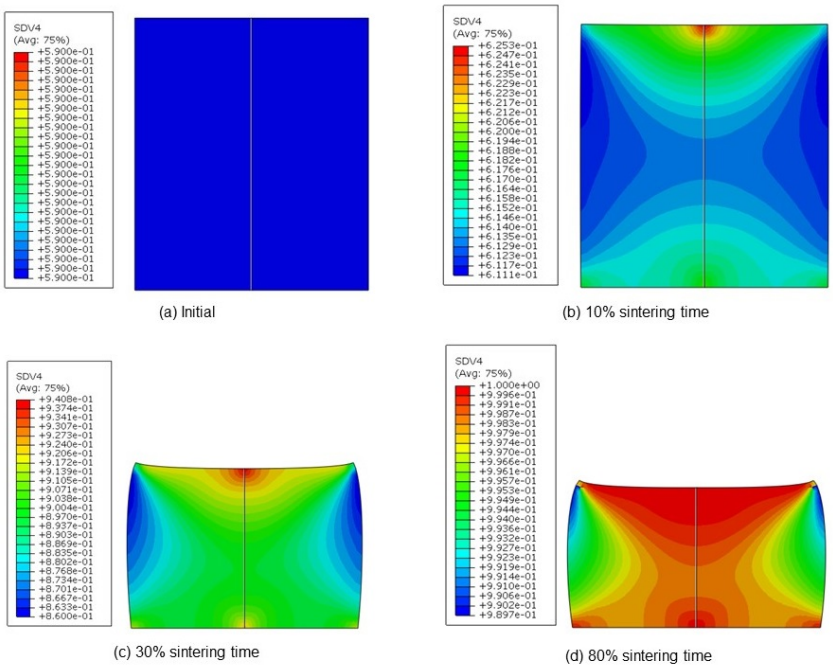

(a) Density distribution at different sintering time from Cox's model.

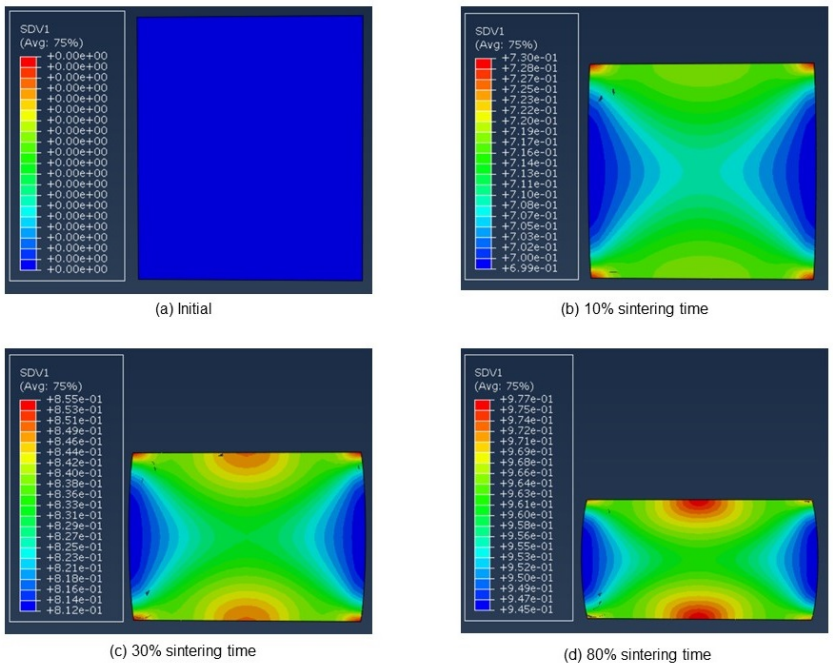

(b) Density distribution at different sintering time from the implemented model.

Figure 6.34 Result comparison with Cox's work [169] for the cylindrical sintering body.

The model has shown good agreement with previous literature work. However, the implementation for this model in actual practice for new materials requires significant experimental work to characterize the materials. The quantities for experimental data input and verification include bulk modulus K_p, shear modulus G_p, and sintering stress σ_s as a function of temperature. The implemented SOVS model utilizes K_p and σ_s to characterize the shrinkage behavior while the shear modulus dictates the distortion of the sintering body. For a new material, experimental sets required for the model includes beam bending test to produce K_p and G_p values and dialometer free sintering to obtain σ_s.

6.7 Conclusion

This chapter presents the sintering process for SS420 and Haynes 214 parts fabricated by the SEAM process. The effect of sintering temperature and addition of sintering aids on final part relative density of SS420 was charazterized using analysis of variance. Subsequently, an optimization matrix was designed and applied to determine optimal sintering conditions for SS420 parts to attain final part relative density of above 99.7% without geometrical distortion. For Haynes 214, part relative density was characterized with respect to holding time and temperature during supersolidus sintering. The transient deformation behavior of the sintered parts with respect to holding time and temperature was also captured, whose results were capitalized to develop a 2-step sintering technique to produce fully dense parts with complete shape retention. The development of a numerical sintering model, the Olevsky-Skorohod model, was studied and implemented in a finite element analysis software, which can be used to aid the prediction of part density evolution and deformation during the sintering process.

Author's note: *A portion of this chapter has been published in: H. X. Nguyen, H. Suen, B. Poudel, P. Kwon, and H. Chung, "Development of an innovative, high speed, large-scaled, and affordable metal additive manufacturing process," CIRP Annals, vol. 69, no. 1, pp. 177–180, Jan. 2020, doi: 10.1016/j.cirp.2020.04.069.*

CHAPTER 7

SELECTIVE LASER MELTING AND MECHANICAL PROPERTIES OF OXIDE DISPERSION STRENGTHENED HAYNES 214 ALLOY

7.1 Introduction

Selective laser melting (SLM), a prominent metal additive manufacturing method, with the capabilities to fabricate components without geometrical limitation and to process high performance metals, has drawn significant attention from industries such as aerospace, nuclear, high-energy physics, and power generation [170]. Heat exchangers, nuclear reactors, turbine engine blades, and other high temperature components have been successfully fabricated using SLM [171, 172]. The enormous design freedom offered by SLM, coupled with the ability to fabricate small features with excellent resolution, has made SLM the method of choice to fabricate complex parts for high temperature applications. Intricate and non-traditional structures, such as three-dimensional fins in heat exchangers [171] and cellular structures for catalytic reactors [173], which cannot be fabricated using conventional manufacturing techniques, can be produced using SLM to further enhance the performance of the components.

Many iron, nickel (Ni), and cobalt-based superalloys have been successfully processed using SLM for high-temperature applications [174, 175]. Notably, the processing of Ni-based superalloys has recently become a topic of special interest due to their excellent mechanical properties at elevated temperatures [174–177]. The formation of gamma prime (γ') precipitate in a gamma (γ) primary phase in combination with the presence of elements such as chromium (Cr) and aluminum (Al) in Ni-based superalloys provides good mechanical and structural stability at elevated temperature as well as excellent corrosion resistance against oxidation and carburization environments [178]. Moreover, the addition of fine oxide dispersed strengthening (ODS) particles, such as yttria (Y_2O_3), zirconia (ZrO_2), titanium oxide (Ti_2O_3), with high melting point and chemical stability into the base alloy can further benefit the mechanical strength by hindering the movement of dislocations

and grain boundaries during high temperature deformation as well as improving creep resistance. SLM has been successfully employed to process several ODS Ni-based superalloys. IN625 with 2% wt.% Y_2O_3 addition was successfully processed to relative density of above 99.5% [178]. 1 wt. % Y_2O_3 was mixed with Inconel 718 (IN718) alloy and processed under different laser energy densities [179]. Highly dense samples with relative density of 99.66% with improved hardness and strength were reported. Oxide addition improved the strength of ODS alloys especially at higher temperature (≈650 °C), with the ultimate tensile strength (UTS) reaching nearly 100 MPa higher than SLM built IN718 part. However, several issues remain while processing ODS alloys with SLM: smaller processing window, agglomeration of oxide nanoparticles and cracking. A study on the processing of IN625 ODS with SLM has demonstrated a wide and stable range of acceptable processing conditions for IN625 and a much narrower processing window for the ODS version [178]. ODS particle size and distribution as well as propensity for of crack formation also remain major limitations with ODS alloys [180]. Nanoparticles smaller than 40 nanometers (nm) are found to have the tendency to agglomerate and form clusters in order to reduce surface energy [181]. High oxide content can induce formation of large vertical cavity networks that prevent complete consolidation of the alloy [180]. The content of oxide nanoparticles must be optimized as lower oxide content results in difficulty to exhibit dispersion strengthening effects and higher oxide content deteriorate the consolidation of alloys and lead to severe agglomeration issues [179]. Nevertheless, when processed optimally, addition of ODS particles into the metal matrix can provide substantial benefits on the mechanical properties and performance of the base alloy under the high temperatures working conditions.

Haynes 214, a nickel-chromium based superalloy, has recently been explored at Michigan State University (MSU) for high-temperature applications due to its ability to form passivation layers of Cr_2O_3 and Al_2O_3 in corrosive environments as well as maintain high strength and structural integrity under high temperature working conditions [182]. Additionally, the introduction of Y_2O_3 ODS nanoparticles into the metal matrix allows for the potential of high-temperature operation up to 1100° C under supercritical CO2 (sCO_2) environments. A modular flat heat exchanger assembly

with closed channels and three-dimensionally shaped fins was designed (Fig. 7.1) to demonstrate the performance in these conditions with SLM-processed Haynes 214 and its ODS versions.

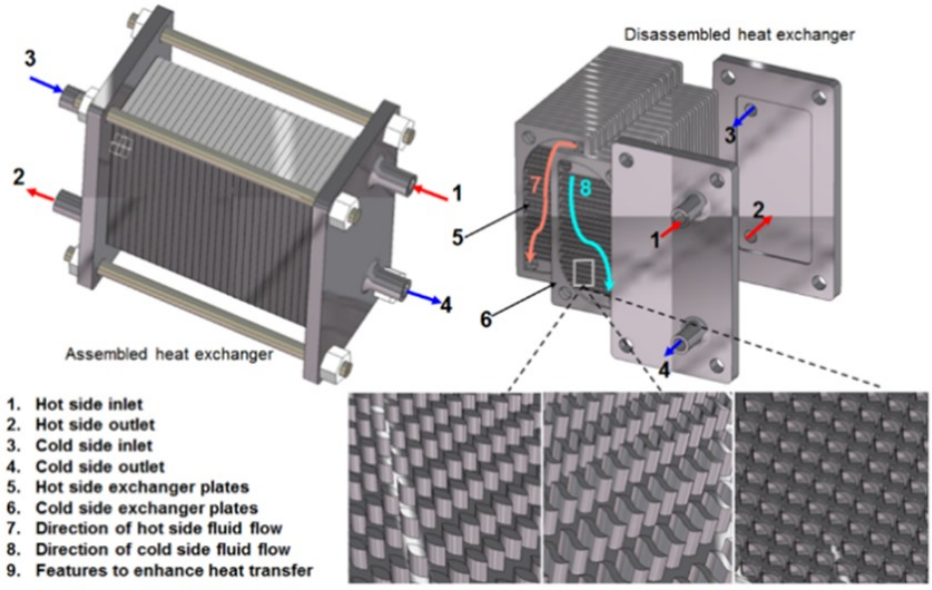

Figure 7.1 Heat exchanger assembly concept for operation at high temperature and sCO_2 environment.

This chapter presents the processing route for Haynes 214 and its ODS versions using SLM with the final objectives of attaining fully dense and crack-free final parts with fine dispersion of ODS nanoparticles and improved mechanical properties. First, the concept of processing condition matrix is introduced, which was designed and employed throughout the study to systematically identify the optimal processing parameters for Haynes 214 and the ODS versions with the addition of Y_2O_3 nanoparticle of 0.3 wt.% (denoted as ODS 1) and 1.5 wt.% (denoted as ODS 2). The relative density of the final part was used as the initial quality evaluation parameter for the optimization process. For the processing of ODS 1, the effect of laser energy density on the part relative density, as well as the dispersion of Y_2O_3 nanoparticles in the metal matrix with respect to feedstock preparation methods were examined. For the processing of ODS 2, the dispersion of Y_2O_3 nanoparticles was also evaluated, and the benefit of laser remelting on reducing cracking behavior was investigated. Thereafter, using the optimal processing parameters obtained for Haynes 214 and its ODS versions, a fabrication strategy was devised for the successful fabrication of high

temperature testing coupons to assess the mechanical properties at 1000 °C and 1100 °C. Finally, the impact of Y_2O_3 nanoparticles addition on the mechanical properties will be presented.

7.2 Materials and methods

The gas atomized powder material of Haynes 214 was provided by Oerlikon Metco (Plymouth, Michigan, USA) having size -45/+10 μm. The chemical composition of Haynes 214 can be found in the Appendix. The Y_2O_3 nanoparticles used in this study (US Research nanomaterials - Houston, Texas) are between 30-45 nm in diameter and of 99.99% purity. The SLM machine used here was the ProX DMP 200 SLM machine, manufactured by 3DSystems (Rock Hill, South Carolina, USA). The machine was equipped with a 270 W Nd:YAG fiber laser with a wavelength of 1067 nm. For all the experiments in this study, the oxygen level in the build chamber was kept below 1000 ppm during the fabrication process. The building substrate was made of stainless steel with dimensions of 14 cm x 14 cm x 2 cm.

For post-fabrication analysis, samples were separated from the build plates using wire electro-discharge machining (w-EDM) and their relative densities were measured using 2 methods: Archimedes and cross-sectional analysis. For the Archimedes method, the fluid medium used was isopropyl alcohol. For the cross-sectional analysis, samples were sectioned, mounted in phenolic thermosetting resin, ground, and polished on a surface polisher with the final polishing step using 60 nm colloidal silica. Images of the cross-sections were taken using a scanning electron microscope (SEM) operating on a field emission at 12kV (JEOL 6610LV - Tokyo, JAPAN). ImageJ software was used to determine the porosity from the cross-sectional image, and hence the relative density. Three images were taken to measure three relative densities on each sample, and the relative density of a sample was taken as the average of the three measurements. The chemical composition analysis was performed using an Energy Dispersive Spectra (EDS) detector (Oxford Instruments X-Max detector - Abingdon, UK) for a detailed chemical characterization on the selected location of the prepared surface on the fabricated samples.

Table 7.1 Initial processing condition matrix for SLM parameters optimization of Haynes 214 powder.

		Laser scan speed (mm/s)				
		2800	2350	1900	1450	1000
Laser power (W)	120	A1	B1	C1	D1	E1
	150	A2	B2	C2	D2	E2
	180	A3	B3	C3	D3	E3
	210	A4	B4	C4	D4	E4
	240	A5	B5	C5	D5	E5

7.2.1 The processing condition matrix

The selected parameters for the optimization of the fabrication process corresponding to all materials in this study are laser power (P) and laser scan speed (v), as they have been found to be the dominant factors in the processing of numerous metals using SLM [183]. The layer thickness (t) and hatch spacing (h) for all experiments in this study were fixed at 45 μm and 50 μm, respectively. Throughout this manuscript the volumetric energy density E is calculated by:

$$E = \frac{P}{v * h * t} \tag{7.1}$$

The technique carried out throughout this study to identify the optimal processing parameters is based on the processing condition matrix. Table 7.1 shows an example of the processing condition matrix. Each sample of A1-E5 was assigned to have a unique laser scan speed and laser power and, consequently, a unique laser energy density. 25 cylindrical coupons of 10 mm diameter and 20 mm height were fabricated according to the designed values (Fig. 7.2), and their relative density values were measured for sample quality evaluation. The relative density values of the samples can be mapped against laser volumetric energy density to capture their relationship, as well as to identify the optimal laser energy density level. The processing conditions matrix provides a systematic optimization approach to efficiently identify an appropriate combination of processing parameters and laser energy levels for new materials. The optimal processing conditions for Haynes 214 and

its ODS versions were determined using this technique.

7.3 Processing of Haynes 214

7.3.1 Experimental setup

The initial processing condition matrix for Haynes 214 was designed with the laser power varied from 120 W to 240 W while the laser scan speed varied from 1000 mm/s to 2800 mm/s (Table 7.1), which resulted in the lowest laser volumetric density on sample A1 and the highest on sample E5. Noticeably, the laser power and scan speed values were assigned on a relatively wide range due to the limited knowledge of the appropriate processing parameters of this particular material.
A second processing condition matrix was designed to have a narrower range of laser power and scan speed to further refine the processing parameters. The selected values were chosen based on the results obtained from the first processing condition matrix. The laser power was varied from 210 W to 250 W, and laser scan speed was varied from 1700 mm/s to 1900 mm/s.

7.3.2 Results and discussion

The results from the first processing condition matrix have shown that the C4 sample (210 W - 1900 mm/s) produced sample with the highest relative density of 99.1%, by the measurement using the Archimedes method. Cross-sectional analysis arrived at the same conclusion but at the relative density of 99.6% using ImageJ. C4 sample's parameter set was used as a baseline for the second processing condition matrix, i.e., it was set in the center of the second processing condition matrix. From the second processing conditions matrix, the highest relative densities achieved were 99.32% and 99.7% using Archimedes and ImageJ methods, respectively. The parameter set of 240 W laser power and 1800 mm/s scan speed is taken as the optimal processing condition for Haynes 214. SEM images of the best samples from each processing condition matrix show a significant reduction of porosity and defect in the optimal sample from the second matrix (Fig. 7.3). The optimal processing condition of Haynes 214 was also used as a baseline to optimize the processing condition for ODS 1.

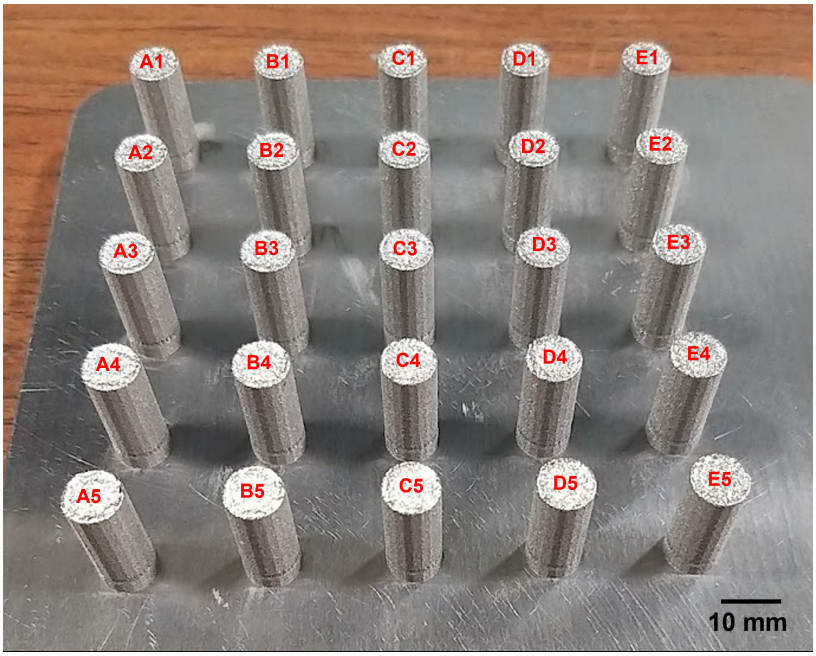

Figure 7.2 Fabricated Haynes 214 cylindrical coupons from the initial processing condition matrix.

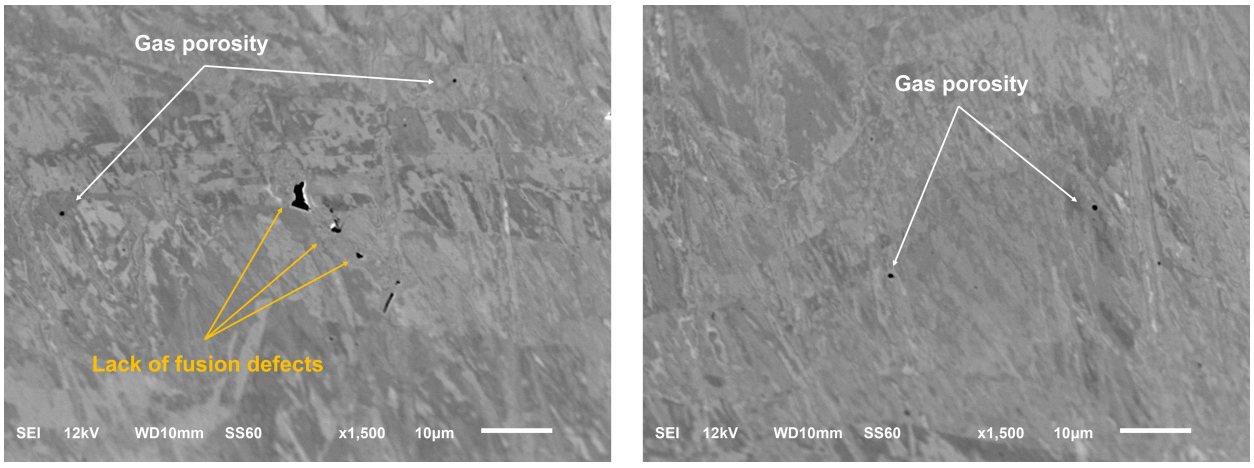

Figure 7.3 SEM images of best samples from the initial processing condition matrix (left) and second processing condition matrix (right).

7.4 Processing of Haynes 214 ODS 1

7.4.1 Experimental setup

Two different mixing methods were employed to disperse Y_2O_3 nanoparticles into the Haynes 214 powder: High-speed mixing and ball milling. For high-speed mixing, the process was carried out on a bench top high-speed mixer (FlackTek DAC 150.1 FVZ – SC, USA). The rotational speed was

set at 1500 rpm with a mixing time of 90 seconds. The ball milled feedstock was prepared in a planetary ball mill with zirconia media, working at 60 rpm rotational speed and mixing time of 40 hours.

With the dispersed Y_2O_3 nanoparticles, another 5x5 processing conditions matrix was designed with varied laser power from 210 W to 250 W and laser scan speed from 1200 mm/s to 2800 mm/s. 25 rectangular coupons with dimensions of 15 mm x 15 mm x 20 mm were successfully fabricated for each feedstock.

7.4.2 Results and discussion

7.4.2.1 Effect of laser energy density on part relative density

Figure 7.4 (left) shows the measured relative densities corresponding to different laser energy density levels for the ODS 1 samples fabricated using the ball-milled feedstock. The result indicated that as laser energy density increased, there was a general uptrend of part relative density up to a maximum threshold, followed by a gradual decline. This result agrees with numerous studies on SLM with various alloys [183, 184]. As laser melting mode transitioned from insufficient melting to conduction mode and eventually keyhole mode, part relative density peaks in the conduction mode zone, with minimal defects formed such as balling and keyhole porosity at low and high laser energy density, respectively. In comparison with previous research findings on SLM processing of IN625, another Ni-based superalloy, the behaviors of Haynes 214 ODS with respect to laser energy density input were similar. Both materials display a very small optimal processing window on laser energy input. This finding on Ni-based alloys in contrast with iron-based alloys, such as SS316 ODS, can be processed to full density with several laser energy densities [184].

The optimal laser power and laser scan speed for ODS 1 were determined to be 250 W and 1800 mm/s, respectively, which were used to produce the sample with a relative density of 99.65% with the powder feedstock prepared by ball milling.

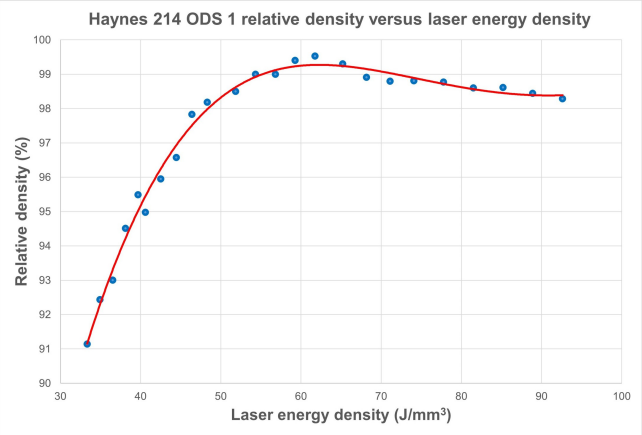

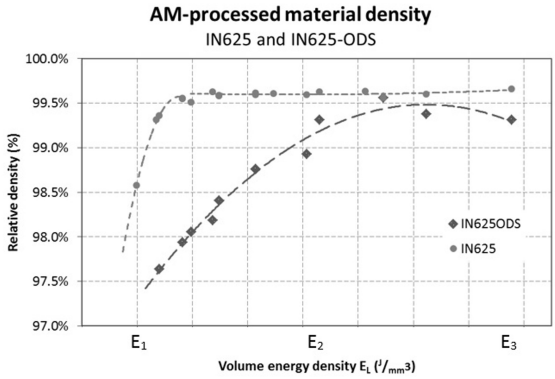

Figure 7.4 Relative density and laser energy density plots for Haynes 214 ODS 1 using ball-milled powder (left) and IN625 ODS (left).

7.4.2.2 Mixing method and nanoparticle dispersion in the feedstocks

Figure 7.5 shows the SEM images of the pure Haynes 214 powder and ODS 1 prepared by high-speed mixer and ball milling, respectively. The presence of Y_2O_3 nanoparticles is evident on the surface of the metal powder particles in the ODS versions. However, large clumps of Y_2O_3 nanoparticles of microns size were observed in ODS 1 prepared by a high-speed mixer. On the other hand, the ball-milled feedstock displayed a better distribution of Y_2O_3 nanoparticles with no significant clustering.

7.4.2.3 Yttria and aluminum agglomerations

SEM images and EDS analysis revealed the formation of Y_2O_3 and Al agglomerations (denoted Y_2O_3-Al) of up to 20 microns in size across the microstructure of ODS 1. They appear as bright white zones under the SEM where yttrium, oxygen, and aluminum are found in high concentrations (Fig. 7.6).

The agglomeration of ODS particles is a well-known problem in AM laser processes and has been studied extensively [185, 186]. Due to their extremely high melting temperature, the oxide particles generally experience insufficient energy for a complete melting during laser processing, which results in the particles floating on top of the melt pool [179]. This behavior coupled with the

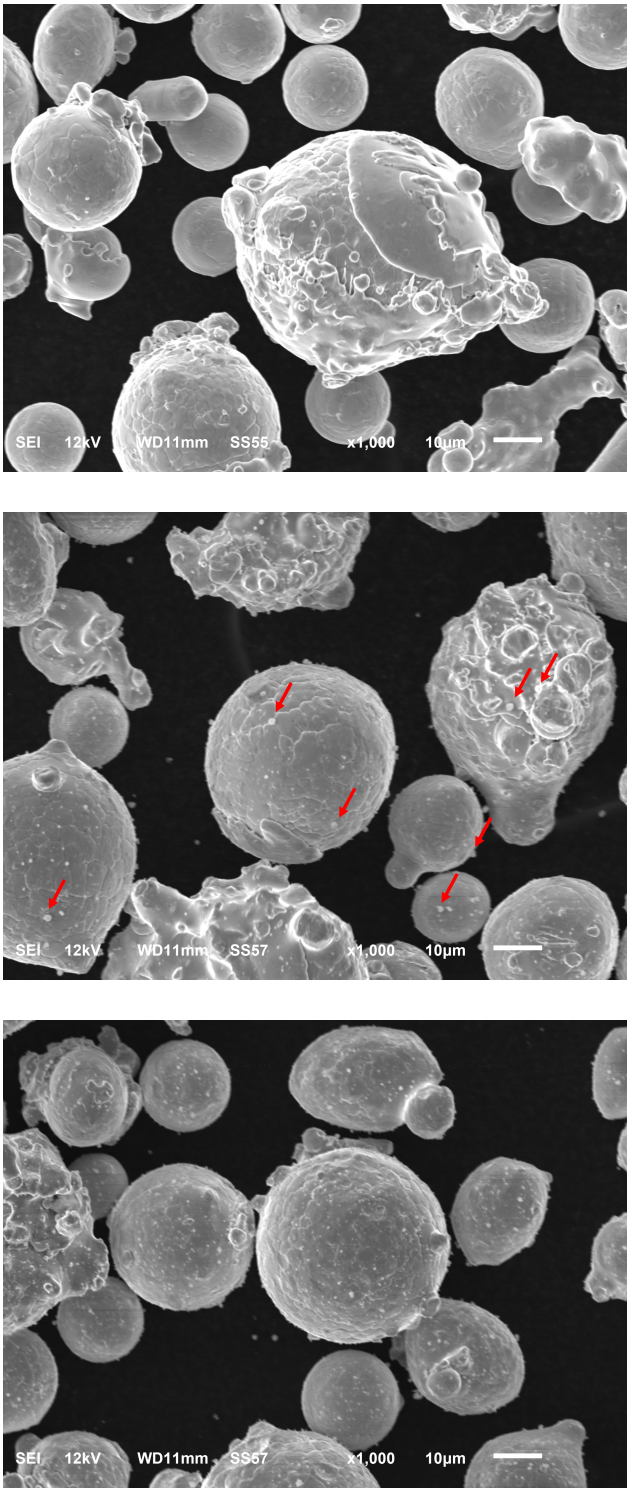

Figure 7.5 SEM images of Hanyes 214 powder (top) and Haynes 214 ODS 1 powder prepared by high-speed mixing (middle) and ball milling (bottom. The red arrows show the locations of large Yttria particle clusters.

Marangoni convection effect, which drives the un-melted particles to the edges of the laser beam, and ultimately to the end of the scan path, creating the agglomerations [187]. The agglomeration behavior further intensifies with a longer solidification time of the melt pool, which provides more time for the particles to form clusters [186].

7.4.2.4 Ball milling and improvement in Yttria dispersion on the smaller scale

High magnification SEM images revealed Y_2O_3 nanoparticles distribution in the metal matrix (Fig. 7.7). Clusters of micron size oxide particles can be observed in the sample fabricated using the high-speed mixing method. In contrast, a fine dispersion of Y_2O_3 particles in nanoscale was attained in the sample fabricated using ball-milled powder as shown in Fig. 7.7(b). The distribution of the oxide particles in the initial feedstock has been proven to be critical in their distribution and size in the subsequently fabricated samples.

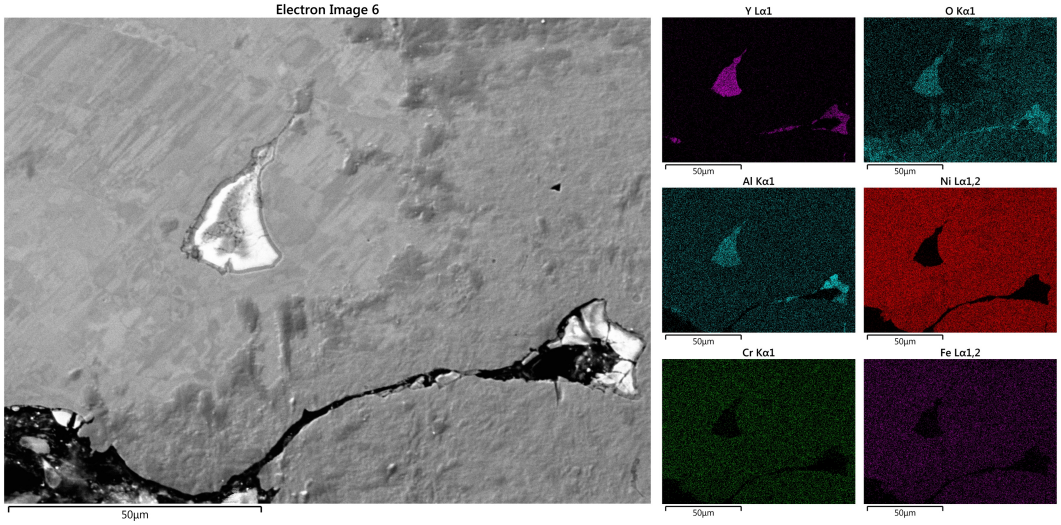

Figure 7.6 EDS mapping of Haynes 214 ODS 1 optimal sample showing yttria agglomeration site.

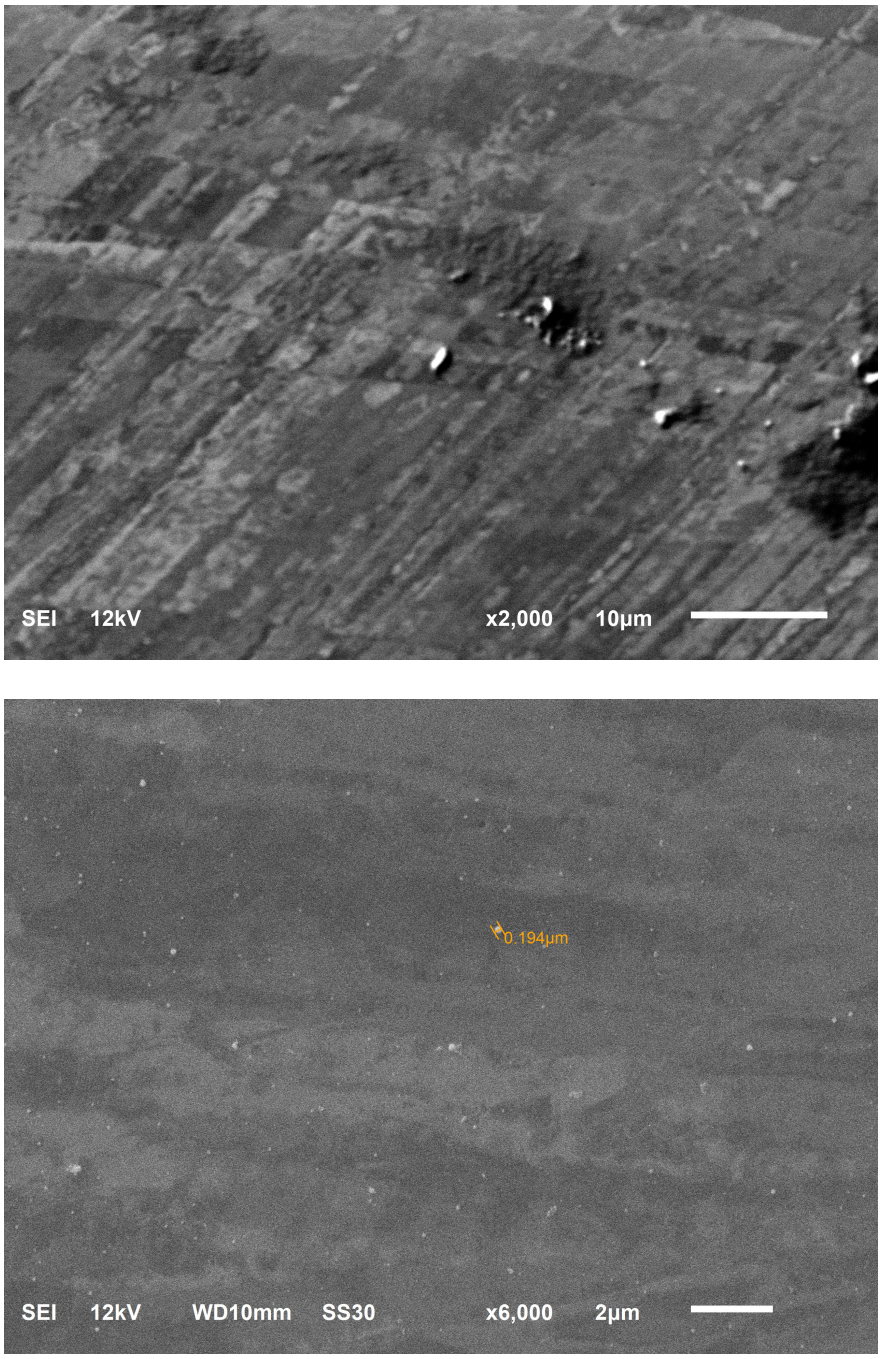

Figure 7.7 SEM images of the best samples fabricated by high-speed mixing (top) and ball milled (bottom) feedstocks, showing fine yttria distribution in the latter.

7.5 Processing of Haynes 214 ODS 2

7.5.1 Experimental setup

1.5 wt.% of Y_2O_3 nanoparticles were added to the initial Haynes 214 powder material. The feedstocks were prepared in the same manner as ODS 1, by high-speed mixing and ball milling.

A 5x5 processing condition matrix was designed with varied laser power from 200 W to 260 W and laser scan speed from 900 mm/s to 2500 mm/s. The values were selected using the optimal processing condition of ODS 1 as a baseline. 25 rectangular coupons with dimensions of 15 mm x 15 mm x 20 mm were successfully fabricated for each feedstock.

7.5.2 Results and discussion

7.5.2.1 Optimal processing parameters

The optimal processing conditions for ODS 2 was determined to be 230 W laser power and 900 mm/s laser scan speed using ball milled feedstock, which produced the sample with relative density of 98.76% and 99.42%, measured using Archimedes and cross-sectional analysis methods, respectively. Table 7.2 summarizes the optimal processing conditions for all feedstocks, with the corresponding laser energy density input. Notably, the ODS formulations, especially ODS 2, require much higher laser energy input for ODS to be fully consolidated [179], as the addition of oxide nanoparticles altered the metal particles surface morphology and the consolidation front of the alloy [187].

Table 7.2 Optimal processing conditions for Haynes 214 and its ODS version.

Feedstock	**Mixing method**	**Optimal processing conditions**	**Laser energy input**	**Relative density**
Haynes 214	As received	240 W - 1800 mm/s	59 J/mm^3	99.97%
Haynes 214 ODS 1	Ball milling	250 W - 1800 mm/s	62 J/mm^3	99.65%
Haynes 214 ODS 2	Ball milling	230 W - 900 mm/s	114 J/mm^3	98.62%

7.5.2.2 Y_2O_3-Al agglomeration in ODS 2

ODS 2 samples fabricated using both feedstocks experienced intense agglomeration of Y_2O_3-Al. Agglomeration sites with hundreds of microns in size can be found throughout the cross-sections, usually accompanied by open cavities (Fig. 7.8). Studies have found that Y_2O_3-Al agglomerations have the tendency to transport to and accumulate at the cooler melt pool edges, due to their lower

density and Marangoni convection driven by surface tension [187]. As the laser energy input increases, the size of the melt pool also increases, resulting in the greater formation of Y_2O_3-Al agglomerations per melt area, which ultimately accumulates and forms the large clusters at the edges of the melt zones. The significantly high laser energy input used for ODS 2, and the formation of large agglomeration sites directly support this finding.

On the smaller scale, SEM images in high magnification revealed a similar dispersion behavior to ODS 1 samples. Coarse and clustered Y_2O_3 particles were found in the sample fabricated using the high-speed mixing feedstock, while a fine dispersion was achieved in the sample produced with ball-milled powder (Fig. 7.9). Nanovoids were also observed at this magnification.

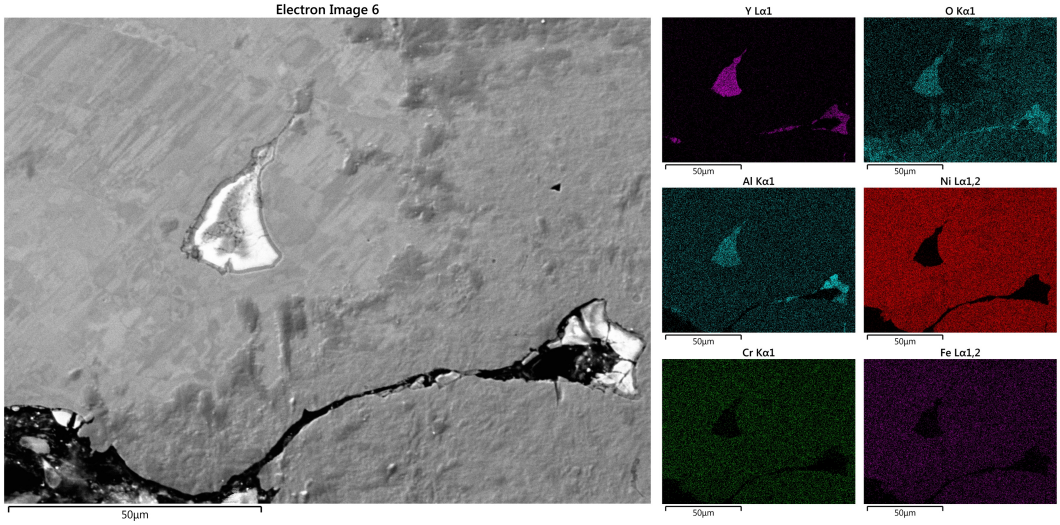

Figure 7.8 EDS mapping of a large yttria agglomeration zone in ODS 2.

7.5.2.3 Crack network formation

SEM images of the samples fabricated with both feedstocks displayed an extensive microcrack network formation. The observed crack networks propagated along the build direction, spanning over the depth of multiple layer thicknesses. A close examination of the cracks revealed that the crack cavities were embedded with Y_2O_3-Al agglomerations (Fig. 7.10). Several studies on processing ODS Ni alloys using SLM have reported similar behaviors [186, 187]. The thermal stress generated by the rapid solidification and cooling nature of the laser process, coupled with the

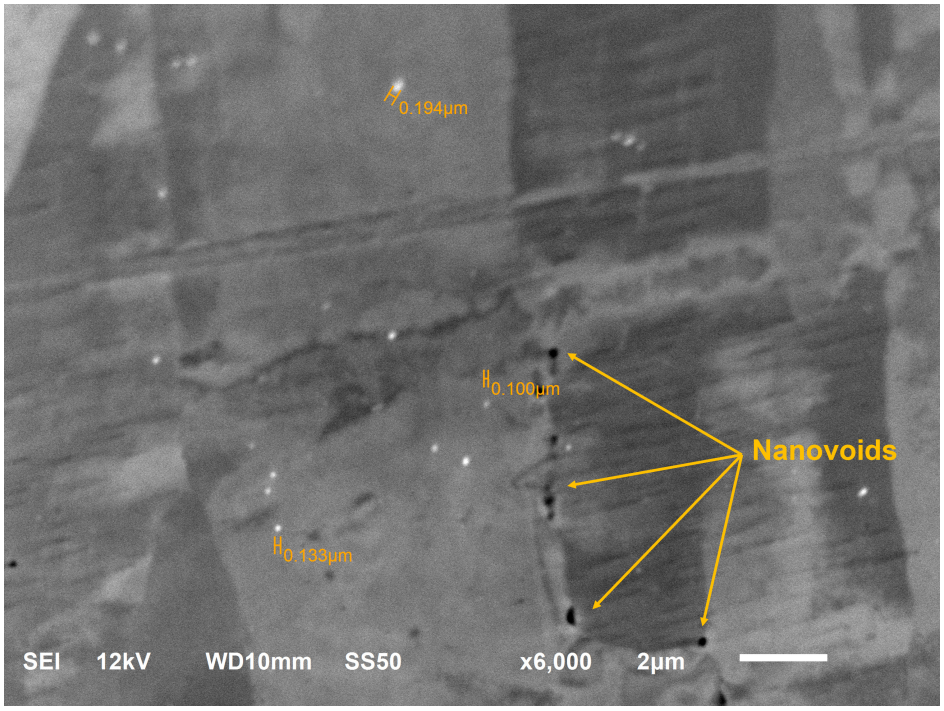

Figure 7.9 SEM image at high magnification of ODS 2 sample fabricated with ball milled powder showing fine yttria dispersion and nanovoids.

significant thermal conductivity difference between the metal matrix and the large oxide zones can lead to poor bonding and delamination of the Y_2O_3-Al agglomerations from the rest of the metallic structure. The brittle nature of oxides can also induce cracking of the Y_2O_3-Al agglomeration zone itself, which initiated the crack network formation. Moreover, the high laser energy input used in ODS 2 processing conditions can produce extremely large and deep melt pools, which induce the growth of high angle columnar grains across many layers [188]. The intense strain concentration at high-angle columnar grain boundary triple points, in combination with the decrease of grain boundary strength due to the presence of oxide particles agglomerations, can result in ductility-dip cracking, a common defect known to occur in welding of Ni-based superalloys [189, 190].

7.5.2.4 Laser remelting strategy and crack reduction

Several studies have demonstrated the benefits of laser remelting strategy on reducing cracking behavior of SLM processed parts, as discontinuous columnar grains can be refined and transformed into homogenous and equiaxed grains using this strategy [191, 192]. By applying multiple laser

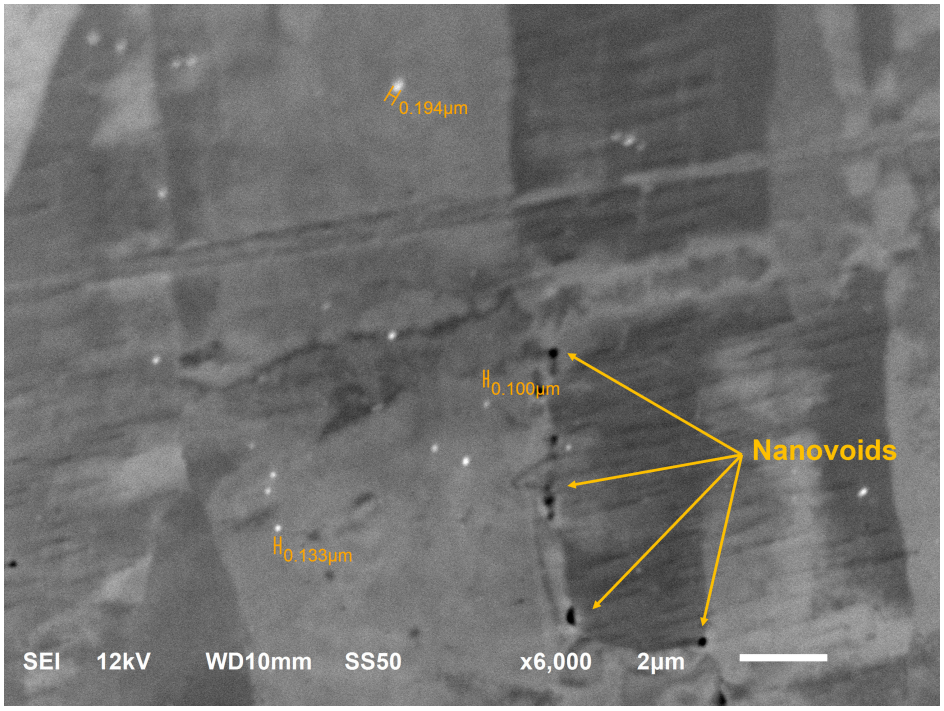

Figure 7.10 SEM image of ODS 2 sample fabricated with high-speed mixing powder showing vertical crack network accompanied by Y_2O_3-Al agglomerations.

scans on the same layer, reduction of columnar grains' aspect ratio as well as an increase in equiaxed grains fraction in the microstructure can be achieved. Fine equiaxed grains play a vital role in inhibiting cracking initiation and growth as these grains allow for easy grain rotation and deformation, resulting in significant strain accommodation and thermal stress relaxation [193].

The laser remelting strategy was carried out on ODS 2 powder prepared by ball milling, with the laser scan being applied twice for each layer using the obtained optimal processing conditions (230 W laser power, 900 mm/s laser scan speed). The fabricated sample's SEM images have shown that there was a significant reduction on the extent of the crack network propagation, as well as size of the crack lines (Fig. 7.11). However, cracking behavior had not been completely eliminated. The laser remelting strategy can be a viable option to produce crack free Haynes 214 ODS parts at a lower ODS particles weight addition. Additionally, in the sample fabricated with the feedstock prepared by high-speed mixing using the laser remelting strategy, fine distribution of yttria nanoparticles was observed (Fig. 7.12). It is possible that the second scan of the laser can break up the previously formed agglomerations and redistribute the oxide particles, resulting in dispersion improvement in

dispersion.

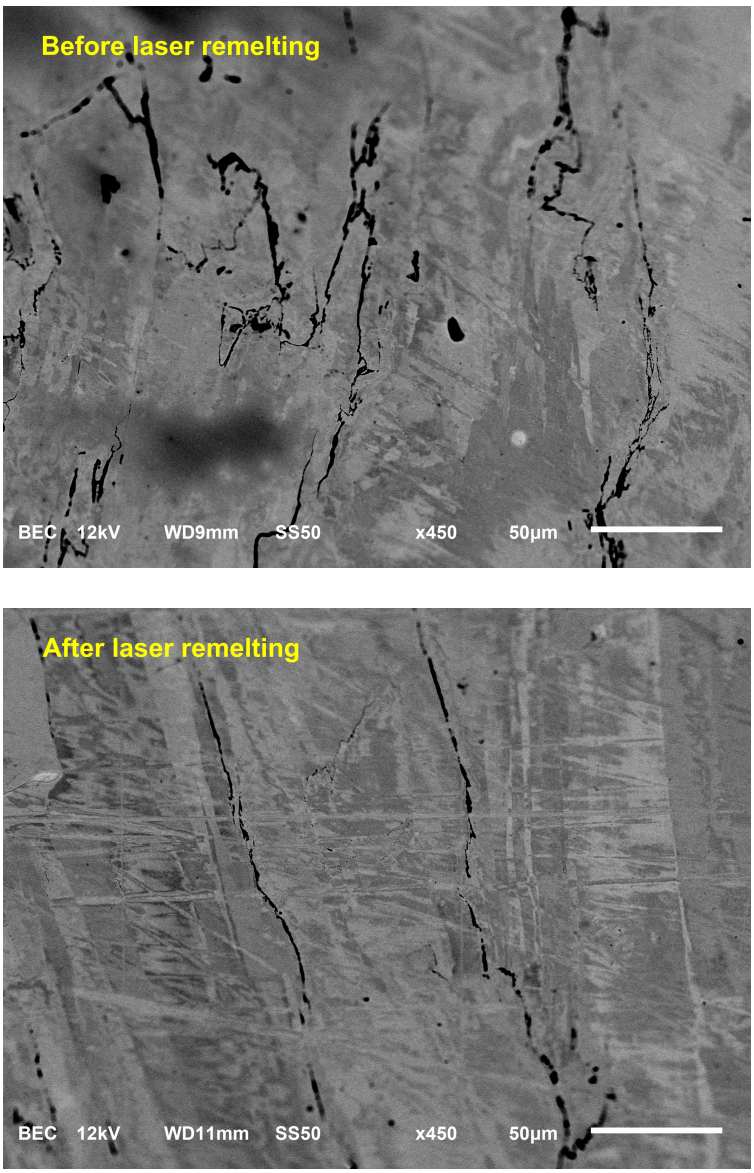

Figure 7.11 SEM images of Haynes 214 ODS 2 sample fabricated with high-speed mixing powder before laser remelting (top) and after laser remelting (bottom) showing a reduction in cracking behavior.

7.6 High temperature tensile coupons fabrication

According to ASTM E21, the dimensions of high-temperature testing coupons must be 120 mm x 10 mm x 2mm, with a 5 mm gage sections. Attempts were made to fabricate Haynes 214 rectangular blocks of 130 mm x 16 mm cross-section, which subsequently can be cut into high-

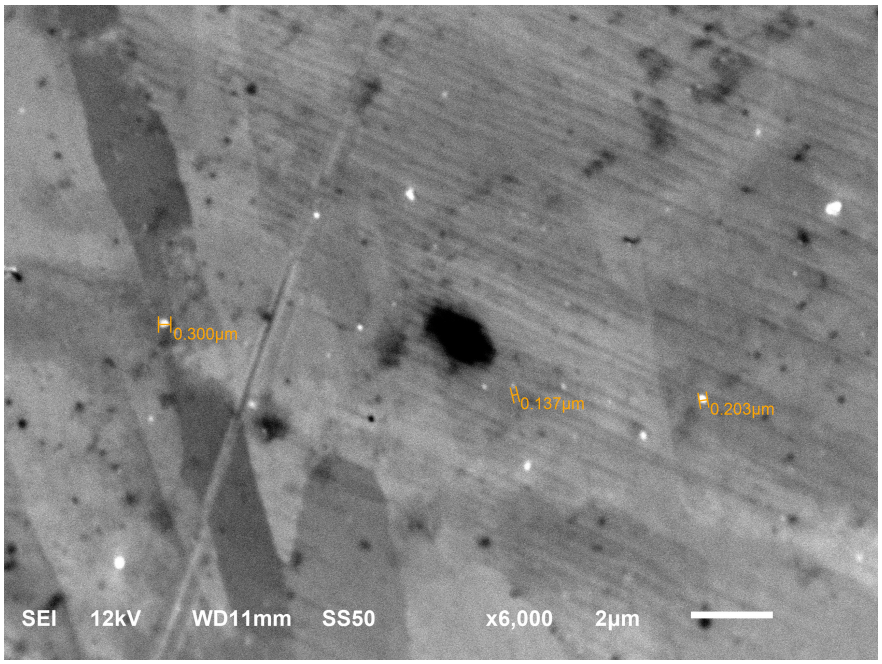

Figure 7.12 SEM image of ODS 2 sample fabricated with high-speed mixing powder and laser remelting showing good yttria nanoparticles distribution.

temperature tensile bars using w-EDM. However, severe spattering phenomena were observed during the fabrication process. Molten metal droplets were ejected from the melt pool, deposited onto the fabricated layer, forming metal balls of significant size and obstructing the motion of the machine's scraper, which lead to fabrication failure. In laser processing of metal, the spattering phenomenon is induced by an excessively high laser energy density, which is accompanied by an extremely high melt pool temperature [194]. When the melt pool temperature exceeds the evaporation temperature of the metal, the vapor-driven recoil pressure in combination with melt pool surface instability produced the ejected molten droplets [195]. The excessive melt temperature in the fabrication of the rectangular blocks can be attributed to the geometrical effects on surface temperature in laser processing. Thinner and smaller specimens such as the fabricated optimization blocks experience a higher cooling rate as most of their cross-section is free surface exposed to the loose powder [196]. In the large rectangular blocks, the conductive sidewalls are distant from the inner melt pool, resulting in a higher temperature in the middle of the layer. As the fabrication process proceeds, layer temperature gradually increased due to heat accumulation [197], and

eventually exceeds the evaporation temperature of the metal, causing spattering phenomena as discussed.

Therefore, it is critical to minimize the heat accumulation in the parts for a successful fabrication process. The large rectangular blocks were replaced with tensile bar-shaped blocks with cross-sectional of exact dimensions provided by ASTM E21, which resulted in over 40% reduction in surface area in comparison with the previous rectangular blocks. Tensile bar-shaped blocks of Haynes 214 and both of its ODS versions were successfully fabricated using this strategy (Fig. 7.13 (top)), and tensile coupons were produced using w-EDM for high-temperature testing.

Additionally, using Haynes 214 powder and the obtained optimal processing conditions, a real sized heat exchanger was successfully fabricated (Fig.7.13 (right)), which consists of 3 individual heat exchanger plates with closed and connected flow channels. Loose powders between the channels were removed by compressed air. The fabricated assembly performance under high temperature and sCO_2 is being evaluated and will be presented in a future study.

7.7 Mechanical testing

7.7.1 Experimental setup

High-temperature testing experiments were conducted using a high-temperature furnace and controller (Amteco - Cincinnati, Ohio). Samples elongation was measured with an extensometer (Epsilon - Jackson, Wyoming). The high-temperature grips were provided by MTS (Eden Prairie, Minnesota) with a maximum loading of 4kN.

7.7.2 Results and discussion

Figure 7.14 shows the tensile properties of Haynes 214 and ODS 1 at 1000 °C and 1100 °C. ODS 2 data could not be obtained due to the tensile bars experiencing premature failure during testing, caused by the existing defects of oxide agglomerations, voids, and microcracks as discussed. For ODS 1, the effect of Y_2O_3 nanoparticles addition in the base alloy on improving Young's modulus was evident at both testing temperatures. However, with regards to yield strength and

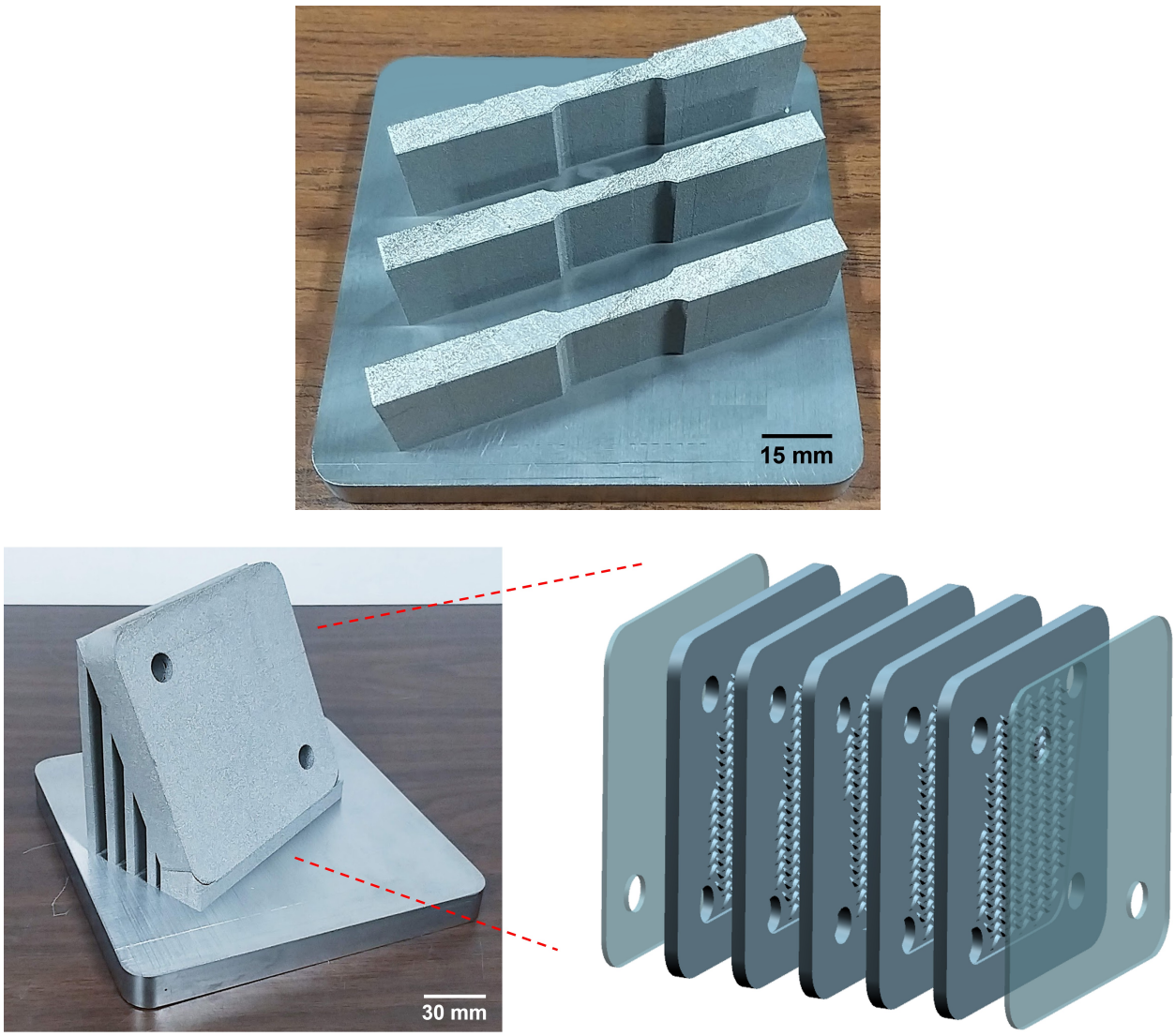

Figure 7.13 Fabricated tensile bar shaped blocks (left) and heat exchanger assembly (right).

UTS, the changes in the measured values were relative insignificant, indicating that the oxide strengthening effect has not been effectively realized at this level of Y_2O_3 inclusion. The topic of obtaining an appropriate level of ODS particles in the metal matrix to optimally improve the mechanical properties of the Hayes 214 base alloy while maintaining good processability of the powder mixture to produce parts with sufficient structural integrity will be a subject of study in the future.

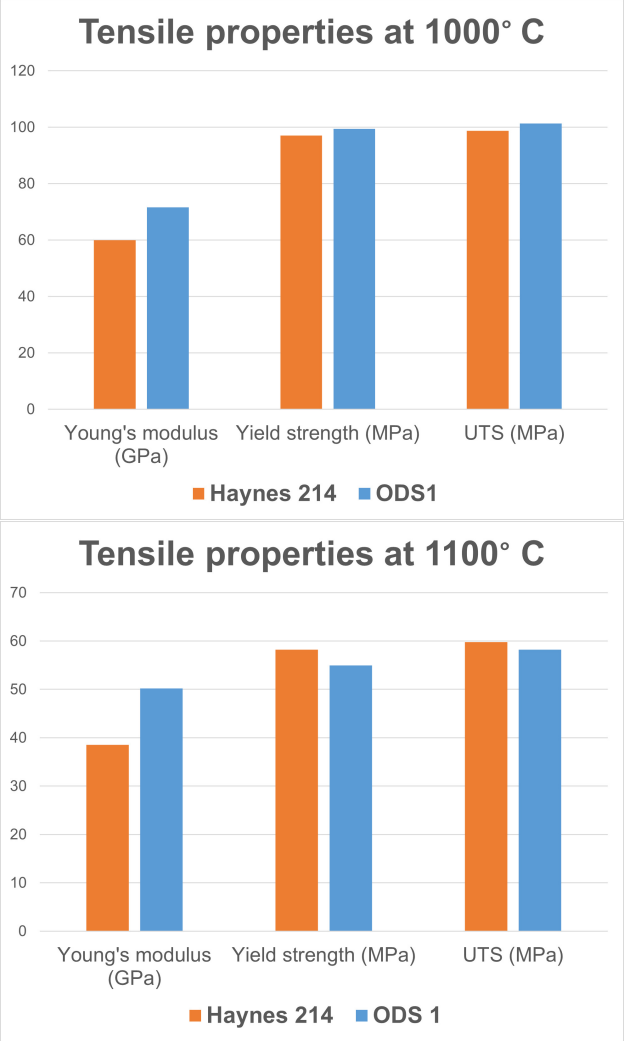

Figure 7.14 Mechanical testing results for Haynes 214 and ODS 1.

7.8 Conclusion

1. A systematic approach in identifying the optimal processing conditions was devised and carried out for all formulations of Haynes 214 and Haynes 214 ODS. This technique can be applied and refined for other materials.

2. Defect-free coupons of Haynes 214 and Haynes 214 + 0.3 wt. % of Y_2O_3 nanoparticle have been successfully fabricated using SLM. Haynes 214 + 1.5 wt. % of Y_2O_3 nanoparticle displayed a crack network formation as well as significant agglomerations of Y2O3 and Al. Both ODS formulations displayed a small processing window to obtain the parts with near

full density.

3. Initial feedstock preparation is proven crucial to disperse oxide nanoparticles in the metal matrix. Ball milling of the initial ODS feedstock improved the nanoparticle dispersion on a smaller scale. Fine nanoparticles of under 100 nm size were found evenly distributed in the SEM cross-sectional images.

4. Laser remelting refined the grain and significantly reduced the severity of crack network formation in the Haynes 214 + 1.5 wt.% formulation. However, cracking was not completely eliminated.

5. At 1.5 wt.% addition of Y_2O_3, tensile properties could not be obtained due to premature failure of the fabricated tensile bars during testing emanating from the agglomeration of nano oxide particles and formed crack network. At 0.3 wt. % of Y_2O_3, tensile coupons were produced, which exhibited good structural integrity and significant enhancement in Young's modulus. However, the oxide strengthening effect could not be effectively realized with respect to yield strength and UTS due to the low Y_2O_3 addition level. Future studies to determine the optimal Y2O3 addition level will be carried out to enhance the mechanical properties

CHAPTER 8

SUMMARY AND FUTURE WORK

This dissertation presents the development of the scalable and expeditious additive manufacturing (SEAM) process. After several proof-of-concepts, two fully functional prototypes were designed specifically for the processing of metal suspension, and subsequently constructed at Michigan State University. The relationships between cure depth and metal particle size for several metal suspensions were characterized, whose results were used to determine the appropriate processing conditions for each suspension. An innovative 2-step curing strategy was devised and applied to the printing process, which not only prevents sedimentation of metal powder particles in the print bed but also enables the fabrication of overhang geometry without supporting structures. Using the developed printing technique and processing parameters, 3D green objects were successfully fabricated for all the metallic alloys of interests. A series of experiments were subsequently carried out to characterize the thermal decomposition of the photopolymer, whose results were used to develop a debinding cycle that completely removes the binder while maintaining part structural integrity. The activated liquid phase sintering process of SS420 parts were optimized by utilizing analysis of variance, which arrived at an optimal sintering conditions that produce parts with above 99.7 % relative density without any geometrical distortion. For Haynes 214, the supersolidus sintering behavior was characterized with respect to sintering temperature and holding time. The transient deformation behavior of the sintered parts with respect to holding time and temperature was also captured, whose results were capitalized to develop a 2-step sintering technique to produce fully dense parts with complete shape retention. The development of a numerical sintering model, the Olevsky-Skorohod model, was studied and implemented in a finite element analysis software, which can be used to aid the prediction of part density evolution and deformation during the sintering process.

While significant progress has been made, the author believes that the development of SEAM process is still at its infancy stage. For further development towards an eventual industrial adop-

tion, many fundamental challenges must be resolved: segregation of metal suspension, undesirable composition change during debinding, and precision and tolerance of the sintered parts.

It is also the author's belief that future development of the SEAM process will head heavily towards material development, specifically the development of new polymer and additive system specifically suitable for metal suspension processing. The current 2-step curing technique to prevent material segregation while effective, is still more or less a temporary solution, which were not able to address the underlying problem. Formulation of a binder system capable of not only enhancing the curing behavior of the suspension but also prevent metal powder sedimentation will open up doors to a commercially successful printing system, with removal of the mixing and dispensing module to create an even more compact, simpler, and affordable machine design.

A clean binder removal process without chemical composition change of the metal powder is just as critical. Access to hydrogen furnaces can greatly simplify the debinding process, in most cases. Copper has no affinity towards carbon and can be feasibly processed in hydrogen environment, with possibly a debinding and sintering process combined into a single heating cycle. On the contrary, it remains a challenge to completely remove carbon residue from iron-based materials even with a full hydrogen environment due to their high diffusivity in each other. Nevertheless, it is of great interest to seek a binder system compatible with the metal material, not only for the green part fabrication process but also the debinding step. It is also very possible that there will never be an optimal polymer system, a one-solution-fit-all, but rather each metal powder material will require a polymer with compatible properties. A simple example is aluminum alloys' sintering point is typically between 300-500 °C, which would require the polymer removal process to occur below that temperature range. On the other hand, higher melting point materials have more flexibility in terms of the burnout temperature. In all cases, retaining the purity of the metal powder through the debinding process should be of utmost priority.

The sintering process remains an insurmountable challenge for SEAM process. The emphasis on density and distortion control in this dissertation is well-aligned with industrial interests. Densification is directly linked to mechanical performances, and precise dimensional control is a critical

requirement for any industrial applications. While analytical models provide a possible solution to predict part deformation, the optimization process can take an extensive amount of time to fine-tune. Recent development in machine learning and AI poses an exciting alternative solution to the problem, though it appears to be more suitable to be utilized by the industry, due to the huge number of data point needed to effectively train any accurate prediction models.

Despite these challenges, the author remains optimistic and excited about the future development of the SEAM process. The efficient layer generation technique, simplicity in system design, excellent green part resolution, and high production readiness are unrivaled qualities that cannot be matched by any other currently available metal AM technology. If the SEAM process can be developed into a practical metal AM technology, it will be the breakthrough that metal AM field has not seen in decades.

APPENDICES

APPENDIX A

CHEMICAL COMPOSITION OF METAL POWDERS

Table A.1 Nominal chemical composition of stainless steel 420.

Stainless steel 420							
Element	**Fe**	**Cr**	**C**	**Mn**	**Si**	**P**	**S**
Weight %	Bal.	12.0 - 14.0	<0.15	<1	<1	<0.04	<0.03

Table A.2 Nominal chemical composition of stainless steel 316.

Stainless steel 316								
Element	**Fe**	**Ni**	**Mo**	**Cr**	**S**	**P**	**Si**	**C**
Weight %	Bal.	16 -13.0	2.0 - 2.5	16.5 - 18.5	<0.02	<0.05	<1.0	<0.07

Table A.3 Nominal chemical composition of Haynes 214.

Haynes 214											
Element	**Ni**	**Cr**	**Al**	**Fe**	**Co**	**Mn**	**Mo**	**Ti**	**W**	**Nb**	**C**
Weight %	Bal.	16	4.5	3	<2	<0.5	<0.5	<0.5	<0.5	<0.15	<0.04

Table A.4 Nominal chemical composition of Amdry 386.

Amdry 386						
Element	**Ni**	**Co**	**Cr**	**Al**	**Y**	**Hf**
Weight %	Bal.	19.0 - 26.0	14.0 - 21.0	11.0 - 14.0	0.2 - 0.8	0.1 - 0.5

APPENDIX B

SEAM FIRST-GENERATION PROTOYPE SPECIFICATIONS

Table B.1 Pressure slurry dispenser specifications.

Pressure slurry dispenser - 5-RPD-D1B	
Dimension	200 x 100 x 100 mm
Nominal operating pressure	70 - 100 psi
Maximum mixing speed	100 rpm

Table B.2 3DLP9000 specifications.

Curing module - 3DLP9000	
Working distance	320 - 530 mm
Projection width	192 - 320 mm
Resolution	2560 x 1600
Power output	3.25 W
LED wavelength	405 nm
Pixel size at image plane	100 μm
Distortion	0.1%
Uniformity	90%

Table B.3 SEAM first-generation prototype printing platform specifications.

Printing platform	
Dimension	125 x 125 mm
Minimum travel distance	50 μm
Maximum z height	50 mm μm

Table B.4 ETH032 high-force screw drive cylinder specifications.

High-force screw drive cylinder - ETH032	
Drive axis type	Screw
Maximum load	3700 N
Maxmium stroke length	1000 mm
Repeatability	30 μm
Maximum travel speed	1 m/sec

APPENDIX C

SEAM SECOND-GENERATION PROTOYPE SPECIFICATIONS

Table C.1 Laboratory mixer - L5M-A specifications.

Laboratory mixer - L5M-A	
Dimensions	37 x 12 x 20 inches
Capacity	Up to 12 liters
Motor	750W, 220 volt, 8000 rpm maximum speed
Stirrer material	SS316

Table C.2 Ball screw FSI-195-9702.

Ball screw FSI-195-9702	
Nominal diameter	25 mm
Lead	10 mm
Dynamic load capacity	13.2 kN
Static load capacity	25.4 kN
Travel length	350 mm

Table C.3 Servo motor NTE-212-CONS specifications.

Servo motor NTE-212-CONS	
Peak torque	2.54 Nm
Torque constant	0.58 Nm/A
Rated power	0.432 kW
Shaft diameter	9.5 mm

Table C.4 Servo motor NTE-320-CONS specifications.

Servo motor NTE-320-CONS	
Peak torque	6.67 Nm
Torque constant	0.806 Nm/A
Rated power	1.668 kW
Shaft diameter	12.7 mm

APPENDIX D

PYTHON CODE: OPTIMAL POWDER MIXTURE CALCULATION

```
import matplotlib
import numpy as np
import math
import sys
import random

def powder_packing(beta,d,r):
    import numpy as np
    import ternary

    beta = np.array(beta)
    Gamma_i = []
    y_sol  = []
    Sum1 = 0
    Sum2 = 0
    d = np.array(d)*10E-6
    n = len(d)
    s = 1
    resolution = 1/r
    vol_frac = np.arange(0,1+resolution,resolution)

    for y1 in vol_frac:
        y2 = 1-y1
```

```
        y = [y1, y2]
        Gamma_i_temp = []
        for i in range(n):
            Sum1 = 0
            Sum2 = 0
            for j in range(0,i):
                b = 1-(1-d[i]/d[j])**1.5
                Sum1 += (1 - beta[i]+b*beta[i]*(1-1/beta[j]))*y[j]
            for j in range(i+1,n):
                a = (1-(1-d[j]/d[i])**1.02)**0.5
                Sum2 += (1 - a*beta[i]/beta[j])*y[j]

        Gamma_i_temp.append(beta[i]/(1 - Sum1 - Sum2))
        Gamma_i.append(min(Gamma_i_temp))
        y_sol.append([y1, y2,min(Gamma_i_temp)])
    return np.array(y_sol[np.argmax(Gamma_i)]),np.array(y_sol)

beta = [0.59735, 0.60277]
d = [30, 14]
r = 10000
y = powder_packing(beta,d,r)
y_sol_max = y[0]
y_sol = y[1]

y_sol_max
```

BIBLIOGRAPHY

BIBLIOGRAPHY

[1] T. Pereira, J. V. Kennedy, and J. Potgieter, "A comparison of traditional manufacturing vs additive manufacturing, the best method for the job," *Procedia Manufacturing*, vol. 30, pp. 11–18, Jan. 2019.

[2] J. J. Beaman, D. L. Bourell, C. C. Seepersad, and D. Kovar, "Additive Manufacturing Review: Early Past to Current Practice," *Journal of Manufacturing Science and Engineering*, vol. 142, Sept. 2020.

[3] G. Da Silveira, D. Borenstein, and F. S. Fogliatto, "Mass customization: Literature review and research directions," *International Journal of Production Economics*, vol. 72, pp. 1–13, June 2001.

[4] M. M. Tseng, J. Jiao, and M. E. Merchant, "Design for Mass Customization," *CIRP Annals*, vol. 45, pp. 153–156, Jan. 1996.

[5] W. Gao, Y. Zhang, D. Ramanujan, K. Ramani, Y. Chen, C. B. Williams, C. C. L. Wang, Y. C. Shin, S. Zhang, and P. D. Zavattieri, "The status, challenges, and future of additive manufacturing in engineering," *Computer-Aided Design*, vol. 69, pp. 65–89, Dec. 2015.

[6] M. Ziaee and N. B. Crane, "Binder jetting: A review of process, materials, and methods," *Additive Manufacturing*, vol. 28, pp. 781–801, Aug. 2019.

[7] A. Mostafaei, A. M. Elliott, J. E. Barnes, F. Li, W. Tan, C. L. Cramer, P. Nandwana, and M. Chmielus, "Binder jet 3D printing—Process parameters, materials, properties, modeling, and challenges," *Progress in Materials Science*, vol. 119, p. 100707, June 2021.

[8] F. Dini, S. A. Ghaffari, J. Jafar, R. Hamidreza, and S. Marjan, "A review of binder jet process parameters; powder, binder, printing and sintering condition," *Metal Powder Report*, vol. 75, pp. 95–100, Mar. 2020. Publisher: Elsevier.

[9] S. A. Skoog, P. L. Goering, and R. J. Narayan, "Stereolithography in tissue engineering," *Journal of Materials Science: Materials in Medicine*, vol. 25, pp. 845–856, Mar. 2014.

[10] J. Huang, Q. Qin, and J. Wang, "A Review of Stereolithography: Processes and Systems," *Processes*, vol. 8, p. 1138, Sept. 2020. Number: 9 Publisher: Multidisciplinary Digital Publishing Institute.

[11] F. P. W. Melchels, J. Feijen, and D. W. Grijpma, "A review on stereolithography and its applications in biomedical engineering," *Biomaterials*, vol. 31, pp. 6121–6130, Aug. 2010.

[12] S.-H. Park, D.-Y. Yang, and K.-S. Lee, "Two-photon stereolithography for realizing ultraprecise three-dimensional nano/microdevices," *Laser & Photonics Reviews*, vol. 3, no. 1-2, pp. 1–11, 2009. _eprint: https://onlinelibrary.wiley.com/doi/pdf/10.1002/lpor.200810027.

[13] C. Y. Yap, C. K. Chua, Z. L. Dong, Z. H. Liu, D. Q. Zhang, L. E. Loh, and S. L. Sing, "Review of selective laser melting: Materials and applications," *Applied Physics Reviews*, vol. 2, p. 041101, Dec. 2015. Publisher: American Institute of Physics.

[14] S. Li, J. Yang, and Z. Wang, "Multi-laser powder bed fusion of Ti-6.5Al-2Zr-Mo-V alloy powder: Defect formation mechanism and microstructural evolution," *Powder Technology*, vol. 384, pp. 100–111, May 2021.

[15] S. Chen, F. Tao, C. Jia, and J. Yang, "Status and Progress of Selective Laser Melting Forming Technology," pp. 1295–1298, Atlantis Press, Nov. 2015. ISSN: 2352-538X.

[16] S. Liu, H. Zhu, G. Peng, J. Yin, and X. Zeng, "Microstructure prediction of selective laser melting AlSi10Mg using finite element analysis," *Materials & Design*, vol. 142, pp. 319–328, Mar. 2018.

[17] J.-P. Kruth, J. Deckers, E. Yasa, and R. Wauthlé, "Assessing and comparing influencing factors of residual stresses in selective laser melting using a novel analysis method," *Proceedings of the Institution of Mechanical Engineers, Part B: Journal of Engineering Manufacture*, vol. 226, pp. 980–991, June 2012. Publisher: IMECHE.

[18] R. M. German, P. Suri, and S. J. Park, "Review: liquid phase sintering," *Journal of Materials Science*, vol. 44, pp. 1–39, Jan. 2009.

[19] B. Vasudevarao, D. P. Natarajan, and M. Henderson, "Sensitivity of Rp Surface Finish to Process Parameter Variation," *undefined*, 2000.

[20] "ISO/ASTM 52900:2015(en), Additive manufacturing — General principles — Terminology."

[21] T. J. Horn and O. L. A. Harrysson, "Overview of Current Additive Manufacturing Technologies and Selected Applications," *Science Progress*, vol. 95, pp. 255–282, Sept. 2012. Publisher: SAGE Publications Ltd.

[22] C. Achillas, D. Tzetzis, and M. O. Raimondo, "Alternative production strategies based on the comparison of additive and traditional manufacturing technologies," *International Journal of Production Research*, vol. 55, pp. 3497–3509, June 2017. Publisher: Taylor & Francis _eprint: https://doi.org/10.1080/00207543.2017.1282645.

[23] B. Westerweel, R. J. I. Basten, and G.-J. van Houtum, "Traditional or Additive Manufacturing? Assessing Component Design Options through Lifecycle Cost Analysis," *European Journal of Operational Research*, vol. 270, pp. 570–585, Oct. 2018.

[24] L. E. Murr, S. M. Gaytan, E. Martinez, F. Medina, and R. B. Wicker, "Next Generation Orthopaedic Implants by Additive Manufacturing Using Electron Beam Melting," *International Journal of Biomaterials*, vol. 2012, p. e245727, Aug. 2012. Publisher: Hindawi.

[25] G. Costabile, M. Fera, F. Fruggiero, A. Lambiase, and D. Pham, "Cost models of additive manufacturing: A literature review," *International Journal of Industrial Engineering Computations*, vol. 8, no. 2, pp. 263–283, 2017.

[26] M. Attaran, "The rise of 3-D printing: The advantages of additive manufacturing over traditional manufacturing," *Business Horizons*, vol. 60, pp. 677–688, Sept. 2017.

[27] B. P. Conner, G. P. Manogharan, A. N. Martof, L. M. Rodomsky, C. M. Rodomsky, D. C. Jordan, and J. W. Limperos, "Making sense of 3-D printing: Creating a map of additive manufacturing products and services," *Additive Manufacturing*, vol. 1-4, pp. 64–76, Oct. 2014.

[28] "Five Questions to Shape a Winning 3-D Printing Strategy," July 2015. Section: Brief.

[29] "3D printing trend report."

[30] N. Tuncer and A. Bose, "Solid-State Metal Additive Manufacturing: A Review," *JOM*, vol. 72, pp. 3090–3111, Sept. 2020.

[31] M. Vaezi, P. Drescher, and H. Seitz, "Beamless Metal Additive Manufacturing," *Materials*, vol. 13, p. 922, Jan. 2020. Number: 4 Publisher: Multidisciplinary Digital Publishing Institute.

[32] M. Rombouts, J. P. Kruth, L. Froyen, and P. Mercelis, "Fundamentals of Selective Laser Melting of alloyed steel powders," *CIRP Annals*, vol. 55, pp. 187–192, Jan. 2006.

[33] K. A. Mumtaz, P. Erasenthiran, and N. Hopkinson, "High density selective laser melting of Waspaloy®," *Journal of Materials Processing Technology*, vol. 195, pp. 77–87, Jan. 2008.

[34] D. Buchbinder, H. Schleifenbaum, S. Heidrich, W. Meiners, and J. Bültmann, "High Power Selective Laser Melting (HP SLM) of Aluminum Parts," *Physics Procedia*, vol. 12, pp. 271–278, Jan. 2011.

[35] L. Thijs, F. Verhaeghe, T. Craeghs, J. V. Humbeeck, and J.-P. Kruth, "A study of the microstructural evolution during selective laser melting of Ti–6Al–4V," *Acta Materialia*, vol. 58, pp. 3303–3312, May 2010.

[36] X. Zhao, S. Li, M. Zhang, Y. Liu, T. B. Sercombe, S. Wang, Y. Hao, R. Yang, and L. E. Murr, "Comparison of the microstructures and mechanical properties of Ti–6Al–4V fabricated by selective laser melting and electron beam melting," *Materials & Design*, vol. 95, pp. 21–31, Apr. 2016.

[37] B. Song, X. Zhao, S. Li, C. Han, Q. Wei, S. Wen, J. Liu, and Y. Shi, "Differences in microstructure and properties between selective laser melting and traditional manufacturing for fabrication of metal parts: A review," *Frontiers of Mechanical Engineering*, vol. 10, pp. 111–125, June 2015.

[38] B. Zhang, Y. Li, and Q. Bai, "Defect Formation Mechanisms in Selective Laser Melting: A Review," *Chinese Journal of Mechanical Engineering*, vol. 30, pp. 515–527, May 2017. Number: 3 Publisher: SpringerOpen.

[39] A. Bauereiß, T. Scharowsky, and C. Körner, "Defect generation and propagation mechanism during additive manufacturing by selective beam melting," *Journal of Materials Processing Technology*, vol. 214, pp. 2522–2528, Nov. 2014.

[40] Y. J. Liu, S. J. Li, H. L. Wang, W. T. Hou, Y. L. Hao, R. Yang, T. B. Sercombe, and L. C. Zhang, "Microstructure, defects and mechanical behavior of beta-type titanium porous structures manufactured by electron beam melting and selective laser melting," *Acta Materialia*, vol. 113, pp. 56–67, July 2016.

[41] J. Gardan, "Additive manufacturing technologies: state of the art and trends," *International Journal of Production Research*, vol. 54, pp. 3118–3132, May 2016. Publisher: Taylor & Francis _eprint: https://doi.org/10.1080/00207543.2015.1115909.

[42] M. Yakout, M. A. Elbestawi, and S. C. Veldhuis, "A Review of Metal Additive Manufacturing Technologies," *Solid State Phenomena*, vol. 278, pp. 1–14, 2018. Conference Name: Manufacturing Engineering and Process VII ISBN: 9783035713701 Publisher: Trans Tech Publications Ltd.

[43] G. B. Kannan and D. K. Rajendran, "A Review on Status of Research in Metal Additive Manufacturing," in *Advances in 3D Printing & Additive Manufacturing Technologies* (D. I. Wimpenny, P. M. Pandey, and L. J. Kumar, eds.), pp. 95–100, Singapore: Springer, 2017.

[44] J. H. Martin, B. D. Yahata, J. M. Hundley, J. A. Mayer, T. A. Schaedler, and T. M. Pollock, "3D printing of high-strength aluminium alloys," *Nature*, vol. 549, pp. 365–369, Sept. 2017. Number: 7672 Publisher: Nature Publishing Group.

[45] W. Li, K. Yang, S. Yin, X. Yang, Y. Xu, and R. Lupoi, "Solid-state additive manufacturing and repairing by cold spraying: A review," *Journal of Materials Science & Technology*, vol. 34, pp. 440–457, Mar. 2018.

[46] S. Mirzababaei and S. Pasebani, "A Review on Binder Jet Additive Manufacturing of 316L Stainless Steel," *Journal of Manufacturing and Materials Processing*, vol. 3, p. 82, Sept. 2019.

[47] A. Lauder, M. J. Cima, E. Sachs, and T. Fan, "Three Dimensional Printing: Surface Finish and Microstructure of Rapid Prototyped Components," *MRS Online Proceedings Library (OPL)*, vol. 249, 1991. Publisher: Cambridge University Press.

[48] Y. L. Yap, C. Wang, S. L. Sing, V. Dikshit, W. Y. Yeong, and J. Wei, "Material jetting additive manufacturing: An experimental study using designed metrological benchmarks," *Precision Engineering*, vol. 50, pp. 275–285, Oct. 2017.

[49] J. Dilag, T. Chen, S. Li, and S. A. Bateman, "Design and direct additive manufacturing of three-dimensional surface micro-structures using material jetting technologies," *Additive Manufacturing*, vol. 27, pp. 167–174, May 2019.

[50] S.-I. Park, D. W. Rosen, S.-k. Choi, and C. E. Duty, "Effective mechanical properties of lattice material fabricated by material extrusion additive manufacturing," *Additive Manufacturing*, vol. 1-4, pp. 12–23, Oct. 2014.

[51] J. E. Seppala, S. H. Han, K. E. Hillgartner, C. S. Davis, and K. B. Migler, "Weld formation during material extrusion additive manufacturing," *Soft Matter*, vol. 13, pp. 6761–6769, Oct. 2017. Publisher: The Royal Society of Chemistry.

[52] A. R. Torrado, C. M. Shemelya, J. D. English, Y. Lin, R. B. Wicker, and D. A. Roberson, "Characterizing the effect of additives to ABS on the mechanical property anisotropy of specimens fabricated by material extrusion 3D printing," *Additive Manufacturing*, vol. 6, pp. 16–29, Apr. 2015.

[53] P. Nandwana, A. M. Elliott, D. Siddel, A. Merriman, W. H. Peter, and S. S. Babu, "Powder bed binder jet 3D printing of Inconel 718: Densification, microstructural evolution and challenges," *Current Opinion in Solid State and Materials Science*, vol. 21, pp. 207–218, Aug. 2017.

[54] A. Mostafaei, E. L. Stevens, E. T. Hughes, S. D. Biery, C. Hilla, and M. Chmielus, "Powder bed binder jet printed alloy 625: Densification, microstructure and mechanical properties," *Materials & Design*, vol. 108, pp. 126–135, Oct. 2016.

[55] T. Do, P. Kwon, and C. S. Shin, "Process development toward full-density stainless steel parts with binder jetting printing," *International Journal of Machine Tools and Manufacture*, vol. 121, pp. 50–60, Oct. 2017.

[56] T. Do, T. J. Bauder, H. Suen, K. Rego, J. Yeom, and P. Kwon, "Additively Manufactured Full-Density Stainless Steel 316L With Binder Jet Printing," American Society of Mechanical Engineers Digital Collection, Sept. 2018.

[57] H. Z. Yu, M. E. Jones, G. W. Brady, R. J. Griffiths, D. Garcia, H. A. Rauch, C. D. Cox, and N. Hardwick, "Non-beam-based metal additive manufacturing enabled by additive friction stir deposition," *Scripta Materialia*, vol. 153, pp. 122–130, Aug. 2018.

[58] A. Hehr and M. Norfolk, "A comprehensive review of ultrasonic additive manufacturing," *Rapid Prototyping Journal*, vol. 26, pp. 445–458, Jan. 2019. Publisher: Emerald Publishing Limited.

[59] M. R. Sriraman, S. S. Babu, and M. Short, "Bonding characteristics during very high power ultrasonic additive manufacturing of copper," *Scripta Materialia*, vol. 62, pp. 560–563, Apr. 2010.

[60] T. A. Rodrigues, V. Duarte, R. M. Miranda, T. G. Santos, and J. P. Oliveira, "Current Status and Perspectives on Wire and Arc Additive Manufacturing (WAAM)," *Materials*, vol. 12, p. 1121, Jan. 2019. Number: 7 Publisher: Multidisciplinary Digital Publishing Institute.

[61] S. Yin, P. Cavaliere, B. Aldwell, R. Jenkins, H. Liao, W. Li, and R. Lupoi, "Cold spray additive manufacturing and repair: Fundamentals and applications," *Additive Manufacturing*, vol. 21, pp. 628–650, May 2018.

[62] S. Pathak and G. C. Saha, "Development of Sustainable Cold Spray Coatings and 3D Additive Manufacturing Components for Repair/Manufacturing Applications: A Critical Review," *Coatings*, vol. 7, p. 122, Aug. 2017. Number: 8 Publisher: Multidisciplinary Digital Publishing Institute.

[63] M. Dressler, T. Studnitzky, and B. Kieback, "Additive manufacturing using 3D screen printing," in *2017 International Conference on Electromagnetics in Advanced Applications (ICEAA)*, pp. 476–478, Sept. 2017.

[64] C. L. Cramer, N. R. Wieber, T. G. Aguirre, R. A. Lowden, and A. M. Elliott, "Shape retention and infiltration height in complex WC-Co parts made via binder jet of WC with subsequent Co melt infiltration," *Additive Manufacturing*, vol. 29, p. 100828, Oct. 2019.

[65] C. L. Cramer, T. G. Aguirre, N. R. Wieber, R. A. Lowden, A. A. Trofimov, H. Wang, J. Yan, M. P. Paranthaman, and A. M. Elliott, "Binder jet printed WC infiltrated with pre-made melt of WC and Co," *International Journal of Refractory Metals and Hard Materials*, vol. 87, p. 105137, Feb. 2020.

[66] J. W. Lee, I. H. Lee, and D.-W. Cho, "Development of micro-stereolithography technology using metal powder," *Microelectronic Engineering*, vol. 83, pp. 1253–1256, Apr. 2006.

[67] P. J. Bartolo and J. Gaspar, "Metal filled resin for stereolithography metal part," *CIRP Annals*, vol. 57, pp. 235–238, Jan. 2008.

[68] S. Corbel, O. Dufaud, and T. Roques-Carmes, "Materials for Stereolithography," in *Stereolithography: Materials, Processes and Applications* (P. J. Bártolo, ed.), pp. 141–159, Boston, MA: Springer US, 2011.

[69] S. Zakeri, M. Vippola, and E. Levänen, "A comprehensive review of the photopolymerization of ceramic resins used in stereolithography," *Additive Manufacturing*, vol. 35, p. 101177, Oct. 2020.

[70] C.-J. Bae, A. Ramachandran, K. Chung, and S. Park, "Ceramic Stereolithography: Additive Manufacturing for 3D Complex Ceramic Structures," *Journal of the Korean Ceramic Society*, vol. 54, no. 6, pp. 470–477, 2017. Publisher: The Korean Ceramic Society.

[71] W. Zhou, D. Li, and H. Wang, "A novel aqueous ceramic suspension for ceramic stereolithography," *Rapid Prototyping Journal*, vol. 16, pp. 29–35, Jan. 2010. Publisher: Emerald Group Publishing Limited.

[72] M. L. Griffith and J. W. Halloran, "Freeform Fabrication of Ceramics via Stereolithography," *Journal of the American Ceramic Society*, vol. 79, no. 10, pp. 2601–2608, 1996. _eprint: https://onlinelibrary.wiley.com/doi/pdf/10.1111/j.1151-2916.1996.tb09022.x.

[73] Z. Chen, D. Li, W. Zhou, and L. Wang, "Curing characteristics of ceramic stereolithography for an aqueous-based silica suspension," *Proceedings of the Institution of Mechanical Engineers, Part B: Journal of Engineering Manufacture*, vol. 224, pp. 641–651, Apr. 2010. Publisher: IMECHE.

[74] S. Banerjee and C. Joens, "Debinding and sintering of metal injection molding (MIM) components," pp. 133–180, Dec. 2012.

[75] R. M. German and A. Bose, *Injection Molding of Metals and Ceramics*. Metal Powder Industries Federation, 1997. Google-Books-ID: jXINAAAACAAJ.

[76] M. Trunec and J. Cihlář, "Thermal debinding of injection moulded ceramics," *Journal of the European Ceramic Society*, vol. 17, pp. 203–209, Jan. 1997.

[77] D.-F. Lii, J.-L. Huang, C.-H. Lin, and H.-H. Lu, "The effects of atmosphere on the thermal debinding of injection moulded Si3N4 components," *Ceramics International*, vol. 24, pp. 99–104, Jan. 1998.

[78] Z. Lu, K. Zhang, and C. Wang, "Research on thermal debinding of powder injection moulded SiC parts in air atmosphere," *Materials Research Innovations*, vol. 15, pp. s263–s265, Feb. 2011. Publisher: Taylor & Francis _eprint: https://doi.org/10.1179/143307511X12858957673879.

[79] B.-S. Kim, E. Kim, H.-S. Jeon, H.-I. Lee, and J.-c. Lee, "Study on the Reduction of Molybdenum Dioxide by Hydrogen," *Materials Transactions - MATER TRANS*, vol. 49, pp. 2147–2152, Sept. 2008.

[80] J. Wendel, S. Manchili, E. Hryha, and L. Nyborg, "Reduction of surface oxide layers on water-atomized iron and steel powder in hydrogen: Effect of alloying elements and initial powder state," *Thermochimica Acta*, vol. 692, p. 178731, Aug. 2020.

[81] M. V. C. Sastri, R. P. Viswanath, and B. Viswanathan, "Studies on the reduction of iron oxide with hydrogen," *International Journal of Hydrogen Energy*, vol. 7, pp. 951–955, Jan. 1982.

[82] J. Dang, K.-C. Chou, X.-J. Hu, and G.-H. Zhang, "Reduction Kinetics of Metal Oxides by Hydrogen," *steel research international*, vol. 84, no. 6, pp. 526–533, 2013. _eprint: https://onlinelibrary.wiley.com/doi/pdf/10.1002/srin.201200242.

[83] D. F. Heaney, "8 - Vacuum sintering," in *Sintering of Advanced Materials* (Z. Z. Fang, ed.), Woodhead Publishing Series in Metals and Surface Engineering, pp. 189–221, Woodhead Publishing, Jan. 2010.

[84] Z. A. Munir, "Surface Oxides and Sintering of Metals," *Powder Metallurgy*, vol. 24, pp. 177–180, Jan. 1981. Publisher: Taylor & Francis _eprint: https://doi.org/10.1179/pom.1981.24.4.177.

[85] X. Ye, Y. Li, Y. Ai, and Y. Nie, "Novel powder packing theory with bimodal particle size distribution-application in superalloy," *Advanced Powder Technology*, vol. 29, pp. 2280–2287, Sept. 2018.

[86] R. German, "Prediction of sintered density for bimodal powder mixtures," 1992.

[87] J. W. Oh, S. K. Ryu, W. S. Lee, and S. J. Park, "Analysis of compaction and sintering behavior of 316L stainless steel nano/micro bimodal powder," *Powder Technology*, vol. 322, pp. 1–8, Dec. 2017.

[88] C. W. Corti, "Sintering Aids in Powder Metallurgy," *Platinum Metals Review*, vol. 30, pp. 184–195, Aug. 1986.

[89] P. E. Zovas, R. M. German, K. S. Hwang, and C. J. Li, "Activated and Liquid-Phase Sintering—Progress and Problems," *JOM*, vol. 35, pp. 28–33, Jan. 1983.

[90] M. Maneshian and A. Simchi, "Solid state and liquid phase sintering of mechanically activated W–20wt.% Cu powder mixture," *Journal of Alloys and Compounds*, vol. 463, pp. 153–159, Sept. 2008.

[91] J. Johnson, "Activated Liquid Phase Sintering of W-Cu and Mo-Cu," *International Journal of Refractory Metals and Hard Materials*, vol. 53, Apr. 2015.

[92] M. Braginsky, V. Tikare, and E. Olevsky, "Numerical simulation of solid state sintering," *International Journal of Solids and Structures*, vol. 42, pp. 621–636, Jan. 2005.

[93] T. Kraft and H. Riedel, "Numerical simulation of solid state sintering; model and application," *Journal of the European Ceramic Society*, vol. 24, pp. 345–361, Jan. 2004.

[94] G. C. Kuczynski, "Self-Diffusion in Sintering of Metallic Particles," in *Sintering Key Papers* (S. Sōmiya and Y. Moriyoshi, eds.), pp. 509–527, Dordrecht: Springer Netherlands, 1990.

[95] R. L. Coble, "Sintering Crystalline Solids. I. Intermediate and Final State Diffusion Models," *Journal of Applied Physics*, vol. 32, pp. 787–792, May 1961. Publisher: American Institute of Physics.

[96] W. D. Kingery and M. Berg, "Study of the Initial Stages of Sintering Solids by Viscous Flow, Evaporation-Condensation, and Self-Diffusion," *Journal of Applied Physics*, vol. 26, pp. 1205–1212, Oct. 1955. Publisher: American Institute of Physics.

[97] V. A. Ivensen, "Phenomenological Theory of Sintering," in *Densification of Metal Powders During Sintering* (V. A. Ivensen, ed.), Studies in Soviet Science, pp. 135–165, New York, NY: Springer US, 1973.

[98] "Sintering Theory and Practice | Wiley."

[99] D. L. Johnson, "New Method of Obtaining Volume, Grain-Boundary, and Surface Diffusion Coefficients from Sintering Data," *Journal of Applied Physics*, vol. 40, pp. 192–200, Jan. 1969. Publisher: American Institute of Physics.

[100] W. D. Kingery, "Densification during Sintering in the Presence of a Liquid Phase. I. Theory," *Journal of Applied Physics*, vol. 30, pp. 301–306, Mar. 1959. Publisher: American Institute of Physics.

[101] P. Raj, A. Odulena, and W. Cannon, "Anisotropic shrinkage during sintering of particle-oriented systems—numerical simulation and experimental studies," 2002.

[102] M. Reiterer, T. Kraft, and H. Riedel, "Manufacturing of a gear wheel made from reaction bonded alumina—numerical simulation of the sinterforming process," *Journal of the European Ceramic Society*, vol. 24, pp. 239–246, Jan. 2004.

[103] M. Ashraf, I. Gibson, and M. G. Rashed, "CHALLENGES AND PROSPECTS OF 3D PRINTING IN STRUCTURAL ENGINEERING," Jan. 2018.

[104] Q. Ge, Z. Li, Z. Wang, K. Kowsari, W. Zhang, X. He, J. Zhou, and N. X. Fang, "Projection micro stereolithography based 3D printing and its applications," *International Journal of Extreme Manufacturing*, vol. 2, p. 022004, June 2020. Publisher: IOP Publishing.

[105] S. Deshmane, P. Kendre, H. Mahajan, and S. Jain, "Stereolithography 3D printing technology in pharmaceuticals: a review," *Drug Development and Industrial Pharmacy*, vol. 47, pp. 1362–1372, Sept. 2021. Publisher: Taylor & Francis _eprint: https://doi.org/10.1080/03639045.2021.1994990.

[106] P. Y. Cheng and H. K. Schachman, "Studies on the validity of the Einstein viscosity law and Stokes' law of sedimentation," *Journal of Polymer Science*, vol. 16, no. 81, pp. 19–30, 1955. _eprint: https://onlinelibrary.wiley.com/doi/pdf/10.1002/pol.1955.120168102.

[107] D.-K. Yang and S.-T. Wu, *Fundamentals of Liquid Crystal Devices*. John Wiley & Sons, Dec. 2014. Google-Books-ID: W53mBQAAQBAJ.

[108] "What is Liquid Crystal Display (LCD)? Definition, Construction, Working and Applications of LCD," Jan. 2019.

[109] A. Stefan, "Liquid Crystal Displays," May 1995.

[110] A. Muravsky, A. Murauski, X. Li, V. Chigrinov, and H. Kwok, "Optical rewritable liquid-crystal-alignment technology," *Journal of The Society for Information Display - J SOC INF DISP*, vol. 15, Apr. 2007.

[111] H. Quan, T. Zhang, H. Xu, S. Luo, J. Nie, and X. Zhu, "Photo-curing 3d printing technique and its challenges," vol. 5, no. 1, pp. 110–115.

[112] T. Z. Kosc, A. A. Kozlov, S. Papernov, K. R. P. Kafka, K. L. Marshall, and S. G. Demos, "Investigation of parameters governing damage resistance of nematic liquid crystals for high-power or peak-intensity laser applications," *Scientific Reports*, vol. 9, p. 16435, Nov. 2019. Number: 1 Publisher: Nature Publishing Group.

[113] M. A. Quijada, A. Travinsky, D. Vorobiev, Z. Ninkov, A. Raisanen, M. Robberto, and S. Heap, "Optical evaluation of digital micromirror devices (DMDs) with UV-grade fused silica, sapphire, and magnesium fluoride windows and long-term reflectance of bare devices," vol. 9912, p. 99125V, July 2016. Conference Name: Advances in Optical and Mechanical Technologies for Telescopes and Instrumentation II ADS Bibcode: 2016SPIE.9912E..5VQ.

[114] "FSQ-KG5 Heat Absorbing Glass Filter."

[115] H. Ryoo, D. W. Kang, and J. W. Hahn, "Analysis of the effective reflectance of digital micromirror devices and process parameters for maskless photolithography," *Microelectronic Engineering*, vol. 88, pp. 235–239, Mar. 2011.

[116] J. Alvarez and J. Richuso, "Application report getting started with ti dlp® display technology," *Scientific Reports*, Mar. 2020.

[117] "What to Look for in a DLP Projector - ViewSonic Library."

[118] DrTune, "English: Color wheel from a DLP projector. Wheel has 6 segments," Apr. 2018.

[119] J. Huang, Y. Wang, and C.-C. Kuo, "Spectral Multiplex 3D Cinema Projector," May 2013.

[120] B. K. Suryatal, S. S. Sarawade, and S. P. Deshmukh, "Fabrication of medium scale 3D components using stereolithography system for rapid prototyping," *Journal of King Saud University - Engineering Sciences*, Feb. 2021.

[121] I. Cohen, Z. Dubinsky, and J. Erez, "Light Enhanced Calcification in Hermatypic Corals: New Insights from Light Spectral Responses," *Frontiers in Marine Science*, vol. 2, 2016.

[122] M. Kaur and A. K. Srivastava, "Photopolymerization: A Review," *Journal of Macromolecular Science, Part C*, vol. 42, pp. 481–512, Jan. 2002. Publisher: Taylor & Francis _eprint: https://doi.org/10.1081/MC-120015988.

[123] A. Bagheri and J. Jin, "Photopolymerization in 3D Printing," *ACS Applied Polymer Materials*, vol. 1, pp. 593–611, Apr. 2019. Publisher: American Chemical Society.

[124] A. B. Scranton, A. C. Society, C. N. Bowman, A. C. S. Meeting, and A. C. S. Staff, *Photopolymerization: Fundamentals and Applications*. American Chemical Society, 1997. Google-Books-ID: MRnwAAAAMAAJ.

[125] M. L. Griffith, T. M. Chu, W. Wagner, and J. W. Halloran, "Ceramic Stereolithography for Investment Casting and Biomedical Applications," 1995. Accepted: 2018-10-03T19:55:01Z.

[126] V. Tomeckova and J. W. Halloran, "Cure depth for photopolymerization of ceramic suspensions," *Journal of the European Ceramic Society*, vol. 30, pp. 3023–3033, Nov. 2010.

[127] W. Du, X. Ren, Y. Chen, C. Ma, M. Radovic, and Z. Pei, "Model Guided Mixing of Ceramic Powders With Graded Particle Sizes in Binder Jetting Additive Manufacturing," American Society of Mechanical Engineers Digital Collection, Sept. 2018.

[128] S. Banerjee and C. J. Joens, "7 - Debinding and sintering of metal injection molding (MIM) components," in *Handbook of Metal Injection Molding (Second Edition)* (D. F. Heaney, ed.), Woodhead Publishing Series in Metals and Surface Engineering, pp. 129–171, Woodhead Publishing, Jan. 2019.

[129] G. Singh, J.-M. Missiaen, D. Bouvard, and J.-M. Chaix, "Additive manufacturing of 17–4 PH steel using metal injection molding feedstock: Analysis of 3D extrusion printing, debinding and sintering," *Additive Manufacturing*, vol. 47, p. 102287, Nov. 2021.

[130] M. A. Omar, R. Ibrahim, M. I. Sidik, M. Mustapha, and M. Mohamad, "Rapid debinding of 316L stainless steel injection moulded component," *Journal of Materials Processing Technology*, vol. 140, pp. 397–400, Sept. 2003.

[131] M. F. F. A. Hamidi, W. S. W. Harun, N. Z. Khalil, S. A. C. Ghani, and M. Z. Azir, "Study of solvent debinding parameters for metal injection moulded 316L stainless steel," *IOP Conference Series: Materials Science and Engineering*, vol. 257, p. 012035, Oct. 2017. Publisher: IOP Publishing.

[132] M. I. H. Chua, A. Sulong, M. F. Abdullah, and N. Muhamad, "Optimization of injection molding and solvent debinding parameters of stainless steel powder (SS316L) based feedstock for metal injection molding," *undefined*, 2013.

[133] T. Barriere, B. Liu, and J. C. Gelin, "Determination of the optimal process parameters in metal injection molding from experiments and numerical modeling," *Journal of Materials Processing Technology*, vol. 143-144, pp. 636–644, Dec. 2003.

[134] B. Levenfeld, A. Várez, and J. M. Torralba, "Effect of residual carbon on the sintering process of M2 high speed steel parts obtained by a modified metal injection molding process," *Metallurgical and Materials Transactions A*, vol. 33, pp. 1843–1851, June 2002.

[135] M. Jeandin, J. L. Koutny, and Y. Bienvenu, "Liquid Phase Sintering of Nickel Base Superalloys," *Powder Metallurgy*, vol. 26, pp. 17–22, Jan. 1983. Publisher: Taylor & Francis _eprint: https://doi.org/10.1179/pom.1983.26.1.17.

[136] A. Rayner, "SUPERSOLIDUS LIQUID PHASE SINTERING AND GRAIN GROWTH ACTIVATION IN A METAL INJECTION MOLDED NICKEL-BASE SUPERALLOY," Apr. 2020. Accepted: 2020-04-09T17:41:49Z.

[137] W. W. Smeltzer, "Oxidation of Aluminum in the Temperature Range 400°–600°C," *Journal of The Electrochemical Society*, vol. 103, p. 209, Apr. 1956. Publisher: IOP Publishing.

[138] U. R. Evans, "Oxidation of iron in the range 100–400°C," *Nature*, vol. 164, pp. 909–910, Nov. 1949. Number: 4178 Publisher: Nature Publishing Group.

[139] A. Zahs, M. Spiegel, and H. J. Grabke, "Chloridation and oxidation of iron, chromium, nickel and their alloys in chloridizing and oxidizing atmospheres at 400–700°C," *Corrosion Science*, vol. 42, pp. 1093–1122, June 2000.

[140] R. M. GERMAN, "Supersolidus liquid phase sintering. II: Densification theory," *Supersolidus liquid phase sintering. II: Densification theory*, vol. 26, no. 1, pp. 35–43, 1990.

[141] R. M. GERMAN, "Supersolidus liquid phase sintering. I: Process review," *Supersolidus liquid phase sintering. I: Process review*, vol. 26, no. 1, pp. 23–34, 1990.

[142] R. M. German and Z. A. Munir, "Surface Area Reduction During Isothermal Sintering," *Journal of the American Ceramic Society*, vol. 59, no. 9-10, pp. 379–383, 1976. _eprint: https://onlinelibrary.wiley.com/doi/pdf/10.1111/j.1151-2916.1976.tb09500.x.

[143] R. German, *Sintering: From Empirical Observations to Scientific Principles*. Butterworth-Heinemann, Feb. 2014. Google-Books-ID: eimSAgAAQBAJ.

[144] R. M. German and K. S. Churn, "Sintering Atmosphere Effects on the Ductility of W- Ni-Fe Heavy Metals," *Metallurgical Transactions A*, vol. 15, pp. 747–754, Apr. 1984.

[145] R. M. German, "Prediction of sintered density for bimodal powder mixtures," *Metallurgical Transactions A*, vol. 23, pp. 1455–1465, May 1992.

[146] R. M. German, "The contiguity of liquid phase sintered microstructures," *Metallurgical Transactions A*, vol. 16, pp. 1247–1252, July 1985.

[147] J. L. JOHNSON and R. M. GERMAN, "Chemically activated liquid phase sintering of tungsten-copper," *Chemically activated liquid phase sintering of tungsten-copper*, vol. 30, no. 1, pp. 91–102, 1994. Place: Princeton, NJ Publisher: APMI International.

[148] J. Liu, A. Lal, and R. M. German, "Densification and shape retention in supersolidus liquid phase sintering," *Acta Materialia*, vol. 47, pp. 4615–4626, Dec. 1999.

[149] K. S. Hwang, R. M. German, and F. V. Lenel, "Capillary forces between spheres during agglomeration and liquid phase sintering," *Metallurgical Transactions A*, vol. 18, pp. 11–17, Jan. 1987.

[150] R. M. German, "Supersolidus liquid-phase sintering of prealloyed powders," *Metallurgical and Materials Transactions A*, vol. 28, pp. 1553–1567, July 1997.

[151] R. M. German, *Sintering Theory and Practice*. Jan. 1996. Publication Title: Sintering Theory and Practice ADS Bibcode: 1996stp..book.....G.

[152] S. L. Lu, G. K. Meenashisundaram, P. Wang, S. M. L. Nai, and J. Wei, "The combined influence of elevated pre-sintering and subsequent bronze infiltration on the microstructures and mechanical properties of 420 stainless steel additively manufactured via binder jet printing," *Additive Manufacturing*, vol. 34, p. 101266, Aug. 2020.

[153] S. Cui, S. Lu, K. Tieu, G. K. Meenashisundaram, L. Wang, X. Li, J. Wei, and W. Li, "Detailed assessments of tribological properties of binder jetting printed stainless steel and tungsten carbide infiltrated with bronze," *Wear*, vol. 477, p. 203788, July 2021.

[154] L. Sun, Y.-H. Kim, D. D.-W. Kim, and P. Kwon, "Densification and Properties of 420 Stainless Steel Produced by Three-Dimensional Printing With Addition of Si3N4 Powder," *Journal of Manufacturing Science and Engineering*, vol. 131, Oct. 2009.

[155] J. L. Johnson, J. J. Brezovsky, and R. M. German, "Effect of liquid content on distortion and rearrangement densification of liquid-phase-sintered W-Cu," *Metallurgical and Materials Transactions A*, vol. 36, pp. 1557–1565, June 2005.

[156] J. L. Johnson, A. Upadhyaya, and R. M. German, "Microstructural effects on distortion and solid-liquid segregation during liquid phase sintering under microgravity conditions," *Metallurgical and Materials Transactions B*, vol. 29, pp. 857–866, Aug. 1998.

[157] X. Shi, S. Duan, W. Yang, H. Guo, and J. Guo, "Solidification and Segregation Behaviors of Superalloy IN718 at a Slow Cooling Rate," *Materials*, vol. 11, p. 2398, Nov. 2018.

[158] F. Wang, D. Ma, and A. Bührig-Polaczek, "Microsegregation behavior of alloying elements in single-crystal nickel-based superalloys with emphasis on dendritic structure," *Materials Characterization*, vol. 127, pp. 311–316, May 2017.

[159] R. M. German, "Coarsening in Sintering: Grain Shape Distribution, Grain Size Distribution, and Grain Growth Kinetics in Solid-Pore Systems," *Critical Reviews in Solid State and Materials Sciences*, vol. 35, pp. 263–305, Nov. 2010. Publisher: Taylor & Francis _eprint: https://doi.org/10.1080/10408436.2010.525197.

[160] "Sintering of Advanced Materials - 1st Edition."

[161] V. Vitry, *Electroless Nickel-Boron deposits: Synthesis, formation and characterization; Effect of heat treatments; Analytical modeling of the structural state*. PhD thesis, Jan. 2010.

[162] M. Beletskij, A. Gajdarenko, and G. Batalin, "Contact interaction of KH20N80 nichrome with boron nitride," *Poroshk Metall*, no. 5, pp. 31–39, 1976. Place: USSR INIS Reference Number: 8332261.

[163] V. V. Skorokhod, "Development of the ideas of Ya. I. Frenkel' in the contemporary rheological theory of sintering," *Powder Metallurgy and Metal Ceramics*, vol. 34, pp. 521–527, Sept. 1996.

[164] E. A. Olevsky, "Theory of sintering: from discrete to continuum," *Materials Science and Engineering: R: Reports*, vol. 23, pp. 41–100, June 1998.

[165] P. Raj, A. Odulena, and W. Cannon, "Anisotropic shrinkage during sintering of particle-oriented systems—numerical simulation and experimental studies," 2002.

[166] M. Reiterer, T. Kraft, and H. Riedel, "Manufacturing of a gear wheel made from reaction bonded alumina—numerical simulation of the sinterforming process," *Journal of the European Ceramic Society*, vol. 24, pp. 239–246, Jan. 2004.

[167] K. Shinagawa, "Micromechanical modelling of viscous sintering and a constitutive equation with sintering stress," *Computational Materials Science*, vol. 13, pp. 276–285, Jan. 1999.

[168] C. Nguyen Van, S. Sistla, and S. van Kempen, "A comparative study of different sintering models for Al2O3," *Journal of the Ceramic Society of Japan*, vol. 124, pp. 301–312, Feb. 2016.

[169] N. Cox, "Modeling Shape Distortion of 3-D Printed Aluminum Oxide Parts During Sintering," June 2018. Num Pages: 79 Publisher: University of Pittsburgh.

[170] C. Y. Yap, C. Chua, Z. Dong, Z. Liu, D. Zhang, L. Loh, and S. L. Sing, "Review of selective laser melting: Materials and applications," *Applied Physics Reviews*, vol. 2, p. 041101, Dec. 2015.

[171] J. Kuehndel, B. Kerler, and C. Karcher, "Selective laser melting in heat exchanger development - experimental investigation of heat transfer and pressure drop characteristics of wavy fins," *Heat and Mass Transfer*, vol. 54, Aug. 2018.

[172] D. Lesyk, S. Martinez, V. Dzhemelinkyi, and A. Lamikiz, "Additive Manufacturing of the Superalloy Turbine Blades by Selective Laser Melting: Surface Quality, Microstructure and Porosity," in *New Technologies, Development and Application III* (I. Karabegović,

ed.), Lecture Notes in Networks and Systems, (Cham), pp. 267–275, Springer International Publishing, 2020.

[173] L. Fratalocchi, G. Groppi, C. Visconti, L. Lietti, and E. Tronconi, "Adoption of 3D printed highly conductive periodic open cellular structures as an effective solution to enhance the heat transfer performances of compact Fischer-Tropsch fixed-bed reactors," *Chemical Engineering Journal*, vol. 386, p. 123988, Dec. 2019.

[174] T. Bauer, K. Dawson, A. Spierings, and K. Wegener, "Microstructure and mechanical characterisation of SLM processed Haynes® 230®," 2015.

[175] L. N. Carter, X. Wang, N. Read, R. Khan, M. Aristizabal, K. Essa, and M. M. Attallah, "Process optimisation of selective laser melting using energy density model for nickel based superalloys," *Materials Science and Technology*, vol. 32, pp. 657–661, May 2016. Publisher: Taylor & Francis _eprint: https://doi.org/10.1179/1743284715Y.0000000108.

[176] J. Strößner, M. T., and U. Glatzel, "Mechanical and Microstructural Investigation of Nickel-Based Superalloy IN718 Manufactured by Selective Laser Melting (SLM)," *Advanced Engineering Materials*, vol. 17, June 2015.

[177] M. L. Montero-Sistiaga, S. Pourbabak, J. Van Humbeeck, D. Schryvers, and K. Vanmeensel, "Microstructure and mechanical properties of Hastelloy X produced by HP-SLM (high power selective laser melting)," *Materials & Design*, vol. 165, p. 107598, Mar. 2019.

[178] A. Spierings, T. Bauer, K. Dawson, A. Colella, and K. Wegener, "PROCESSING ODS MODIFIED IN 625 USING SELECTIVE LASER MELTING," 2015.

[179] C. Jang, D. Kim, D. Kim, I. Sah, W.-S. Ryu, and Y.-s. Yoo, "Oxidation behaviors of wrought nickel-based superalloys in various high temperature environments," *Transactions of Nonferrous Metals Society of China*, vol. 21, pp. 1524–1531, July 2011.

[180] C. Kenel, A. De Luca, S. S. Joglekar, C. Leinenbach, and D. C. Dunand, "Evolution of Y2O3 dispersoids during laser powder bed fusion of oxide dispersion strengthened Ni-Cr-Al-Ti gamma/gamma' superalloy," *Additive Manufacturing*, vol. 47, p. 102224, Nov. 2021.

[181] C. Dai, C. Schade, and D. Apelian, "Processing Techniques for ODS Stainless Steels," *Metallurgical and Materials Transactions. B, Process Metallurgy and Materials Processing Science*, vol. 49, Dec. 2018.

[182] "Principal Features."

[183] T. Peng and C. Chen, "Influence of energy density on energy demand and porosity of 316L stainless steel fabricated by selective laser melting," *International Journal of Precision Engineering and Manufacturing-Green Technology*, vol. 5, pp. 55–62, Jan. 2018.

[184] Y. Zhong, L. Liu, J. Zou, X. Li, D. Cui, and Z. Shen, "Oxide dispersion strengthened stainless steel 316L with superior strength and ductility by selective laser melting," *Journal of Materials Science & Technology*, vol. 42, pp. 97–105, Apr. 2020.

[185] T. Boegelein, S. N. Dryepondt, A. Pandey, K. Dawson, and G. J. Tatlock, "Mechanical response and deformation mechanisms of ferritic oxide dispersion strengthened steel structures produced by selective laser melting," *Acta Materialia*, vol. 87, pp. 201–215, Apr. 2015.

[186] T. Boegelein, E. Louvis, K. Dawson, G. Tatlock, and A. Jones, "Characterisation of a complex thin walled structure fabricated by selective laser melting using a ferritic oxide dispersion strengthened steel," *Materials Characterization*, vol. 112, Nov. 2015.

[187] M. Ghayoor, K. Lee, Y. He, C.-h. Chang, B. K. Paul, and S. Pasebani, "Selective laser melting of austenitic oxide dispersion strengthened steel: Processing, microstructural evolution and strengthening mechanisms," *Materials Science and Engineering: A*, vol. 788, p. 139532, June 2020.

[188] S. Zhang, Y. Lei, Z. Chen, W. Pei, W. Liu, S. Yao, and B. Lu, "Effect of Laser Energy Density on the Microstructure andTexture Evolution of Hastelloy-X Alloy Fabricated by Laser Powder Bed Fusion," *Materials*, vol. 14, p. 4305, July 2021.

[189] A. J. Ramirez and J. C. Lippold, "High temperature behavior of Ni-base weld metal: Part II – Insight into the mechanism for ductility dip cracking," *Materials Science and Engineering: A*, vol. 380, pp. 245–258, Aug. 2004.

[190] J. H. Boswell, D. Clark, W. Li, and M. M. Attallah, "Cracking during thermal post-processing of laser powder bed fabricated CM247LC Ni-superalloy," *Materials & Design*, vol. 174, p. 107793, July 2019.

[191] E. Yasa, J. Deckers, and J. Kruth, "The investigation of the influence of laser re-melting on density, surface quality and microstructure of selective laser melting parts," *Rapid Prototyping Journal*, vol. 17, pp. 312–327, Jan. 2011. Publisher: Emerald Group Publishing Limited.

[192] J. W. Xie, P. Fox, W. O'Neill, and C. J. Sutcliffe, "Effect of direct laser re-melting processing parameters and scanning strategies on the densification of tool steels," *Journal of Materials Processing Technology*, vol. 170, pp. 516–523, Dec. 2005.

[193] J. Xu, Y. Ding, Y. Gao, H. Wang, Y. Hu, and D. Zhang, "Grain refinement and crack inhibition of hard-to-weld Inconel 738 alloy by altering the scanning strategy during selective laser melting," *Materials & Design*, vol. 209, p. 109940, Nov. 2021.

[194] D. Wang, S. Wu, F. Fu, S. Mai, Y. Yang, Y. Liu, and C. Song, "Mechanisms and characteristics of spatter generation in SLM processing and its effect on the properties," *Materials & Design*, vol. 117, pp. 121–130, Mar. 2017.

[195] V. Gunenthiram, P. Peyre, M. Schneider, M. Dal, F. Coste, I. Koutiri, and R. Fabbro, "Experimental analysis of spatter generation and melt-pool behavior during the powder bed laser beam melting process," *Journal of Materials Processing Technology*, vol. 251, pp. 376–386, Jan. 2018.

[196] N. Farjam, M. Nematollahi, M. Taheri Andani, M. J. Mahtabi, and M. Elahinia, "Effects of size and geometry on the thermomechanical properties of additively manufactured NiTi shape memory alloy," *The International Journal of Advanced Manufacturing Technology*, vol. 107, Apr. 2020.

[197] L. Cai and S. Y. Liang, "Analytical Modelling of Temperature Distribution in SLM Process with Consideration of Scan Strategy Difference between Layers," *Materials*, vol. 14, p. 1869, Jan. 2021. Number: 8 Publisher: Multidisciplinary Digital Publishing Institute.